UNIVERSITY OF NAPLES FEDERICO II
Department of Structures for Engineering and Architecture

PH.D. PROGRAMME IN STRUCTURAL ENGINEERING,
GEOTECHNICS AND SEISMIC RISK
COORDINATOR PROF. IUNIO IERVOLINO
XXXIV CYCLE

FAUSTO SOMMA

PH.D. THESIS

The contribution of Geotechnical Seismic Isolation to the mitigation of seismic risk on existing buildings

TUTOR PROF. ALESSANDRO FLORA
CO-TUTOR PROF. EMILIO BILOTTA

2022

Old Walking Song

The Road goes ever on and on
Down from the door where it began.
Now far ahead the Road has gone,
And I must follow, if I can,
Pursuing it with eager feet,
Until it joins some larger way
Where many paths and errands meet.
And wither then? I cannot say.

The Road goes ever on and on
Out from the door where it began.
Now far ahead the Road has gone,
Let others follow it who can!
Let them a journey new begin,
But I at last with weary feet
Will turn towards the lighted inn,
My evening-rest and sleep to meet.

Still round the corner there may wait
A new road or a secret gate;
And though I oft have passed them by,
A day will come at last when I
Shall take the hidden paths that run
West of the Moon, East of the Sun.

Tolkien, The Lord of the Rings

Il canto della Strada

La Via prosegue senza fine
Lungi dall'uscio dal quale parte.
Ora la Via è fuggita avanti,
Devo inseguirla ad ogni costo
Rincorrendola con piedi alati
Sin all'incrocio con una più larga
Dove si uniscono piste e sentieri.
E poi dove andrò? Nessuno lo sa.

La Via prosegue senza fine
Lungi dall'uscio dal quale parte.
Ora la Via è fuggita avanti,
Presto, la segua colui che parte!
Cominci pure un nuovo viaggio,
Ma io che sono assonnato e stanco
Mi recherò all'osteria del villaggio
E dormirò un sonno lungo e franco

Voltato l'angolo forse si trova
Un ignoto portale o una strada nuova;
Spesso ho tirato oltre, ma chissà,
Finalmente il giorno giungerà,
E sarò condotto dalla fortuna
A est del Sole, ad ovest della Luna

Tolkien, Il Signore degli Anelli

Ringraziamenti

I miei più sentiti ringraziamenti vanno:

- **Al Prof. Ing. Flora** per avermi dato l'opportunità, con grande professionalità ed esperienza, di sviluppare una tematica quale l'Isolamento Sismico Geotecnico che ho fin da subito amato. Grazie per aver sempre creduto in me e per avermi trattato mai da Studente ma da Collega ed Amico e avermi difeso in molte occasioni.
- **Al Prof. Ing Bilotta** per tutto il tempo dedicatomi, per gli indispensabili consigli che mi ha fornito, per essere riuscito sempre a creare sempre la situazione più idonea alla mia ricerca.
- **Alla Prof. Ing. Viggiani** per come sono stato accolto in Cambridge, per ogni parola che ha speso riguardo la mia ricerca, fonte di saggezza e conoscenza.
- **A mio Padre ed alla mia famiglia Tutta** che mi ha sempre dispensato di saggi consigli, i quali nei momenti più difficili di questo cammino sono stati come una sorgente di nuova forza.
- **Ad Eva Cozzolino**, senza la quale, forse, oggi, non sarei qui a scrivere questi ringraziamenti per la mia tesi di dottorato. Nei momenti più bui di questo percorso ci sei sempre stata.
- **Al Cielo ed al Mare ed alla mia Terra,** che ogni mattina di questi quasi quattro anni ho avuto la fortuna di vedere.
- **Alla Musica** mia eterna accompagnatrice di vita.

Questo lavoro di tesi è stato finanziato nell'ambito nel Progetto POR CAMPANIA FSE 2014/2020 – Asse III – obiettivo specifico 14 – azione 10.4.5 – Dottorati di Ricerca con Caratterizzazione industrale – XXXIV ciclo. Ringrazio, inoltre, l'azienda Partner Keller Holding ed in particolare l'Ing. Clemens Kummerer per il supporto fornito ed per i significativi contributi che ha apportato a tale ricerca.

Candidate's declaration

I hereby declare that this thesis submitted to obtain the academic degree of Philosophiæ Doctor (Ph.D.) in Ingegneria Strutturale, Geotecnica e Rischio Sismico is my own unaided work, that I have not used other than the sources indicated, and that all direct and indirect sources are acknowledged as references.

Parts of this dissertation have been published in international journals and/or conference articles (see list of the author's publications at the end of the thesis).

Napoli, March 01, 2022

Summary

List of Figures

Chapter 2

Chapter 3

Chapter 4

Chapter 5

List of Tables

Chapter 3

Chapter 4

Chapter 5

1. INTRODUCTION

1.1 Overview

"*People are killed by buildings, not by earthquakes*"

These words were pronounced by the Priest Domenico Pompili during the commemoration for the victims of Amatrice earthquake (24 August 2017→299 dead, 388 injured).

There are approximately fifteen thousand earthquakes per year worldwide above magnitude four on the Richter scale. Most of these earthquakes occur in remote locations and have little impact on communities. However, when large earthquakes do occur close to densely populated areas, as happened in Haiti (Jan 2010), Sumatra (Dec 2004) and Christchurch, New Zealand (Feb & Dec 2011), large numbers of casualties and fatalities can occur. In the last ten years there have been over six hundred thousand people killed as a consequence of earthquake damage; over two hundred and thirty thousand of these fatalities being a consequence of the Haiti earthquake alone. Even in economically developed countries with established engineering practises regarding earthquake resistant design and construction of buildings, building collapse still frequently occur (i.e. Amatrice Aug 2014, Emilia May 2012, Aquila Dec 2009).

There are two options when designing a structure itself to withstand seismic loading. The structure can be designed to be strong and stiff, leading to an expensive design using a lot of construction materials (in addition, this can lead to limitations on the architectural design as the need for shear walls to provide rigidity reduces the possibility for open plan spaces). Alternatively, the structure can be designed to be flexible such that it is capable of deforming when subjected to seismic loading without experiencing damage. The deforming structure will dissipate energy through either inherent structural damping or with the aid of additional engineered structural damping solutions.

Currently, structural engineers tend to lead construction projects and sub-contract the design of the foundations to geotechnical engineers. Due to the conception that soil, as an engineering material, is challenging to understand and predict the behaviour of, the structural engineers often request foundations to be designed in such a way that little relative movement will occur between the soil and the foundation slab. This almost perfect coupling between the soil and foundation results in the foundation being subjected to the full force of the earthquake. Therefore, to minimise the energy transfer into the superstructure, a system can be implemented between the foundation and the structure in order to isolate the structure from the shaking motion. There is a huge amount of research and literature on structural isolating systems, whose detailed description is out of the scope of this thesis. The isolation system normally consists of rubber shear bearing blocks or roller bearings, both allowing the foundation to move during seismic shaking while the structure above remains relatively stationary. Such methods have been widely implemented and have been shown to be very effective at protecting structures from seismically induced damage. However, this isolation method requires high quality design and construction procedures leading to costly designs. Furthermore, in many countries, like Italy, a large part of the existing buildings are old or extremely old, some dating back centuries, and most of the modern constructions were designed in the early 1950s-60s, in the post second world war reconstruction effort, with little or no care to concepts of anti-seismic design. Nowadays, one of the most important challenges of civil engineering is therefore to ensure that an existing building, designed without any anti-seismic design criteria, will not collapse during a strong earthquake. A simple anecdote can well express the complexity of the problem when dealing with existing – i.e. old or very old - buildings:

"It is easier to raise a child than taking care of an elderly person"

This anecdote highlights the simplicity of designing a new building in contrast with the difficulties of seismically retrofitting existing ones. In fact, especially in some contexts (i.e. in all the the historical centers of Italian cities), this objective can be particularly difficult to achieve without affecting the aesthetic and material integrity of the structures themselves.

Questions therefore arise as to why rubber bearings are being used between a foundation designed to interact with the soil in a rigid manner and the superstructure when, if it were allowed for in design, the soil itself could act as a ‘rubber’ bearing.

Geotechnical Seismic Isolation (G.S.I.) could be the solution as it is not invasive for the structure and can guarantee excellent anti-seismic improvements. The basic idea of geotechnical seismic isolation is to modify the soil around the structure, or part of it, to ensure a different soil-structure interaction in such a way to mitigate the seismic action on the building itself. Using the soil to dissipate energy would allow for simpler design, simpler construction and significantly reduced costs. The issue with this design philosophy is that it is not currently easy to predict the settlements, rotations and degree of isolation that will occur by allowing a less rigid connection between the foundation and the soil. This is because soil is a highly complicated material, especially when heterogeneity and soil stratification occur below the foundation.

1.2 Scope of Work, Contributions, and Objectives

This new research aims to study two different geotechnical seismic isolation techniques. Experimental and numerical results will allow to highlight the strengths and weaknesses of the proposed techniques. The technological aspects will also be addressed to ensure the applicability of such techniques on real buildings.

In particular, the following were specific objectives of this research:

- Investigate the "*Shallow Foundation Lateral Disconnection from the soil"* from a dynamic and static point of view highlighting the parameters that most control the effects of this technique.
- Investigate the "*Soft Lateral and Horizontal Inclusions"* from a dynamic point of view.
- Use the two different technique on a complex real case study to show the applicability of these ideas.
- Highlight the importance of considering the effect of soil-structure-interaction and local seismic response on the dynamic response of structures.

1.3 Structure of the Thesis

As will be shown, this thesis develops and deepens two different ideas of Geotechnical Seismic Isolation. The thesis will be articulated in the following chapters:

Chapter two will deal with the review literature about the Geotechnical Seismic Isolation and the Soil Structure Interaction. In particular, this chapter highlights all the fundamental aspects of the Geotechnical Seismic Isolation. To this aim, ample space will be also given to the Soil Structure Interaction literature as knowledge of these aspects is essential for any type of GSI intervention.

Chapter three will deal with the "*Shallow Foundation Lateral Disconnection from the soil*". This first geotechnical seismic isolation technique is completely new in the world of research. It is based on removing the lateral soil adjacent to buildings footing. In some conditions, this simple technique can greatly contribute to the period increase and, depending on different parameters, reduce the seismic actions that will affect the structure. Starting from a centrifuge test conducted at the University of Cambridge, it was possible to validate the effectiveness of the technique, and then numerically investigate various some a-dimensional parameter controlling the effect of this technique.

Chapter Four, will deal with the "*Soft Lateral and Horizontal Inclusions as seismically isolated barrier*". Starting from a severe dynamic characterization of the material to be used for the creation of the soft barriers, it was possible to know the dynamic properties of these mixtures such as shear waves velocity or mobilized damping. Both one- and two-dimensional analyses were carried out to evaluate the effectiveness of this technique. A rigorous design procedure is outlined showing, in addition, the possibility of using simplified design tools such as dynamic two degree of freedom system. Finally, through the collaboration with the partner company Keller Holding, different technological alternatives have been proposed in order to create such soft barriers in the ground.

Chapter Five will deal with a case study. The two geotechnical seismic isolation techniques will be implemented for an historic building, specifically Tower 19 of the walls of Constantinople (UNESCO site). The building was modelled starting from the available drawings and plans, and then characterized materially through current knowledge. One-dimensional and three-dimensional analyses allowed to know with sufficient reliability the conditions in which Tower 19 stood before the Kocaeli earthquake almost entirely destroyed it. The two techniques of geotechnical seismic isolation are proposed and implemented showing the benefits but also the undesired effects.

Chapter 6 will discuss the conclusions and the possible developments of this thesis work.

2. LITERATURE REVIEW

2.1 Introduction

Earthquakes generate the majority of casualty losses worldwide (Figure 2. 1, relative to the 20-year period 1998-2017).

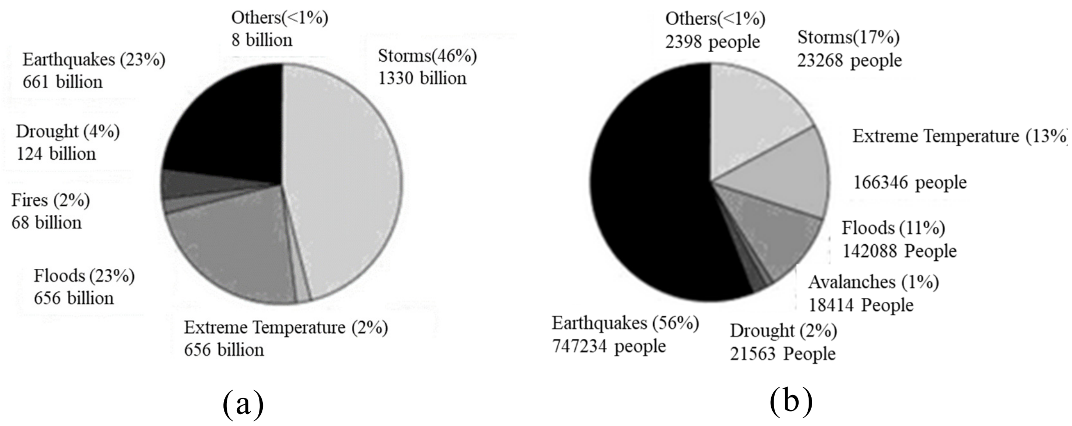

Figure 2. 1. (a) Relative importance of earthquakes among natural events in the 20-year period 1998-2017 concerning economic losses in billions of US dollars and (b) victims (Modified from Iervolino, 2021)

However, earthquakes cause losses predominantly through their effects on civil works. For this reason, generally, the seismic design is the most important in structural engineering. This thesis focuses on some innovative approaches to deal with one of the biggest challenges for civil engineers, i.e. the reduction of seismic risk (R). The seismic risk can be formally defined as, Eq.(2. 1):

$$R = H \cdot V \cdot E \tag{2. 1}$$

where:

- H is called hazard, that is the probability of exceedance of a given level of a selected strong ground motion parameter in a given time interval;
- V is the vulnerability, that is the probability of exceeding a given damage level due to the occurrence of a given ground motion level;
- E is the exposure, a qualitative and quantitative estimation of the elements at risk;

In the performance-based design approach, the two key elements for a seismic safety assessment of a building are the seismic demand and the capacity curve. This latter is often referred to as a ‘pushover curve’, relating the base shear force, V_b, to a reference horizontal displacement, Δ, for instance at the top of the building (Figure 2. 2a). The seismic demand for the pseudo-static analysis of a rigid system can be typically defined in terms of a seismic coefficient (proportional to the design peak ground acceleration, a_{max}); for deformable systems, the most conventional way to express it is by using the spectral acceleration $S_a(T)$, the spectral displacement $S_d(T)$, or both (Figure 2. 2b). For a structure with a given fundamental period, T, $S_a(T)$ and $S_d(T)$ can be viewed as proportional to the above-defined shear force and displacement, respectively. As a consequence, they represent a convenient and synthetic way to analyse seismic demand. $S_a(T)$ and $S_d(T)$ depend on the regional seismic hazard, the seismic site response and the system ductility. For example, considering the typical seismic Hazard of the Italian Apennines, it is expected that structures characterised by a low natural period (*i.e.* less than 0.4-0.5sec) of vibration will be subject to high demands in terms of acceleration but low demands in terms of displacement. Conversely, structures with a high natural period of vibration will experience high displacements but low accelerations. The safety assessment can therefore be expressed by comparing demand and capacity, individuating a ‘performance point’ at the intersection of the curves. If such a performance point does not exist (i.e. the capacity is lower than the demand, and safety cannot be guaranteed) or it is too close to the limit capacity (i.e. the safety margins are not sufficient or do not respect codes of practice specifications), seismic risk mitigation interventions are necessary.

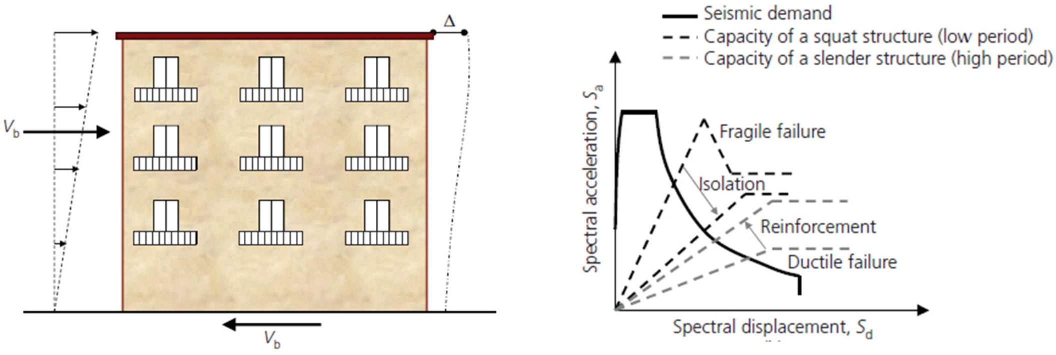

(a) (b)

Figure 2. 2.(a) Scheme adopted for a Push Over Analysis; (b) Different kind of structural possibility to increase the structural vulnerability (modified from Lombardi, 2014)

Nowadays, with reference both to existing and new buildings, a certain number of techniques has been developed to tackle seismic risk. Considering the exposure (E) as a parameter that cannot be modified, the only way to deal with the risk reduction is to modify the seismic vulnerability or the seismic hazard. Theoretically, the two approaches should be joined in order to obtain the best possible mitigation effect (Dolce, 2010). However, since the seismic site hazard depends on physical variables that are very difficult to be modified, the common sense suggests the possibility of modify only the structural seismic vulnerability. Indeed, the foremost solution to tackle seismic risk R for existing structures is structural retrofitting, i.e. the use of structural techniques aimed at reducing the vulnerability V. Specific techniques such as reinforcing both beams or columns tend to stiffen the structure and lowering the natural period of vibration. For this reason, a lower displacement demand is expected. Other techniques tend to increase the global ductility of the structure without modifying its stiffness (for example, the use of *Fiber Reinforcement Polymer*). Achieving equality between system capacity and seismic demand is called *"Total Seismic Retrofitting"* while increasing the seismic capacity of a building without matching its seismic demand is called *“Partial Seismic Retrofitting”*. In the case of old or very old structures it is practically impossible to achieve the *"Total Seismic Retrofitting"* with canonical structural techniques and other systems, such as seismic isolation, are necessary.

Currently, it is common for new strategic structures to design specific structural element such as seismic isolators and or seismic dampers. In order to increase the fundamental period of the isolated system (i.e. structure plus isolation system), the traditional seismic isolation, usually, involves the addition of elements of very low stiffness and high dissipative capacity compared to those of the structure to be isolated. In this way, the system is in an area of the response spectrum where accelerations are particularly low and therefore the stresses transmitted to the superstructure are low (Figure 2. 3a). For this reason, a large spectral displacement demand is expected. However, this huge displacement demand will be concentrated in the isolation system (Figure 2. 3b).

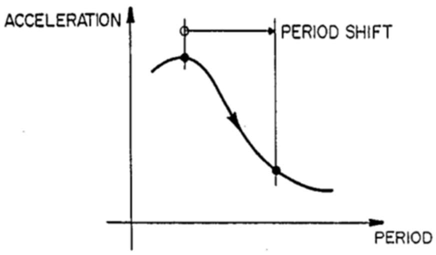

(a)

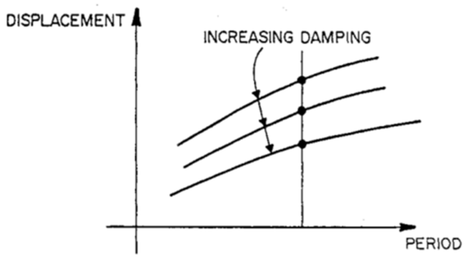

(b)

Figure 2. 3. (a) Reduction in spectral acceleration; (b) Increase in spectral total displacement

The design of the isolation system requires that special attention is given to the local seismic hazard and to the accepted level of risk. In fact, it may happen that, due to particular stratigraphic conditions, there are significant amplifications of accelerations for high periods of vibration. The likelihood of these types of motions occurring at a particular site can sometimes be foreseen, such as with deep deposits of soft soil which may amplify low-frequency earthquake motions; the old lake bed zone of Mexico City being the best-known example. However, while the implementation of a structural seismic isolation is relatively simple in the construction of a new buildings, for existing structures this can be extremely complex or in some cases impossible. It is still possible to increase the seismic capacity with traditional structural interventions but in the case of buildings of historical or architectonical relevance these structural solutions cannot be considered satisfactory. Indeed, traditional techniques are not suitable for cultural heritage buildings because of different reasons:

- Are based on the increasing of strength and ductility
- Are often not reversible
- Make use of materials different and incompatible with the original ones
- Determine changes of the original structural conception
- Under earthquakes of high intensity can just guarantee against the collapse cannot avoid heavy damage to structural and non-structural elements. Existing historic buildings have usually been designed without accounting the seismic actions and are vulnerable even to moderate events because of:
    - irregular shape, both in plan and in elevation.
    - not effective vertical connections between the walls.
    - in-plane flexibility of floor slabs.
    - shallow foundations.

Furthermore, the seismic rehabilitation of historic buildings is quite delicate due to the very high safety level required and to the daily presence of tourists. As matter of fact, the seismic protection of existing buildings, especially the historical ones, is still an issue.

Perhaps solving this engineering challenge requires asking equally bold questions: How many other anti-seismic intervention techniques can be found if the structure is considered as a system that interacts with the surrounding ground?

A possible alternative approach to modify the energy and frequency content of the seismic actions transferred to the superstructure without interposing a structural isolator may be to implement the isolation system in the subsoil. This is referred to as Geotechnical Seismic Isolation (GSI), in contrast to the most commonly used Structural Seismic Isolation (SSI) (Tsang, 2009). Before discussing about the GSI, a brief overview on the principles of soil-structure interaction will be delineated as knowledge of these issues is fundamental to understanding any GSI technology.

2.2 Soil Structure Interaction

As already outlined, this thesis will investigate two seismic isolation technique called *"Lateral disconnection of foundations from adjacent soil"* and *"SAP-sand mixtures as seismically isolating barrier"*. As will be seen later, both techniques presuppose knowledge of the principles of dynamic soil-structure interaction.

2.2.1 Introduction

The response of a structure under seismic conditions strongly depends on the geometric and mechanical characteristics of the foundation and the significant volume of soil, as well as on the characteristics of the seismic input. Specifically, the presence of the foundation within the soil modifies the characteristics of the motion that stresses the superstructure. The foundation, in fact, typically has a different stiffness from that of the surrounding soil, opposing the motion imposed by the latter and reflecting part of the incident seismic waves. The motion of the foundation structure (Foundation Input Motion, hereinafter FIM) is, therefore, generally different from the free-field conditions. This effect, usually referred to as *"kinematic interaction"*, is particularly pronounced in the presence of caisson as foundation structures, due to their high stiffness and the fact that they are in contact with the ground for a large part of their height. The superstructure is also subject to the inertia forces generated by the earthquake, thus imposing additional stresses and displacements on the foundation structure: this phenomenon is referred to as *"inertial interaction"*. The two interaction phenomena are simultaneous and influence each other. As matter of fact, the dynamic characteristics of the structure are different from those of the superstructure in a fixed base condition. Due to the deformability of the foundation soil, the soil-foundation-structure system is characterised by an equivalent period (T_{eq}) greater than the fixed base one (T_s); furthermore, since the energy introduced into the system by the earthquake can be dissipated not only within the superstructure, but also within the soil by radiation (geometric damping) and hysteresis (material damping), the damping ratio of the system (ξ_{eq}) is also typically greater than that of the superstructure (ξ_s). Generally, these effects are considered beneficial. Indeed, while the period lengthening leads to lower spectral accelerations the increase of damping generates an homothetic reduction of the acceleration spectrum (Figure 2. 4).

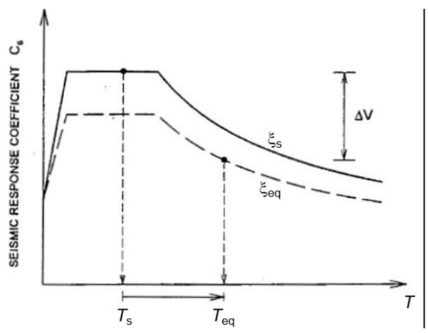

Figure 2. 4. Reduction in shear at the base of the superstructure caused by the increase in eigen period and damping ratio as a result of soil-structure interaction phenomena (modified from Mylonakis and Gazetas, 2000).

The soil-structure interaction is therefore rarely considered in the design as the fixed base condition is considered cautelative. This approach, however, is not rigorous for several reasons. First of all, the decrease in base shear for high periods depends on the properties of the seismic input and of the foundation soils; Mylonakis and Gazetas (2000) showed that some recordings referring to high intensity seismic events can present the maximum spectral ordinates for high periods, greater than 1 s (Figure 2. 5).

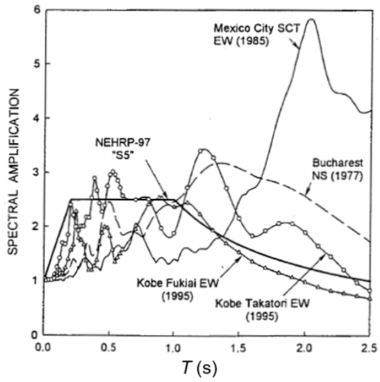

Figure 2. 5. Comparison of design response spectrum and spectra of catastrophic seismic events characterised by maximum values for high periods (modified from Mylonakis and Gazetas, 2000).

Moreover, in a performance approach, the assessment of the displacements of the structure is a central aspect: since the spectral displacement typically increases with period, neglecting the change in dynamic characteristics generating by the soil-structure interaction would lead to an underestimation of the displacements of the structure. In addition, not considering the foundation-soil system and its dissipative capacity leads to an "unbalanced" design, in which all energy dissipation is concentrated in the superstructure (Anastasopoulos *et al.*, 2010; Godoy *et al.*, 2012; Drosos *et al.*, 2012; Zafeirakos and Gerolymos, 2012; Gazetas, 2015). Finally, the motion at the base of the superstructure (FIM) is not equal to the motion free field conditions.

In order to study the soil-foundation-structure interaction, it is necessary to understand the type of foundation as function of its slenderness ratio (Figure 2. 6).

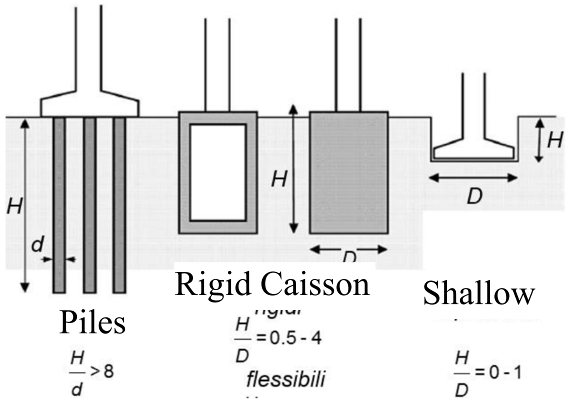

Figure 2. 6. Classification of foundations according to slenderness ratio (modified from Gerolymos and Gazetas, 2006 a).

In the scientific literature we refer to "embedded shallow foundations" for foundations characterised by an *H/D* ratio (ratio between the embedment and the width of foundation) between 0.5 and 1 (Elsabee and Morray, 1977; Gazetas, 1991 a, b; Conti *et al*., 2015), and to "caisson foundations" for *H/D* between 2 and 6 (Varun *et al*., 2009). For this type of foundation, the resistant mechanism to external actions is characterised by comparable contributions of the base and lateral surface, in contrast to shallow foundations and piles. In case of shallow foundation, the contribution of the base prevails while in case of piles the contribution the lateral surface prevails.

Different methods can be used to consider the effects described above. In particular, in a direct analysis, the structure and the soil are included in the same model and analysed as a single system. As shown in the Figure 2. 7, the soil is represented as a continuous medium (with finite elements or finite differences methods), capable of transmitting actions to the structure itself.

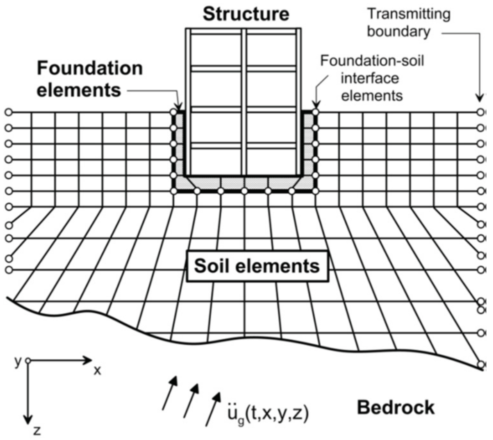

Figure 2. 7. Direct approach model. (from NIST, 2012)

The direct approach is able to describe all the SSI effects; however, it is computationally complex to calibrate and calculate the model, especially when structural or ground non-linearities are included.

In the substructure approach, on the other hand, the soil-structure interaction (SSI) is analysed into different parts which are combined to provide a complete solution. The approach to substructures requires several steps (Figure 2. 8):

1) The computation of free field motions at the base of the structure.
2) The evaluation of the transfer function to convert the free field motion into FIM.
3) The calibration of springs and dampers (or more complex non-linear elements such as macro-elements) to represent the stiffness and damping at the soil-foundation interface.
4) The response of the structure-foundation-ground system.

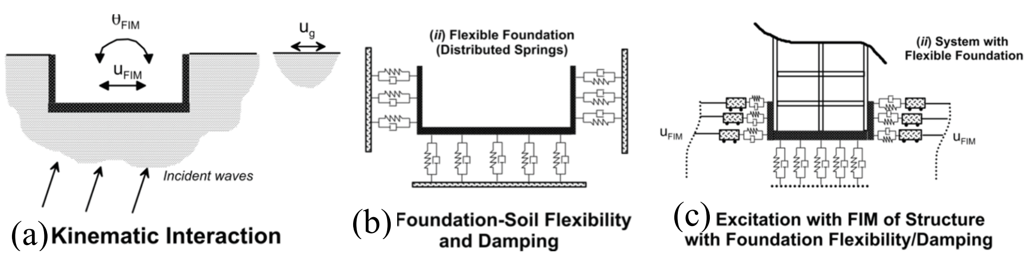

Figure 2. 8. Several steps needed to conduct an analysis using the substructure approach: (a) Kinematic Interaction, (c) calibration of foundation-soil stiffness and dashpot, (c) Excitation with FIM. (modified from NIST, 2012)

2.2.2 Inertial Interaction

As already mentioned, the inertial interaction refers to the shear and moment transmitted to the foundation. For this reason, the foundation will undergo translations and rotations. It is possible to analyze the soil foundation structure interaction with the so-called "*lumped mass models*" (L.M.M.). In order to simulate the link between the forces (moments) applied in the foundation and the resulting displacements (rotations) a nodal mass, representing the foundation, is concentrated at the base of the superstructure, while a further nodal mass, connected in series to that of the foundation, will represents the mass of the superstructure. The foundation-soil system is, therefore, modelled with a set of dynamic impedances, along all degrees of freedom of the foundation. In the hypothesis of a rigid foundation, the degrees of freedom of the foundation in 3D space are six, three associated with translation and three with rigid rotation (Figure 2. 9).

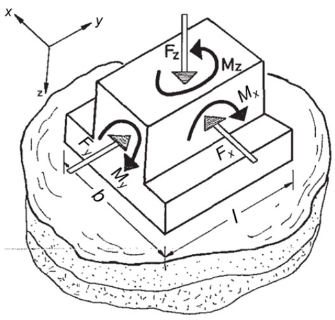

Figure 2. 9. Load applied along the 6 degrees of freedom of an infinitely rigid foundation (modified from Gazetas, 1991 a)

In the hypothesis of a harmonic load applied to the foundation:

$$P(t) = Pcos(\omega t + \alpha) \tag{2. 2}$$

where P represents the amplitude of the applied load, ω is the pulsation and α is the time lag with respect to the instant t = 0. The resulting (generalised) displacement, along the same degree of freedom considered, is characterised, in general, by the same pulsation as the load and by a time shift angle, φ:

$$u(t) = u \cdot \cos(\omega t + \alpha + \varphi) \qquad (2.3)$$

where u represents the amplitude of the displacement. The dynamic impedance is the ratio between the generalised force $P(t)$ and the generalised displacement $u(t)$(Gazetas, 1991 a, b):

$$\widetilde{K} = \frac{P(t)}{u(t)} \qquad (2.4)$$

The expression of the dynamic impedance can be reformulated by expressing (2. 2) and (2. 3) using the complex notation, obtaining:

$$\widetilde{K}(\omega) = K(\omega) + i\omega C(\omega) \qquad (2.5)$$

The impedance $\widetilde{K}$ is represented by a complex number, where $K(\omega)$ is the real part and $C(\omega)$ is the complex part; i is the imaginary number $i = \sqrt{-1}$. The term $K(\omega)$ represents the dynamic stiffness of the foundation - soil system that depends on the pulsation ω of the load, since the latter influences the inertia of the system. The term $C(\omega)$ represents the damping coefficient and includes the two components of energy dissipation generated within the foundation soils: radiation damping (geometrical) and hysteretic (material) damping (Figure 2. 10).

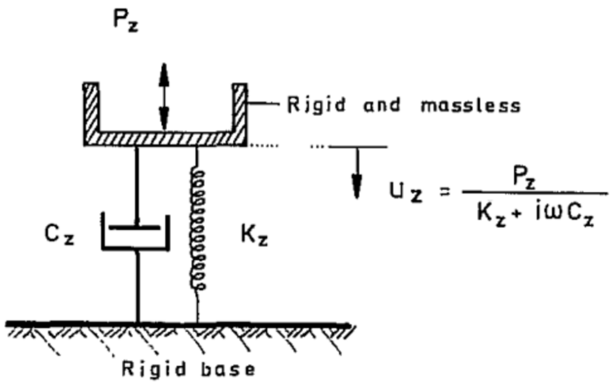

Figure 2. 10. Schematization of the dynamic vertical stiffness and dashpot (modified from Gazetas, 1991 a)

At this point it is necessary to take an insight into the concepts of dynamic stiffness and dynamic damping. In static conditions of load application, it would be very simple to calculate stiffness as the ratio between the applied force (or moment) and the displacement generated (translational or rotational). However, when the load is imposed dynamically, it is necessary to introduce an amplification coefficient to calculate the dynamic displacement. In particular, the dynamic displacement will be equal to the static displacement multiplied by the amplification factor. In general, the amplification factor will depend on the resonance conditions between the frequency of application of the load and the resonance frequency of the system considered ($\frac{\omega}{\omega_0}$). In this specific case, $\frac{\omega}{\omega_0}$ is the ratio between the frequency of the load and the resonance frequency of the foundation system. By means of various mathematical steps, it is possible to prove that the inverse of the amplification factor depends on the factor:

$$\alpha_0 = \omega B / V_S \tag{2. 6}$$

Where B is the width of foundation and $V_S$is the shear waves velocity of the soil in a portion of the ground affected by the foundation-induced motion. Sometimes, it is convenient, to select a single of α_0. This will allow to select a constant value of dynamic stiffness of the foundation during the all seismic excitation. However, in the scientific literature, there is always much ambiguity regarding the physical meaning of ω. Some authors recommend selecting ω as the predominant frequency of the seismic signal, other authors as the predominant period of the structure (i.e. the period associated with the first mode of vibration) (NIST, 2012). Both approaches are a simplification of the correct way to proceed, which would require an update of the dynamic stiffness value as the frequency of applied load changes. Dynamic impedance functions are defined with reference to cyclic pulsation loads but can obviously also be used for non-harmonic loads to be decomposed by Fourier analysis (Gazetas, 1991 a, b). Given the dynamic impedances representative of the foundation-soil system, the inertial interaction analysis is carried out by applying, at the foundation, the FIM (Figure 2. 11).

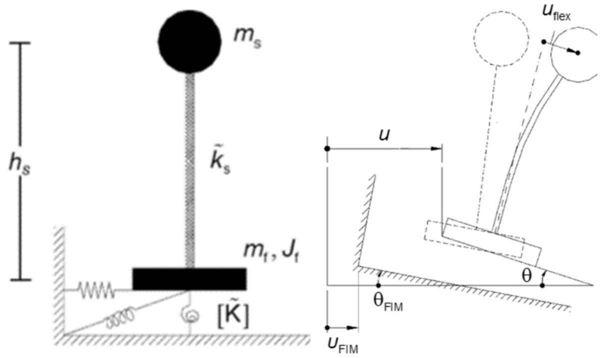

Figure 2. 11. Elemental oscillator and foundation block kinematics for inertial interaction analysis (modified from Mylonakis et al., 2006)

In order to write the dynamic equilibrium equations for the L.M.M., the foundation-soil system could be modelled with a dynamic impedance matrix *[K]*; The structure has a height equal to h_s and could be schematised with a simple visco-elastic linear oscillator with flexural stiffness k_s and damping coefficient c_s with a concentrated mass m_s at the top. The system is subject to the horizontal displacement obtained at ground level in presence of foundation resulting from the vertical propagation of shear waves. The unknowns of the problem are constituted by the time histories of the horizontal displacement and rotation of the foundation, $u(t)$ and $\theta(t)$ respectively, and the horizontal displacement of the concentrated mass associated with the bending of the simple oscillator, $u_{flex}(t)$. The D'Alembert's dynamic equilibrium requires that:

$$\omega^2\{m_f \cdot u(t) + m_s[u(t) + \theta(t) \cdot h_s + u_{flex}(t)]\} = \widetilde{K_{xx}}(\omega) \cdot (u - u_{FIM}) + \widetilde{K_{xr}}(\omega) \cdot (\theta - \theta_{FIM}) \quad (2.\ 7)$$

$$\omega^2\{J_f \cdot \theta(t) + m_f[u(t) + \theta(t) \cdot h_s + u_{flex}(t)] \cdot h_s\} = \widetilde{K_{xr}}(\omega) \cdot (u - u_{FIM}) + \widetilde{K_{rr}}(\omega) \cdot (\theta - \theta_{FIM}) \quad (2.\ 8)$$

$$\omega^2\{m_s[u(t) + \theta(t) \cdot h_s + u_{flex}(t)]\} = \widetilde{k_s} \cdot u_{flex}(t) \quad (2.\ 9)$$

$\widetilde{K_{xx}}$, $\widetilde{K_{xr}}$, $\widetilde{K_{rr}}$, represent the translational, coupled and rotational impedances of the foundation-soil system; $\widetilde{k_s} = k_s + i\omega c_s$ is the dynamic impedance of the elementary oscillator. Equations (2. 7) and (2. 8) represent the translation and rotation equilibrium of the foundation, while equation (2. 9) represents the translation equilibrium of the superstructure mass. Particular attention should be paid to the $\widetilde{K_{xr}}$ and $\widetilde{K_{rx}}$terms of the foundation stiffness matrix. In fact, these terms, especially in the case of deep foundations, assume values comparable with the terms arranged on the main diagonal of the foundation stiffness matrix. In general, for values of *H/B>2* (ratio between the embedment and width of foundation), these terms cannot be ignored. In order to conduct the soil-structure interaction study, it is therefore necessary to calculate u_{FIM} and θ_{FIM} and to evaluate the dynamic stiffness matrix of the foundations.

Sometimes, however, it is only useful to know the period elongation and the increase in damping produced by the deformability of the soil at the base of the structure. Considering a one-degree-of-freedom system characterised by a certain lateral stiffness, *K*, and mass, m, under fixed base conditions (Figure 2. 12a), it is easy to calculate the lateral displacement, *Δ*, as:

$$\Delta = \frac{F}{K} \quad (2.\ 10)$$

The vibration frequency, *ω*, and period, *T*, of the structure will be:

$$\omega = \sqrt{\frac{K}{m}};\ T = \frac{2\pi}{\omega} = 2\pi\sqrt{\frac{m}{K}} \quad (2.\ 11)$$

By combining Eq.(2. 10) with Eq.(2. 11) one can obtain:

$$T^2 = (2\pi)^2 \frac{m}{\left(\frac{F}{\Delta}\right)} = (2\pi)^2 \frac{m\Delta}{F} \quad (2.\ 12)$$

In a complaint base condition, there will be a vertical springs, K_z, horizontal springs, K_x, and rotational springs at the base, K_{yy}, representing the deformability of the soil with respect to the foundation (Figure 2. 12b).

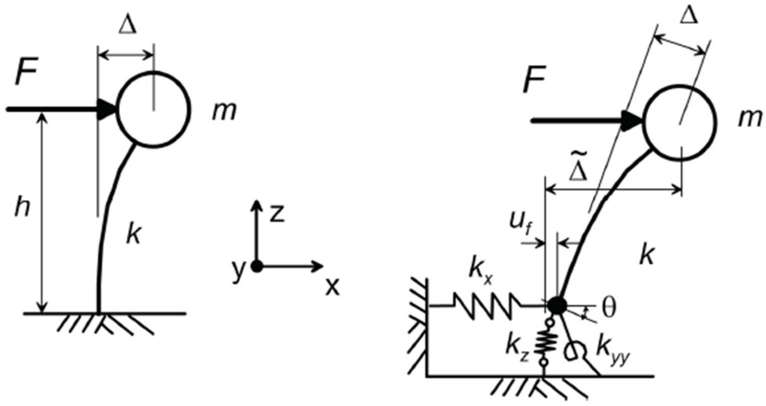

Figure 2. 12.(a) Fixed base system; (b) Complaint base system (from NIST, 2012)

If a horizontal force is applied to the mass, it will produce different displacement components:

$$\tilde{\Delta}= \frac{F}{K} + u_f + \theta h \tag{2. 13}$$

$$\tilde{\Delta}= \frac{F}{K} + \frac{F}{K_x} + (\frac{Fh}{K_{yy}})h \tag{2. 14}$$

Substituting Eq.(2. 14) into Eq. (2. 12):

$$\widetilde{T^2} = (2\pi)^2 \frac{m\tilde{\Delta}}{F} = (2\pi)^2 \cdot m \cdot (\frac{1}{K} + \frac{1}{K_x} + \frac{h^2}{K_{yy}}) \tag{2. 15}$$

Combining Eq.(2. 15) with Eq.(2. 16) results in:

$$\left(\frac{\tilde{T}}{T}\right)^2 = \frac{K}{m} \cdot m \cdot (\frac{1}{K} + \frac{1}{K_x} + \frac{h^2}{K_{yy}}) \tag{2. 16}$$

Eq. (2. 16) corresponds to the famous period lengthening formula evaluated by Veletsos and Meek (1974):

$$\left(\frac{\tilde{T}}{T}\right)^2 = \sqrt{(1 + \frac{K}{K_x} + \frac{Kh^2}{K_{yy}})} \tag{2. 17}$$

Although this formula was derived in the case of a system with one degree of freedom, it can be adopted in the case of a structure with several degrees of freedom. In this case the height, h, will refer to the height of the centre of mass of the structure calculated with reference to the first modal form. ASCE/SEI 7-10 (ASCE, 2010) suggests adopting two-thirds of the total height of a multi-storey building. It is of absolute importance to realise that if the participating mass of the first modal form is rather low (*i.e.* the contribution of vibration modes higher than the first one is not negligible), this formulation is unsuitable to describe the period lengthening of the soil-foundation-structure system. Nowadays, Maravas *et al.* (2014) evaluated the exact formulation that leads to the calculation of period elongation and found that the Veletsos & Meek's formulation is very effective while Luco (2013) proposed a formulation which allows the calculation of the period elongation considering the coupling stiffnesses (translation-rotation) as well as the mass of the foundation.

In addition to period lengthening, the interaction of the structure with the ground leads to a change in damping ratio. In particular, additional damping arises such as radiative damping (i.e. energy moving away from the structure towards the ground) and hysteretic damping (i.e. due to hysteresis cycles). The damping introduced by the foundation can be incorporated into the soil-foundation-structure system:

$$\beta_0 = \beta_f + \frac{1}{\left(\frac{\tilde{T}}{T}\right)^n}\beta_i \qquad (2.\ 18)$$

Where β_i is the structural damping (typically 5%). The exponent, n, is 3 for linear visco-elastic structural systems and 2 in other cases (hysteretic damping) (Givens, 2013). Currently, there are several analytical models to evaluate the damping introduced by the presence of the foundation (Veletsos and Nair (1975), Bielak (1975 and 1976), Roesset (1980), Wolf (1985), Aviles and Perez-Rocha (1996), Maravas *et al.* (2014), and Givens (2013)). Some of these formulations, such as Wolf (1985), do not consider the dependence of damping terms on frequency. Considering the frequency dependence, Wolf's formula can be rewritten as:

$$\beta_f = \left[\frac{(\frac{\tilde{T}}{T})^{n_i}-1}{(\frac{\tilde{T}}{T})^{n_i}}\right]\beta_s + \frac{1}{\left(\frac{\tilde{T}}{T_x}\right)^{n_x}}\beta_x + \frac{1}{\left(\frac{\tilde{T}}{T_{yy}}\right)^{n_{yy}}}\beta_{yy} \tag{2. 19}$$

Where β_s is the hysteretic damping, while β_x and β_{yy} is the damping related to the radiative damping given by translation and rotation. On the other hand, T_x and T_{yy} are fictitious modes of vibration, calculated as if the only source of vibration were translational or rotational:

$$T_x = 2\pi\sqrt{m/k_x} \tag{2. 20}$$

$$T_{yy} = 2\pi\sqrt{mh/k_{yy}} \tag{2. 21}$$

Hysteretic damping is strain dependent, and can be calculated from a local seismic response analysis. Wolf's solution neglects the damping contributions from the product of the two damping ratios. Instead, in the Maravas's (2014) formula these terms are included.

By plotting the period elongation as well as the increase in damping as a function of the structure to soil relative stiffness (h/V_sT), for different aspect ratio (h/B), the importance of the soil-structure interaction can be understood (Figure 2. 13).

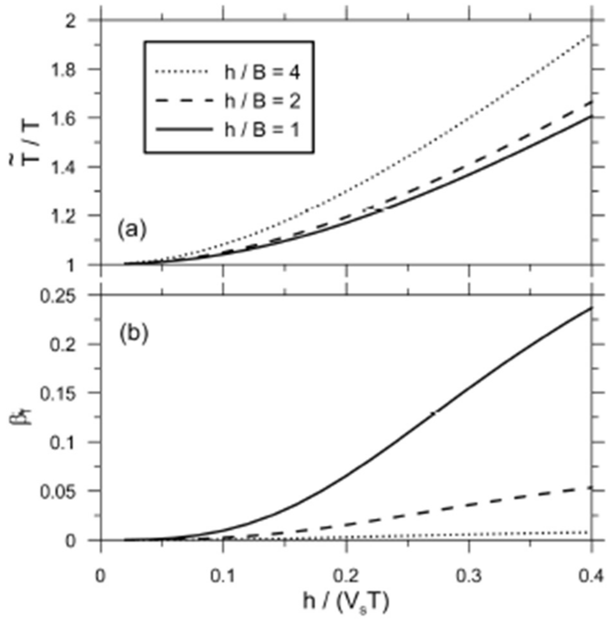

Figure 2. 13. (a) Lengthening of the period generated by the soil deformability compared to the fixed base case as a function of the structure to soil relative stiffness.; (b) Soil damping generated as a function of the structure to soil relative stiffness (from NIST, 2012)

It is possible to say that the soil-structure interaction cannot be neglected when h/V_sT is greater than 0.1.

2.2.3 Kinematic Interaction

Kinematic interaction results from the presence of stiff foundation elements on or in soil, which causes motions at the foundation to deviate from free-field motions. One cause of these deviations is the *base-slab averaging*, in which spatially variable ground motions within the building envelope are averaged within the foundation footprint due to the stiffness and strength of the foundation system. The *base-slab averaging* can be understood by recognising that the movement that would have occurred in the absence of the structure is spatially variable. The positioning of a foundation through these variations produces an averaging effect in which the movement of the foundation is less than the localised maxima that would have occurred in the free field. The motion of the surface foundation is modified compared to the free field motion when the seismic waves are *incoherent*. The *incoherence* of the seismic waves at two different points means that they have variations in their phase angle. One of the simplest causes of *incoherence* in seismic waves is that they may not be perfectly vertical (Figure 2. 14a). Incoherence that remains when waves are aligned to have common arrival times is stochastic, and is quantified by *lagged coherency* models. In the presence of "incoherent" waves, translational base-slab motion is reduced with respect to the free field and a rotational component of motion is introduced. In general, these effects tend to be more pronounced as the frequency of the seismic signal increases. The frequency dependence of these effects is associated with:

1) The relative increase of the foundation width with respect to the wavelength of a high frequency seismic signal

2) Significant reductions in lagged coherency with increasing frequency

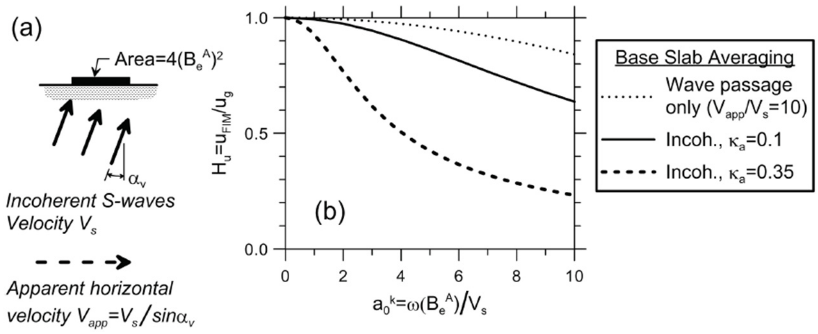

Figure 2. 14 Illustration of foundation subjected to inclined shear waves: (a) schematic geometry; (b) transfer functions between FIM and free-field motion for wave passage using a semi-empirical model for incoherent waves. (from NIST, 2012).

There are numerous relations for deriving the FIM from free-field motion. Mylonakis *et al.* (2006) summarised the following models with the following expressions:

$$u_{FIM} = H_u \cdot u_g \quad (2.\ 22)$$

$$H_u = \frac{\sin\left(a_0^k\left(\frac{V_s}{V_{app}}\right)\right)}{a_0^k\left(\frac{V_s}{V_{app}}\right)}, a_0^k \leq \frac{\pi V_{app}}{2V_s} \quad (2.\ 23)$$

$$H_u = \frac{2}{\pi}, a_0^k > \frac{\pi\, V_{app}}{2V_s} \quad (2.\ 24)$$

Where a_0^k can be calculated using:

$$a_0^k = \frac{\omega B_e}{V_s} \quad (2.\ 25)$$

where B_e is related to foundation area. V_{app} ranges from approximately 2.0 km/s to 3.5 km/s, then for a typical soil site, a reasonable estimate of the velocity ratio, $\frac{V_s}{V_{app}}$, is approximately 10. In Figure 2. 14b, the result labeled "wave passage only" shows the transfer function between u_{FIM} and u_g based on Equation (2. 23).

Another cause of deviation of motion from free field the is the so-called *embedment effects*, in which foundation-level motions are reduced as a result of ground motion reduction with depth below the free surface. Infact, if the base slab of a building is embedded below the ground surface, foundation-level motions are further reduced as a result of ground motion reduction with depth below the free surface. Rotations in the vertical plane are also introduced as a result of differential displacements imposed upon the lateral side of foundation over their embedded depth. Analytical solutions by Kausel et al. (1978) and Day (1978) describe foundation input motions at the base of embedded cylinders as a function of free-field surface ground motion *ug*. These solutions can be adapted for rectangular foundation as:

$$H_u = \frac{u_{FIM}}{u_g} = \cos\left(\frac{D}{B_e} a_0^k\right) = \cos\left(\frac{D\omega}{V_s}\right), \frac{D\omega}{V_s} < 1.1 \quad (2.\ 26)$$

$$H_u = 0.45, \frac{D\omega}{V_s} > 1.1 \quad (2.\ 27)$$

$$H_{yy}(\omega) = \frac{\theta L}{u_g} = 0.26\left[1 - cos\frac{D\omega}{V_s}\right], \frac{D\omega}{V_s} < \frac{\pi}{2} \quad (2.\ 28)$$

$$H_{yy}(\omega) = 0.26, \frac{D\omega}{V_s} > \frac{\pi}{2} \quad (2.\ 29)$$

where D is the embedment depth, as shown in Figure 2. 15a. Velocity, Vs, in this case should be interpreted as the average effective profile velocity.

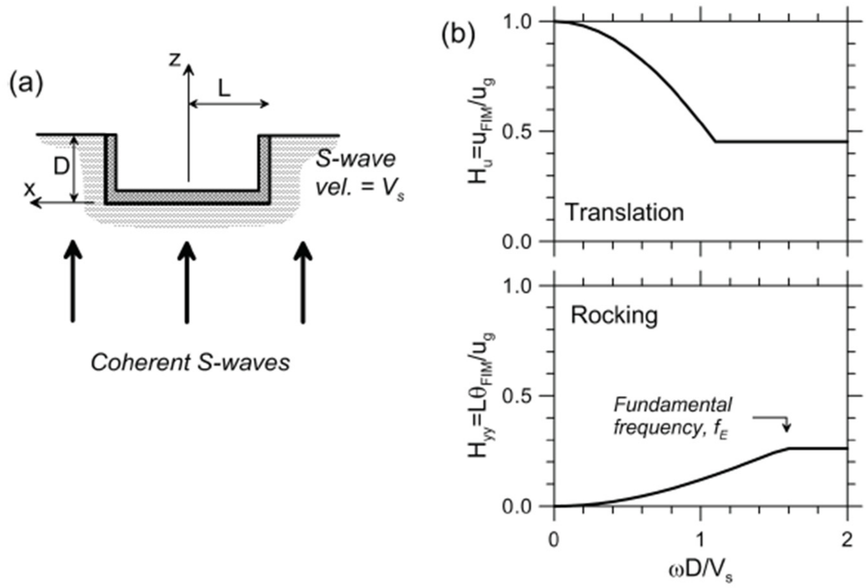

Figure 2. 15. Effect of the foundation embedded into the ground; (b) Trasfer function for an embedded foundation in the soil. (NIST, 2012)

As can be seen from Figure 2. 15b, the reduction in translational motion is substantial at high frequencies. With a deamplification up to 0.45, the effect of the embedment can be greater than the *base slab averaging*. Conversely, foundation rotations will increase with signal frequency.

2.2.4. On the dynamic impedance matrices calculation for embedded shallow foundation

As reported in § 2.2.1, the foundation - soil interaction is typically reduced to a dynamic impedance system of equations reproducing, globally, the link between forces (moments) – displacements (rotations). Questions therefore arise as to how calculate these dynamic impedance functions. Gazetas (1983 and 1991 a, b) grouped together the available solutions of the scientific literature. These solutions were obtained by using different approaches such as analytical, semi-analytical, boundary element, finite element. As already outlined, the dynamic impedance, associated with the generic degree of freedom of the foundation (horizontal, vertical translation, rotation, torsion), may be expressed as:

$$\widetilde{K}(\omega) = K \cdot k(\omega) + i\omega C(\omega) \qquad (2.\ 30)$$

in which the real part $K \cdot k(\omega)$ is the product of the static stiffness $K(\ \omega = 0)$ and the dynamic stiffness coefficient $k(\omega)$ and the imaginary part presents the damping coefficient $C(\omega)$. The relationships available in the literature for the estimation of K, $k(\omega)$ and $C(\omega)$ have been obtained by the various authors by describing the mechanical behaviour of foundation soils with a linear visco-elastic medium, characterised by a constant or variable shear modulus of rigidity, with a Poisson's coefficient and a hysteretic damping ratio. The soil deposit was schematised as a layer of a certain depth resting on bedrock or on an half-space. The foundation is typically schematised as a rigid body. Under such conditions, the dynamic impedances of the foundation depend mainly on:

- The shape and size of the foundation cross-section;
- The height of the foundations;
- The quality of the foundation-soil contact, expressed by the height d ≤ H;
- The presence of the rigid base formation, located at depth Z;
- The excitation frequency, generally expressed in terms of dimensionless frequency, $\alpha_0 = \omega B / V_S$
- The heterogeneity of the foundation soils in terms of shear modulus G (constant profile or increasing with depth);
- The anisotropy of the foundation soils in terms of shear modulus G (Gazetas, 1983);
- The expected degree of nonlinearity of the foundation soils and the consequent deformation level, for which "operational" values of the shear modulus G and the damping ratio should be obtained.

Pais and Kausel (1988) and Gazetas (1991, a, b) provided analytical relations for the calculation of dynamic impedances at the base of embedded shallow foundations. Specifically, the cases of a foundation in homogeneous semi-space (Figure 2. 16a) and in homogeneous deposit of thickness Z resting on a rigid formation (Figure 2. 16b) were considered.

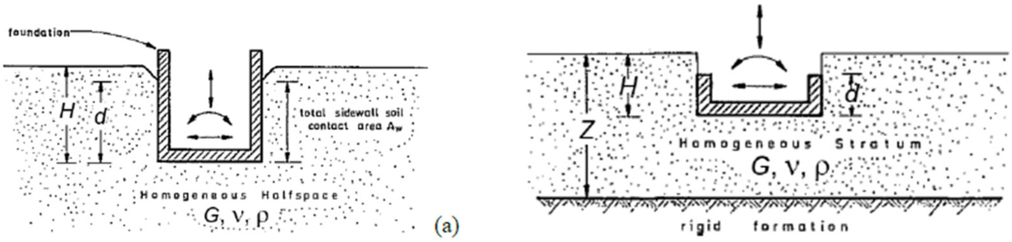

Figure 2. 16. Schemes for calculating the impedance of embedded foundations: homogeneous half-space (a) and homogeneous layer resting on bedrock (b) (modified from Gazetas, 1991 a)

For infinitely stiff foundations, the impedance matrix is symmetrical, so that we have $K_{rx} = K_{xr}$ and $C_{rx} = C_{xr}$. For a cylindrical embedded foundation of radius *R*, the dynamic translation stiffness is:

$$K_{xx}(\omega) = \left[K_{xx,surf}(1+\frac{d}{R})(1+\frac{1.25H}{Z})\right] \cdot k_{xx}(\omega) \quad (2.\ 31)$$

where the term in square brackets represents the static stiffness K_{xx}, expressed as a function of the static stiffness of the relative shallow foundation ($d = H = 0$) of radius *R*, $K_{xx,surf}$:

$$K_{xx,surf} = \frac{8GR}{2-v}(1+\frac{0.5R}{Z}) \quad (2.\ 32)$$

and where $k_{xx}(\omega)$ is the dynamic stiffness coefficient, which can be obtained from different charts proposed by the author. An example of these charts is given in Figure 2. 17a for the case of a circular foundation.

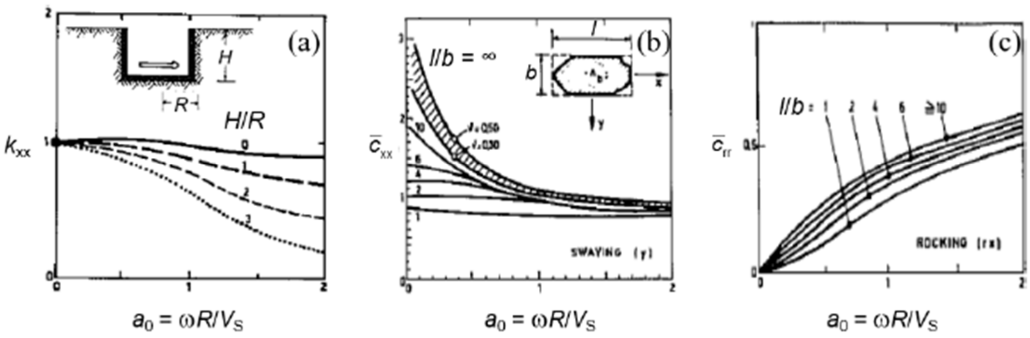

Figure 2. 17. Dynamic impedance functions of embedded foundations in homogeneous half-space as function of dimensionless frequency (a) translational stiffness dynamic coefficient (b) translational damping dynamic coefficient (c) rotational damping dynamic coefficient;(from Gazetas, 1991 a)

The expression of the dynamic stiffness associated with the rotational mode $K_{rr}(\omega)$is equal to:

$$K_{rr}(\omega) = \left[K_{rr,sur}\left(1+\frac{2d}{R}\right)\left(1+\frac{0.65H}{Z}\right)\right]k_{rr}(\omega) \tag{2. 33}$$

$$K_{rr,sur} = \frac{8GR^3}{3(1-v)}\left(1+\frac{0.17R}{Z}\right) \tag{2. 34}$$

$$k_{rr}(\omega) = 1 - 0.2a_0 \tag{2. 35}$$

The expression of the coupled dynamic stiffness $K_{xr}(\omega)$ can be evaluated in a simplified way as:

$$K_{xr}(\omega) = \left[\frac{1}{3}dK_{xx}(\omega=0)\right]\cdot k_{xr}(\omega) \tag{2. 36}$$

where $K_{xx}(\omega = 0)$ is the static stiffness of the embedded foundation while $k_{xr}(\omega) = 1$. The expression of the damping coefficient for radiation $C_{xx}(\omega)$ is:

$$C_{xx}(\omega) = C_{xx}(\omega) + pV_sA_{ws} + pV_{La}A_{wce} \tag{2. 37}$$

where V_{La} is the Lysmer's analog wave velocity, equal to $V_{La} = 3.4\cdot V_s/[\pi(1-v]$, and A_{ws} and A_{wce} are, respectively, the lateral area of the foundation in contact with the soil (d < H), which generate shear and compressive waves in the soil itself; $C_{xx,surf}(\omega)$ is the radiation damping coefficient of the shallow foundation of radius R, equal to:

$$C_{xx,surf} = \begin{cases} 0 & if \quad f < \frac{3}{4} f_{0,s} \\ pV_s A_b \overline{C_{xx}} & if \quad f > \frac{3}{4} f_{0,s} \\ linear\ interpolation & if \quad \frac{3}{4} f_{0,s} < f < \frac{4}{3} f_{0,s} \end{cases} \tag{2. 38}$$

where A_b is the cross-section area of the foundation, $f_{0,s} = 4Z/V_s$ is the fundamental frequency of the soil (i.e shearing modes of vibration) and $\overline{C_{xx}}$ is a dimensionless coefficient which depends on the dimensionless frequency a_0 and the plan dimensions of the foundation (Figure 2. 17b). The expression of the radiation damping coefficient, $C_{rr}(\omega)$, associated with rotation is:

$$C_{rr}(\omega) = C_{rr,surf}(\omega) + pV_{La} I_{wce} \overline{c_1} + pV_s (J_{ws} + \sum_i [A_{wce,i} \cdot \Delta_i^2]) \overline{c_1} \tag{2. 39}$$

in which J_{ws} and I_{wce} represent, respectively, the total moment of inertia, related to the foundation base, of the lateral surface of the foundation in contact with the soil (*d* < *H*), which generates shear and compression stresses in the ground ; Δ_i represents the distance of the A_{wce} areas which generate compression in the soil; $\overline{c_1}$ is a dimensionless coefficient whose expression is:

$$\overline{c_1} = 0.25 + 0.65\sqrt{a_0} \left(\frac{d}{H}\right)^{-\frac{a_0}{2}} \left(\frac{H}{R}\right) \tag{2. 40}$$

$C_{rr,surf}(\omega)$ is the radiation damping coefficient of the shallow foundation of radius R, equal to:

$$C_{rr,surf} = \begin{cases} 0 & if \quad f < f_{0,c} \\ pV_{La} I_{bx} \overline{C_{rr}} & if \quad f > f_{0,c} \end{cases} \tag{2. 41}$$

where I_{bx} is the moment of inertia of the cross-section around the x-axis, $f_{0,c} = 4Z/V_{La}$ is the fundamental frequency of compressive modes of vibrations and

$\overline{C_{rr}}$ is a dimensionless coefficient depending on the dimensionless frequency a_0 and the dimensions of the cross-section (Figure 2. 17c).

Finally, the expression of the damping coefficient $C_{xr}(\omega)$:

$$C_{xr}(\omega) = \frac{1}{3} d C_{xx}(\omega) \tag{2. 42}$$

As the embedment (*H*) and quality ($d \leq H$) of the foundation-soil contact increase, there is an increase both in terms of the dynamic stiffness and the damping coefficient. Due to the increase of the foundation-soil contact area, the energy radiated from the foundation to the outside increases. However, the soil-foundation contact can be reduced due to non-linear phenomena at the interface. For example, due to the reaching of interface shear strength or interface tensile strength, phenomena such as sliding and gapping may occur. In particular, these phenomena take palce close to ground level where the effective confinement is reduced.

The presence of the bedrock ($Z \neq 0$) contributes to increasing the rigidity of the foundation-soil system, as it constitutes a kinematic constraint for the foundation. If the significant volume of soil extends to a depth $z \geq Z$, this effect is significant. The extent of the significant volume depends on the dominant mode of the foundation, being maximum for the vertical mode and minimum for the rotational mode (Figure 2. 18).

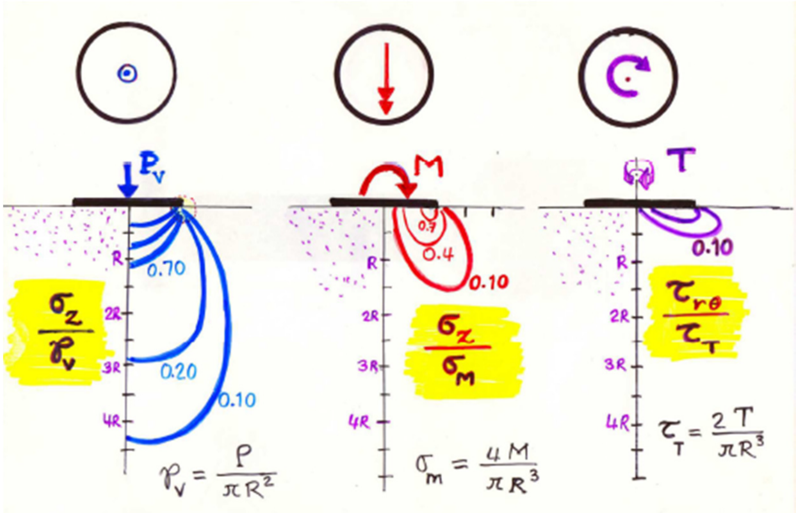

Figure 2. 18. Extent of the significant volume for different degree of freedom (i.e. Vertical, Rotational, Torsional)

The damping coefficient is affected in two ways by the presence of the bedrock. Firstly, in the presence of the bedrock, the waves emanating from the foundation are completely reflected by the bedrock affecting the foundation itself and increasing the amplitude of the movement. In addition, the presence of the bedrock introduces into the system the frequency of the deposit f_0 ($f_{0,s}$ or $f_{0,c}$ depending on the motion of the foundation) which is a cut-off frequency for the radiation damping: in particular, for $f < f_{cut-off}$ the radiation damping is null, while for $f > f_{cut-off}$ the radiation damping assumes the maximum value, equal to what would be obtained for the half-space ($Z \rightarrow \infty$). For $f < f_{cut-off}$, in fact, no surface waves can be generated inside the deposit, which are responsible for the distancing of the seismic waves from the foundation and, therefore, for the dissipation of energy by radiation.

The damping coefficient also depends on the vibration mode of the foundation: specifically, as for the extension of the significant volume, it assumes maximum values for the vibration mode in the vertical direction and minimum values for the rotational (rocking) mode. In fact, when the foundation is subject to oscillations in the vertical direction, the waves radiated into the foundation are in phase with each other; conversely, when the foundation is subject mainly to a rotational mode, the waves emitted from two points located symmetrically with respect to the centre of the foundation are in phase opposition (= 180°) and tend to "cancel out" each other: radiation damping, even in the case of a foundation immersed in a semi-space, is therefore minimal.

For a bedrock with a non-infinite shear stiffness, G_r, the dynamic stiffnesses and damping coefficients depend on the ratio between the shear modulus of the deposit G and the base formation G_r,. Specifically, the dynamic stiffnesses and damping coefficients take on intermediate values between those of the boundary solutions outlined.

The excitation frequency, represented by the dimensionless frequency $\alpha_0 = \omega B/V_S$, leads to a reduction in the translational and rotational dynamic stiffness, $K_{xx}(\omega)$ and $K_{rr}(\omega)$, and in the translational damping coefficient $C_{xx}(\omega)$ (Figure 2. 17); conversely, it leads to an increase in the rotational damping coefficient $C_{rr}(\omega)$.

The heterogeneity of the soil deposit in which the foundation is placed influences the values assumed by the damping coefficients $C(\omega)$. Compared to homogeneous half-space conditions, if the shear modulus G increasing with depth, the static stiffness increases too and the radiation damping decreases. In fact, the waves emitted by the foundation can also be entirely reflected by the presence of an underlying soil of greater stiffness affecting the foundation again. This effect is reduced as the dimensionless frequency α_0 increases: at high frequencies, in fact, the wavelengths, $\lambda = \frac{V_S}{f}$, are reduced and the deposit appears as a homogeneous medium with a constant shear modulus equal to the one where the wave is emitted.

The anisotropy of the soil is the dependence of the elastic characteristics of the soil on the direction of application of the load, whether horizontal or vertical. In this case, five parameters are required to describe the behaviour of soils, G_h, G_v, ν_{hv}, ν_{hh} and G_{vh}, where h indicates the horizontal direction and v the vertical direction. It is possible to introduce the degree of anisotropy n = G_h/G_v. The anisotropy of the soil affects the values assumed by the translational static stiffnesses K_{xx} and K_{yy} and the rotational static stiffnesses, $K_{rr,x}$ and $K_{rr,y}$: specifically, these stiffnesses increase as the degree of anisotropy n increases too. The frequency dependence of the impedances is little affected by the degree of anisotropy n (Gazetas, 1983).

The non-linear behaviour of foundation soils has a significant influence on the dynamic impedances of the foundation-soil system. In particular, as the shear deformation level of the foundation soils increases, there is a decay of the modulus of stiffness G and an increase of the hysteretic damping ratio (Vucetic and Dobry, 1991). This modification of the parameters can be considered by using the above solutions with 'operational' values of the shear modulus and the damping ratio, derived from the results of the local free-field seismic response analysis conducted with the equivalent linear method. In this way it is possible to consider the nonlinearities induced by the seismic motion in the free-field conditions ('primary nonlinearities') but not those caused by the interaction phenomena ('secondary nonlinearities', Mylonakis et al., 2006).

Having recalled the main concepts of soil-structure interaction, it is now possible to discuss about the GSI starting from some historical example of structural and no structural seismic mitigation techniques.

2.3 Hystorical Examples of Seismic Isolation

Since ancient times, humans have explored ways to protect the structures they build from earthquakes. Several archaeological campaigns and historiographical researches show that the seismic risk was particularly felt even thousands of years ago (Giovannardi, 2013; Naderzadeh, 2009). Although the ancients had no knowledge of the principles of modern civil engineering, they began to modify not only the structure but also the foundation soil to prevent seismic actions. In particular, the ancients understood very well the necessity of incorporating elements to mitigate and filter the effects of earthquakes. For example, in some constructions of ancient Crete (2000 to 1200 B.C., Minoic period), archaeologists have found numerous structures that had very regular shapes, and in particular all stone walls were always connected by wooden elements in order to create the so called "box effect", a very important effect to reduce the seismic vulnerability of masonry structures. In addition, frequently, the structures were resting on a layer of medium coarse sand to level the ground and filter seismic actions. A similar technique was also found during excavations of the ancient city of Troy, where a layer of compacted soil was deliberately placed between the walls of the city and the rock below. In Greece and Persia, builders used to interpose between the foundations and the ground a layer of clay and ceramic, where the latter had the sole task of protecting the clay from dehydration, ensuring high plasticity. As it is possible to see, the interposition of some element between the structure and the ground has always been the key for the ancient builders. The Mausoleum of Cyrus the Great in Pasargadae (Figure 2. 19a), for example, was characterized by the interposition of smooth stones, able to slide at the arrival of horizontal actions. The Buddhist temple in Sanjusangendo (Kyoto) (Figure 2. 19b) is founded on alternating layers of clay and sand and was not damaged during the earthquake Hyogoken-Nambu (1995).

(a)

(b)

Figure 2. 19.(a) The Mausoleum of Cyrus the Great in Pasargadae; (b) Buddhist temple in Sanjusangendo (Kyoto).

One of the most famous seismic isolation projects that included foundation soil was the one designed by Frank Lloyd Writh and his collaborators for the Imperial Hotel in Tokyo (Figure 2. 20).

Figure 2. 20. Imperial Hotel Tokyo (Japan)

Specifically, the building was founded on a very thick layer of muddy silts. During the Great Kantō earthquake of 1923 (7.9 on the Moment magnitude scale, MW), the building did not suffer any form of damage. However, due to the fact that the foundations were basically floating on the layer of muddy silt, it subsequently began to sink and, for this reason, was then demolished. This is a great lesson that teaches not to neglect the static problems in order to eliminate the dynamic ones. Unfortunately, during the 1900s, builders focused all their attention on modifying the structure or interposing elements at the base of it, neglecting the possibility of using the ground itself as a seismic isolator.

2.4 Modern Examples of Seismic Isolation

The first patent for a structural seismic isolation system dates back to 1870 and is due to Jules Touaillon. He devised a system where the foundation rested on cylindrical elements (wooden trunks) that could rotate in special elliptical spaces created in the foundation (Figure 2. 21).

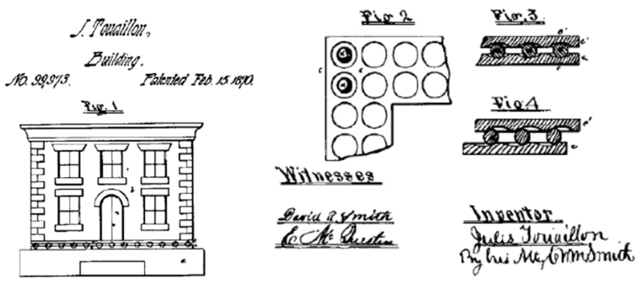

Figure 2. 21. First idea in the field of seismic isolation (Jules Touaillon, 1870).

A variety of seismic isolation and energy dissipation devices has been developed over the years, all over the world. The most successful of these devices also satisfy an additional criterion, namely they have a simplicity and effectiveness of design which makes them reliable and economic to produce and install, and which incorporates low maintenance, so that a passively isolated system will perform satisfactorily. Recent seismic isolation devices could be divided into three categories: Laminated Rubber Bearing (LRB), Friction Pendulum System (FPS), and Hybrid Isolation System (HIS). To date, it has been estimated that approximately 16,000 buildings have been seismically isolated (Martelli et al. 2012). Most of these are located in Japan. Below are some of the world's most impressive structures seismically isolated at the base:

- Sabiha Gökçen International Airport, Istanbul Turkey

Figure 2. 22. Sabiha Gökçen International Airport, Istanbul Turkey (Image Source: Arup)

Sabiha Gökçen (Figure 2. 22) is one of Instabul's two airports, isolated by 300 isolators at the base. According to the designer (Ove Arup) this airport would be able to withstand up to Magnitude 8 earthquakes.

- *Burj Khalifa*

Figure 2. 23. Burj Khalifa

Burj Khalifa is simply one of the most iconic supertall structures in the world and it's also earthquake resistant (Figure 2. 23). composed of mechanical floors where outrigger walls connect the perimeter columns to the interior walling. By doing this, the perimeter columns are able to contribute support for the lateral resistance of the structure and the verticality of the columns also help with carrying the gravity loads. As a result, Burj Khalifa is exceptionally stiff in both lateral and torsional directions. A complex system of base and foundation design was derived by conducting extensive seismic and geotechnical studies which gave the skyscraper stringent structural measures against earthquakes.

- *Taipei 101*

(a)

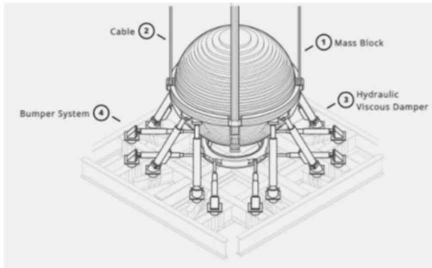

(b)

Figure 2. 24.(a) Taipei 101 tower; (b) Taipei 101's tuned mass damper

The architectural exterior design, by C.Y. Lee, was inspired by the Asian mentality "we climb in order to see further" (Figure 2. 24a). Putting aside the architecture, the mind-blowing fact about Taipei 101 is that it houses the biggest tuned mass damper (TMD) in the world (Figure 2. 24b). It's a gigantic metal ball that counteracts big transient loadings like wind and earthquake to reduce the sway of the supertall tower. The TMD is supported by hydraulic viscous damper arms and bumper system which function in the same way as a car's shock absorber. When large forces act upon the tower the TMD sway in the opposite direction bringing the entire building in equilibrium by damping out the transient forces using the ball's mass. This earthquake damper system is located between the 87th floor up until the 92nd level.

2.5 Seismic isolation of existing structures

The previous chapter showed that for new structures there are several possibilities and solutions for seismic isolation. On the contrary, the seismic protection of existing buildings, which have not been designed following the latest refined dynamic or pseudo-static approaches, is still a matter of great concern. In countries like Italy, with a high seismic hazard and old or very old towns, this is one of the most relevant problems for the protection of both population and cultural heritage (Costanzo et al., 2007). The recent tragedy of Amatrice earthquake (Italy, 24 August 2016) is a paradigm in this sense. In some and rare cases, existing structures have been seismically isolated with passive structural systems installed underneath the buildings with a complex procedure of partial uplifts and setting of isolators and dampers (see for instance Martelli, 2009; Alterio, 2012). Generally, the tradition seismic isolation of existing buildings is generated by cutting the base of the load-bearing masonry and creating a reinforced concrete beam under which the isolators will be placed. Lignola *et al.* (2016) have proposed a special system to lift the load-bearing masonry and install the isolators. Examples of such complex procedures are: the Salt Lake City & County Building (USA), the San Francisco City Hall (USA), the Maritime Museum of Auckland (New Zealand), the Church of San Giovanni in Carife (Italy), the Los Angeles City Hall (Figure 2. 25).

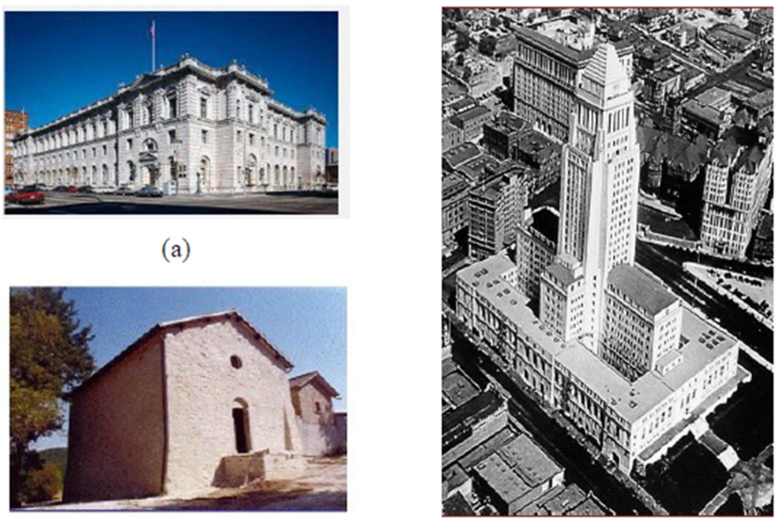

(b) (c)

Figure 2. 25 San Francisco City Hall, San Francisco, CA, USA (a); Church of San Giovanni in Carife (Italy) (b);Los AngelesCity Hall, CA, USA (c).

It should be noted that these procedures can be particularly expensive and not always feasible for all buildings. For example, the building to be isolate may be part of an urban aggregate. In these cases, it is very difficult to ensure that the building can move freely. Another issue is that the isolators behave as concentrated supports under continuous masonry walls, and that the distance between isolators influences the stresses in the walls and supporting tie beams (Mezzi, Comodini, and Rossi 2011). Moreover, in order to prevent global torsional effects, when positioning the isolation devices in layout, special care has to be taken. In addition, the installation of seismic isolators in structures of artistic and historical significance cannot be accepted. In fact, the historical importance of these places generates severe constraints on the interventions that can be implemented. It is necessary to remember that the most important aspect of historical integrity concerns the iconic integrity: the external form, the image, must not be altered (Viggiani 2017). Another important aspect is the material integrity. Materials, construction techniques, and structural schemes are essential features to preserve a monument. Finally, the harmony that must exist between a monument and the city that surrounds it cannot be forgotten.

2.5 Concepts of Geotechnical Seismic Isolation (GSI)

The concept of geotechnical seismic isolation is often unfamiliar to many civil engineers. Geotechnical seismic isolation (GSI) is one of the most innovative techniques to deal with seismic actions. A GSI system can be defined as a seismic isolation system that involves the direct interaction with the natural soil and/or man-made reinforced soil materials, in contrast to the commonly well-known structural seismic isolation system, in which the flexible or sliding interface is positioned between a structure and its foundation. As time goes by, the geotechnical seismic isolation has attracted so many researchers over time such as Yegian and Lahlaf (1992), Kavazanjian *et al.* (1991), Yegian and Catan (2004), Yegian and Kadakal (2004), Georgarakos *et al.* (2005), Kirtas *et al.* (2009) and Kirtas and Pitilakis (2009). In particular, the specific name

"*Geotechnical Seismic Isolation*" was first introduced by Tsang in 2009 (Tsang, 2009). Through a simple parallelism Tsang was able to make extremely clear what is meant by "*Geotechnical Seismic Isolation*" (Figure 2. 26).

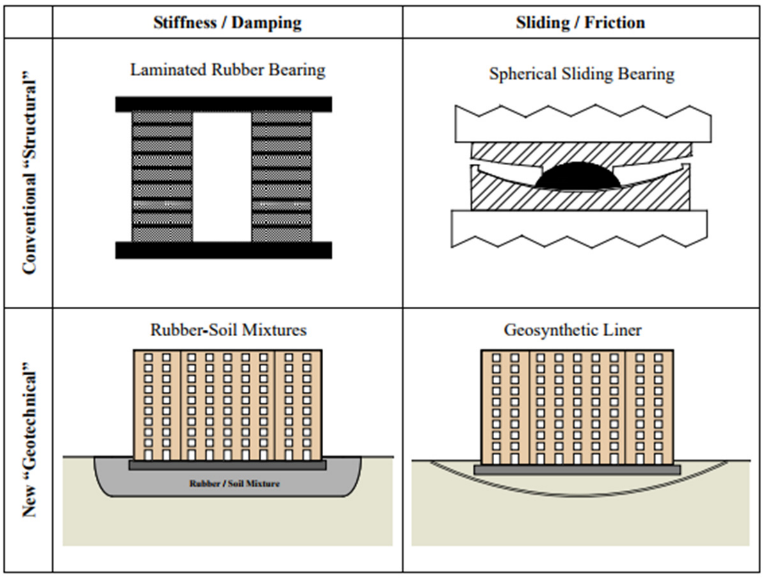

Figure 2. 26. Simple parallelism between geotechnical seismic isolation and classical structure isolation at the base of a buidings. (from Tsang, 2009)

It is possible to note that geotechnical seismic isolation can be considered as a simple transposition into the ground of the effects of classical structural seismic isolation. As a common rubber isolator is able, through a high horizontal deformability (and high damping), to isolate a structure, in the same way the creation of a foundation soil characterized by a mix of soil and rubber pieces (*rubber soil mixture*) would be able to perform the same function. And again, as well as a classic sliding isolator manages, through its low shear resistance, to slide during an earthquake, so the interposition of a geotextile, characterized by a very low angle of friction, below the foundation would ensure the same effect. Conceptually, earthquakes produce different kinds of seismic waves that propagate even tens of kilometres away from the seismic fault. Spreading, initially through the rock located deep in the earth and then through the last deformable layers of soil, these waves reach the earth's surface. In this regard, it is essential to clarify some concepts of reflection and refraction of seismic waves. The case of waves vertically propagating into a layered soil may be solved analytically, at least in the case of linear elastic materials. It is of interest to note that the theoretical solutions (Kramer, 1996) as well as common sense indicate that when the travelling (incident) wave reaches the interface with a soil layer having different properties, part of the energy rebounds at the boundary, generating a reflected wave, and part enters into the subsequent layer as a transmitted or refracted wave. Theory says that, for a given incident wave, the partitioning of the energy at the interface depends not on the absolute values of the physical and mechanical properties of the single strata, but only on the ratio α of the specific dynamic impedances η ($\eta = \rho V_s$ where ρ is the material density and V_s is the shear wave velocity) of the two materials separated by the interface, defined as:

$$\alpha = \frac{\eta_2}{\eta_1} = \frac{\rho_2 V_2}{\rho_1 V_1} \tag{2. 43}$$

where the suffixes 1 and 2 indicate, respectively, the material from which the waves are coming and that into which they are transmitted. Furthermore, theoretical solutions also indicate that if the wave is transmitted into a softer layer ($\alpha < 1$), the displacement amplitude will be increased (and the stress amplitude reduced), while in the opposite case (stiffer layer, $\alpha > 1$), the transmitted displacement amplitude will be reduced (and the stress amplitude increased). The reflected wave amplitude is always smaller than the incident one both in terms of displacements and stresses, but the value of α influences its sign (which for displacements inverts at interfaces having $\alpha > 1$ and keeps the same value if $\alpha < 1$). At the extreme, if the impedance ratio α is equal to 0 the interface behave as a free end and no energy is transmitted above it. The amplitude of the generated waves can be expressed as a function of the incident wave one, imposing the appropriate continuity conditions on displacements and tensions. For instance, if a P-wave orthogonally touches a discontinuity surface, only compression stresses will be generated. In this case, if A_i is the amplitude of the incident wave and A_r and A_t are respectively the reflected and refracted (transmitted) amplitude, the following two non- dimensional parameters can be defined as:

$$c_r = \frac{A_r}{A_i} = \frac{1-\alpha}{1+\alpha} \tag{2. 44}$$

$$c_t = \frac{A_t}{A_i} = \frac{2}{1+\alpha} \tag{2. 45}$$

The two ratios previously reported are generally named respectively coefficients of reflexion and of transmission, and their variation depends on the dynamic impedance ratio α (Figure 2. 27). If the waves travel from a stiffer medium to a softer one (α < 1) the transmitted wave amplitude increases with respect to the incident wave amplitude ($c_t > 1$). Lowering the stiffness of the incoming media, the wave amplitude increases. If a wave touches a medium infinitely stiff with respect to the outcoming one (α tends to ∞) the reflection coefficient c_r tends to -1, while the transmission coefficient tends to 0, actually the wave will be completely reflected into the outcoming medium.

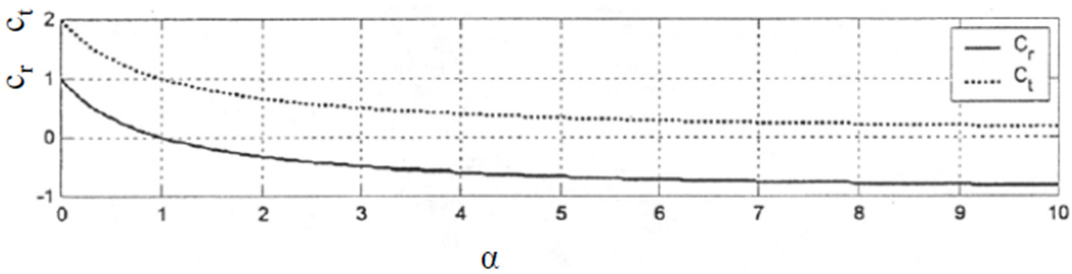

Figure 2. 27. Variations of c_r and c_t with respect to α.

For this reason, the last layers of deformable soil have a relevant role in the propagation of these seismic waves because they act as "filters" of seismic actions; considering a complex signal, as it is always the case in nature, some frequencies may be attenuated passing through the soils, some others may be amplified (Richart et al., 1970; Kramer, 1996; Chavez-Garcia, 2011). In order to isolate buildings from antropically induced vibration (i.e. trains, industrial machinery) the idea of inserting some materials into the ground is widely used. In this sense, some authors have devised systems that consist of inserting very rigid horizontal barriers (Figure 2. 28) in the ground (a kind of artificial bedrock).

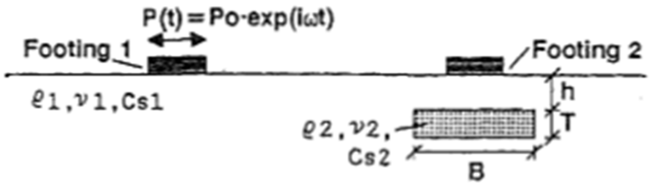

Figure 2. 28. Screen barrier for superficial waves.

According to these studies if the predominant frequency of excitation of the signal is lower than the resonance frequency of the rigid layer, then there would be a reduction of vibrations (Kellezi, 2011). Noteworthy is also the technology devised by Massarsch (Massarsch 2004, 2005) which consists in inserting air-filled cushion placed vertically in the ground. This technology was implemented in *Düsseldorf* (Germany) (Figure 2. 29).

Figure 2. 29. Air-filled cushion placed vertically in the ground to isolate a building from train vibration. (Massarsch 2004, 2005)

Of course, the most effective vertical barrier to reduce vibration is certainly a barrier characterized by the presence of a vacuum in the ground (i.e. open trench), because it can be seen as a reflecting barrier with zero refraction ($\alpha = 0$). However, in practice it is very difficult to create such fully reflecting barriers, and often lightweight materials. It is essential to understand that, in order to isolate a building from human induced vibration, it is necessary to create a layer in the ground characterized by an abrupt change in dynamic impedance. However, the density as well as the stiffness increases with depth and, for this reason, a lateral barrier should resist to the lateral pressure of the ground but without changing its impedance with depth. As a matter of fact, during the last years, an increasing number of researchers have been studying dynamic properties of treated soils in order to understand and control the modifications introduced by various treatments to the mechanical and dynamical ground properties (Saxena et al., 1987; Cai and Liang, 2003; Spencer, 2010). However, it is important to understand that the isolation from antropically induced vibration deeply differs from the isolation from earthquake-induced vibration. First of all, the position of the source of the vibrations. In general, in the case of antropically induced vibrations, the source is at ground level, while in the case of earthquakes the vibrations propagate almost vertically from the depth up to the surface. In order to seismically isolate a building, this has an important effect on the shape such barriers will need to have. Needless to say, in the case of existing buildings the isolation from earthquake induced vibrations is far more difficult, because it involves the need to place a barrier beneath the building, with obvious technological difficulties. Of considerable importance is also the difference between the frequency content and the intensity of these two kinds of different vibrations (antropically or earthquake induced). In some cases, engineering applications of conventional superficial grouting have been proposed in literature as a mean to mitigate seismic actions, but always considering cemented (and therefore improved) soils in the topmost part of the subsoil. Numerical one-dimensional site response analyses proved that stiffening the uppermost soil layers by grouting reduces the overall ground motion, but has little or no effect on the high-frequency content of the seismic motion transmitted to the surface, which can therefore still be potentially dangerous to stiff massive buildings to be protected

(D’Onofrio et al., 1999). The following subsections will discuss some effective geotechnical seismic isolation techniques. To the author's knowledge, none of these techniques has ever been implemented on real buildings.

2.5.1 On the use of sliding surfaces in the ground

There are numerous studies that consider the insertion of a low shear strength surface below the foundations of a building. The concept is physically simple to understand. Because of the low friction angle of such an interface, there will be a considerable dissipation of seismic energy. Sliding will possibly take place because of the shear stresses caused on horizontal planes by the upwards propagation of shear waves. Sliding will obviously be a function of the properties of the sliding interface, as well as of the vertical axial load and ground motion frequency. Many authors have studied different slip layers beneath a building slab foundation to provide this kind of base isolation. Yegian and Kadakal (2004) have proposed a sliding system interface characterized by the presence of a geotextile placed over an ultra-high molecular weight polyethylene sheet to be placed immediately in contact with the foundations (Figure 2. 30) or involving a portion of ground (Figure 2. 30b).

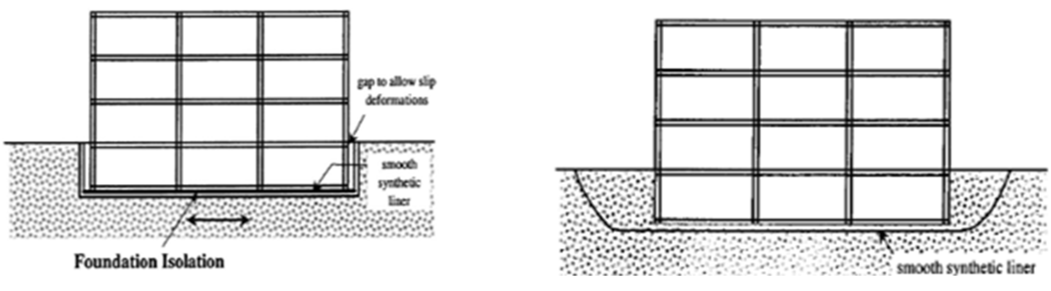

(a) (b)

Figure 2. 30(a) Smooth synthetic liner placed around the foundation; (b) Smooth synthetic liner placed beneath the structure. (modified from Yegian and Kadakal, 2004)

In particular, this system has been studied through shake table tests and analytical evaluations showing excellent reductions in peak and spectral accelerations. Doudomis *et al.* (2002) proposed to lay the foundations of a building on a soil characterized by low shear stiffness such as talc, chlorite, serpentine. However, this system seems to be very difficult to implement for new buildings and probably impossible to create for existing ones. A particularly complex system from a technological point of view is the one designed by (Tashkov *et al.*, 2010, Tashkov *et al.*, 2004). In this system, the foundation of the structure is placed on a sliding plate positioned on a recess containing oil under pressure, which has the purpose of lowering the sliding resistance between the foundation and the ground. A small-scale (1/3.5) model of St. Nicholas Church was tested on the seismic shaking table (Figure 2. 31a) showing a very good results in terms of accelerations reduction. Again, this system, while very effective, relies on the ability of pressurized oil to isolate the structure (Figure 2. 31b). Its implementation on existing structures seems very challenging and expensive.

(a)

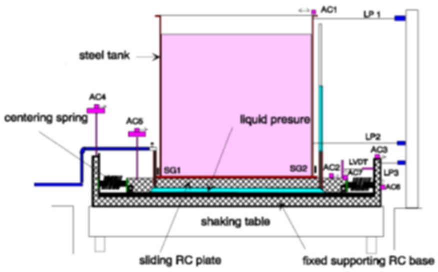

(b)

Figure 2. 31(a) Small-scale (1/3.5) model of St. Nicholas Church; (b) Scheme of the pressurized oil to isolate the structure (Tashkov, 2004).

Finally, it is important to remember the geotechnical seismic isolation proposed by Diez and Woods (2006). The two authors devised a system composed of vertical barriers characterized by soft material and a lower sliding surface (Figure 2. 32). The bottom weak layer had a low value of the shear strength angle, thanks to the use of the roller bearings, which the experimental box sits on, whereas soft trenches (made with cylinders of neoprene) offered negligible shear stiffness. The shake table test performed with this technique show excellent results in terms of reductions in seismic actions.

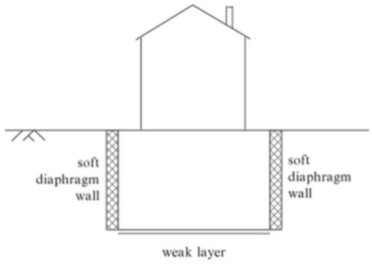

Figure 2. 32. Scheme adopted by Wood (2006) for his isolation typology.

2.5.2 On the use of rubber-soil mixtures

The use of small pieces of rubber mixed with the in situ-soil (*rubber-soil mixture*) has been particularly investigated over the past 20 years. There are several reasons that make rubber fundamentally different than soil. These can be summarized as:

- Much greater elastic deformability.
- Lower strength and shear modulus.
- Absence of a yield limit in the stress-strain curve.
- Recovery of large strains when stress is removed.

Depending on the amount of rubber in the soil mixture ($D_{50,\ rubber}/D_{50,\ soil}$), the rubber soil mixture changes its behaviour from soil like to rubber like. Tsang (2009) proposed to include the rubber-soil mixtures as a large portion of the foundation soil (Figure 2. 33a). According to Tsang, the soil layers surrounding foundation (considered having G=222MPa at a confining pressure of 345kPa; V_s = 350m/s) can be replaced by a medium which is made up of soil mixed with a designed proportion of rubber and sand (G=7,5MPa at a confining pressure of 345kPa; V_s = 90m/s), with both an important increase in damping and a decrease in shear stiffness.

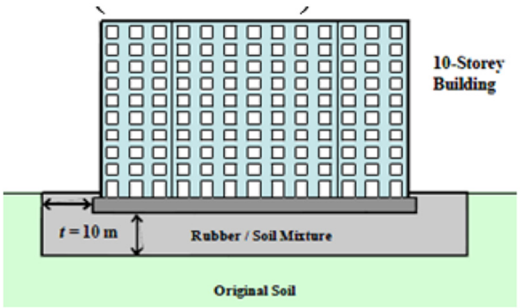

(a)

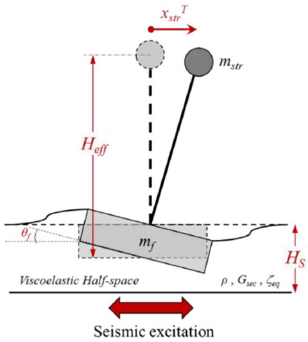

(b)

Figure 2. 33.(a) RSM system around the foundation of a building; (b) The corresponding idealized model. (Tsang et al., 2009, 2019)

Using this system, the authors predict an average reduction of 40-60% in horizontal accelerations, above all for wider buildings (low to medium rise buildings) with a remarkable increase in the fundamental structural period. Based on this result, Tsang *et al.* (2019) proposed a very simple analytical model to predict both the elongation of structural period and the effects generated by the rubber soil (Figure 2. 33b).

It is possible to summarize the advantages of using rubber soil:

- Scrap tires are available in abundance with an urgent need of recycling.
- Rubber has been studied widely, both static and dynamic properties are available (Kim and Santamarina 2008, Feng and Sutter, 2000, Anastasiadis *et al.* 2009)
- R.S.M. (Rubber soil mixture) are characterized by nonlinearity and high damping in the medium to high strain range (depend on rubber content %).
- Low shear modulus.

and disadvantages:

- Contamination problems specially with under water table.
- Difficult to mix soil and plastic under existing structures.
- Aging effect, temperature sensibility (need to replace after time).

In particular, this last aspect could be very detrimental to the efficiency of the rubber-soil. In fact, it is very difficult to predict both the durability of rubber soil and the possible effect in terms of environmental aspects.

Moreover, while the creation of a foundation-soil mixed with rubber could be easy to implement for new buildings, the rubber-soil foundation can be extraordinarily difficult to implement for existing buildings.

2.5.3 On the use of Soft and Stiff Barriers in the ground

Kirtas (2009) has studied, numerically and by centrifuge testing, the inclusion of different stiff and soft treatments into a soil deposit, considering the presence of a SDOF (Single Degree of Freedom) at ground surface simulating the case of structures with surface foundations. Actually, he has studied the insertion of horizontal layers beneath the foundation, vertical diaphragms next to the foundation and caissons, which are the combination of two vertical diaphragms and one horizontal layer to form an isolated soil-structure area; any modification of the foundation soil properties may affect the structural response through soil-structure interaction mechanisms in a beneficial or a detrimental way. Evaluation of foundation subsoil stiffening and stiff diaphragm intervention effects has revealed that the specific approaches are not efficient in reducing the seismic part of the structural response. On the contrary, the seismic acceleration for several soil-structure combinations could increase after the intervention compared to the initial system, although the adequacy of the methods in soil strength enhancement and excessive settlement reduction is not under question. Kirtas analysed the effectiveness of the barriers by varying several dimensionless parameters which influence the soil-structure interaction such as:

$$m_{norm} = \frac{m_{str}}{pB^3} \tag{2. 46}$$

$$h_{norm} = \frac{h_{str}}{B} \tag{2. 47}$$

where:

- m_{str} is the superstructure mass;
- h_{str} is the superstructure height;
- p is the soil density;
- B is the characteristic foundation dimension (half the foundation width for strip foundation type).

According to Kirtas (2009) incorporating a short-length soft horizontal layer in the foundation subsoil does not affect significantly the structural seismic response (see Figure 2. 34).

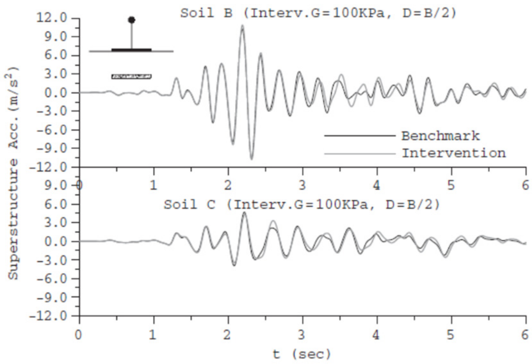

Figure 2. 34. Effect of soft short-length horizontal layer in time domain (Kirtas, 2009).

On the other hand, the construction of vertical flexible barriers near the foundations generates much better results. The author introduces a parameter called "*accelerations ratio*" or "*displacements ratio*" to quantify the reduction or increase in accelerations compared to the case without GSI intervention. The superstructure acceleration ratio in the case of the *''soft vertical diaphragms''* presents a wide range of values below unity near the fundamental effective period of the structure (Figure 2. 35a and Figure 2. 35b), indicating an efficient mitigation of the seismic response.

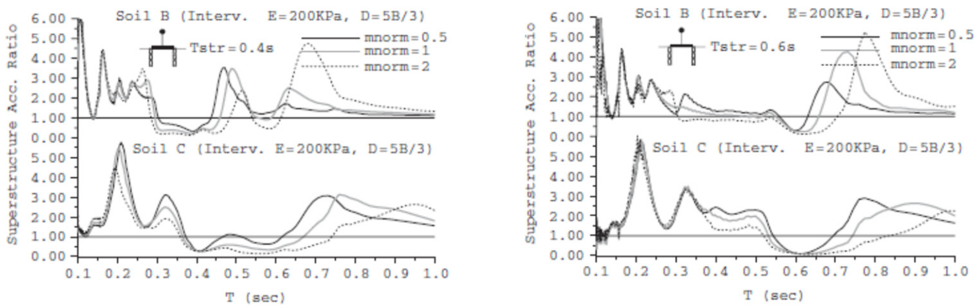

(a) (b)

Figure 2. 35. Effect of soft vertical layer in the frequency domain: (a) with a structure of first resonant period equal to 0.4sec; (b) with a structure of first resonant period equal to 0.6sec (Kirtas, 2009)

It is also possible to note the beneficial effects of vertical barriers in the time domain for the structure with a period of $T_{str}=0.6sec$ (Figure 2. 36) and two different excitations. The excitations are: EQ1with predominant period between 0.15s-0.40s and EQ2 with a wide range of frequencies with an important frequency content for T=0.6s-0.8s (period range closer to the structural effective period).

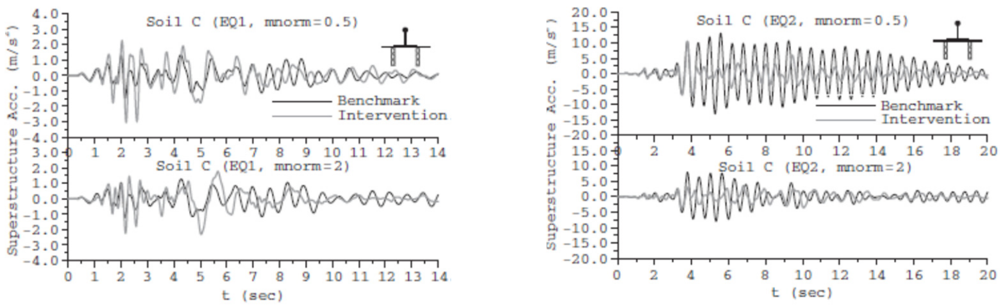

(a) (b)

Figure 2. 36. Effect of soft vertical layer in time domain: (a) EQ1; (b) EQ2.(Kirtas, 2009).

The increase of the dynamic response due to the presence of the proposed system during the EQ1 excitation is of minor importance since the structure is out of resonance with the seismic motion, which is obvious considering the low level of the superstructure acceleration developed in the initial system. On the other hand, applying the EQ2 input motion where resonance phenomena occur, the soft diaphragms induce a significant reduction of structural response. Due to the increase in deformability generated by this intervention compared to the original condition, an increase in displacements of the structure-soil system can be expected. Another type of system studied by Kirtas is the so-called '*caisson*'. In this case, in addition to the flexible vertical barriers, a horizontal layer is added characterised by very low shear stiffness (Figure 2. 37).

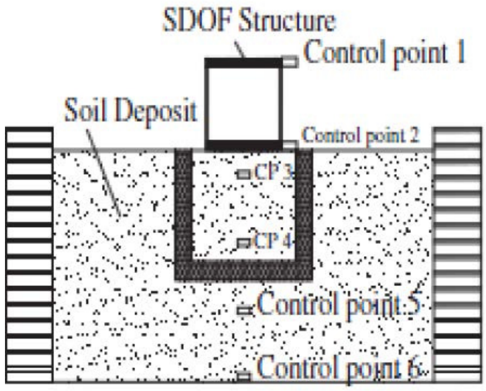

Figure 2. 37 .Soft caisson model in a centrifuge test conducted by Kirtas.(Kirtas, 2009)

According to authors, significant alteration of the dynamic properties of the system shifts the SDOF response to higher period values, out of the frequency range of common earthquake records, resulting in beneficial effect of the implemented intervention (Figure 2. 38a and Figure 2. 38b). The beneficial effects of these interventions can also be seen in the time domain (Figure 2. 38c and Figure 2. 38d).

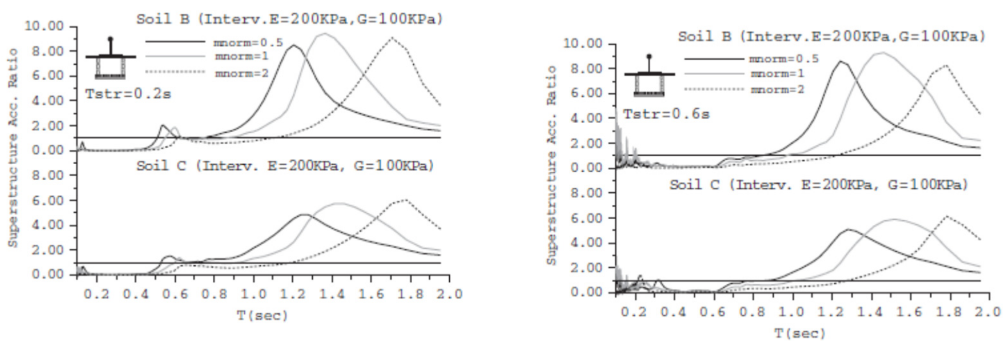

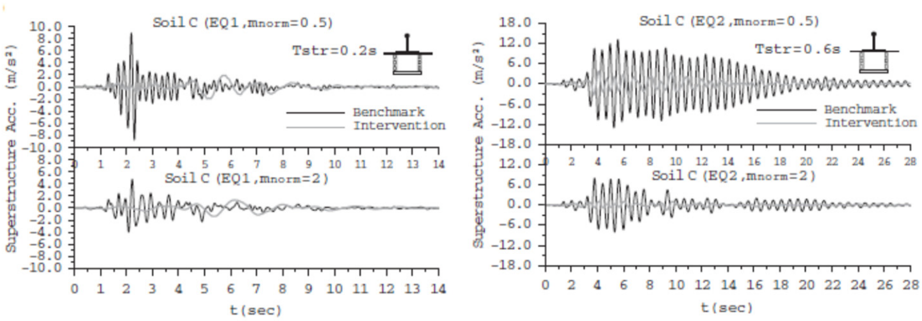

Figure 2. 38. Soft caisson: superstructure ratios for Tstr=0.2s (a) and Tstr=0.6s (b); superstructure acceleration time-histories for Tstr=0.2s (c) and Tstr=0.6s (d) (Kirtas (2009).

However, according to Kirtas (2009), by considering such a system, an increase of the soil deformations and structural displacements are expected and should be handled appropriately considering the specific nature of the implicated materials (Figure 2. 39).

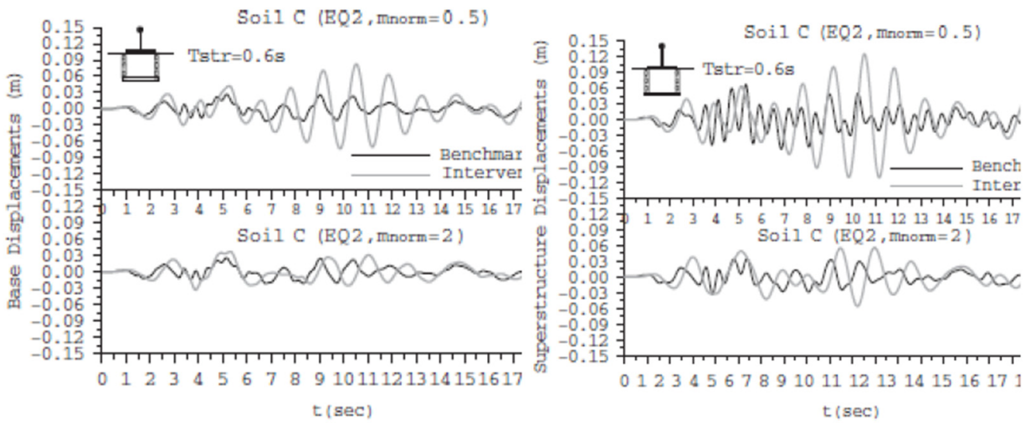

Figure 2. 39. Base displacement generated by the soft caisson effect (Kirtas, 2009).

However, Kirtas does not identify any specific material for the creation of such soft barriers. He selects a very low value of normal stiffness, *E*, for vertical barriers (200kPa) and a very low value of shear stiffness, *G*, for horizontal barriers (100kPa). On the basis of Kirtas' studies, there have been several research projects based on soft barriers. In particular, there have been two doctoral theses that have explored this topic: Lombardi 2014 and Nappa 2018. Due to the fact that part of this thesis work was aimed at continuing the research on these aspects, an attempt will be made below to quickly summarise the results found.

In order to study the efficiency of different geometric schemes, Lombardi (2014) focused his studies on 1D and 2D numerical dynamic and static analyses. In particular, numerous geometric and mechanical configurations were varied in order to highlight the potential and limitations of soft barriers. The 1D analyses have been carried out using either EERA or NERA, supposing the soil layers to be horizontally homogenous, horizontally unlimited, and subjected only to a horizontal excitation from the bedrock. The results confirmed that the insertion of a soft layer, at a certain depth in the soil, is extremely effective to reduce the accelerations in the soil. 2D dynamic analyses were then carried out by Lombardi. The 2D dynamic analyses have been carried out using FLAC7. In contrast to Kirtas (2009), one of Lombardi's most important findings is that such a GSI technique is useless if the volume of soil is not completely isolated by soft barriers. For this reason, different geometrical and mechanical configurations of the soft caisson have been considered. In particular, two different geometrical schemes of the isolated mass have been investigated: a rectangular one, with a horizontal base (Figure 2. 40a) and vertical sides, and a V-shaped one (Figure 2. 409b).

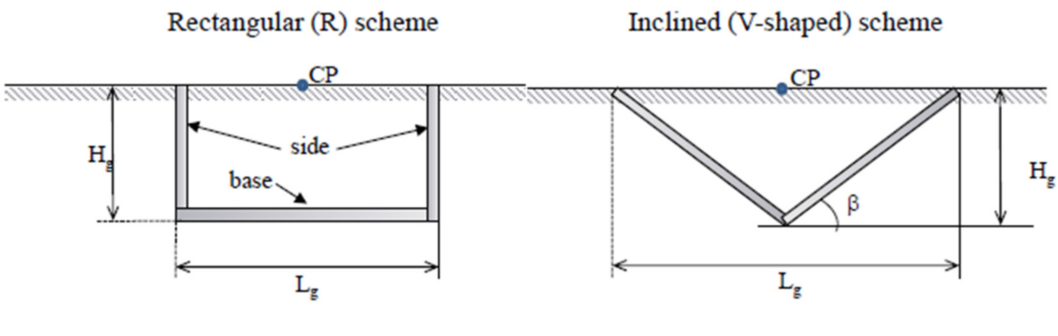

Figure 2. 40. Different geometrical schemes for soft barrier: (a) soft rectangular caisson; (b) V-shaped. (Lombardi, 2015)

The parametric analyses conducted by Lombardi showed that the insertion of soft barriers in the soil changes its resonance period. As also assessed by Kirtas

(2009), in particular, soft barriers tend to amplify low frequencies and de-amplify high frequencies. For this reason, it is confirmed that this system can be effective in reducing the maximum dynamic effects on squat structures, which have lower natural frequencies. Another particularly interesting and unexpected result is that the soft barriers would be able to cut the seismic energy depending more on the value of the shear strength of the soft layer than on the dynamic impedance between the two layers (soft layer and soil). In particular, the results presented by Lombardi indicate that both the shear wave velocity of the soft layers and the impedance ratio are relevant parameters in the propagation of the signal through the insulating box, but the former plays a more significant role. This result would lead one to believe that soft barriers can be used independently of the stiffness of the surrounding soil. It is important to note that all findings by Lombardi do not consider the presence of structure. Concerning the static problems generated by the insertion of the soft barriers, Lombardi only carried out some preliminary numerical modelling evaluating the increase in settlements and the reduction of the bearing capacity. In particular, at ground level, a gravity load distribution has been considered, whose amplitude q_w and length L_s have been varied together with the width, height and mechanical properties of the soft caisson. As expected, the soft barriers, worsening the soil properties, increase the vertical settlements and reduce the bearing capacity (Figure 2. 41).

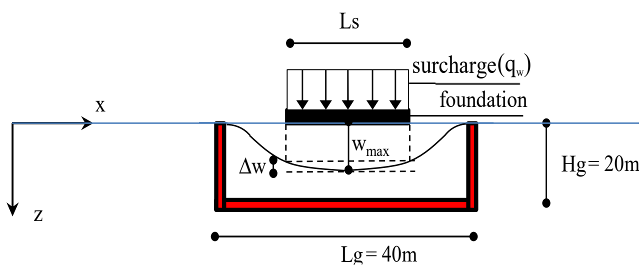

Figure 2. 41. Estimation of settlements and bearing capacity in presence of soft barrier. (Lombardi, 2015)

However, the most important result of this analysis is that the volumetric stiffness K of the grouted layers plays a relevant role on the effectiveness of the isolating barrier. In the case of a rectangular caisson, the best solution is to have an extremely low value of K on the vertical sides, and a higher one at the base. So, doing, the static settlements induced by the creation of the barrier would be reduced. In the case of the V-shaped barrier, this separation is not possible. In this regard, it is emphasised that V-shaped barrier is less effective than the rectangular one having the same depth, since the isolated mass is smaller and the filtering effect of the grouted layer is influenced also by the bulk stiffness. Finally, Lombardi assesses the effect of the constitutive model adopted on the effectiveness of soft barriers. As to be expected, the use of an elastic linear constitutive model leads to more conservative results while the use of an elasto-plastic material model (i.e. Mohr Coulomb) generates a better efficiency of the barriers. Actually, in the case of seismic inputs that induce yielding into the soft layers of the soft caisson, the detrimental effects for the lower frequencies are largely attenuated.

In the last part of his thesis, Lombardi experimentally identifies two possible materials to create the soft barriers. The first material is a self-expanding polyurethane insulating foam, essentially a hydrophobic material, resistant to water, chemicals and moisture. Laboratory tests have been carried out to quantify its density and its shear stiffness when injected to pressures higher than the atmospheric one. Some resonant column tests have been performed to quantify the shear stiffness at low shear strains as well. Tests results indicate that the polyurethane foam cannot be considered a suitable material for soft layers, because even though it shows a low density even under high pressures, it is rather stiff.

The second tested material is a super absorbent polymer (SAP), which is a hydrophilic network being able to absorb and retain huge amounts of water or aqueous solutions. These specimens have been subjected to a few traditional laboratory tests (direct shear tests, ring tests, oedometer tests, triaxial tests). These laboratory tests, although very difficult to carry out due to the extreme deformability of SAP, showed a range of shear stiffness values suitable for the construction of soft barriers. One of the objectives of the following PhD thesis is to further investigate the dynamic properties of sand-SAP mixtures through the use of Bender Elements, Resonant Column, and Simple Cyclic Shear tests.

Regarding the second doctoral thesis on this topic, Nappa (2018) started her research by performing two centrifuge tests with the use of soft barriers made by S.A.P. Two reduced scale models of soft barriers in a sand layer underwent a series of ground shaking. The aim of the study was to get experimental evidence of the capability of such soft barriers to isolate a volume of soil thus reducing amplification of ground motion induced by earthquake loading. The two models tested in centrifuge at 50 and 80 g consisted each in a layer of dense Hostun sand, free to be shaken along its main horizontal axis thanks to the adopted container (a laminar box). In the first model a thin horizontal layer made of latex balloons filled with a cross-linked gel was created at about mid-height of the sand layer (Figure 2. 42a). In the second, the same balloons were installed to form a V-shaped barrier aimed at isolating a relatively shallow volume of sand (Figure 2. 42b). The experimental results confirm the effectiveness of such soft barriers to reduce amplification in the isolated volume during seismic events (Figure 2. 43a), although V-shaped isolating barriers are less effective than a full horizontal barrier (Figure 2. 43b).

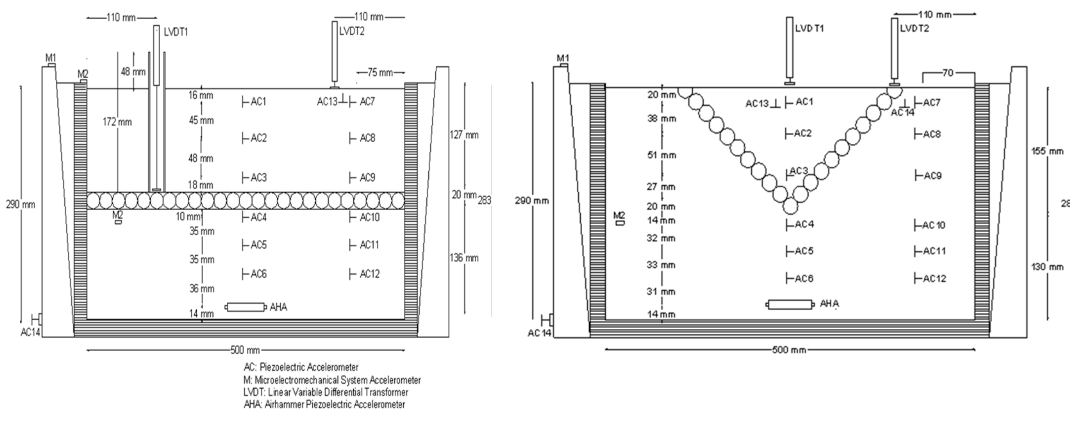

Figure 2. 42 Centrifuge Models: (a) horizontal layer of SAP encapsulated in latex cilinders; (b) V Shaped geometrical configuration. (Nappa, 2018)

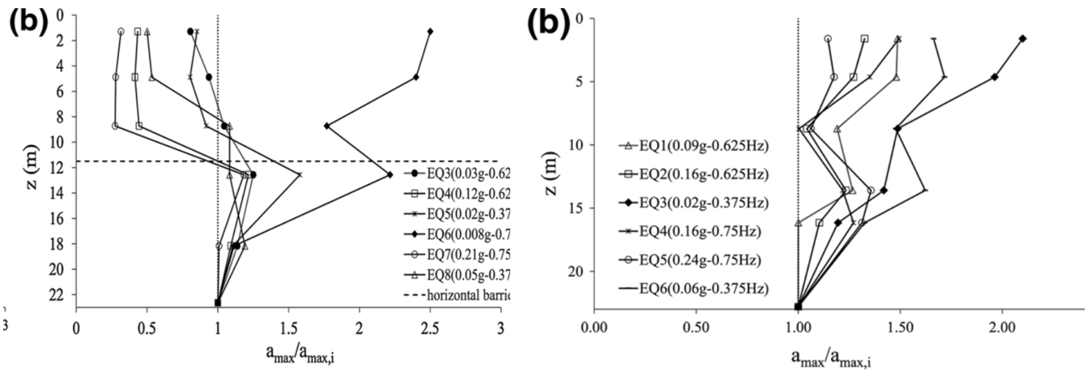

Figure 2. 43. Profile of amplification with depth: (a) horizontal layer; (b) V shaped layer. (Nappa, 2018)

After the centrifuge test, a numerical F.E. model was built to replicate the centrifuge test and to have a model without the barriers as a benchmark condition. With this numerical model, it was possible to analyse the effect of inserting soft barriers with different sand-SAP concentrations both statically and dynamically. From a static point of view, Nappa focused mainly on the problem of bearing capacity reduction by considering different sand-SAP concentrations and different geometric schemes such as V-shape (Figure 2. 44) and rectangular one (Figure 2. 45).

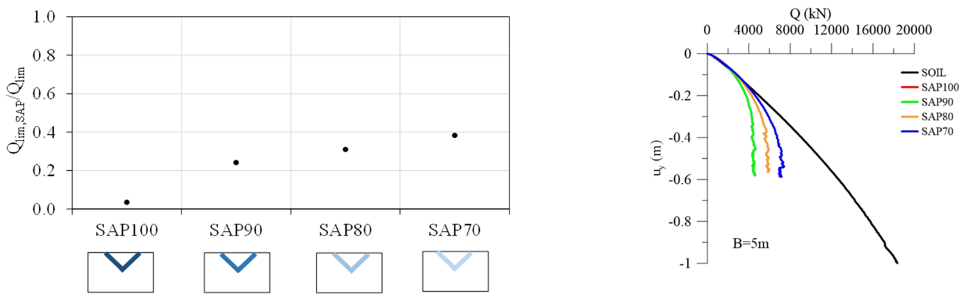

Figure 2. 44. Reduction of bearing capacity with V-shape geometrical barriers. (Nappa, 2018)

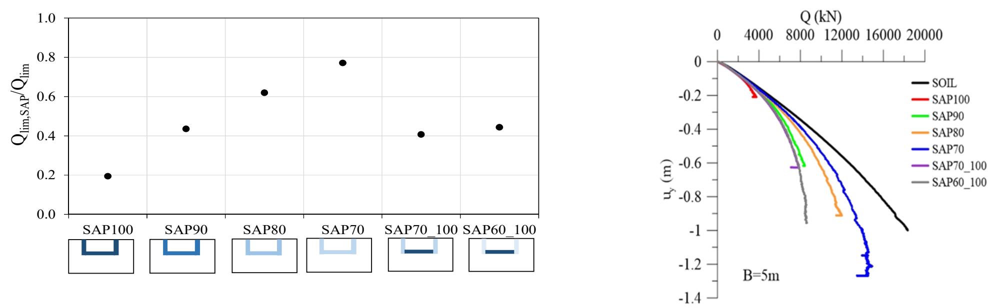

Figure 2. 45 . Reduction of bearing capacity with rectangular shape. (Nappa, 2018)

As far as the dynamic aspects are concerned, using seven spectrum-compatible accelerograms, Nappa evaluated the reduction of the maximum accelerations at the top surface of the isolated volume of soil as well as the lowering of the average Pseudo Acceleration spectrum for V-shaped (Figure 2. 46) and rectangular shape (Figure 2. 47).

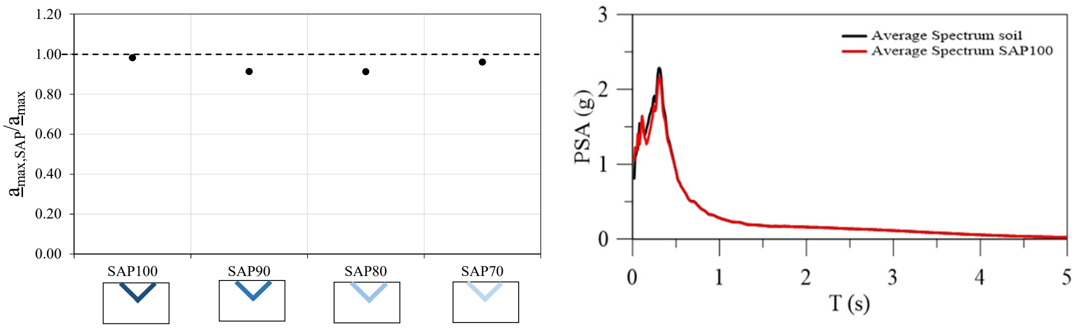

Figure 2. 46 Reduction of maximum acceleration provided by V shaped barrier. And (b) relative average pseudo spectral acceleration. (Nappa, 2018)

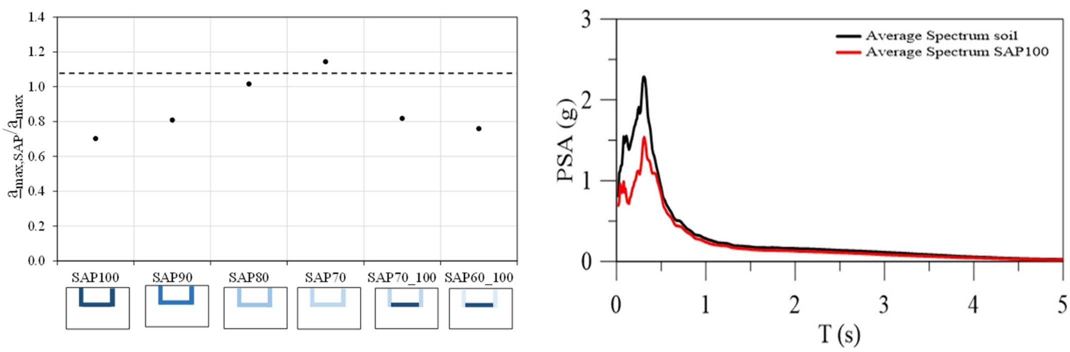

Figure 2. 47. Reduction of maximum acceleration provided by caisonn barrier and (b) relative average pseudo spectral acceleration. (Nappa, 2018)

As it is possible to see, the reduction obtained in terms of mean maximum accelerations was of about 10 % for V shaped barrier. Therefore, the use of the V barrier is not recommended. The optimum scheme (both in static and dynamic conditions) is the rectangular caisson made by two different materials (100% SAP at the base and 60% SAP or 70% SAP along the sides of the rectangular caisson). This is an finding that this thesis will explore further.

With the aim of evaluating the bearing capacity reduction provided by the soft barriers in a practical way, Nappa then focused her research on the creation of a static macro element. The entire soil-foundation system is considered as a single element located near the foundation area, which is introduced to analyse the non-linear and irreversible behaviour of the soil-foundation interaction that can takes place at the near field zone. This theory is expanded by Nova and Montrasio (1991) in a case of shallow strip footing on sand under monotonic loading with an isotropic hardening elasto-plastic law to define the bearing capacity of the foundation in a vertical (V), horizontal (H) and overturning moment plane (M). Numerical parametric analyses were performed to calibrate the 9 macro-element parameters in presence of the soft barrier. The calibration and validation of the static macro element established that the introduction of the soft barriers entirely reduces the whole failure domain (H-V-M). However, it was also assessed that this reduction seems to be mainly influenced by the distance of the vertical barriers from the foundation (Figure 2. 48).

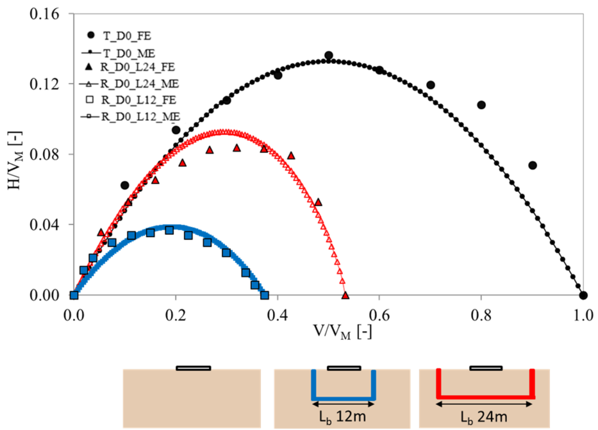

Figure 2. 48 Contraction of the failure envelope as a function of the caisson width (Nappa, 2018)

The results of the analyses carried out clearly indicate that the insertion of the barrier leads to a significant reduction in safety conditions in the case of structures with low safety margins with respect to the vertical limit load. On the contrary, the reductions may be acceptable for structures with high safety margins with respect to vertical loads.

In the last part of her doctoral thesis, Nappa evaluated the effectiveness of SAP to isolate a volume from the antropically induced vibrations. Different full-scale experiments were made. The results of the site tests show that the barriers can be a useful tool for surface vibration mitigation. However, since the objective of this thesis is seismic isolation from earthquake-induced vibrations, no further information will be given on this respect.

From the two theses described, it is clear that it is possible to seismically isolate a portion of soil through the use of soft barriers. By so doing, a beneficial effect in terms of structural response is obtained for three reasons: a reduction of the horizontal, rocking and shear stiffness at the foundation level; an increase of hysteretic damping, and an increase of the structural mass (the isolated portion of soil being part of the foundation mass). All these factors lead to a reduction of the natural period of the structure, which can be tuned to reduce as much as possible the seismic shaking.

Since any numerical result is based on the input parameters used, the present thesis will try to deepen the dynamic characterisation of such mixtures as well as illustrate the most representative dimensionless parameters of the efficiency of this technique. As Nappa has created a tool for easy prediction of bearing capacity reduction, this thesis will develop a simple approach and procedure to evaluate the dynamic effects of soft barriers into the soil on the seismic behaviour of a building. Indeed, the thickness, the percentage of SAP in the mixture, as well as the width and depth of the soft caisson must be chosen according to the parameters of the seismic input motion and local site effects.

References

Alterio L. (2012). "Seismic vulnerability reduction of monumental building by soils treatment". Ph.D. Thesis, Università degli Studi di Napoli Federico II (Italia).

Anastasiadis A, Pitilakis K, Senetakis K. (2009). "Dynamic shear modulus and damping ratio curves of sand/rubber mixtures". *In: Proceedings of the earthquake geotechnical engineering satellite conference*, XVIIth international conference on soil mechanics & geotechnical engineering, Alexandria, Egypt

Anastasopoulos, I., Gazetas, G., Loli, M., Apostolou, M. e Gerolymos, N. (2010). "Soil failure can be used for seismic protection of structures". *Bullettin of Earthquake Engineering*. **8**(2):309-326.

ASCE (2010). "*Minimum Design Loads for Buildings and Other Structures".* ASCE/SEI 7-10, American Society of Civil Engineers, Reston, Virginia.

Aviles, J., Perez-Rocha, L.E. (1996)."Evaluation of interaction effects on system period and the system damping due to foundation embedment and layer depth". *Soil Dynamics and Earthquake Engineering*. **15**:11-27.

Bielak, J. (1975). "Dynamic behavior of structures with embedded foundations," *Earthquake Engineering and Structural Dynamics*. **3**:259-274.

Bielak, J. (1976). "Modal analysis for building-soil interaction," *Journal of Engineering Mechanics*. **102**:771-786.

Cai Y., Liang X. (2003). "Dynamic properties of composite cemented clay Journal of Zhejiang University". Journal of Zhejiang University SCIENCE, Zhejiang (China).

Chavez-Garcia F.J. (2011). "Site effects due to topography and to soft soil layers: progress made and pending issues". *A Personal Perspective. Proc. 5th International Conf. on Earthquake Geotechnical Engineering* – State of the art Lectures, Santiago (Chile).

Conti, R., Morigi, M., Viggiani, G. M. (2015). "Determinazione dell'effetto filtro indotto da fondazioni interrate". In: *Atti dell'Incontro Annuale dei Ricercatori di Geotecnica - IARG 2015, Cagliari,* 24-26 giugno.

Costanzo A., d'Onofrio A., Lanzo G., Pagliaroli A., Penna A., Puglia R., Santucci De Magistris F., Sica S., Silvestri F., Tommasi P. (2007). "Seismic response of historical centers in Italy: selected case studies". *Workshop on 'Geotechnical Earthquake Engineering related to Monuments and Historical Centers'*, 4th ICEGE, Thessaloniki (Greece).

D'Onofrio A., Mancuso C., Silvestri F. (1999). "Reduction of seismic vulnerability by geomaterial attenuation procedures". *Proc. 2nd International Confererence on Earthquake Geotechnical Engineering*, Lisboa (Portugal), pp.725-730.

Day, S.M., (1978). "Seismic response of embedded foundations". *Preprints of Conference Proceedings of ASCE Convention and Exposition, Chicago, IL*, Preprint No. 3450, American Society of Civil Engineers, New York, New York.

Dietz, M.S., Wood, D. M. (2006). "Shake table testing of a soft caisson for geotechnical seismic retrofit". *Proc. 4th International Conference on Earthquake Geotechnical Engineering, Thessaloniki (Greece).*

Dolce, M., Ponzo, F.C., Di Cesare, A., Arleo, G. (2010). "Progetto di edifici con isolamento sismico". IUSS PRESS, Pavia (Italy), pp.215.

Doudomis, N., Papadopoulos, P. Papaliangas, T. (2002). "Low-cost base isolation system on artificial soil layers with low shearing resistance". *Proc. 12th European Conference on Earthquake Engineering, paper reference 661.*

Drosos, V., Georgarakos, T., Loli, M., Anastasopoulos, I., Zarzouras, O., Gazetas G. (2012). "Soil-Foundation-Structure Interaction with Mobilization of Bearing Capacity: Experimental Study on Sand". *Journal of Geotechnical and Geoenvironmental Engineering*. **138**:1369-1386.

Elsabee, F., Morray, J. P. (1977). "Dynamic behavior of embedded foundations*". Research Report R77-33,* Department of Civil Engineering, Massachussetts Institute of Technology, Cambridge.

Feng Z-Y, Sutter KG. (2000). "Dynamic properties of granulated rubber/sand mixtures". *Geotech Test J.* **23**(3):338–344

Gazetas, G. (1983). "Analysis of machine foundation vibrations: state of the art". *Soil Dynamics and Earthquake Engineering,* **2**(1):2-42.

Gazetas, G. (1991). "Formulas and charts for impedances of surface and embedded foundations". *J Geotech Eng.* **117**:1363–1381. doi:10.1061/(ASCE)0733-9410(1991)117:9(1363)

Gazetas, G. (2015). "4th Ishihara Lecture: Soil - foundation - structure systems beyond conventional seismic failure thresholds". *Soil Dynamics and Earthquake Engineering*. **68**:23-39.

Georgarakos P., Yegian M.K., Gazetas, G. (2005). "In-Ground isolation using geosynthetic liners".*9th World Seminar on Seismic Isolation, Energy Dissipation and Active Vibration Control of Structure*. Kobe

Gerolymos, N. e Gazetas, G. (2006). "Development of Winkler model for static and dynamic response of caisson foundations with soil and interface nonlinearities". *Soil Dynamics and Earthquake Engineering,* **26**, 363-376.

Gerolymos, N., Gazetas, G. (2006). "Static and dynamic response of massive caisson foundations with soil and interface nonlinearities - validation and results". *Soil Dynamics and Earthquake Engineering,* **26**, 377-394

Gerolymos, N., Gazetas, G. (2006). "Winkler model for lateral response of rigid caisson foundations in linear soil". *Soil Dynamics and Earthquake Engineering.* **26**:347-361.

Giovannardi F., Gulsasola A. (2013) . "Basic isolation: dalle origini ai giorni nostri". http://it.calameo.com/read/001671591369645c5959a.

Givens, M.J. (2013). "Dynamic Soil-Structure Interaction of Instrumented Buildings and Test Structures". *Ph.D. Dissertation, Department of Civil and Environmental Engineering*, University of California, Los Angeles, California.

Godoy, A., Chatzigogos, C. e Pecker, A., (2012). "Safety margins in structural design of a bridge pylon: assessment of dynamic response through incremental dynamic analyses". *In: Proceedings of the 2nd International Conference on Performance-Based Design in Earthquake Engineering*, Taormina, 28-30 May, 1455-1466.

Iervolino I. (2021). "Dinamica delle strutture ed Ingegneria Sismica". Hoepli.

Kausel E., Whitman A., Murray J., Elsabee F. (1978). "The spring method for embedded foundations," *Nuclear Engineering and Design*. **48**:377-392

Kavazanjian, E., Hushmand, B., Martin, G.R. (1991). "Frictional Base Isolation Using a Layered Soil-Synthetic Liner System". *Proc. 3rd U.S. Conference on Lifeline Earthquake Engineering*, ASCE Technical Council on Lifeline Earthquake Engineering Monograph. **4**:1139-1151.

Kellezi L. (2001). "Dynamic behavior of a softer layer overlying hard soil / bedrock and vibration reduction". *GEO-Danish Geotechnical Institute, Lyngby (Danmark).*

Kim, H.K., Santamarina, J.C. (2008). "Sand-rubber mixtures (large rubber chips)". *Can Geotech J.* **45**:1457–1465

Kirtas E., Pitilakis K. (2009). “Subsoil Interventions Effect on Structural Seismic Response. Part II: Parametric Investigation”. *Journal of Earthquake Engineering*. **13**(3):328-344.

Kirtas E., Rovithis E., Pitilakis K. (2009). “Subsoil Interventions Effect on Structural Seismic Response. Part I: Validation of Numerical Simulations”. *Journal of Earthquake Engineering*. **13**(2):155-169.

Kramer, S.L. (1996). “Geotechnical earthquake engineering”. *Prentice-Hall*, Upeer Saddle River, New Jersey (USA), pp.653.

Lignola, G. P., Di Sarno, L., Di Ludovico, M., Prota, A. (2016). “The protection of artistic assets through the base - isolation of historical buildings: A novel uplifting technology”. *Materials and Structures*. doi:10.1617/s11527-015-0785-1.

Lombardi D., Flora A., Lirer S., Silvestri F. (2014). “Soil grouting for the seismic protection of existing buildings”. *Proceedings of the Institution of Civil Engineers - Ground Improvement*. **167**(3):206-218

Lombardi, D. (2014). “An Innovative Ground Treatment Approach for Seismic Risk Mitigation of Existing Structures”. Ph.D. Thesis, Università degli Studi di Napoli Federico II (Italia).

Luco, J. (2013). “Bounds for natural frequencies, Dunkerley’s formula and application to soil–structure interaction”. *Soil Dyn Earthq Eng.* **47**:32–37. doi:10.1016/j.soildyn.2012.08.007

Maravas, A., Mylonakis, G. e Karabalis, D. L. (2014). “Simplified discrete systems for dynamic analysis of structures on footings and piles”. *Soil Dynamics and Earthquake Engineering*. **61**:29-39

Martelli A., Clemente P., Saitta F., Forni M. (2012). “Recent worldwide application of seismic isolation and energy dissipation to steel and other materials structures and conditions for their correct use”. *In Behaviour of steel structures in seismic areas: STESSA , ed. F. Mazzolani, and R. Herrera. London, UK: Taylor and Francis Group.*

Martelli, A., (2009). “Proceedings of International Conference Prohitech09.Rome June 2009 Italy.ICOMOS 1964. The Venice Charter (1964) - International charter for the conservation and restoration of monuments and sites”. *Proc. 2nd International Congress of Architects and Technicians of Historic Monuments*, Venice. ICOMOS, Int. Council on Monuments and Sites. internet: www.icomos.org/charters/venice_e.pdf

Massarsch, K.R. (2004). “Mitigation of Traffic-induced Ground Vibrations”. *Proc. 11th international conference on earthquake geotechnical engineering, pp.22–31. Berkeley, California (USA).*

Massarsch, K.R. (2005). “Vibration isolation using gas-filled cushions”. *Proc. Sessions of the Geo-Frontiers Congress, Austin, Texas (USA).*

Mezzi M., Comodini F., Rossi L. (2011). “A base isolation option for the full seismic protection of an existing masonry school building”. *In Proceedings of the Thirteenth International Conference on Civil, Structural and Environmental Engineering Computing*, eds. B. H. V. Topping, and Y. Tsompanakis, 1–14. Chania, Crete, Greece: Civil-Comp Ltd.. 6–9 September

Mylonakis, G., Gazetas, G. (2000). “Seismic soil-structure interaction: beneficial or detrimental”. *Journal of Earthquake Engineering*. **4**(3):277-301.

Mylonakis, G., Nikolaou, S., Gazetas, G. (2006). “Footings under seismic loading: Analysis and design issues with emphasis on bridge foundations”. *Soil Dynamics and Earthquake Engineering*. **26**:824-853.

Naderzadeh, A. (2009). “Historical Aspects of Seismic Base Isolation Application”. *Proc. JSSI 15th Anniversary International Symposium on Seismic Response Controlled Buildings for Sustainable Society*, 16-18 Sept. 2009, JSSI, Tokyo (Japan).

Nappa, V. (2018). “SOFT GROUTING FOR SEISMIC ISOLATION: Numerical and Physical modelling”. Ph.D. Thesis, Università degli Studi di Napoli Federico II (Italia).

Nova, R. and Montrasio, L. (1991). "Settlements of shallow foundations on sand". *Géotechnique*. **41**(2): 243-256.

Pais, A., Kausel, E. (1988). "Approximate formulas for dynamic stiffnesses of rigid foundations," *Soil Dynamics and Earthquake Engineering*. **7**(4):213-227.

Richart, F.E, Woods, R.D. (1970). "Vibrations of soils and foundations". *Prentice-Hall*, Upeer Saddle River, New Jersey (USA).

Roesset, J.M. (1980). "Stiffness and damping coefficients of foundations," *Proceedings*, ASCE Geotechnical Engineering Division National Convention, pp. 1-30.

Saxena, K. S., Avramidis, A. S., Reddy, K. R. (1987). "Dynamic moduli and damping ratio for cemented sand at low strains". *Can. Geotech.Journ.* **25**:353-368.

Spencer, L. M. (2010). "Evaluation of sand treated with colloidal silica gel". *Phd Thesis Georgia Institute of Technology*, Atlanta, Georgia (USA).

Taskov L., Manova K., Krstevska L., Garevski M. (2010). "Evaluation of efficiency of ALSC floating-sliding base-isolation system based on shake table test and floor response spectra". *Bull. Earthquake Eng.* **8**:995-1018.

Taskov, L., Antimovki, A., Kokalevki, M. (2004). "Shaking table test of efficiency of ALSC base-isolation system". *Proc. 13th World Conference on Earthquake Engineering Paper No. 785, Vancouver (Canada).*

Tsang, H., Kyriazis, P. (2019). "Mechanism of geotechnical seismic isolation system: Analytical modelling". *Soil Dynamics and Earthquake Engineering*. **122**: 171-184. ISSN 0267-7261. https://doi.org/10.1016/j.soildyn.2019.03.037.

Tsang, H.H. (2009). "Geotechnical seismic isolation". *Earthquake Engineering: New Research*. Nova Science Publishers, New York (USA), pp.55-87

Varun, Assimaki, D., Gazetas, G. (2009). "A simplified model for lateral response of large diameter caisson foundations - Linear elastic formulation". *Soil Dynamics and Earthquake Engineering,* **29**(2):268-291.

Veletsos, A.S., Meek, J.W. (1974). "Dynamic behavior of building-foundation systems," *Earthquake Engineering and Structural Dynamics*. **3**:121-138.

Veletsos, A.S., Nair, V.V. (1975). "Seismic interaction of structures on hysteretic foundations," *Journal of Structural Engineering*. **101**:109-129.

Viggiani C. (2017). "Geotechnics and Heritage". *19th International conference on Soil Mechanics and Geotechnical Engineering 17-22 September 2017*, Seoul Korea

Vucetic, M., Dobry, R. (1991). "Effect of soil plasticity on cyclic response". *Journal of Geotechnical Engineering Division*. **17**:89-107.

Wolf, J.P. (1985). "*Dynamic Soil-Structure Interaction". Prentice-Hall, Upper Saddle River*, New Jersey.

Yegian M.K. and Catan M. (2004). "Soil Isolation for seismic protection using a smooth synthetic liner". *Journal of Geotechnical and geo-environmental Engineering,* ASCEE (Nov):1131.

Yegian M.K., Kadakal U. (2004). "Foundation isolation for seismic protection using a smooth synthetic liner". *Journal of Geotechnical and geo-environmental Engineering*. **130**(11).

Yegian, M.K., Lahlaf, A.M. (1992). "Dynamic interface shear properties of geomembranes and geotextiles". *Journal of the Geotechnical Engineering*, ASCE.**118**(5):760-779

Zafeirakos, A., Gerolymos, N. (2012). "Seismic performance of caisson supported piers". *In: Proceedings of the 2nd International Conference on Performance-Based Design in Earthquake Engineering*, Taormina, 28-30 may, 900-914.

3. LATERAL DISCONNECTION OF SHALLOW FOUNDATION FROM THE SOIL

3.1 Introduction

In this chapter the technique called *"lateral disconnection of the shallow foundations from the adjacent soil"* will be studied from an experimental, numerical and analytical point of view.

This idea is an innovative yet extremely simple approach to reduce the seismic vulnerability of existing buildings on shallow foundations, based on removing the lateral contact between the embedded foundation and the surrounding soil. Current practice and capacity design demand that the foundations of buildings have large safety factors with reference to design limit states. It follows that, in seismic conditions, the design of ordinary structures is typically carried out assuming fixed restraints at the base, *i.e.*, neglecting the effects of dynamic soil-structure interaction. To minimise energy transfer into the superstructure, seismic isolators can be adopted in new buildings with relative ease. However, the seismic protection of existing buildings is still an issue. Traditional seismic retrofitting of historical structures, based *e.g.*, on the adoption of fibre reinforced polymers or cross stiffening brackets, may impact adversely their artistic or aesthetic integrity. As already stated, a possible alternative approach to modify the energy and frequency content of the seismic actions transferred to the superstructure without interposing a structural isolator may be to implement the isolation system in the subsoil. This is referred to as Geotechnical Seismic Isolation (GSI), in contrast to the most commonly used Structural Seismic Isolation (SSI) (Tsang, 2009). As already outlined in chapter 2, in the last decades, a variety of GSI interventions have been reported in the technical literature. All the reported GSI solutions modify the dynamic soil-structure interaction, with the aim of increasing the predominant period and/or the damping of the soil-structure system. The predominant period considering soil structure interaction can be expressed as (Veletsos *et al*., 1974):

$$T_{SSI} = 2\pi\sqrt{\frac{m_{str}}{K_{str}}}\sqrt{1+\frac{K_{str}}{K_{xx}}+\frac{K_{str}\left(H_{eff}\right)^2}{K_{\theta\theta}}} = T_{FB}\sqrt{1+\frac{K_{str}}{K_{xx}}+\frac{K_{str}\left(H_{eff}\right)^2}{K_{\theta\theta}}} \quad (3.\ 1)$$

in which m_{str} is the mass of the superstructure, K_{str} is the horizontal stiffness of the superstructure, K_{xx} and $K_{\theta\theta}$ are the dynamic lateral and rotational soil-foundation stiffnesses, H_{eff} is the effective height, that is the height of the centroid of the superstructure related to the foundation base, and T_{FB} is the fundamental natural period of the fixed-base structure. Eq. (3. 1) indicates that a possible way to increase the predominant period of the structure, and thus to reduce the seismic demand, is the reduction of the horizontal and/or rotational soil-foundation stiffnesses. A simple and effective way to decrease the lateral and rotational stiffness of a shallow foundation is its lateral disconnection of from the adjacent soil. It is worth noting that the damping of the structural system considering soil-structure interaction (ξ_{SSI}) is usually higher than the one corresponding to fixed base conditions (ξ_{FB}), because of energy losses associated to both radiation damping and material damping. It is expected that, while beneficial in terms of stiffness, the effect of a lateral disconnection may imply a detrimental reduction of the radiation damping. For the typical embedment ratios of shallow foundations, however, the increased natural period is far more relevant than the reduction of damping, with an overall beneficial effect of the lateral disconnection in terms of seismic demand. A schematic representation of the effects of the lateral disconnection technique is shown in Figure 3. 1.

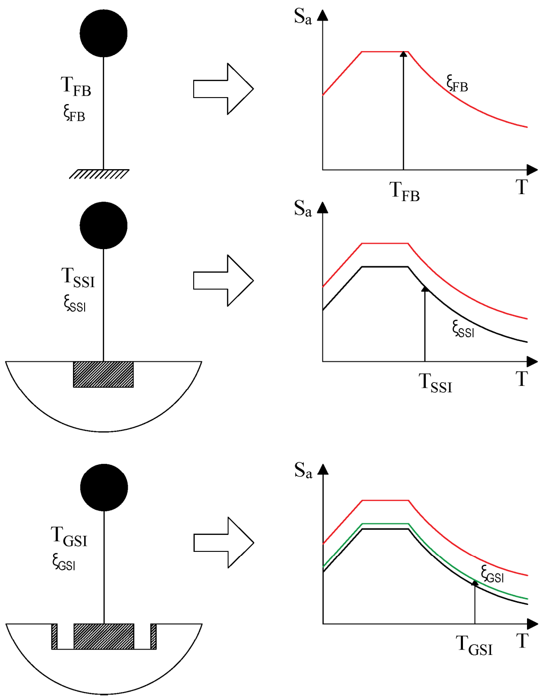

Figure 3. 1 Response spectra of a SDOF structure with: (a) fixed base, (b) embedded compliant foundation, (c) laterally disconnected embedded compliant foundation. (from Somma et al.2021)

3.2 Centrifuge test on Lateral Disconnection

The effectiveness of a GSI based on a lateral disconnection at foundation level was investigated by a centrifuge test on two identical structures, resting on identical shallow foundations at the same depth but having different lateral constraints. The test was carried out at the Schofield centre, the geotechnical laboratory of the Cambridge University. The basic principles of centrifugal modelling, instrument calibration and model preparation will be briefly recalled.

3.2.1. Basic principles of centrifuge modelling

A centrifuge test is a sophisticated system in which a model of both geotechnical and structural nature can be tested. Materials such as soil or rock are characterised by non-linear mechanical properties that depend on the effective confining stress as well as stress history. Geotechnical modelling requires the behaviour of soils to be reproduced in terms of both strength and stiffness. For this reason, in a centrifuge test, an increment of gravity acceleration is applied in order to reproduce identical stress states between the model and the prototype. By placing the model at one end of the centrifuge arm, it undergoes the radial acceleration generated by the rotation of the centrifuge. As far as the model is concerned, this acceleration will act as a pseudo acceleration of gravity. The physics of the problem creates relationships between quantities at the scale of the model and those at the scale of the prototype. These relationships are called scaling laws. For example, if the same soil is used in the model and in the prototype, and if the model is subjected to a similar stress history, then for the centrifugal model subjected to a gravity acceleration equal to N times the earth's gravity (9.81m/s^2), the vertical tension at depth h_m (σ_{Vm}) (where m denotes the model) will be equal to that of the prototype at a depth equal to h_p=N*h_m. This is the most important scaling law; stress similarity is achieved at homologous points by accelerating a model of reduced scale equal to N to N times Earth's gravity:

$$\sigma_{Vp} = p \cdot g \cdot h_p \tag{3. 2}$$

$$\sigma_{Vm} = p \cdot N \cdot g \cdot \frac{h_m}{N} \tag{3. 3}$$

$$\sigma_{Vp} = \sigma_{Vm} \tag{3. 4}$$

The most common scale laws (Schofield, 1980) are summarized in Table 3. 1.

Table 3. 1.Relevant centrifuge scaling laws.

Parameter	Model/Prototype	Units
Length	1/N	m
Mass	1/N^3	Kg
Force	1/N^2	N
Stiffness	1/N	Nm^{-1}
Time	1/N	s
Frequency	N	Hz
Acceleration	N	ms^{-2}
Velocity	1	ms^{-1}
Displacement	1/N	m

The Turner beam centrifuge, used for this test, was designed by Philip Turner and was built in the workshops of the Department of Engineering at the University of Cambridge (Figure 3. 2)

Figure 3. 2. Turner beam centrifuge designed by Philip Turner

Different types of transducers can be used to monitor a centrifuge test; linear variable displacement transducer (LVDT), Piezoelectric accelerometers, micro electro mechanical system (MEMS). In addition, it is possible to use techniques based on particle image velocimetry (PIV) as well as instruments to evaluate the properties of the soil, during the centrifuge test (i.e. in flight) such as the Air Hammer (AH) and the Cone Penetration Test (CPT). All these instruments were used in this test.

3.2.2. Calibration of instruments.

All the instruments are calibrated using a data logger with the software Dasylab 9.0. Each instrument must be calibrated before testing. Depending on the number of instruments one decides to use this can take a considerable amount of time. Questions there arises as to why it is necessary to recalibrate the same instruments used in each test. The answer is that, generally, after a centrifuge test, even if only slightly, the calibration coefficients of the various transducer change. In addition, each instrument should be connected to a junction box (i.e. a special device in which all instruments are connected). Because of the different sensitivity of each junction box, it is wise to calibrate each instrument to the precise channel of the junction box, which has been pre-set to accept the specific transducer itself. It is important to remember that *"calibrating"* means creating a correlation between the response of the transducers in Volts and the and the variable they measure (*i.e.* LVDT = length, MEMS = acceleration, etc.). The instrument will always give information in Volts which can be transformed by means of correlation factors.

3.2.2.1 Piezo accelerometer calibration

Piezo accelerometers are very important instruments because they allow to know the accelerations in the ground (Figure 3. 3).

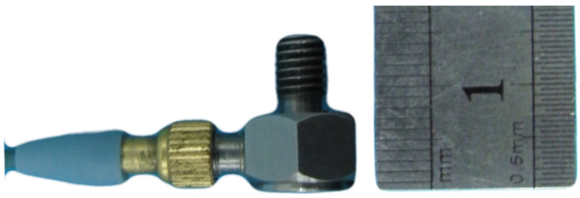

Figure 3. 3 Piezoelectric accelerometer.

The accelerometers are calibrated using a calibrator, which excites the instruments with a sinusoidal input having acceleration amplitude of ±1g. All the calibration factors used in the tests were reported in

Table 3. 2 calibration factor (CF) was calculated from the equation:

$$CF = \frac{2}{|V_{MIN} - V_{MAX}|} \quad (3.\ 5)$$

Table 3. 2 Calibration factor for piezo accelerometer

Channel Number [-]	Piezo Num [-]	Maximum [V]	Minimum [V]	CF [-]
1	8876	0.1697	-0.1697	5.892751915
2	7340	0.1556	-0.1639	6.259780908
3	-			
4	10190	0.1563	-0.1578	6.367398918
5	8838	0.1407	-0.148	6.927606512

6	9082	0.1309	-0.1392	7.404664939
7	1518	0.1532	-0.1602	6.381620932
8	8848	0.1468	-0.144	6.877579092
9	8932	0.1498	-0.1523	6.620324396
10	10176	0.1666	-0.1663	6.007810153
11	10157	0.1553	-0.1624	6.295247088
12	10223	0.1672	-0.1691	5.947071067
13	9989	0.1233	-0.134	7.773027594
14	8830	0.1584	-0.1566	6.349206349
15	8880	0.1611	-0.1584	6.259780908
16	8895	0.148	-0.1517	6.673340007
17	8858	0.155	-0.1559	6.432936636
18	8888	0.1779	-0.1822	5.554012774
19	10089	0.1645	-0.1715	5.952380952
20	10190	0.166	-0.1703	5.947071067
21				
22	8825	0.1349	-0.1398	7.280669822
23	7334	0.1535	-0.1535	6.51465798
24				

In some cases, channels in the junction box did not work and are therefore empty. The last two transducers generally are used to record the signal at the base of the model. A total of 21 ground acceleration transducers were used.

3.2.2.2 MEMS calibration

Micro-Electro-Mechanical System (MEMS) accelerometers are small electrical devices which measure acceleration by measuring the force that a mass applies to a spring. This means that they measure inertial as well as dynamic acceleration. As can be seen from Figure 3. 4, the MEMS is only able to read acceleration in the direction of the single copper line (orthogonally the triple copper lines). MEMS are generally used to monitor accelerations on structures during a centrifuge test. In particular, they are literally *"glued"* on the structures in different orientations and positions. In this case, the calibration is performed by placing the MEMS on a horizontal surface and gradually rotating that surface. By doing so, different components of the gravity acceleration will act on the MEMS and with these it will be possible to calibrate the MEMS.

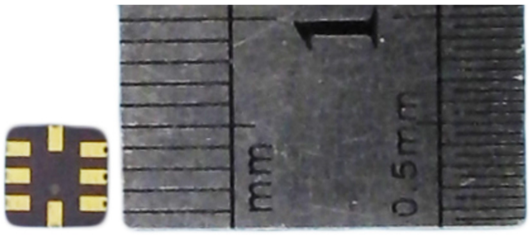

Figure 3. 4. Micro-Electro-Mechanical System (MEMS) accelerometer

Table 3. 3 Calibration of MEMS.

Angle [°]	sin(Angle)	Acc [m/s^2]	MEMS BH1	MEMS BH2	MEMS SH1	MEMS SH2	MEMS BH3	MEMS BV1	MEMS BV2
-90	-1	-9.81						2.5189	2.5058
-60	-0.8660254	-8.4957092	2.4897	2.4874	2.449	2.5132	2.5465	2.5182	2.5024
-40	-0.6427876	-6.3057465	2.4778	2.4747	2.4372	2.5006	2.5306	2.5151	2.4977
-20	-0.3420201	-3.3552176	2.461	2.4576	2.419	2.4833	2.5111	2.5112	2.4921
0	0	0	2.4415	2.4381	2.3997	2.4628	2.4885	2.5046	2.4858
20	0.34202014	3.35521761	2.4217	2.4187	2.3801	2.4446	2.468	2.4972	2.4791
40	0.64278761	6.30574645	2.4042	2.4016	2.363	2.4264	2.4502	2.491	2.4736
60	0.8660254	8.49570921	2.3911	2.3889	2.3502	2.4138	2.4401	2.4848	2.4706
90	1	9.81						2.4818	2.4679

Table 3. 4 Calibration of MEMS.

Angle [°]	Sin(ang) [-]	Acc [m/s^2]	MEMS BH1 GSI	MEMS BH2 GSI	MEMS SH1 GSI	MEMS SH2 GSI	MEMS BH3 GSI	MEMS BV1 GSI	MEMS BV2 GSI
-90	-1	-9.81						2.4732	2.4855
-60	-0.8660254	-8.4957092	2.4914	2.5416	2.5246	2.574	2.5087	2.4713	2.4835
-40	-0.6427876	-6.3057465	2.4806	2.5284	2.5094	2.5611	2.4969	2.4682	2.4797
-20	-0.3420201	-3.3552176	2.4603	2.5115	2.4941	2.5429	2.479	2.463	2.4745
0	0	0	2.4401	2.492	2.4731	2.5236	2.4558	2.4568	2.4684
20	0.34202014	3.35521761	2.4206	2.4721	2.455	2.5048	2.4306	2.451	2.4622
40	0.64278761	6.30574645	2.4054	2.4554	2.4418	2.4895	2.4126	2.4459	2.4564
60	0.8660254	8.49570921	2.3937	2.4431	2.4234	2.4762	2.403	2.4419	2.4519
90	1	9.81						2.4386	2.4488

A total number of 14 MEMS were used for the test. The position and orientation of the MEMS placed on the structures will be discussed later.

3.2.2.3 LVDT calibration

To measure the settlement of the structures Linear Variable Differential Transformers (LVDTs) were utilised (Figure 3. 5). An LVDT, has a relatively slow response meaning they are ineffective at measuring high frequency displacements accurately (over 15Hz). They do however provide an accurate indication of the cumulative settlement.

Figure 3. 5. LVDT displacement transducer.

Prior to use, an LVDT is calibrated by applying known displacements from a screw gauge and its output is measured. The cylindrical body of the LVDT was blocked, instead the metallic stick touched the mini platform and moved with itself. The calibration factor for 4 LVDT's was shown in Table 3. 5.

Table 3. 5 Calibration factor for LVDT's.

Displacements [mm]	LVDT 031 [V]	CF [mm/V]
0	-0.8096	6.0318
2.12	-0.4425	
4.32	-0.0783	
7.23	0.4041	
10.62	0.9672	
13.34	1.4079	
15.83	1.8224	
21.36	2.7284	
30.11	4.2107	
19.79	2.469	
8.64	0.6382	
1.31	-0.5742	

Displacements [mm]	LVDT 031 [V]	CF [mm/V]
0	-2.1669	5.7518
1.92	-1.809	
3.58	-1.5124	
8.04	-0.7401	
11.24	-0.1863	
16.84	0.7888	
20.39	1.3972	
25.14	2.2244	
30.33	3.122	
20.71	1.4333	
10.64	-0.3092	
2.06	-1.8007	

Displacements [mm]	LVDT 031 [V]	CF [mm/V]
0	-3.1317	5.887
3.89	-2.4541	
6.41	-2.0282	
10.32	-1.3596	
14.33	-0.6828	
20.31	0.3332	
25.11	1.14	
31.15	2.1585	
20.92	0.4167	
11.09	-1.2499	
3.99	-2.4603	
0.69	-3.0181	

Displacements [mm]	LVDT 031 [V]	CF [mm/V]
0	-4.7199	3.6961
2.97	-4.0491	
6.14	-3.1823	
10.72	-1.9268	
12.04	-1.5547	
16.66	-0.31	
18.38	0.1811	
23.06	1.4384	
26.56	2.3782	
29.83	3.2782	
21.11	0.8888	
16.4	-0.3874	
7.84	-2.7037	

A total number of 4 LVDTs were used to monitor the settlements of the structure during the centrifuge test.

3.2.2.4 AIR HAMMER

To allow a comparative numerical analysis to be conducted, information about the stiffness of the sand within the model is required. To characterise the soil in-flight, an air-hammer was installed within the soil at the bottom of the model.

Through a set of valves, air pushes a metal pellet backwards and forwards within the air-hammer. Each time the pellet strikes the end of the air-hammer it causes it to move fractionally and consequently induces a shear wave in the soil. The air-hammer is shown in Figure 3. 6. The velocity at which the shear wave moves up and down through the model can be found by placing piezoelectric accelerometers in an array just above the air-hammer. Measuring the time for the shear wave to move from one accelerometer to the next, combined with the distance between the two accelerometers, the shear wave velocity can be calculated. To determine the small strain stiffness, G_0, the smallest possible shear magnitude is required. However, the wave must still be large enough to register in the uppermost accelerometer. The magnitude of the shear wave is controlled by adjusting the pressure of the air supply to the air-hammer. Typically, a pressure of 100 kPa was used. Chapter 3.2.6 will deal with the interpretation of Air Hammer Test.

Figure 3. 6. Air Hammer

3.2.2.5 High Speed Camera

Due to the way that time scales in seismic centrifuge tests, earthquakes in the centrifuge last only about 0.5 seconds (30 seconds prototype scale) at frequency of about 50 Hz (0.83 Hz prototype scale) at 60g-level. Therefore, to capture images, a high-speed camera is required. For this series of tests, a MotionBLITZ EoSensR mini2 camera was used which is capable of recording images at 3-megapixel resolution at up to 523 frames per second. Due to certain parts of the field of view not being of interest, in these tests, the image size was reduced to only look at the relevant section close to the model foundation. This allowed the frequency of image recording to increase up to 1000 frames per second in certain tests. The camera body measures 65x65x65 mm and a c-mount lens with a fixed focal length of 12.5 mm was used, as shown in Figure 3. 7.

Figure 3. 7. High frequency camera used in the centrifuge test.

3.2.2.5 Cone Penetration Test.

In order to assess the strength of the soil, a miniature CPT can also be used during a centrifuge test. The CPT tip has a diameter of 6.4 mm and a maximum stroke of 20 cm (Figure 3. 8).

Figure 3. 8 Miniature C.P.T.

To use a CPT in a centrifuge test, care must be taken to ensure that the tip does not touch the instruments inserted in the ground and that the tip does not reach the bottom of the model. Calibrating a CPT is slightly more complex than others instruments. It is necessary to create a relationship between the Volt response of the CPT and the Force (Newton) that is exerted at the base of the tip. To do this, the tip is fixed at the top end of a support. Using pressurised air, it is possible to move this support (and therefore the tip itself) and touching a Load Cell. Through the Load Cell it will be possible to obtain the value of the force exerted by the tip (Table 3. 6).

Table 3. 6 Calibration factor for LVDT's.

Load Cell [V]	Weight [N]	Volts [V]	CF [N/V]
0.1338	-3.65062	-0.2443	
0.1343	-1.11557	-0.2444	
0.1363	9.02463	-0.2208	
0.1498	77.47098	-0.0777	
0.1618	138.31218	0.0357	448.7
0.1703	181.40803	0.1248	
0.185	255.9385	0.328	
0.1901	281.79601	0.3853	
0.1715	187.49215	0.195	
0.1566	111.94766	0.0025	
0.1452	54.14852	-0.129	
0.1437	46.54337	-0.1344	

3.2.3. Model Layout

The model is characterised by the presence of two identical structures, resting on identical shallow foundations at the same depth but having different lateral constraints. One of the foundations is in full contact with the surrounding soil (frame 1, named "NO GSI"); the other has its sidewalls disconnected from the surrounding soil (frame 2, named "GSI"). The model with the two structures was prepared with a geometrical scaling factor N = 60 and tested at g-level equal to 60 and was contained in a rigid box with internal dimensions W×D×H = 730×250×370 mm^3 (Figure 3. 9). The considerable size of this specific box is quite unusual compared to the typical size of the others. The choice of this box is due to the necessity of testing two structures at the same time, while guaranteeing the absence of interaction between each other and with the lateral boundary.

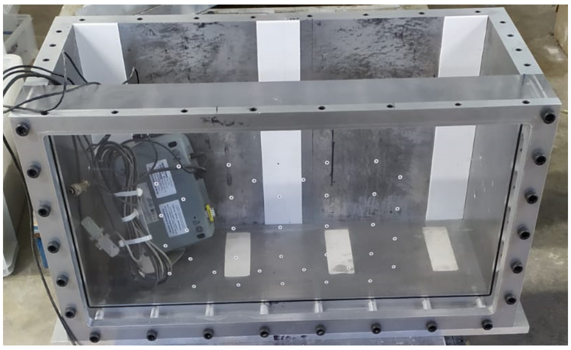

Figure 3. 9. Centrifuge Box used in the centrifuge test.

In addition, two 25 mm thick layers of Duxseal© were used to minimize seismic waves generation and reflection at the lateral boundaries of the container (Steedman & Madhabushi, 1991). The container has an 80 mm thick Perspex window, which allows in-flight measurements of soil deformation and structural displacement on a cross section of the model by Particle Image Velocimetry (PIV).

The foundation soil was dry Hostun HN31 sand, with the properties reported in Table 3. 7(Flavigny *et al.*, 1990; Heron, 2013).

Table 3. 7 Properties of Hostun Sand HN31

Soil [-]	G_s [-]	e_{max} [-]	e_{min} [-]	d_{50} [mm]	d_{10} [mm]	d_{60} [mm]	φ'_{cv} [°]
Hostun HN31	2.65	1.011	0.555	0.335	0.209	1.74	33

To achieve the target relative density D_{r0} = 55% and guarantee its uniformity in the model, the 250 mm thick layer of sand was created using an automatic sand pourer (Madabhushi *et al.*, 2006) (Figure 3. 10). The relative density was evaluated from expression:

$$D_r = \frac{e_{max} - e}{e_{max} - e_{min}} \qquad (3.\ 6)$$

Where the void index was calculated from the expression:

$$e = \frac{G_s \cdot m_s}{V} - 1 \quad (3.\ 7)$$

where m_s is the weight of the sand poured in the box and V is the internal volume of the box.

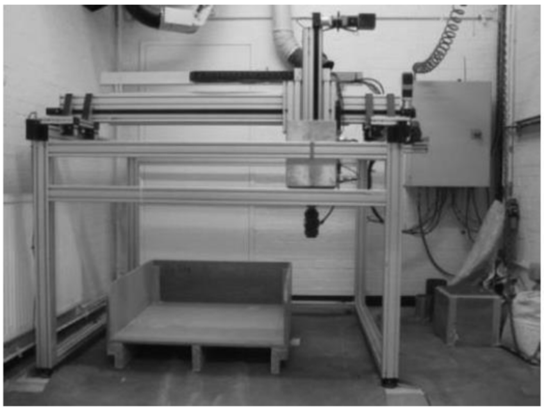

Figure 3. 10. Automatic sand pourer in Scofield Centre.

In this case, the sand was poured from a fall height of 810 mm using a 5 mm nozzle moving at 100 mm/s, and the density checked at the end of the pluviation phase. At the beginning of the centrifuge test the estimated relative density was 55% and the void index equal to 0.76 (so $\gamma_{dry} = 14.77 kN/m^3$). The choice of medium-loose sand in the centrifuge test was made to maximize SSI effects, which would have been less pronounced for a denser, and hence stiffer, foundation soil.

Micro-Electro-Mechanical Systems (MEMS) accelerometers were positioned on the structures, whose vertical displacements were monitored using four Linear Variable Differential Transformers (LVDTs), while piezoelectric accelerometers were placed in the soil along different vertical alignments (Figure 3. 11). It is important to emphasise that one of the most challenging choices when preparing a centrifuge model is the arrangement of the transducers on the structure and in the soil. Figure 3. 12 also show a photograph of the model before testing.

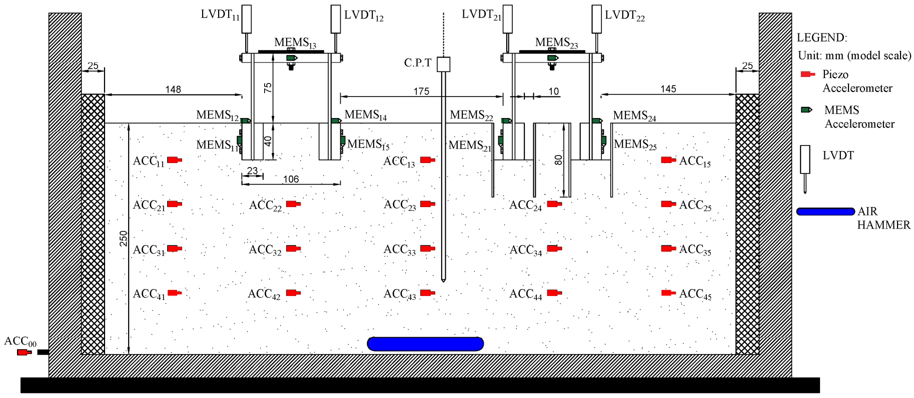

Figure 3. 11. Layout of the centrifuge model showing the position of the instruments and the two frames at model scale (on the left, frame NO GSI with traditional strip footings, on the right frame GSI). (Somma et al. 2021)

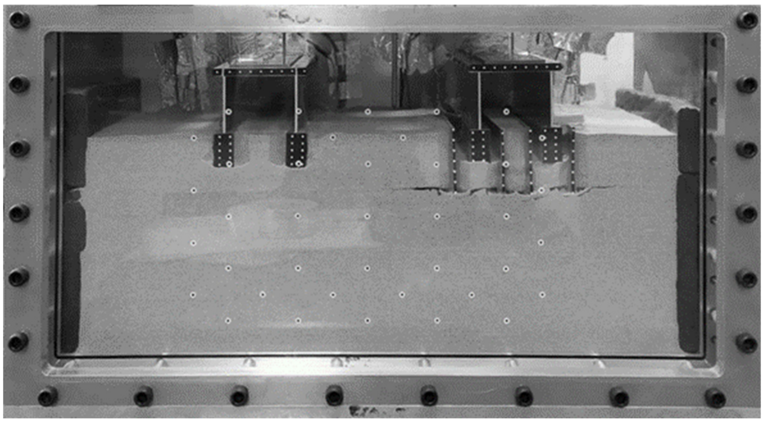

Figure 3. 12. Photograph of the model before the centrifuge test. (Somma et al. 2021)

The frames were positioned at a distance of 175 mm (10.5 m at prototype scale) from each other, and of about 150 mm (9.0 m at prototype scale) from the sides of the box, which complies with the recommendations by Jiang and Yan (1998) to reduce interaction effects. The lateral disconnections of the foundations of GSI frame were obtained placing two pairs of aluminium alloy plates, with dimensions 80×245×2 mm3, at a distance of 10 mm from the footings (0.6 m at prototype scale). During sand pluviation, the space between each pair was covered after reaching foundation level. To ensure the stability of the four cantilever walls, the embedment depth was set equal to the retaining height, while the distance of the cantilever walls from the foundations was kept as small as technically possible to avoid any effect on the foundation bearing capacity.

3.2.4. Structural Model.

This centrifuge test addresses a generic prototype four-storey 12 m-high masonry building with a plan area of about 100 m^2 and a height to width structural ratio of about 1, founded on shallow strip footings with a width of 1.5 m and a characteristic embedment of 2.5 m. The dimensions of the strip foundations reproduce well the typical construction practices of masonry buildings where the foundation was made by enlarging the load-bearing masonry walls sinking them several metres into the ground (Lenza & Ghersi, 2011; Augenti & Parisi, 2019). Assuming an average overall unit load per floor of 10 kPa, the average footing pressure including the self-weight of the foundations would be of the order of 130-140 kPa.

According to Eurocode 8 (BS EN 1998-1, 2004) the fundamental period of a structure can be estimated as:

$$T_1(\mathrm{s}) = C_{\mathrm{t}}(H)^{0.75} \tag{3. 8}$$

where H is the height of the structure and $C_{\mathrm{t}} = 0.05$ is a constant depending on the type of earthquake resistant structural system, in this case masonry shear walls. Using Eq. (3. 8), the fundamental period of the prototype structure is of the order of 0.32–0.33 s, or a frequency of about 3 Hz.

To study the seismic behavior of the prototype structure with and without the proposed mitigation measure, two identical sway-frames were constructed using 6082-T6 aluminium alloy and brass plates (Figure 3. 13), with the physical and mechanical properties reported in Table 3. 8.

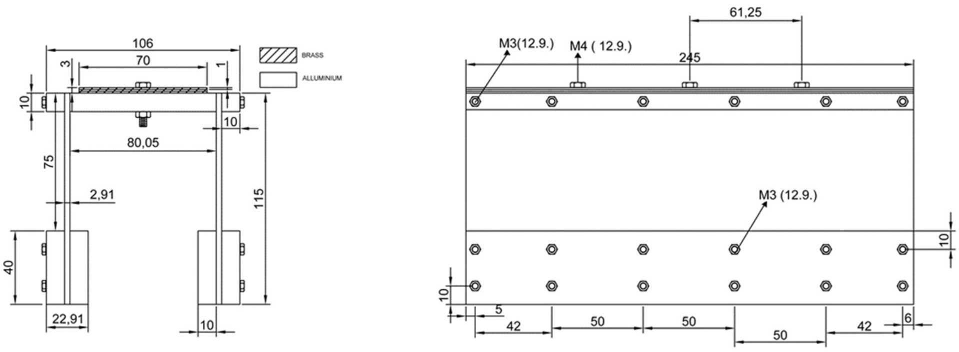

(a) (b)

Figure 3. 13 Structural models with dimensions in mm (model scale);(a) Front view (b) Lateral view.

Table 3. 8 Physical and mechanical properties of the materials used for the model frames.

	6082-T6 aluminium alloy	brass
Young’s modulus, *E* (GPa)	70	100
Uniaxial yield stress, σ_y (MPa)	255	210
Mass density, ρ (kg/m^3)	2600	8550

The natural frequencies of the two frames in a fixed base configuration were determined by impact hammer tests at 1*g*. In particular, the two structural models were fixed to the base by means of several clamps and the roofs were excited by means of a small hammer generating free oscillations in the model. Knowing the free oscillations, it is possible to calculate the resonance frequencies of the two structures and their structural damping. Figure 3. 14a shows the Fourier amplitude spectrum of the accelerations of the crossbeam of the two frames after impact hammer testing; the observed resonant frequency at model scale lies between 175 Hz and 177 Hz, or, using the scaling laws in Table 3. 1, about 3 Hz at prototype scale. Relatively small values of structural damping (between 1.00% and 1.24%), typical of metal structures with multiple bolted connections, were computed from the logarithmic decay (Figure 3. 14b).

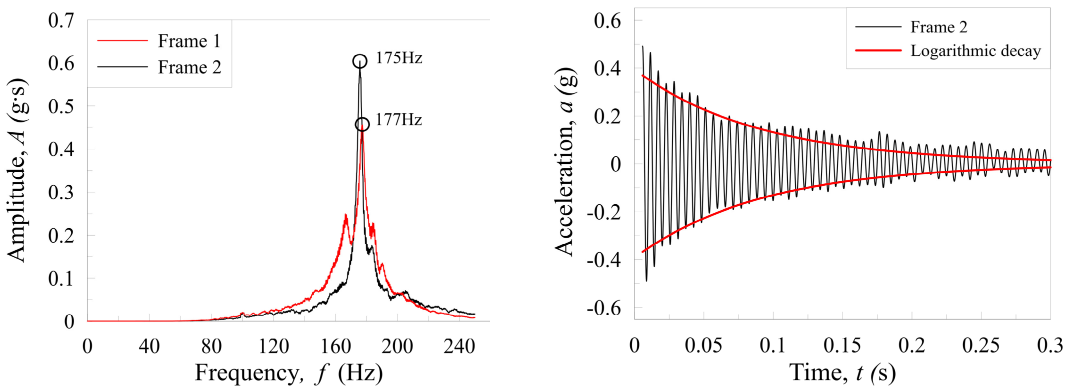

Figure 3. 14. (a) Fast Fourier transform (FFT) of the cross-beam accelerations after impact hammer testing. (b) Free vibrations of Frame 2 after the impact hammer test with the indication of logarithmic decay.

The very small differences of resonant frequency and damping between the two frames are justified by construction tolerances (<0.1 mm) and by the difficulty to replicate experimentally a perfectly fixed base constraint in the impact hammer test. All the key properties of the frames and of the foundations are shown, both at model and prototype scale, in Table 3. 9.

Table 3. 9 Key properties of the frames and of the foundations at model and prototype scale

Parameter	Model	Prototype
Nominal Bearing Pressure	2.21kPa	133kPa
Foundations width	22.91mm	1.37m
Foundation embedment	40mm	2.40m
Natural frequency (fixed base)	~176Hz	~3Hz
Superstructure Mass	1.24Kg	267Mg
Foundation Mass	1.28Kg	276Mg
Base Width	106mm	6.36m
Total Height	115mm	6.9m
Length	245mm	14.7m
Geometrical Aspect Ratio	1.08	1.08
Lateral stiffness	1518 kN/m	91090 kN/m

3.2.5 Dynamic excitation

The choice of earthquakes or dynamic excitations during a centrifuge test is very delicate. Several considerations have to be made especially according to the results one wants to obtain from the test. The seismic excitation, selected to investigate the effect of frequency and intensity on structural response, was provided using a servo-hydraulic actuator (Madabhushi et al., 2012). Hereafter all the results, unless otherwise stated, are given at prototype scale. Table 3. 10 summarises the characteristics of the 10 signals applied to the model in terms of maximum and minimum input acceleration, a_{max} and a_{min}, dominant and mean frequency, f_d and f_m, Arias intensity, IA, and duration, $T_{5\text{-}95}$ (Trifunac & Brady, 1975).

Table 3. 10 Characteristics of the dynamic input motions (at prototype scale).

Name (-)	Typology (-)	a_{max} (g)	a_{min} (g)	f_{d} (Hz)	f_{m} (Hz)	I_{A} (m/s)	$T_{5\text{-}95}$ (s)
SS1	Sine-sweep	0.10	0.091	0.01-2.5	-	-	-
S01	Sinusoidal	0.25	0.245	2.2	-	1.21	-
S02	Sinusoidal	0.221	0.214	2.2	-	1.23	-
S03	Sinusoidal	0.074	0.073	2.2	-	0.15	-
S04	Sinusoidal	0.244	0.232	2.0	-	1.85	-
E01	I.Valley	0.08	0.103	2.27	1.51	0.43	33.98
E02	Cristhchurch	0.150	0.142	2.00	1.66	0.29	5.42
E03	Kobe	0.262	0.203	2.17	1.63	0.80	4.89
E04	Adana	0.158	0.147	1.92	1.21	0.85	19.12

Figure 3. 15 shows the acceleration time history and the corresponding Fourier amplitude spectrum of the sine-sweep signal (SS1 in Table 3. 10) applied to the model at the beginning and at the end of the centrifuge test to evaluate the structural resonant frequency considering the soil-structure interaction.

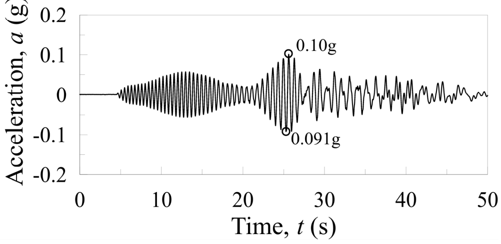

(a)

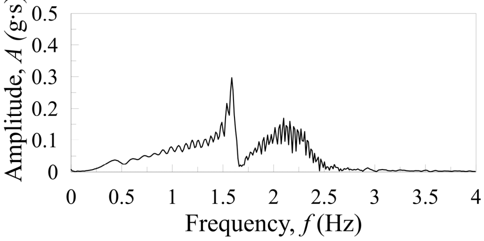

(b)

Figure 3. 15(a) Sinesweep up to 2.5Hz (150Hz at model scale); (b) Acceleration Fourier amplitude spectrum.

After the first sine sweep, four sinusoidal signals (S1 to S4 in Table 3. 10) and four real earthquakes (E1 to E4 in Table 3. 10) were applied to the model. Figure 3. 16 shows the input acceleration time histories and the corresponding Fourier amplitude spectra of the applied pseudo-harmonic signals, as recorded by the accelerometer at the base of the model (ACC_{00}) (Figure 3. 11). Each of these signals consisted of a train of 10 approximately sinusoidal cycles with a main frequency of 2.0 or 2.2 Hz and different amplitudes to assess the dependency of the efficiency of the lateral disconnection on the amplitude of the seismic signal.

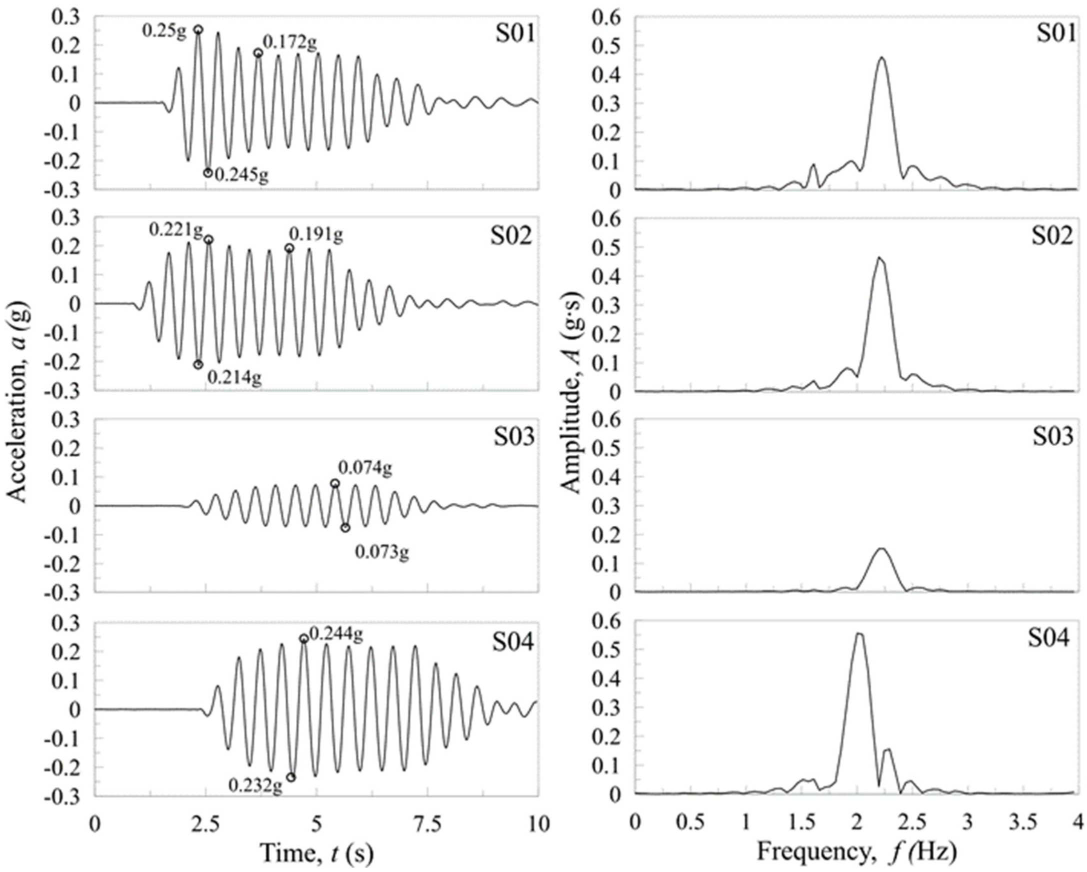

Figure 3. 16. Pseudo-harmonic acceleration time histories and corresponding acceleration Fourier amplitude spectra.

The four real acceleration time histories, scaled to the values of maximum acceleration reported in Table 3. 10, were applied to investigate the effectiveness of the lateral disconnection (GSI) under realistic seismic inputs. Figure 3. 17 shows the acceleration time histories and the corresponding Fourier amplitude spectra of the four natural earthquakes. The mean frequency of the real earthquakes lies between 1.21 Hz to 1.66 Hz.

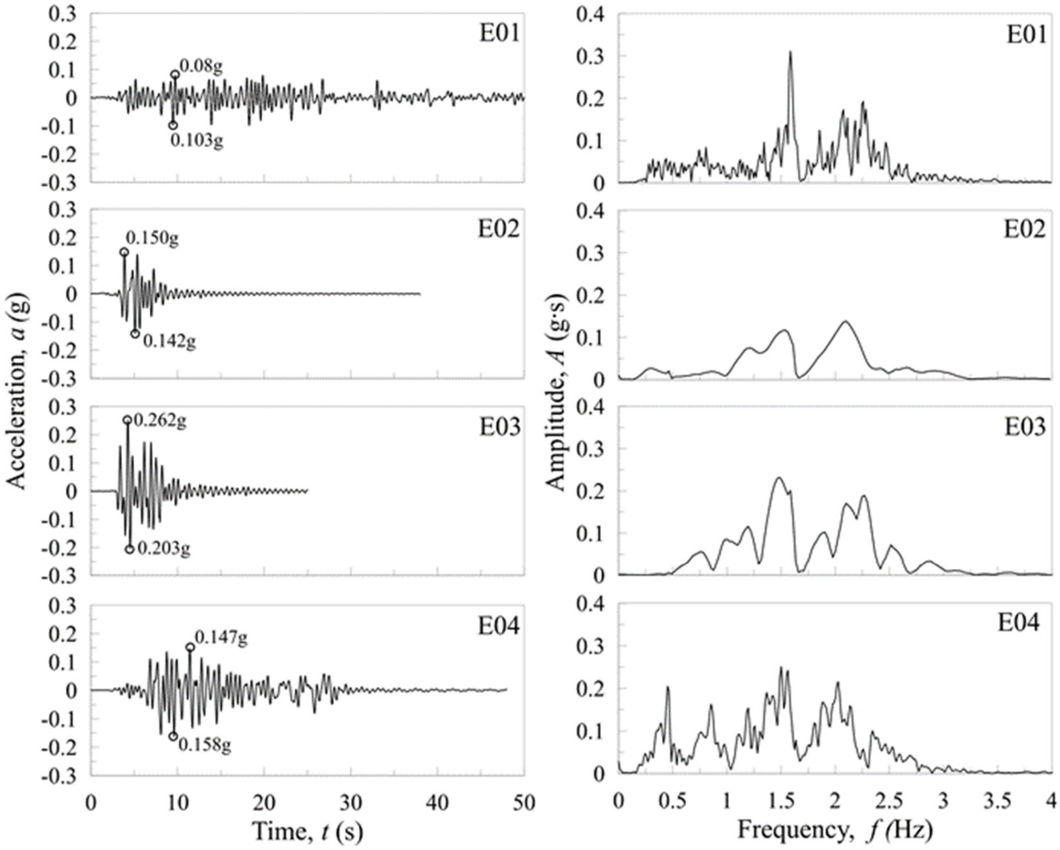

Figure 3. 17. Natural acceleration time histories and corresponding acceleration Fourier amplitude spectra.

3.2.6 Soil characterisation

The small strain shear modulus of the sand, G_0, was obtained from the measured shear wave velocity, V_s, as:

$$G_0 = \rho \cdot V_s^2 \quad (3.\ 9)$$

where ρ is the density of the sand. A mini air hammer was used to generate a shear wave travelling upwards in the soil along the central alignment of accelerometers (see Figure 3. 11); the test was repeated at different g levels during spin up. The shear wave velocity was calculated as $V_s = L/T$, where L is the known distance between two consecutive accelerometers and T is the travel time, which was obtained as the time of maximum cross-correlation of the recorded signals. The estimated strain levels developed during the mini air hammer test are always small enough to be interpreted in terms of initial shear modulus (Ghosh & Madabhushi, 2002). Figure 3. 18a shows the obtained values of V_s as a function of depth, z, at prototype scale. From these, using Eq. (3. 10) (Harding and Black, 1969) the corresponding values of G_0 were calculated and correlated to z with the simple power expression:

$$G_0 = A \cdot f(e) \cdot \left(\frac{p'}{p_{ref}}\right)^m \qquad (3.\ 10)$$

where $A = 80$ and $m = 0.47$ and $f(e) = \frac{(2.17-e)^2}{1+e}$ are parameters suggested by Hoque & Totsuoka (2000) for angular and subangular silica sand such as Hostun Sand. Figure 3. 18b shows a good agreement between the experimental point of G_0 and the expression by Hardin and Black (1969).

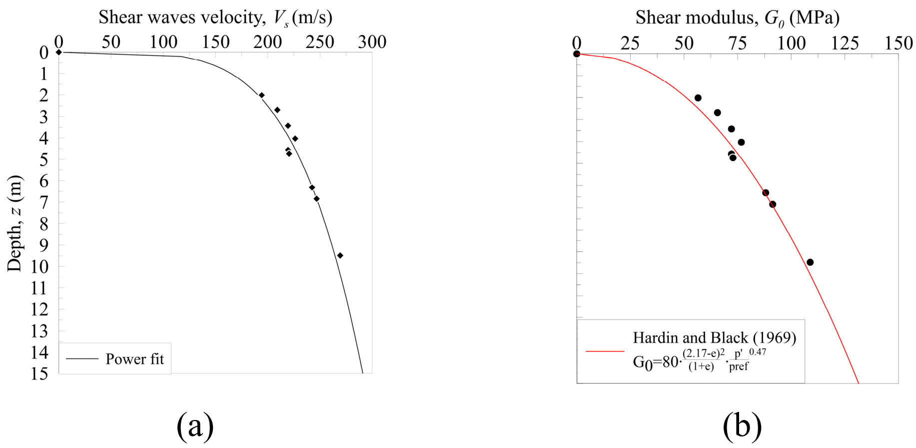

Figure 3. 18 Profiles of: (a) shear wave velocity and (b) small strain shear modulus. The equation $G_0(z)$ by Hardin and Black was calibrated using literature values for Hostun Sand at D_r=55% (Hoque & Tatsuoka, 2000).

The equivalent shear wave velocity, $V_{S,eq}$, and the first period, $T_{1,soil}$, of the sand layer at prototype scale were calculated as:

$$V_{S,eq} = \frac{Z}{\int_0^Z \frac{dz}{V(z)}} = 233\ \mathrm{m/s} \quad \text{and} \quad T_{1,soil} = \frac{4 \cdot Z}{V_{S,eq}} = 0.26\ \mathrm{s} \qquad (3.\ 11)$$

where $Z = 15$ m is the thickness of the sand layer.

Two cone penetration tests were carried out in flight, one before and one at the end of the test (Figure 3. 19). The peak friction angle profiles shown in Figure 3. 19 were obtained from the CPT results, using the correlation proposed by Robertson and Campanella (1983):

$$\varphi' = \arctan[0.10 + 0.38\log(\frac{q_c}{\sigma'_{v0}})] \tag{3. 12}$$

The increase in tip resistance corresponds to a densification that can be estimated using the correlation proposed by Schneider *et al*. (2006):

$$\frac{\Delta D_r}{D_{r0}} = \left(\frac{q_{c,1}}{q_{c,0}}\right)^{0.5} - 1 \tag{3. 13}$$

where $q_{c,0}$ and $q_{c,1}$ are, respectively, the tip resistance at the beginning and at the end of the centrifuge test.

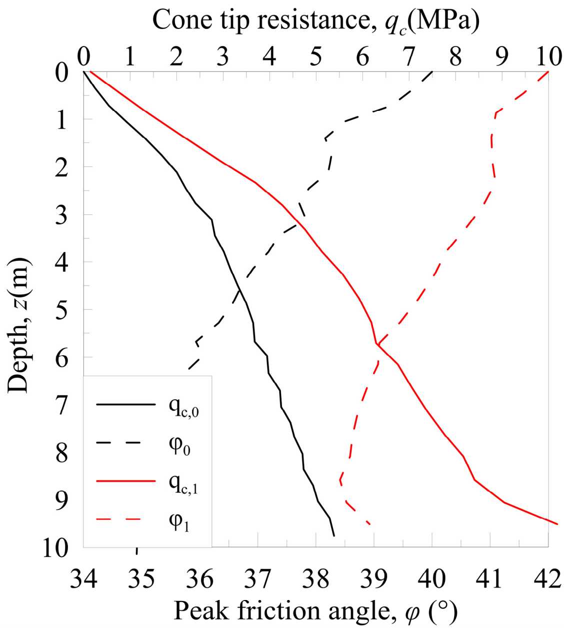

Figure 3. 19. Profiles of CPT strength and peak friction angle before ($q_{c,0}$ and φ_0) and after ($q_{c,1}$ and φ_1) the seismic signals.

The increase of relative density obtained using eq. (3. 13) is not constant with depth, and varies between a maximum of about 16% in the shallower and deeper portions of the model and a constant value of about 12% between the depths of 2 m and 8 m. The soil densification generated as a result of each centrifuge earthquake was also assessed using the PIV technique. In fact, particle image velocimetry analyses also allowed an estimate of the average increase of relative density of the sand. Assuming plane strain condition, the measurement of vertical and horizontal displacements of different soil patches on a cross section of the model allowed to estimate the volumetric variation (reduction) of the soil during the seismic events. Being known the initial void ratio at the beginning of the test and, through the PIV, the volume of the sand both at the beginning, V_0, and at the end, V_f, of the first earthquake fired was calculated. Then, it was possible to calculate the void ratio at the end of the first earthquake, e_f,:

$$\left.\begin{array}{l} 1+e_0=\frac{G_s\gamma_w}{\gamma_d}=\frac{G_s\gamma_w}{\frac{P_d}{V_0}} \\ 1+e_f=\frac{G_s\gamma_w}{\gamma_{d,f}}=\frac{G_s\gamma_w}{\frac{P_d}{V_f}} \end{array}\right\}=1+e_f=\frac{(1+e_0)V_f}{V_0}\rightarrow e_f=\frac{(1+e_0)V_f}{V_0}-1 \tag{3. 14}$$

where G_s is defined in Table 3. 7, γ_w is the specific weight of water, $\gamma_{d,f}$ is the specific soil weight at the end of the first earthquake, and P_d is the soil weight, which is constant during the earthquake. Knowing the void ratio e_f at the end of the first earthquake, equation (3. 14) was then used to calculate the void ratio at the end of the following earthquakes, updating the initial void ratio and the soil volume calculated before and after each seismic event. Using the described procedure, the average increment of relative density of the sand in the model happened during each earthquake was calculated (Table 3. 11).

Table 3. 11. Densification of soil in each earthquake

Seismic Signal	e	D_r
[-]	[-]	[%]
SS1	0.752	56.5
S01	0.724	62.7
S02	0.718	64
S03	0.717	64.2
S04	0.713	65.2
E01	0.712	65.4

E02	0.711	65.6
E03	0.709	66
E04	0.708	66.2
SS1post	0.707	66.4

These measurements indicate that the largest increase of relative density (from 56.5% to about 63%) occurred during the first cycles of the first sinusoidal train, S01, with an amplitude of 0.25g. Successive earthquakes were responsible for increasingly smaller changes of relative density, with a final estimated value at the end of the centrifuge test of about 66.4%, in substantial agreement with what estimated from the CPT results over the depths between 2 m and 8 m. In particular, the natural earthquakes were applied to the model after the sine sweep and four trains of sinusoidal waves with amplitudes of up to 0.25g, and had a very limited effect in terms of soil densification. Based on the formulation by Hardin & Black (1968), with the parameters determined by Hoque & Tatsuoka (2000) for Hostun Sand, these changes of relative density may be responsible for an increase of the shear wave velocity in the range of depths affecting soil structure interaction, namely between about 2.5 m and 5 m below the foundation, of only about 4%, with limited consequences on the effectiveness of the proposed mitigation measure as discussed in the following.

3.2.7 Evaluation of natural frequency of the structures

The natural frequencies of the two soil-structure systems were identified experimentally by applying to the centrifuge model the sine-sweep signal SS1 (see Table 3. 10). Based on preliminary analytical and numerical estimates the applied frequency sweep (2.5→0 Hz) should have included the fundamental frequency of the soil-structure system. Figure 3. 20 shows the acceleration time histories recorded by the accelerometers attached to the crossbeams of the two frames, MEMS13 and MEMS23.

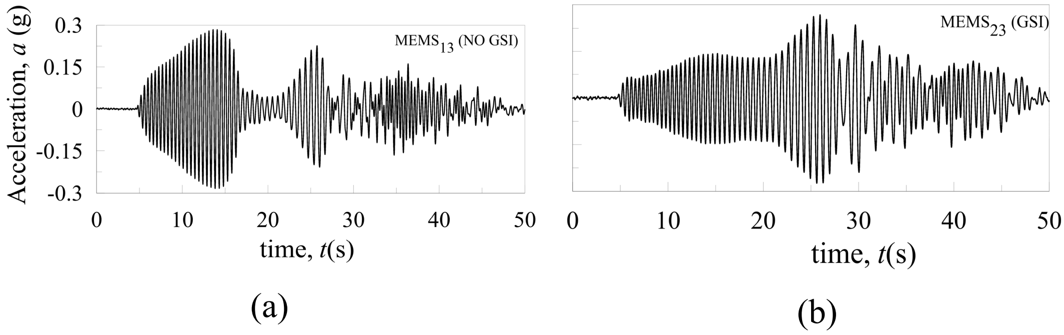

Figure 3. 20. SS1 input signal. Acceleration time histories recorded at the top of: (a) NO GSI and (b) GSI.

Figure 3. 21a and Figure 3. 21b compare the Fourier amplitude spectra of the acceleration time histories recorded in the soil between the two structures at foundation level with those from the two accelerometers attached to the top of the structures. The Fourier amplitude spectrum of the input acceleration time history, already shown in Figure 3. 15b, is shown again for comparison.

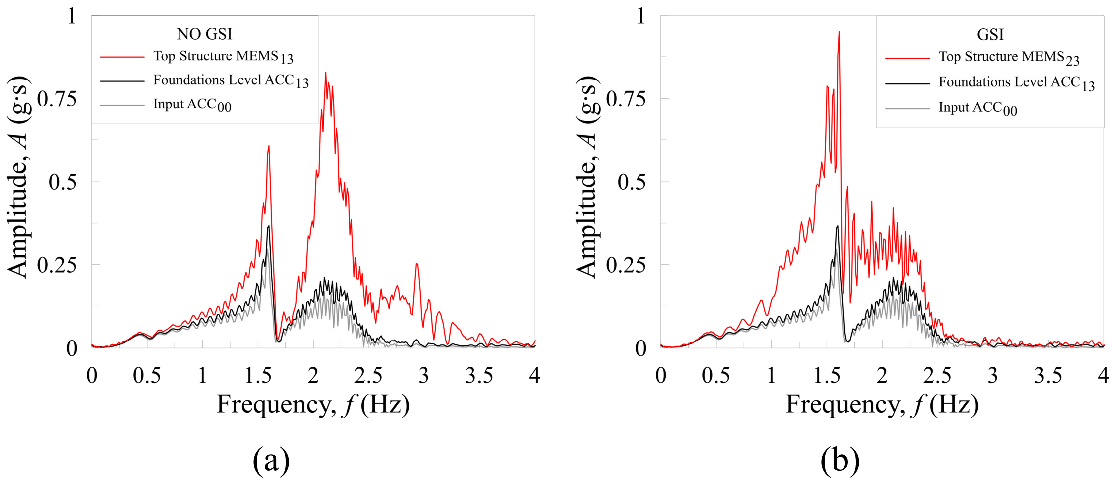

Figure 3. 21. SS1 - Fourier amplitude spectra of input acceleration, acceleration at foundation level and acceleration at the top the structures: (a) NO GSI, (b) GSI.

Finally, Figure 3. 22a shows the ratio between the Fourier amplitude spectra of the acceleration time histories recorded at the top of the structures and in the soil at foundation level (ACC_{13}), highlighting the relevant reduction of amplification induced by the proposed GSI in the 2.5 Hz to 3.5 Hz range. No significant differences were found when the same sinusoidal sweep was applied at the end of the centrifuge test (Figure 3. 22b).

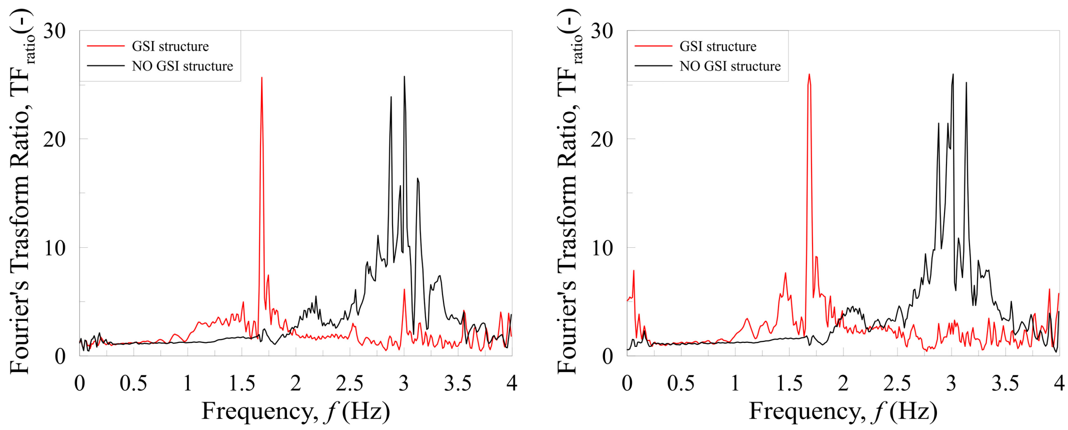

(a) (b)

Figure 3. 22. Fourier's Trasform Ratio for GSI structure and NO GSI structure: (a) at the beginning of the centrifuge test, (b) at the end of the centrifuge test.

The first resonant frequency observed for the frame without the lateral disconnection is around 2.70 Hz, only slightly smaller (~7%) than that observed under fixed base conditions (2.9 Hz), whereas the first resonant frequency of the frame with laterally disconnected foundations, is around 1.66 Hz, which is significantly smaller (~43%) than the fixed base value. This corresponds to an elongation of the natural period of the structure from 0.37 s to 0.60 s, or about (62%), which is further confirmed by the amplification functions computed for the first and last natural earthquakes, namely E01 (Imperial Valley) and E04 (Adana), that were applied to the model (see Figure 3. 23).

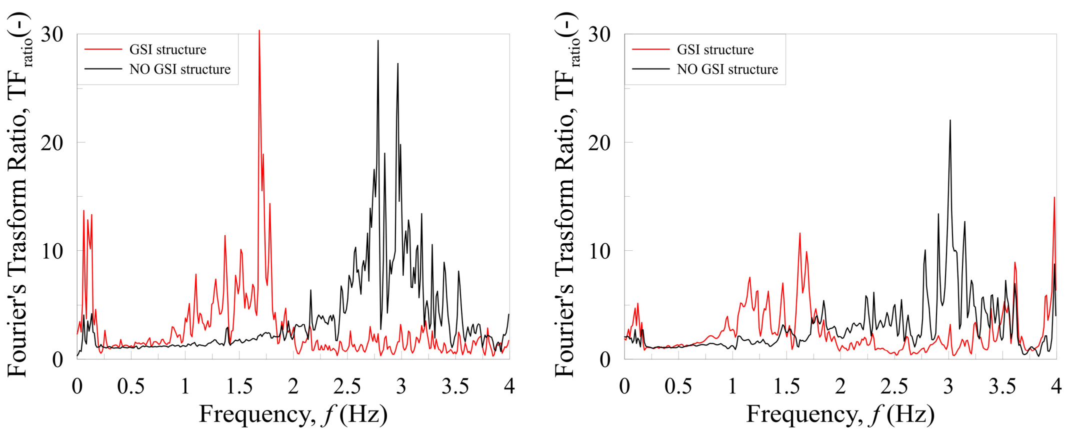

Figure 3. 23. Fourier's Trasform Ratio for GSI structure and NO GSI structure: (a) Imperial Valley, (b) Adana

3.2.8 Structural acceleration response.

Figure 3. 24 and Figure 3. 25 show the acceleration time histories recorded by the accelerometers attached to the cross beams of the two frames for the sinusoidal signals (S01-S02-S03-S04) and real earthquake (E01-E02-E03-E04).

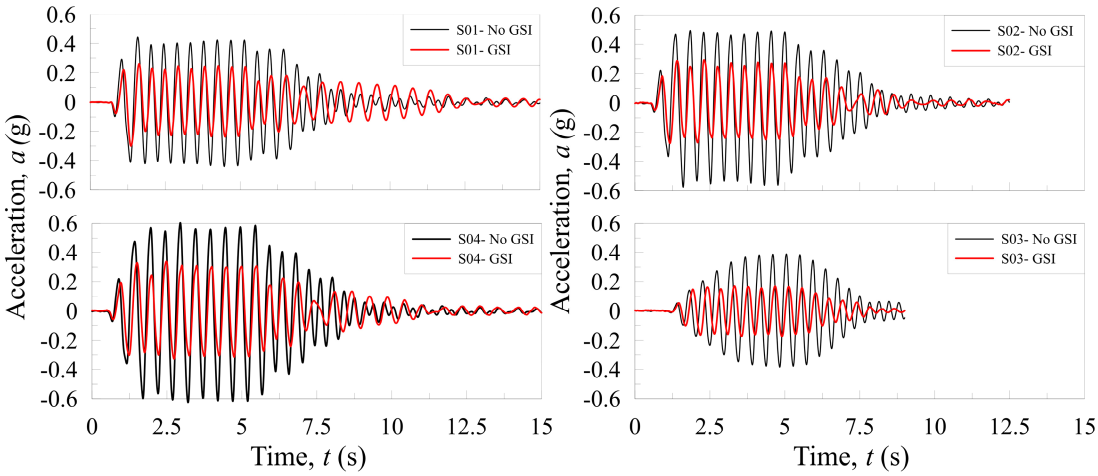

Figure 3. 24. Absolute top structural acceleration time histories for all sinusoidal signals.

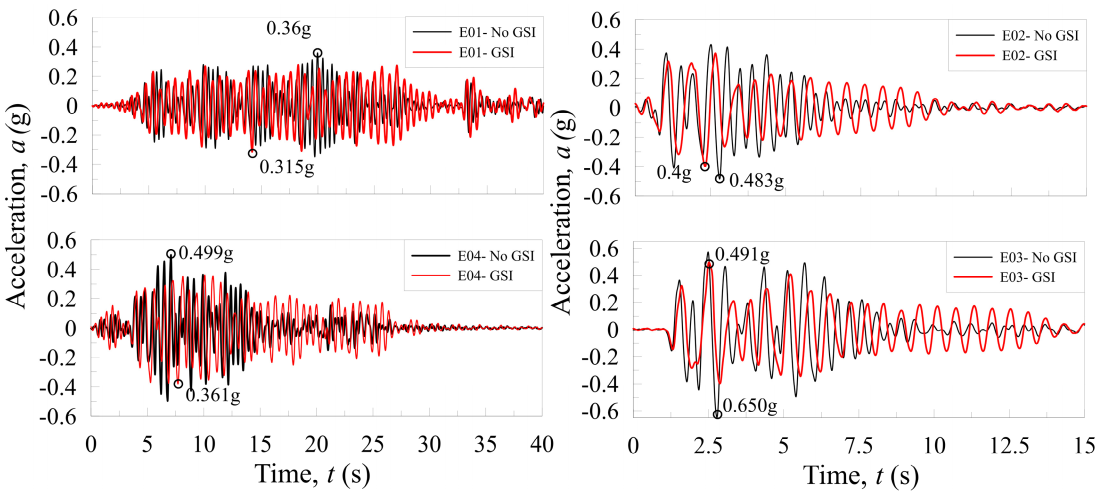

Figure 3. 25. Absolute top structural acceleration time histories for all earthquake signals.

In both cases, the frame with laterally disconnected foundations experiences smaller accelerations, while its free oscillations are generally damped less quickly because of a reduction of lateral radiation damping (Gazetas, 1991). The efficiency of the proposed mitigation measure may be evaluated in terms of the reduction of the maximum absolute structural acceleration:

$$\eta_a = 1 - (a_{\max,\mathrm{GSI}}/a_{\max}) \qquad (3.\ 15)$$

or of integral quantities, such as the Arias Intensity:

$$\eta_{I_A} = 1 - (I_{\mathrm{A,GSI}}/I_{\mathrm{A}}) \qquad (3.\ 16)$$

Figure 3. 26 shows both measures of efficiency as a function of the intensity of the input signal for all the applied signals. For the pseudo-sinusoidal inputs, a_{max} was evaluated as the mean of the positive and negative maxima in the first 10 cycles.

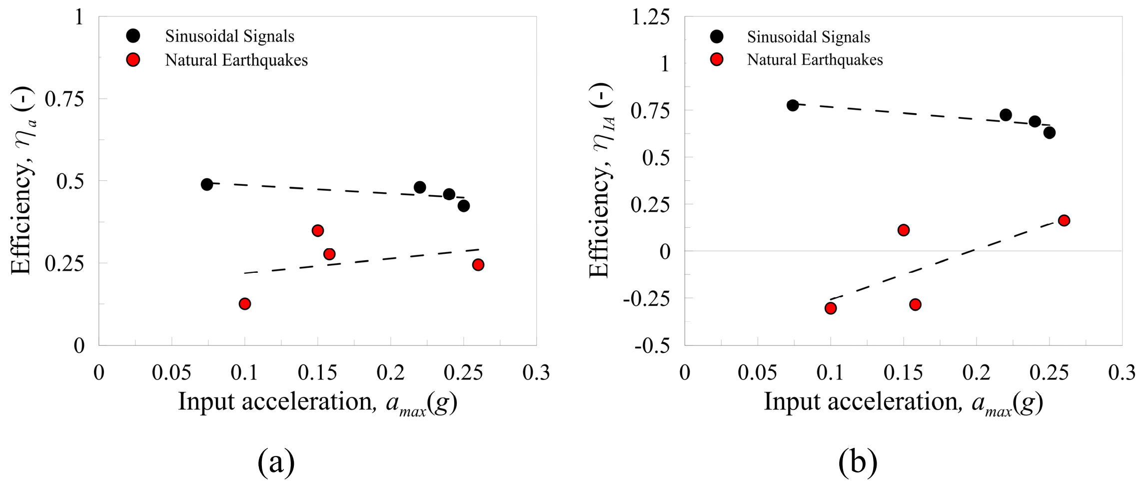

Figure 3. 26. Efficiency of proposed GSI measure in terms of (a) acceleration and Arias intensity as a function of input intensity.

For all sinusoidal inputs, the efficiency of the proposed mitigation measure is rather high and almost independent of the amplitude of the seismic signal both in terms of $a_{\max}$ and IA, while it is much lower, and in some cases negative (η_{I_A}), for the natural earthquakes. This may depend on the fact that the mean frequency of the sinusoidal signals is closer to the natural frequency of NO GSI frame, whereas that of the natural earthquakes is closer to the natural frequency of GSI frame. Even if the lateral disconnection reduces the maximum accelerations experienced by GSI structure, these take more time to be damped, which for the natural earthquakes may result in a slight increase of the Arias intensity, explaining the negative values of η_{I_A} obtained at low input accelerations.

It is clear that the values of absolute acceleration at the top of the structure are only one indicator of the possible effectiveness of the proposed mitigation measure. In fact, the lateral disconnection at foundation level leads to increased rigid body displacements connected to rocking and sliding, and lower structural drifts. As long as rocking and sliding of the foundation do not lead to limit states by overturning or excessive permanent horizontal displacements, they are beneficial mechanisms that dissipate seismic energy without modifying the internal forces in the structural members. Therefore, other quantitative efficiency indicators, based on the ability of the proposed GSI measure to reduce the structural drift and distortional shear forces, are considered below.

3.2.9 Structural drift response.

Figure 3. 27 shows a schematic of the deformed configuration of the frames due to seismic excitation.

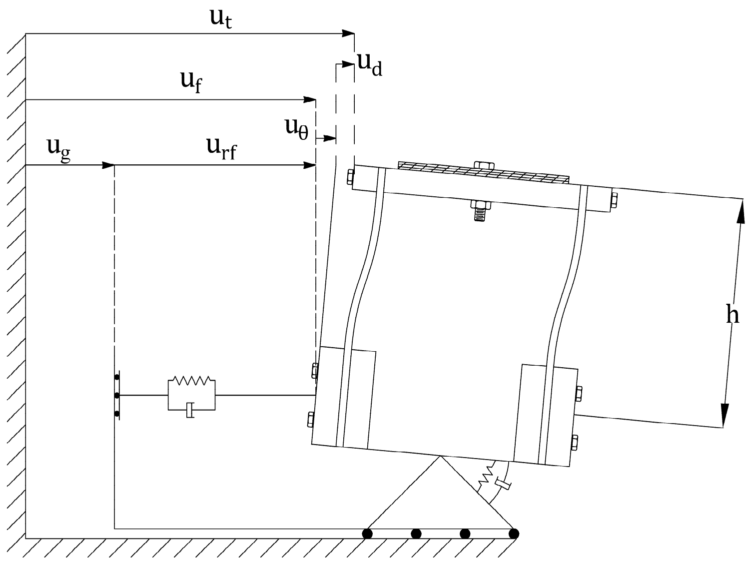

Figure 3. 27. Schematic of the deformed frame due to seismic shaking.

At any time, the absolute horizontal displacement of the top of the structure, u_t, results from the sum of three components: the horizontal displacement of the foundation, u_f, the displacement caused by the rigid rotation of the foundation,

u_θ, and a component caused by structural deformability or drift, u_d, which results from the deflection of the pillars:

$$u_t = u_f + u_\theta + u_d = (u_g + u_{rf}) + \theta h + u_d \tag{3. 17}$$

where u_g is the absolute soil displacement, u_{rf} is the displacement of the centre of gravity of the foundation relative to the soil, θ is the rocking angle and h is the distance between the horizontal plane through the centre of gravity of the foundation (where vertical $MEMS_{11\text{-}15}$ and $MEMS_{21\text{-}25}$ are located) and the crossbeam (where horizontal $MEMS_{13}$ and $MEMS_{23}$ are located).

The horizontal displacements of the cross beam, u_t, and of the foundations, u_f, were obtained by double integration of the acceleration time histories recorded by the accelerometers attached to the top of the structures ($MEMS_{13}$ and $MEMS_{23}$) and to the foundations ($MEMS_{12}$ and $MEMS_{22}$). To prevent divergence, the signal was high-pass filtered at 0.4 Hz, which makes it impossible to compute permanent-residual displacements. Provided that the structure remains in the elastic domain during and after the earthquakes, the frames return to their initial configuration at the end of the base motion and thus high-pass filtering does not result into significant loss of data.

The rotations of the two frames can be calculated from the vertical displacements, v_1 and v_2 obtained through double integration of $MEMS_{11\text{-}15}$ and $MEMS_{21\text{-}25}$ as:

$$\theta = \frac{(v_1 - v_2)}{L} \tag{3. 18}$$

where L is the overall width of the foundation (edge to edge). Further information on the computation of rotations from MEMS and their comparison with those obtained from the displacements measured by LVDTs will be given in section 3.2.11

Finally, the drift can be computed from Eq. (3. 19) as:

$$u_d = u_t - u_f - u_\theta = u_t - u_f - \theta h \tag{3. 19}$$

Figure 3. 28 shows the time histories of the rotational displacements and of the drift of the cross beam of the two frames for earthquakes signals. The displacement components due to rocking are much larger for the frame with laterally disconnected foundations; this implies that for the same frame, the drift, which is proportional to the shear force, is significantly smaller.

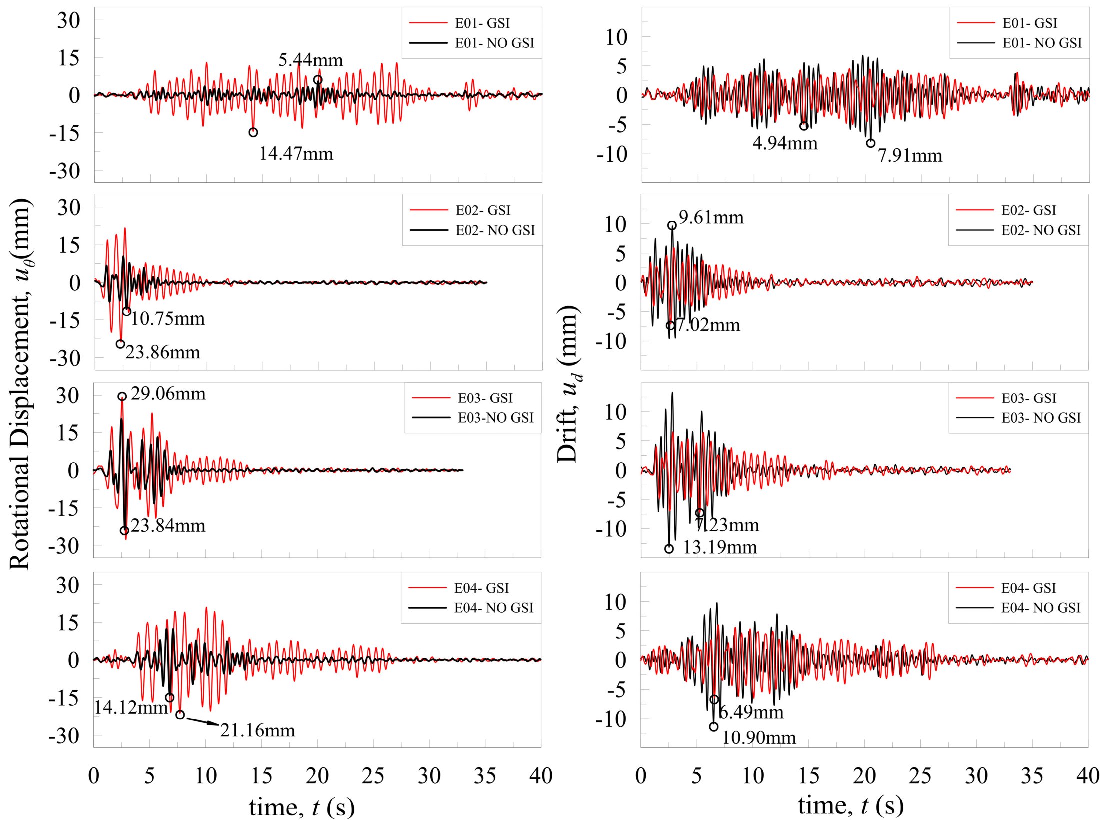

Figure 3. 28. Different displacement components of the structures for earthquake signals

In order to highlight the mitigating effect provided by the lateral disconnection in terms of drift, a structural drift demand, d_d, can be defined as:

$$d_d = \frac{1}{(T_{95}-T_5)} \int_{T_5}^{T_{95}} |u_d| \, dt \qquad (3.\ 20)$$

where $T_{95} - T_5$ is the significative duration of the crossbeam accelerations.

Figure 3. 29 shows the efficiency of the proposed mitigation measure in terms of both maximum drift $\eta_{d,peak} = 1 - u_{d,peak,GSI}/u_{d,peak,NO\ GSI}$, and drift demand, $\eta_d = 1 - d_{\mathrm{d,GSI}}/d_{\mathrm{d,NO\ GSI}}$, as a function of the maximum input acceleration and mean frequency for all natural earthquakes. Even if the results

are somehow scattered, the maximum drift efficiency seems larger than the drift demand efficiency at low values of a_{max}, while similar and typically larger efficiencies are observed at higher values of maximum input acceleration.

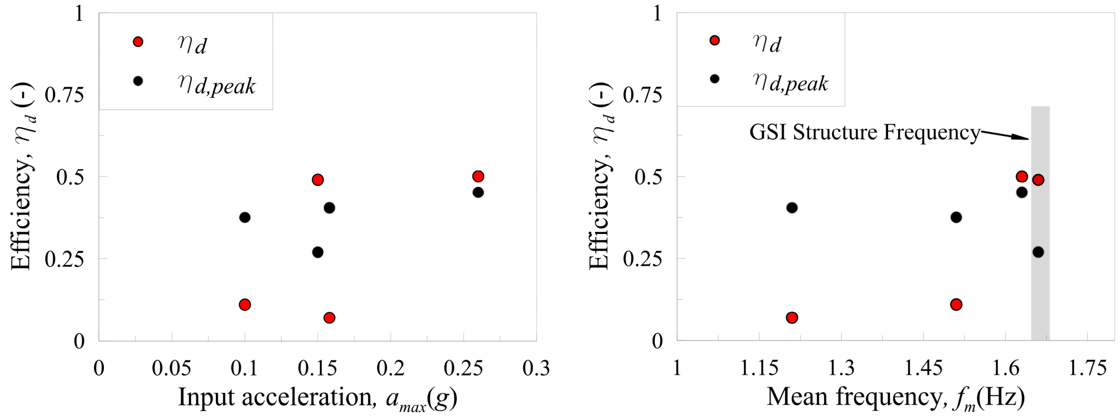

Figure 3. 29. (a) Drift efficiency of the proposed GSI measure as a function of input acceleration for real earthquakes and (b) Drift efficiency of the proposed GSI measure as a function of the mean frequency for the applied real earthquakes.

The largest values of drift demand efficiency occur for earthquakes with a mean frequency close to the natural frequency of the structure with laterally disconnected foundations, indicating a significant increase of the rocking and sliding displacement components. The shear force in the structural members can be computed as:

$$V = m \cdot \ddot{u}_d \qquad (3.\ 21)$$

where m is the mass of the superstructure (Table 3. 9).

Figure 3. 30 shows a plot of shear force vs drift for all natural earthquakes.

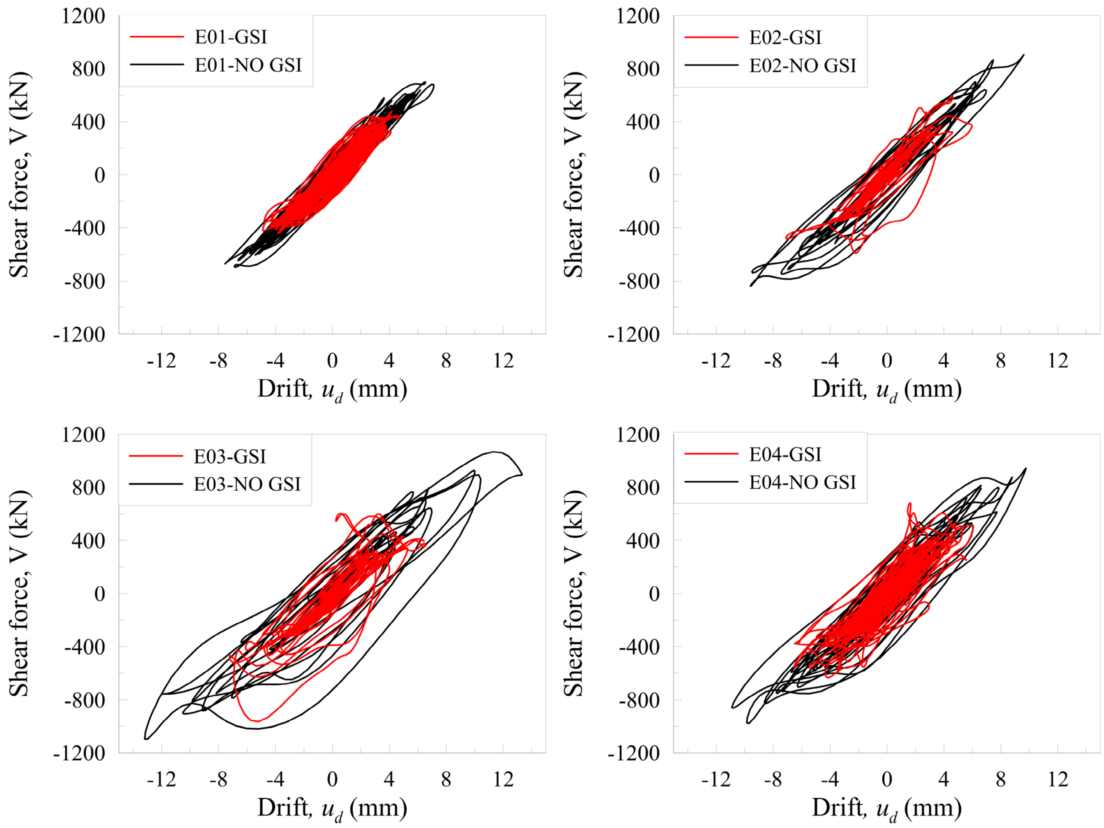

Figure 3. 30. Hysteretic cycles of distortional shear forces vs structural displacements for all earthquake signals

The lateral stiffness, K_{str}, and the damping coefficient, C_{str}, of the frames were obtained by least square best fitting the experimental data with a linear visco-elastic model:

$$V = K_{str} \cdot u_d + C_{str} \cdot \dot{u}_d \tag{3. 22}$$

where u_d and $\dot{u}_d$ are the structural drift and velocity.

The lateral stiffness and the damping coefficient of the frames has been calculated for all the natural earthquakes (Table 3. 12).

Table 3. 12 Lateral stiffness (K_{str}) and damping coefficients (C_{str}) of structural frames.

Name (-)	Lateral Stiffness (kN/m) No GSI	Lateral Stiffness (kN/m) GSI	Damping coeff. (kN·s/m) No GSI	Damping coeff. (kN·s/m) GSI
Imperial Valley	$10.99 \cdot 10^4$	$10.33 \cdot 10^4$	$1.06 \cdot 10^3$	$1.82 \cdot 10^3$
Christchurch	$9.79 \cdot 10^4$	$9.67 \cdot 10^4$	$1.09 \cdot 10^3$	$0.81 \cdot 10^3$
Kobe	$9.53 \cdot 10^4$	$9.84 \cdot 10^4$	$1.70 \cdot 10^3$	$1.34 \cdot 10^3$
Adana	$10.12 \cdot 10^4$	$9.99 \cdot 10^4$	$1.12 \cdot 10^3$	$1.20 \cdot 10^3$

The difference in lateral stiffness and damping coefficient between the earthquakes are irrelevant (±7%) as well as the one between the two frames with and without lateral disconnection. It is possible to assume a constant value of K_{str} equal to 100MN/m, very close to the value obtained from the hammer test results (see Table 3. 9) and $C_{str} = 1.3MN/s$. The fact that the two structures have almost the same lateral stiffness for each earthquake is a further confirmation that the two structures are identical and remained in the elastic range. Since the stiffness is constant, the same efficiency computed for drift reduction may be also applied to shear forces reduction.

3.2.10 Foundation response

Moment-rotation analysis can be used to investigate the soil-foundation interaction during dynamic loading (Cremer *et al.*, 2001; Gajan & Kutter, 2008; Negro *et al.*, 2000; Paolucci *et al.*, 2011; Pender, 2010). A moment-rotation plot can provide information on the maximum moment at the foundation base, the maximum rotation experienced by the foundation, the energy dissipated during cyclic loading and the rotational stiffness of the foundation in the cycle. Assuming that the foundation system can be concentrated in the centre of gravity of the foundation, equilibrium requires that:

$$\begin{Bmatrix} F \\ M \end{Bmatrix} = \begin{bmatrix} K_{xx} & K_{x\theta} \\ K_{\theta x} & K_{\theta\theta} \end{bmatrix} \begin{Bmatrix} u_{rf} \\ \theta \end{Bmatrix} \tag{3. 23}$$

Where F and M are the resultant horizontal force and the resultant moment, u_{rf} and θ are the horizontal displacement of the foundation relative to the soil and the rotation of the foundation, and K_{xx}, $K_{\theta\theta}$, $K_{x\theta}$ are the lateral, rotational, and coupling translational-rotational soil-foundation stiffness. Gerolymos et al. (2006) suggest that off-diagonal coupling terms should be considered for foundations with D/B = 0.5 – 4, where D and B are the embedment and the width of the foundation, and may be computed as:

$$K_{x\theta} = K_{\theta x} = \frac{1}{3} d^* K_{xx} \tag{3. 24}$$

where $d^* \leq D$ is the vertical extension of the lateral contact between the soil and the foundation, which was estimated from the pictures taken by the high-resolution camera in flight. In the case at hand d^* = 2.2 m for the foundations of the NO GSI frame, and d^* = 0 for the laterally disconnected foundations. It follows that the stiffness matrix of the foundations of GSI frame is diagonal. In the following, the equilibrium equations have been written at the base of the foundation.

From Eqs. (3. 25) and (3. 26) the lateral and rotational stiffness of the foundation of NO GSI frame, can be expressed as:

$$K_{xx} = \frac{dF}{du_{rf} + \frac{1}{3} d^* d\theta} = \frac{dF}{d\tilde{u}} \tag{3. 25}$$

$$K_{\theta\theta} = \frac{dM - \frac{1}{3} d^* K_{xx} du_{rf}}{d\theta} = d\widetilde{M}/d\theta \tag{3. 26}$$

where both $\tilde{u}$ and $\widetilde{M}$ incorporate a term accounting for translational-rotational coupling.

It is clear that, for the laterally disconnected foundation, $K_{x\theta} = K_{\theta x} = 0$, and Eqs. (3. 25) and (3. 26) may be rewritten simply as:

$$K_{xx} = \frac{dF}{du_{rf}} \tag{3. 27}$$

$$K_{\theta\theta} = \frac{dM}{d\theta} \tag{3. 28}$$

The rotations of the foundation were computed using Eq. (3. 18) while the relative horizontal soil-foundation displacements, for both structures, were calculated by double integration of the acceleration time histories recorded by $MEMS_{14}$, ACC_{13} and $MEMS_{22}$.

With reference to NO GSI frame, the horizontal displacement of the foundation relative to the soil, the resultant horizontal force on the foundation, and the resultant moment relative to the base of the foundation can be obtained as:

$$u_{rf} = \left(u_{MEMS_{14}} - \theta \cdot D\right) - u_{ACC_{13}} \tag{3. 29}$$

$$F = m_{str} \cdot \ddot{u}_{MEMS_{13}} + m_{fond}(\ddot{u}_{MEMS_{14}} - \ddot{\theta} \cdot \frac{D}{2}) \tag{3. 30}$$

$$M = m_{str} \cdot \ddot{u}_{MEMS13}(H_{str} + D) + m_{fond}\left(\ddot{u}_{MEMS14} - \ddot{\theta} \cdot \frac{D}{2}\right) \cdot \frac{D}{2} \tag{3. 31}$$

where H_{str} is the height of the structure from the top of the foundation to the crossbeam, and m_{str} and m_{fond} are the mass of the superstructure and of foundation, reported in Table 3. 9. The rotational inertia of the foundation and of superstructure about their own axes is negligible, and were not considered.

Similar expressions can be used to compute the horizontal displacements and the resultant horizontal force and moment for the foundation of GSI frame, using the appropriate instrumental recordings.

The lateral stiffness K_{xx} can be evaluated from the foundation shear-displacement plots, such as, e.g., those reported in Figure 3. 31.

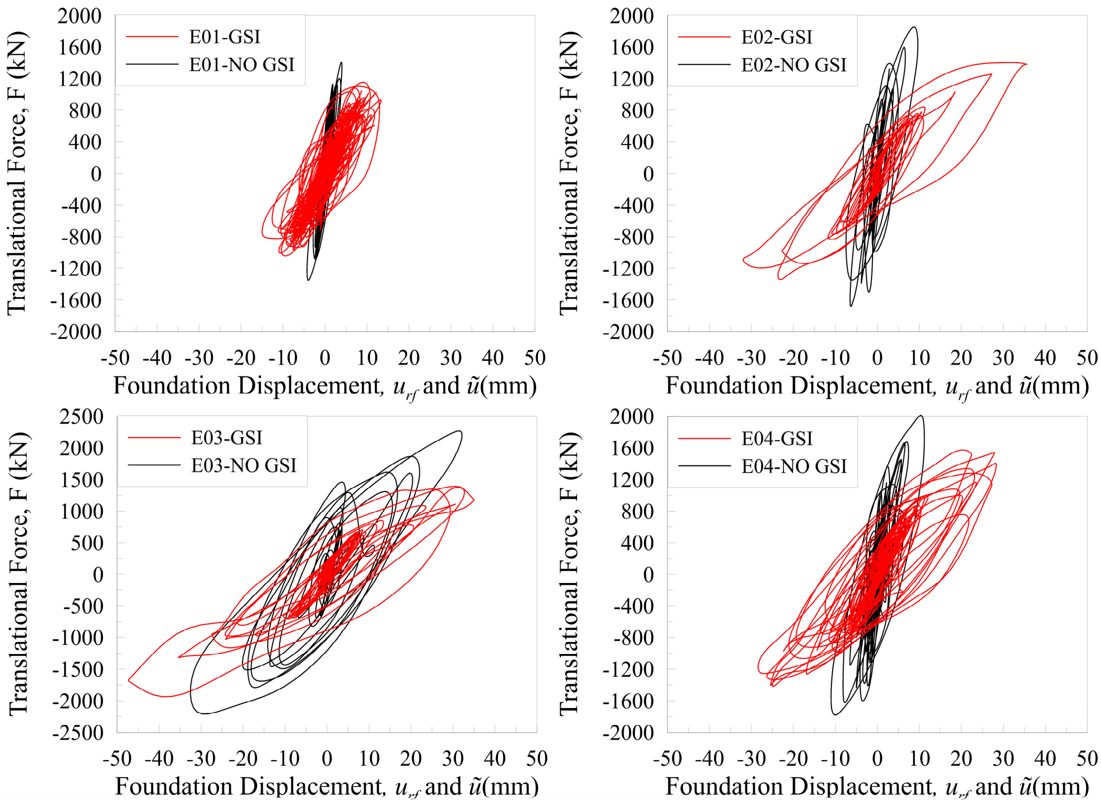

Figure 3. 31. Hysteretic cycles of the translational force of the foundation vs its soil-structure relative displacement for all earthquake signals. (Somma et al.2021)

Table 3. 13 summarises the values of the peak to peak stiffness K_{xx} for the largest cycles obtained for all the natural earthquakes, with and without GSI, clearly indicating the reduced lateral stiffness of the foundation with the lateral disconnection. The table also shows a non-linear response of the system, because the values of K_{xx} pertaining to the lower energy signals are higher.

Table 3. 13 Secant soil-foundation lateral stiffness for GSI and NO GSI structures.

	$K_{xx,NOGSI}$ (kN/m)	$K_{xx,GSI}$ (kN/m)
Imperial Valley	$3.47 \cdot 10^5$	$9.22 \cdot 10^4$
Christchurch	$2.09 \cdot 10^5$	$3.68 \cdot 10^4$
Kobe	$6.80 \cdot 10^4$	$3.50 \cdot 10^4$

Adana	$1.79 \cdot 10^5$	$4.88 \cdot 10^4$

As shown in Figure 3. 31, both structures experienced sliding, i.e., a horizontal displacement of the foundation relative to the surrounding soil, even if this was larger for the structure with GSI. However, at least as far as this experiment is concerned, the horizontal accelerations recorded by $MEMS_{12\text{-}14}$ and $MEMS_{22\text{-}24}$ were the same and no differential horizontal displacements were recorded between the two foundations of the same structure, neither for the GSI structure nor for the NO-GSI structure.

Figure 3. 32 show the moment-rotation cycles obtained for both structures. The data clearly indicates that the rotational stiffness of the laterally disconnected foundation is significantly smaller than that of the ordinary embedded foundation and that the rotational stiffness of both foundations reduces significantly with increasing rotation.

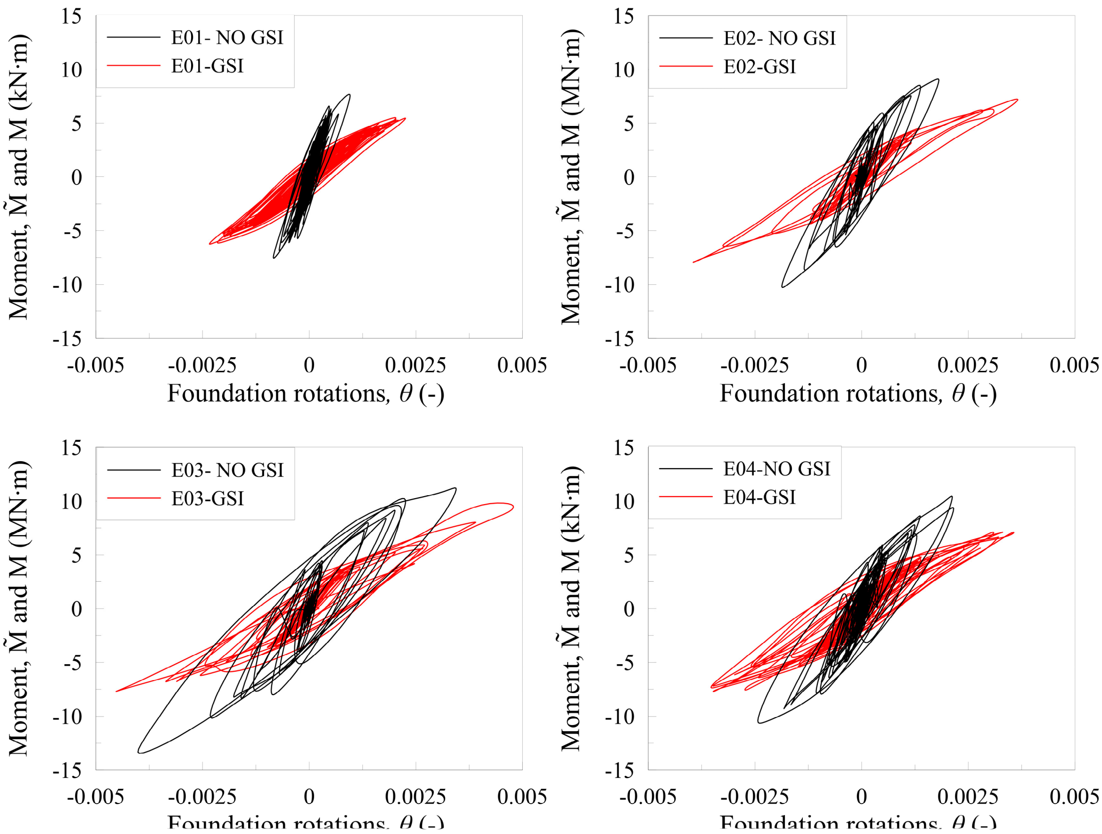

Figure 3. 32. Moment rotations cycles for all earthquake signals (Somma et al.2021)

Figure 3. 33a shows the secant rotational stiffness computed in each cycle as a function of the amplitude of the rotation in the same cycle, $\bar{\theta}$, computed as the mean of the maximum and negative values of rotation, as cycles are not always symmetric about the origin. The observed values of $K_{\theta\theta}$ were interpreted using the model by Hardin & Drnevich (1972) adapted for moment rotation cycles (Eq. (3. 32)) and corresponding to the backbone curve of Figure 3. 33b:

$$\frac{K_{\theta\theta}}{K_{\theta\theta,0}} = \frac{1}{1+\bar{\theta}/\bar{\theta}_r} \qquad (3.\ 32)$$

Where $K_{\theta\theta,0}$ is the initial value of the rotational stiffness (equal to 5558 MNm for GSI and 19342 MNm for NO GSI) and $\bar{\theta}_r$ is the reference value of rotation (equal to 1.9×10-3 rad for GSI and 0.6×10-3 rad for NO GSI).

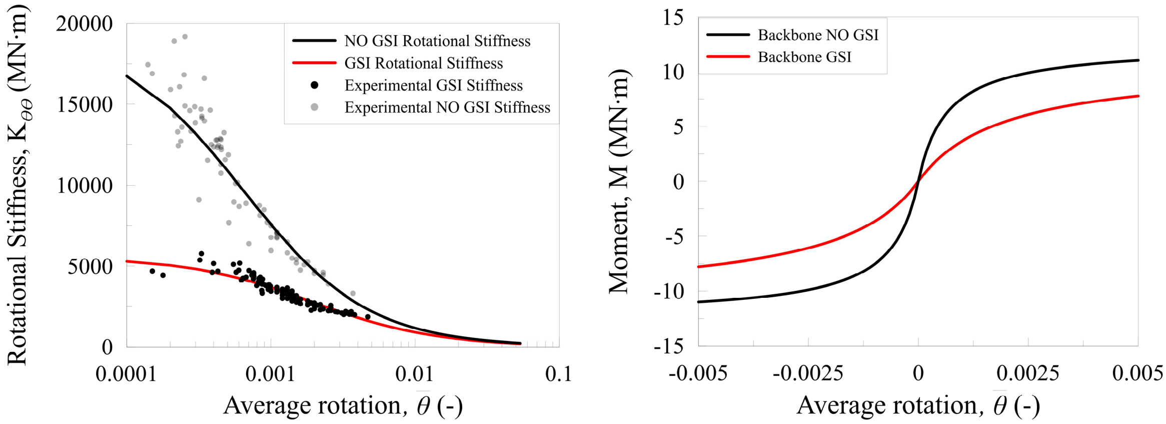

Figure 3. 33. (a) Rotational stiffness vs average rotation cycle amplitude $\bar{\theta}$; (b) Moment-rotation back-bone curves for GSI and NO GSI structure.(Somma et al.2021)

The rotation of the structure causes a redistribution of the bearing pressure under the foundation, resulting in alternate loading and unloading, and hence in energy losses, which were quantified using the moment rotation plots obtained for pseudo sinusoidal cycles, as they have an almost constant frequency. Damping ratio, ξ is a descriptor of the dissipation of energy and can be calculated as:

$$\xi = \frac{W_D}{4\pi W_S} \tag{3. 33}$$

where W_D and W_S are amounts of energy dissipated in a cycle of loading and the elastic energy stored in the same cycle of loading, respectively, see Figure 3. 34a. As shown in Figure 3. 34b, for both frames, the mobilized rotational damping increases from about 1.5% at very small rotations to about 20% at an average rotation of the order of 0.001rad. Also, as expected, damping is larger (by about 10%) for the conventional embedded than for the laterally disconnected foundations.

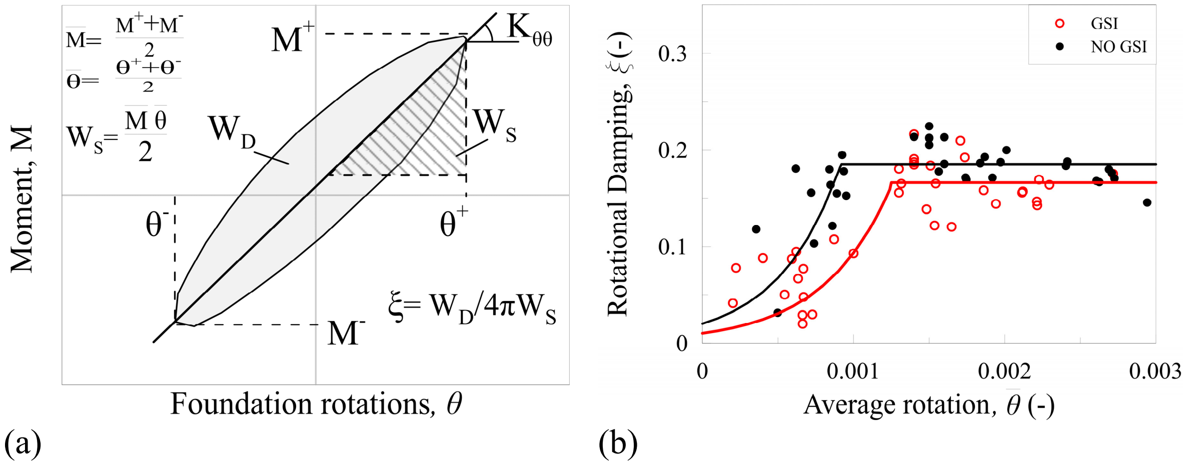

Figure 3. 34. Pseudo-sinusoidal signals: (a) definition of rotational damping; (b) rotational damping as a function of average foundation rotation. (Somma et al.2021).

3.2.11 Settlement-rotation behaviour

The alternate increase and decrease of the contact stress underneath the foundation also induces increasing foundation settlements with cycling. The position of a number of reference targets on the foundations and on the structures were tracked by Particle Image Velocimetry (PIV) using a high-resolution camera taking images at a frequency of 975 Hz during shaking. To assess the reliability of PIV measurements, Figure 3. 35a shows the time histories of the settlement of the foundations of GSI frame as obtained by PIV, LVDT, and from the double integration of the acceleration time histories measured by $MEMS_{25}$. The agreement between the cumulative settlement recorded by $LVDT_{21}$ and the settlement obtained by PIV is remarkable, even if the LVDT does not resolve high frequency oscillations. LVDTs have a relatively slow response, and therefore they cannot measure high frequency displacements (>15Hz). However, they do provide an accurate indication of the cumulative settlement. On the other hand, as discussed in Section 3.2.7, because of high-pass filtering, permanent displacements cannot be obtained by double integration of the accelerations time histories recorded by the MEMS. Then again, as shown in Figure 3. 35b, the rotations obtained from the MEMS are very close to those obtained by PIV, confirming the findings by Heron (2013).

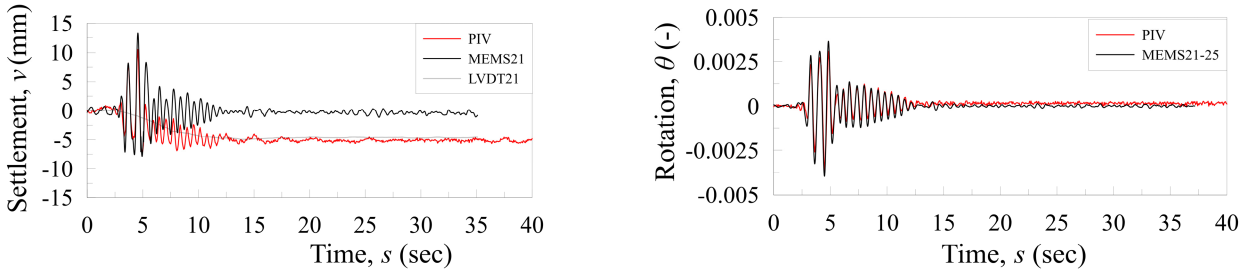

Figure 3. 35. Comparison between measurements from different instrumentation in E02 earthquake: (a) foundation settlements, and (b) foundation rotations.

Figure 3. 36 shows the plots of settlement vs rotation of the foundations of the two frames observed by PIV during earthquakes. While the maximum settlements experienced by the two structures during all-natural earthquakes are very similar (≃4% difference on average), the maximum rotations of the laterally disconnected foundation are significantly larger than those of the foundations without GSI (+37% on average).

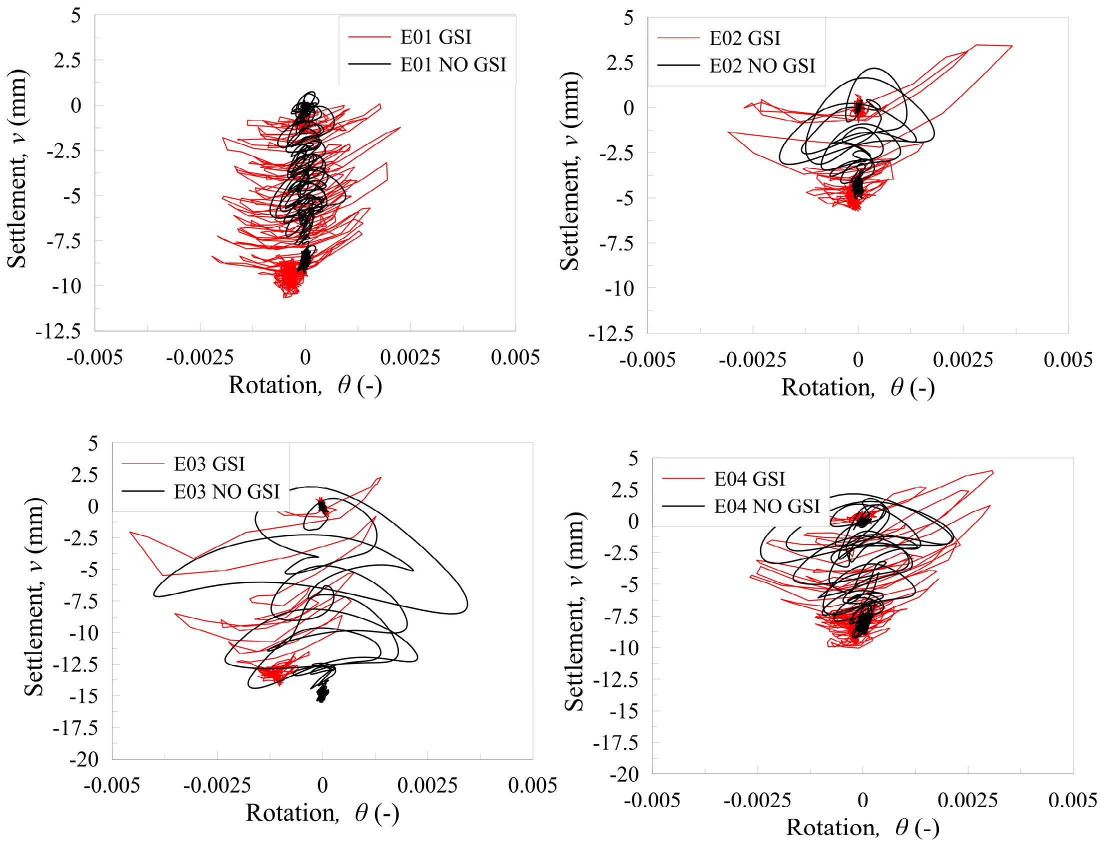

Figure 3. 36. Settlements rotations behaviour for natural earthquakes in centrifuge test evaluated by the PIV technique.

The data shown in Figure 3. 36 are global rotations, or tilt, connected to rigid motions of the structure, and not to differential settlements between the individual foundations, which would cause structural distortion. According to Charles & Skinner (2004), tilt of walls and floors of low-rise buildings typically is noticed when it is in the region of 1/250 to 1/200. Problems associated with serviceability, including, e.g., doors swinging open and drainage falls becoming insufficient, are unlikely until a considerably greater tilt occurs, and structural distress may not occur until a tilt of 1/50. Even if distortions were to be considered, according to Skempton & McDonald (1956), a value of 1/300 can result in damage to non-structural elements, while a value of 1/150 is required for structural elements to suffer damage.

The highest tilt experienced by the GSI structure, observed for the Kobe earthquake, was 0.0045 rad, or less than 1/250, while the residual tilt was just 0.001 rad, or about 1/1000. In all other earthquakes, the peak rotations were lower and the residual rotations almost zero. These appear as perfectly acceptable values, particularly considering that, in a performance-based design approach, controlled damage of the structure is allowed since the primary objective is the protection of human lives. Finally, the fact that the maximum vertical settlements are slightly larger for the structure with laterally disconnected foundations may be explained in terms of a lower vertical stiffness caused by the lack of lateral connection, and therefore of interface vertical shear stresses, between the foundation and the soil. Moreover, the laterally disconnected foundation experienced larger rigid body rotations, which result in the development of larger localized plastic strains at the edges of the foundation, and, in turn, in increased settlements.

3.2.12 Analytical considerations

The dynamic stiffness and damping coefficients can be evaluated using solutions provided by Gazetas (1991) for rigid foundations partly or totally embedded in a visco-elastic continuum of finite depth, loaded by harmonic forces. Since the soil response to seismic loading is non-linear, the stiffness and damping of the soil must be evaluated at a strain level representative of that mobilised during seismic shaking. To this purpose, one-dimensional seismic response analyses were carried out with a visco-elastic non-linear equivalent model, using the code STRATA (Kottke et al., 2019). The sand deposit was subdivided in small layers, and each soil layer was assigned the properties of a non-linear viscoelastic material, namely the small-strain shear modulus G_0, a modulus decay curve, and a damping curve that describes the increment of the equivalent damping ξ with shear strain. Considering a relative density of the model $D_r = 55\%$ (i.e., the initial value), the small strain stiffness of the sand was evaluated considering the increased state of stress due to the loads applied by the foundation. The free-field measurements of shear wave velocity were therefore corrected as (NIST, 2012):

$$V_{s,F}(z) \approx V_s(z)\left(\frac{\sigma'_v(z)+\Delta\sigma'_v(z)}{\sigma'_v(z)}\right)^{\frac{n}{2}} \quad (3.\ 34)$$

where $V_{s,F}$ is the corrected shear wave velocity, V_s and , σ'_v are the shear wave velocity and the vertical effective stress in free-field conditions, $\Delta\sigma'_v$ is the increment of vertical stress due to the loads transmitted by the foundations, computed using the solution by Boussinesq (1885), and $n = 0.5$ is a stress exponent (Hardin and Black, 1968).

The modulus decay $G_{(\gamma)}/G_0$ and the damping curve ξ (γ) for Hostun Sand were obtained from a resonant column test carried out at a confining pressure p' = 55 kPa, on a sample with similar relative density as the sand in the model, D_r = 65-70%, see Figure 3. 37.

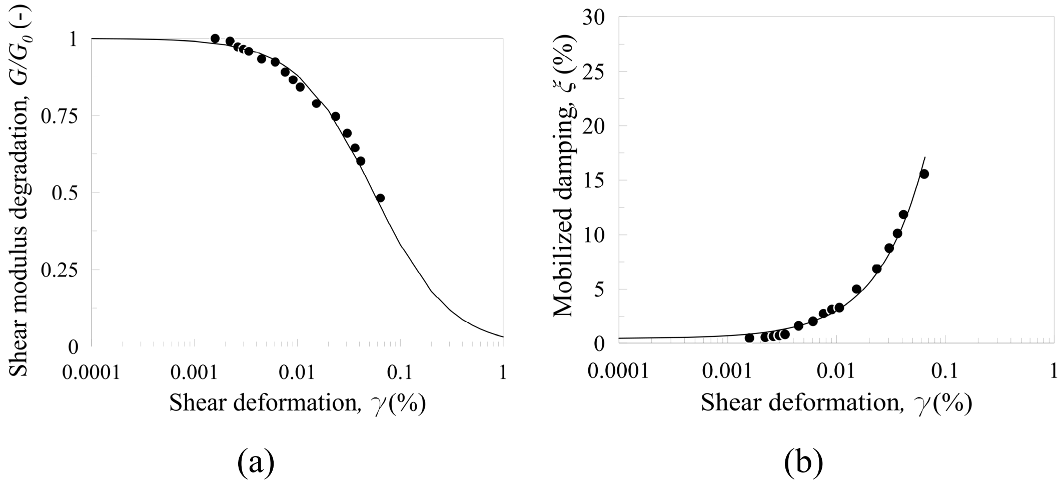

Figure 3. 37. Results of resonant column test on Hostun Sand: (a) $G(\gamma)/G_0$; (b) □(γ)

Figure 3. 38a shows the experimental and numerical profiles of peak acceleration for the four natural earthquakes, which are in remarkable agreement, whereas Figure 3. 38b and Figure 3. 38c show the computed maximum average shear strain and mobilised shear modulus along the depth of the model for the same four natural earthquakes. An average mobilised shear modulus G = 67 MPa and Poisson ratio v = 0.3 can be used as representative of the stiffness of the soil interacting with the foundations.

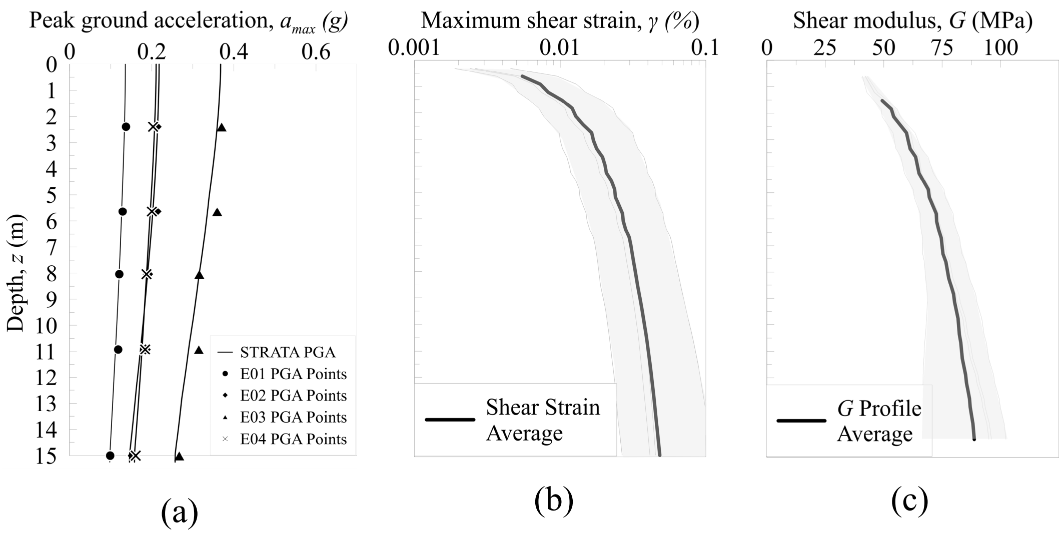

Figure 3. 38. . Dynamic site response analysis for the real earthquakes: (a) numerical and experimental PGA profile, (b) Average maximum shear strain profile γ, (c) Average Reduced G Profile.

The effects of the lateral disconnection on period elongation can be evaluated using Eq. (3. 1). Since both the rotational and lateral stiffness in Eq. (3. 1) depend on the dominant structural frequency, an iterative procedure has been adopted. The analytical value of the natural period increases from 0.385 to 0.620s because of the lateral disconnection, with a 63% increase. The computed elongation of the natural period for the structure with laterally disconnected foundations is in very good agreement with the experimental observations. The above calculations were also repeated considering a relative density of 65.5% (i.e., the relative density estimated for the soil by PIV before applying the natural earthquakes). In this case, the analytical value of the natural period increases from 0.38 s to 0.60 s, or by 58%. This analytical result reinforces the observation that the densification experienced by the soil during the centrifuge test had a limited effect on period lengthening, confirming what already observed applying the same sine-sweep at the beginning and at the end of the centrifuge test (Figure 3. 22).

3.3 Numerical Back Analysis of Centrifuge Test

In the following section a back analysis of the centrifuge test described will be carried out. In particular, reproducing numerically the centrifuge test, it was possible to evaluate the effectiveness of the intervention for other stratigraphic conditions. It was also investigated the variation of the static bearing capacity generated by the lateral disconnection. Numerical simulations of the test centrifuge tests were performed by the FE code Plaxis2D (Brinkgreve *et al.* 2011). For this reason, it is necessary to briefly introduce the calculation code, Plaxis 2D, as well as the material model used to simulate the Hostun Sand in the centrifuge test.

3.3.1. PLAXIS 2D software: general features

PLAXIS 2D is a two-dimensional finite element program, developed for the analysis of deformation, stability and groundwater flow in geotechnical engineering. To carry out a finite element analysis using the PLAXIS 2D program, the first step is to create a two-dimensional geometry model composed of points, lines and other components in the x-y plane and specify material properties and boundary conditions. This is done in the first two tabsheets (Geometry modes) of the Input program. The mesh generation and the definition of the calculation phases is done in the last three tabsheets (Calculation modes) of the Input program. The 15-node triangle is the default element. It provides a fourth order interpolation for displacements and the numerical integration involves twelve Gauss point (stress points). The limit of the model area can be assigned according to the domain extension. Once the problem is drawn, the boundary conditions can be assigned by the user, according to the library constraints, or choosing the standard fixities, which is applied automatically according to the analysis type, which can be static or dynamic. Once the geometric and structural settings are defined, distributed (constant or linear) or concentrated loads or displacements, applied in the created internal or external points, can be introduced in the calculation domain. In the Material section the mechanical properties of the soil layers are fixable: the assignable values are the unit weight, the permeability and the stiffness-strength parameters, which are the elastic modulus E, the Poisson ratio ν, the friction angle φ and the cohesion c. Moreover, the stiffness parameters can be defined as linearly variable with depth. For each soil material created can be assigned a constitutive model and the soil behaviour, assignable between drained and un-drained. For each material the interface soil/structure behaviour is defined through the parameter R, which has 1 as a default value, but can be reduced to values almost null. Once the model features are assigned for each layer and structural element and before the calculation step, the domain is divided in finite elements: the software automatically generates the mesh, without an ordinate structure. In order to get better performance on the analysis results, where the stress variations are very high, the mesh can be denser, around a model point, line or in a selected region. At the end of Input phase, the initial condition is created, performing the generation of pore pressure and effective initial stresses. The initial stress is calculated starting from the K_0 ratio, evaluate from the famous Jaky's (1944) relationship K_0=1-senφ or manually fixed by the user; the lithostatic conditions can be also generated in the Calculation phase, carrying out a plastic analysis without any loads, displacements and structures activated. After the FE model generation, the effective calculation is carried out, defining the type of analysis required. In the Calculation modulus is assigned the analysis phase, the structures and the soil layers are switched on or off, and the loads and the displacements are activated. The calculation is performed, solving a system of equilibrium and congruence equations in the mesh nodes. The Plaxis code permits the execution of 6 types of FE analysis:

- Plastic
- Consolidation
- Fully coupled flow deformation
- Safety
- Dynamic
- Dynamic with consolidation

The Plastic option is an elasto-plastic deformation analysis; the Consolidation option considers the dissipation with time of pore pressure increments; the Safety option carries out a stability analysis reducing the strength parameters in order to evaluate a safety factor; the Dynamic option consists in the application of time histories of loads or displacement, corresponding to a point or a line of the model. Before the analysis starting, some relevant mesh points can be selected, in order to know the variation of some parameters with non-geometric parameters. Each calculation phase is divided in steps, in order to carry out the specific analysis in progressive increments of the variable parameters. When the analysis phase is set, the analysis type, the starting phase, the number of steps, the iterative control parameters should be fixed. Once all the phase condition is defined, the calculation process is started; the analysis is performed in sequence. In the Iteration window, some information of calculation process are showed, including the evolution of the displacement in the selected point, in order to check that the analysis correctly goes forward. Once a FE analysis phase is ended or stopped (manually or automatically due to soil collapse), the results of the calculation can be inspected in the Output modulus. The parameters, which can be displayed in the whole domain, are:

- Total or incremental displacements, velocity and acceleration;
- Total or incremental strain; Cartesian components of total or incremental strain;
- Effective or total stress; Cartesian components of total and effective stresses; total and increments of pore pressure;
- Loads or displacements, stress or strain in the structural elements.

The analysis results were given both as through graphical representation (vectors, contours or shadings) and table lists. The Plaxis user can create a section in the model domain, in order to display the previous listed parameters along the section line (in graph and table form). Concerning the structural elements, the software gives the values of model parameters, but moreover the internal forces in the last calculation steps (hoop load, shear force and bending moment) and the envelops of the previous ones. The procedure to perform dynamic analyses is formally similar to the other types of analyses, but needs some explanations about the additive parameters and conditions compared to the other analyses. In order to perform the seismic shaking of a soil layer, the dynamic loads are applied at the bottom of a bi-dimensional model domain, causing the propagation of the shear waves until the surface of the soil layer. The use of prescribed displacements permits the application of time histories of displacements, velocity or acceleration during the Calculation phase. In the Calculation phase the equation of the wave propagation are solved in the time domain. The basic equation of the dynamic behaviour is:

$$\bar{\bar{M}}\ddot{u} + \bar{\bar{C}}\dot{u} + \bar{\bar{K}}u = F \tag{3. 35}$$

in the (3. 35), M is the mass matrix, C is the damping matrix, K is the stiffness matrix, F is the load vector and u is the displacement vector. The displacement u, the velocity and the acceleration can vary with time. The matrix C represents the material damping and it is formulated as a function of the mass and stiffness matrices (Rayleigh damping) as:

$$\bar{\bar{C}} = \alpha_R\bar{\bar{M}} + \beta_R\bar{\bar{K}} \tag{3. 36}$$

This limits the determination of damping matrix to the Rayleigh coefficients α_R and β_R.

In order to solve the motion equations, an implicit time integration method is used in the software dynamic implementation, according to the Newmark scheme. With this method, the displacement and the velocity at the point in time *t+Δt* are expressed respectively as:

$$u^{t+\Delta t} = u^t + \dot{u}^t\Delta t + \left(\left(\frac{1}{2} - \alpha\right)\ddot{u}^t + \alpha\ddot{u}^{t+\Delta t}\right)\Delta t^2 \tag{3. 37}$$

$$\dot{u}^{t+\Delta t} = \dot{u}^t + ((1-\beta)\ddot{u}^t + \beta\ddot{u}^{t+\Delta t})\,\Delta t^2 \tag{3. 38}$$

In above equation Δt is the time step and the coefficient α and β determine the accuracy of the time integration. The default values for the Newmark coefficients are $\alpha = 0.25$ and $\beta = 0.5$ (average acceleration method).

In the case of static deformation analysis, prescribed boundary displacements are introduced at the boundaries of finite element model. For dynamic calculation, the boundaries should in principle be much further away than those for static calculations, because, otherwise, stress waves will be reflected leading to distortion in the computed results. In the Calculation modulus, some parameters should be accurately defined in each dynamic phase in order to perform a correct seismic analysis. The Dynamic Time, expressed in seconds, for each phase should be assigned. The time step used in dynamic calculation is constant and equal $\delta t = \Delta t/(m \cdot n)$ to where Δt is the duration of the dynamic loading, m is the value of Max steps and n is the Number of the sub steps parameter.

3.3.2. Material Model: Hardening Soil with Small Strain

The non-linear behaviour of foundation soils was described by means of the constitutive model called Hardening - Soil with Small Strain (HS_{ss}). In the HS_{ss} model, the elasto-plastic hardening behaviour is described by two different yield surfaces: a deviatoric surface f_s and a volumetric surface f_v, which are characterised by independent isotropic hardening as a function of the plastic deviatoric strains $\gamma^p = 2\varepsilon_1^p - \varepsilon_v^p$ (with ε_1^p = plastic component of the maximum principal strain) and the plastic volumetric strains ε_v^p, respectively. The deviatoric hardening law is described by the parameter E_{50}, while the volumetric hardening law is controlled by the parameter E_{oed}. Figure 3. 39 shows the shape of the two plasticisation surfaces and shows their evolution schematically, while Figure 3. 40 shows the plasticisation surface in stress space.

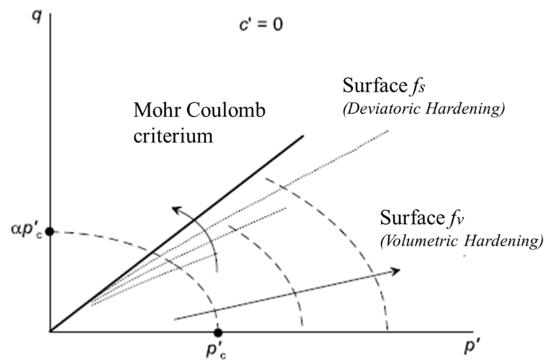

Figure 3. 39. Evolution of plasticisation surfaces in the HS small model (modified from Brinkgreve et al., 2007)

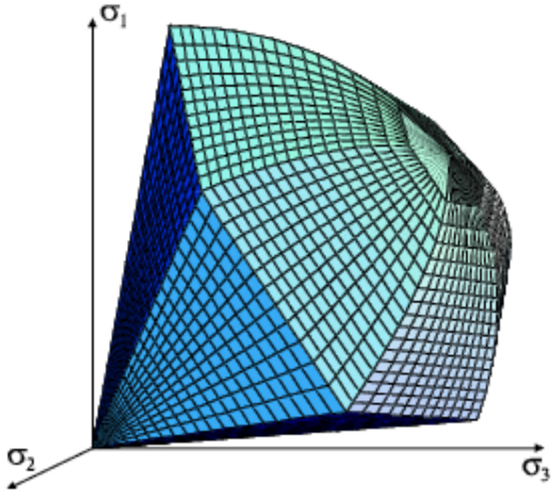

Figure 3. 40. Plasticization surface of HS small model with Mohr - Coulomb resistance criterion in principal stress space (modified from Benz., 2006)

The flow law adopted for the f_v surface is of the associated type; on the contrary, the flow law used for the f_s surface is non-associated and derives from the theory of stress dilatancy theory proposed by Rowe (1962). The mobilised dilatancy angle, ψ_m, depends on the current stress state through the mobilised friction angle, φ'_m, and the friction angle at constant volume φ'_{cv}:

$$sin\psi_m = \frac{sin\varphi'_m - sin\varphi'_{cv}}{1 - sin\varphi'_m sin\varphi'_{cv}} \tag{3. 39}$$

The friction angle at costant volume can be derived from the peak friction angle and dilatancy:

$$sin\psi_{cv} = \frac{sin\varphi' - sin\psi}{1 - sin\varphi' sin\psi} \tag{3. 40}$$

Therefore, if it is a dilatant material, it is sufficient to enter the values of peak friction angle and dilatancy as inputs parameters. Starting from a spherical stress state with *O.C.R=1*, the model predicts a hyperbolic stress-strain relationship with development of plastic deformations from the beginning of the loading path and modulus tangent to the origin equal to $E_0 = 2(1 + \nu_{ur})G_0$ (Figure 3.

41). The deviator failure value, q_f, predicted by the model is equal to $q_f = q_a \cdot R_f$. In particular q_a is the asymptotic value of the deviator and R_f is a model parameter generally equal to 0.9.

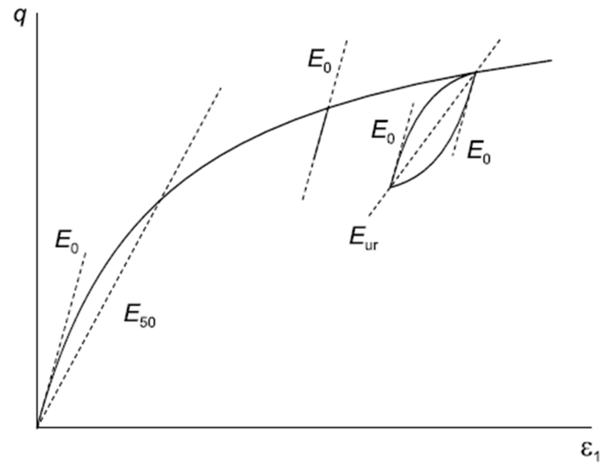

Figure 3. 41. Hyperbolic stress-strain relationship implemented in the HS small model (modified from Brinkgreve et al., 2013)

Under cyclical conditions the behaviour is described by a generalisation of the empirical rules of Masing (1926), calibrated on cyclic shear tests at two- or three-dimensional deformation states. This hysteretic behaviour produces dissipation of energy proportional to the maximum cyclic deformations (Figure 3. 42).

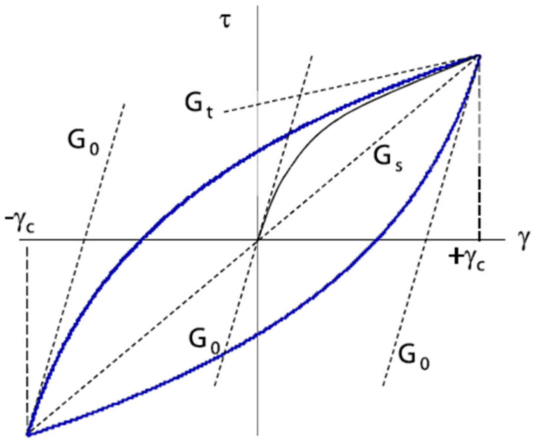

Figure 3. 42. Hysteresis cycle obtained in the HS small model using the rules of Masing (1926) (modified from Brinkgreve et al., 2013)

In order to describe the hysteretic behaviour, it is necessary to define the shear modulus at small deformations and a load-bearing curve that reproduces the decay of the modulus with the level of deformation. In particular, the decay curves of the secant shear modulus G_s and tangent shear modulus G_t with the shear deformation are (Santos and Correia, 2001):

$$G_s = \frac{G_0}{1 + a\left|\frac{\gamma}{\gamma_{0.7}}\right|} \tag{3. 41}$$

$$G_t = \frac{G_0}{\left(1 + a\left|\frac{\gamma}{\gamma_{0.7}}\right|\right)^2} \geq G_{ur} \tag{3. 42}$$

where $a = 0.385$ is a dimensionless parameter and $G_{ur} = \frac{E_{ur}}{2(1+v_{ur})}$ is the secant shear modulus in an unloading - reloading cycle.

In a monotonic loading process, the shear modulus decreases as the level of deformation increases; by partially or totally reversing the direction of loading, the stiffness partially or totally recovers the initial value G_0. The parameter which account of this aspect is the scalar γ_{Hist}, written in the form:

$$\gamma_{Hist} = \sqrt{3}\frac{\left|[H]\Delta\underline{e}\right|}{\left|\Delta\underline{e}\right|} \tag{3. 43}$$

where $\Delta\underline{e}$ is the deviatoric strain increment vector along the main directions and *[H]* is a tensor considering the previous strain history. Damping is evaluated from the hysteresis loops described above and is therefore a response of the model itself (Brinkgreve *et al.*, 2007). The hysteretic damping ratio is defined by the relation:

$$\xi = \frac{E_D}{4\pi E_s} \tag{3. 44}$$

where E_D is the energy dissipated and E_s is the maximum energy accumulated in a discharge-recharge cycle characterised by a cyclic shear strain γ_c:

$$E_D = \frac{4G_0\gamma_{0.7}}{0.385}[2\gamma_c - \frac{\gamma_c}{1+\frac{\gamma_{0.7}}{0.385\gamma}} - \frac{2G_0\gamma_{0.7}}{0.385}\ln\left(1+\frac{0.385}{\gamma_{0.7}}\right)] \tag{3. 45}$$

$$E_S = \frac{1}{2}G_s\gamma_c^2 \tag{3. 46}$$

Equations (3. 45) and (3. 46) are only valid under elastic conditions. The tangent shear modulus G_t and the hysteretic damping ratio vary with the shear deformation until a threshold value, $\gamma_{cut\,off}$, is reached, beyond which they are constant. For $\gamma \geq \gamma_{cut\,off}$ and $G_t = G_{ur}$ and $\xi = \xi(\gamma = \gamma_{cut\,off})$ further decays in shear modulus and increases in damping ratio are predicted by the model when plasticizing conditions are reached. The $\gamma_{cut\,off}$ deformation is given by the relation:

$$\gamma_{cut\,off} = \frac{\gamma_{0.7}}{a}(\sqrt{\frac{G_0}{G_{ur}}} - 1) \tag{3. 47}$$

The development of plastic deformations, from the beginning of a loading process, implies that, in undrained conditions, an increase in the deviatoric stress q produces interstitial overpressures Δu. In cyclic conditions, however, the model predicts the development of plastic deformations, and therefore the generation of interstitial overpressures, but only for cycles of increasing amplitude, which produce an enlargement of the plasticisation surfaces f_s and f_v. For cycles of constant, or decreasing amplitude, the model response becomes elastic, with variations of Δu related only to the variation of p'. The above implies an underestimation of interstitial overpressures under cyclic conditions compared to more advanced constitutive models (PM4Sand).

The Hardening Soil - Small Strain model is able to satisfactorily describe some fundamental aspects of the mechanical behaviour of soils:

1. The non-linearity of the stress-strain relationship, represented by a hyperbolic-shaped relationship between the stress deviator and the axial strain starting from very small strains;
2. The stiffness, in an unloading-loading cycle, which is much greater than that in the first load;
3. The dependence of the stiffness on the current effective stress state;
4. The dependence of the stiffness, along a compression path, on the degree of OCR over-consolidation;
5. The development of plastic deformations even under over-consolidation conditions, for deviatoric stress paths, thanks to the separation of the two plasticisation surfaces f_s and f_v.

Points 1 to 4 represent substantial improvements over the simple linear-perfectly plastic elastic model. Points 2 and 4 differentiate the model used from non-linear elastic models (e.g. Duncan and Chang, 1970). Point 5 is a significant improvement over elastic-plastic models with isotropic hardening governed by plastic volumetric deformations alone (e.g. Modified Cam Clay; Roscoe and Burland, 1968) which overestimate the extent of the elastic domain.

In the model, the elastic behaviour at low levels of deformation depends on the effective stress state through the relationship:

$$G_0 = G_0^{ref} \left(\frac{c' cot\varphi' + \sigma_3'}{c' cot\varphi' + p^{ref}} \right)^m \qquad (3.\ 48)$$

where σ_3' is the minimum principal effective stress, c' is the cohesion, φ' is the angle of resistance of shear strength and p^{ref} = 100 kPa is a reference pressure, while G_0^{ref} and m are model parameters: these last two parameters were derived by means of a least-squares regression carried out on the profile for G_0 (Figure 3. 18). Figure 3. 43 shows the comparison between the profile of G_0 thus obtained and used in the FEM analysis and the one provided by the AIR hammer test in the centrifuge test.

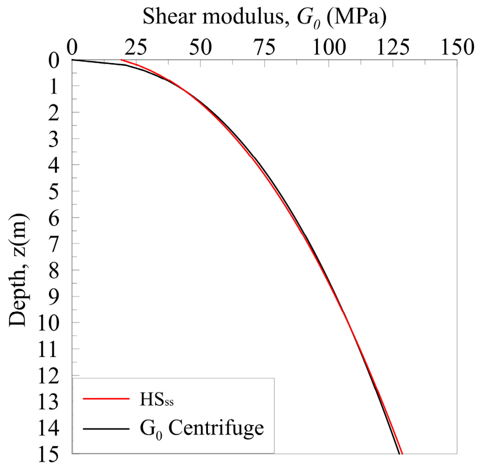

Figure 3. 43. Empirical and numerical shear stiffness profile at the beginning of centrifuge test

Based on the results of the centrifuge test, the following table summarises all the characteristics of Hostun Sand at the beginning of the centrifuge test:

Table 3. 14. Mechanical Properties of Hostun Sand for Numerical Modeling

Soil name [-]	γ [kN/m^3]	c' [kPa]	φ' [°]	Ψ [°]	K_0 [-]
Hostun Sand	14.77	1	37	7	0.39

The value of the peak friction angle, at the beginning of the test, was calculated from the results of the miniature CPT performed in a centrifuge (Figure 3. 19), considering an average value in the significant volume of the foundations of the two structures (namely 2.4 to 5meters). The value of dilatancy was calculated using the simplified formulation $\psi = \varphi' - 30°$ (Brinkgreve, 2011). This formulation provided dilatancy values in substantial agreement with the formulations of Bolton (1986).

Specifically, knowing the value of G_0 it is possible to know E_0 assuming a value of υ_{ur} equal to 0.2:

$$G_0^{ref} = E_0^{ref} / (2(1 + \upsilon_{ur})) \tag{3. 49}$$

At this point, since no triaxial tests have been carried out on Hostun Sand, it is necessary to use empirical relations to know the remaining parameters of HS_{ss} (E_{ur}, E_{50}, E_{ed}).

Alpan (1970) empirically related dynamic soil stiffness to static soil stiffness (Figure 3. 44).The dynamic soil stiffness in Alpan's chart is equivalent to the small-strain stiffness *G0* or *E0*. Considering that the static stiffness E_{static} defined by Alpan equals approximately the unloading/reloading stiffness E_{ur} in the Hardening Soil model with small-strain stiffness, Alpan's chart can be used to find the small-strain stiffness entirely based on its unloading/reloading stiffness *Eur*. Although Alpan suggests that the ratio *E0 / Eur* can exceed 10 for very soft clays, the maximum ratio *E0 / Eur* or *G0 / Gur* permitted in the HSsmall model is limited to 20.

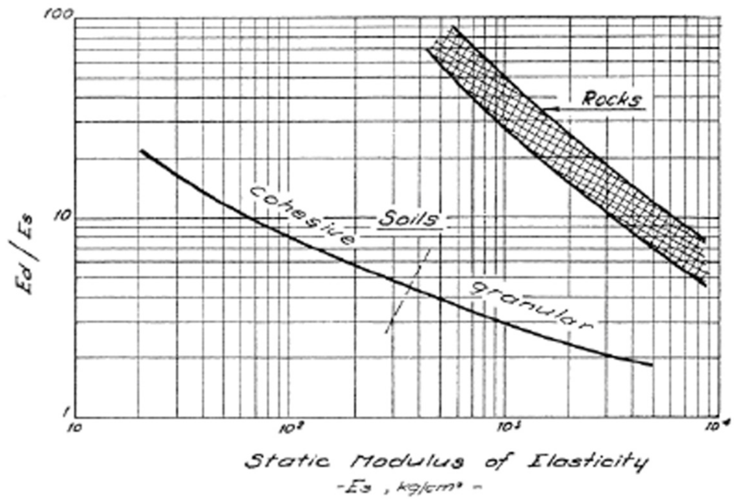

Figure 3. 44. Alpan graph correlating the static stiffness to the dynamic stiffness of a soil.

Using Alfan's graph it is possible to know the value of E_{ur} starting from E_0 and then calculate E_{50} as one thirth of E_{ur}. The definition of the elastic behaviour is completed by one parameter: a shear strain threshold value, $\gamma_{0.7}$, corresponding to a shear modulus $G \approx 0.7G_0$. Using the original Hardin-Drnevich relationship (1972), the threshold shear strain $\gamma_{0.7}$ might be related to the model's failure:

$$\gamma_{0.7} \approx \frac{1}{9G_0}[2c'(1+\cos(2\varphi')) - \sigma_1'(1+K_0)\sin(2\varphi')] \tag{3. 50}$$

Where:

K_0 = The earth pressure coefficient at rest.

σ_1' = The effective vertical stress (pressure negative).

The following parameters have been selected for Hostun Sand:

Table 3. 15. Stiffness parameters for Hostun Sand with HSss material model

G_0^{ref} [MPa]	m [-]	E_{50}^{ref} [MPa]	E_{oed}^{ref} [MPa]	E_{ur}^{ref} [MPa]	$\gamma_{0.7}$ [-]
140.496	*0.45*	35	35	115	0.00029

The $\gamma_{0.7}$ value derived from Equation (3. 50) is nearly coincident with the $\gamma_{0.7}$ value derived from the resonant column test on Hostun Sand equal to 0.00027 (Figure 3. 37).

3.3.3. Results and interpretations

The finite element model used in the numerical analyses is shown in Figure 3. 45.

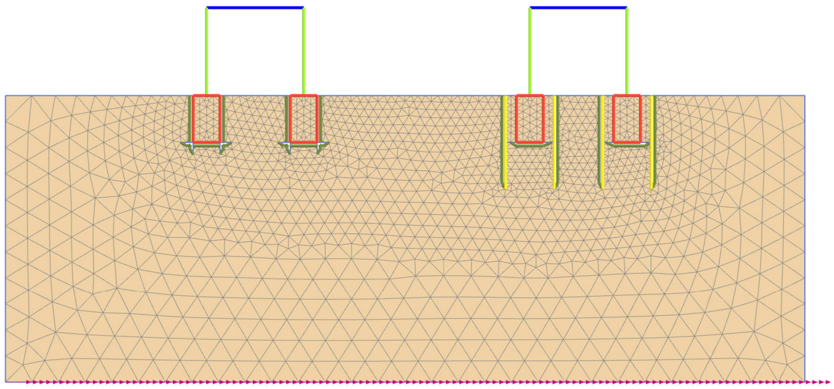

Figure 3. 45. Numerical model

The dimensions of the model correspond to the dimensions of the box minus the thickness of the Duxseal absorbent barriers (730-50=680mm at model scale or 40.80 meters at prototype scale). The height of the soil bank corresponds to the height of the pluviated soil in the model (250mm = 15m at prototype scale). In the static initialisation of the model, horizontal displacements are prevented along the vertical boundaries of the domain, while all displacement components are prevented at the base. In the dynamic analysis, the boundary conditions reproduced those of the box used in the test: viscous boundary at the lateral sides and reflective boundary at the base, through simple rigid supports. Discretization was carried out using 2778 triangular elements with 15 nodes each. The foundation soils are modelled using cluster elements, whose constitutive model is HS small strain (see Table 3. 14 and Table 3. 15 for the material properties). The foundations of the structures are also modelled as zone elements with non porous linear-elastic constitutive model while the beams and columns of the structure are modelled as plate elements. As already stated, the material used for the foundations were 6082-T6 aluminium alloy with the following properties:

Table 3. 16. Mechanical properties of the foundation material

γ [kN/m^3]	E [GPa]	v [-]
26	70	0.33

The properties of the beam and column plates were chosen in order to represent exactly the dimensions of the structural elements in the centrifuge test. The value of the structural damping was set equal to 1% and assigned to the structural elements by means of double frequency approach (with f_1 the first natural frequency of the structure and $f_2=3f_1$). The following properties have been used:

Table 3. 17. Properties of plate elements for modelling the centrifuge frame.

Plate element [-]	EA [kN/m]	EI [kNm^2/m]	v [-]	w [kN/m/m]
Column	12.22E6	31.05E3	0.33	4.53
Beam	42.00E6	1.260E6	0.33	25.75

The weight (w) of the beam added to that of the columns and foundations generates the same bearing load as in the centrifuge test ($\approx 130kPa$). It is important to understand that the lateral stiffness of the columns during the centrifugal test did not correspond exactly to the stiffness of a *GRINTER* shear type frame ($24EI/h^3$) but to a lower value (around $16EI/h^3$). This is generated by the fact that the bolted connections were not able to generate a perfect interlocking constraint for the upper and lower ends of the columns. However, in Plaxis, when structural elements are connected, by default they share all degrees of freedom in the connected node, wich implies that the connection is rigid. In the calculation modes it is possibile to customize the connection between a plate and a beam by explicity defining a point hinges. In order to reproduce the same lateral stiffness as in the centrifuge test 4 point hinges were introduced for each frame with the following stiffness 60kNm/m/rad. As done for the centrifuge test, in order to evaluate the fixed-base period of the numerical frame, it's base was fixed and an horizontal force was applied to the crossbeam (Figure 3. 46a). As the frame is visco-elastic, the intensity of the force does not influence the resonance period of the frame. From the Fourier Displacement Amplitude trasform it is possible to know the resonant frequency in fixed base condition (Figure 3. 46b). The fixed-base resonance frequency is the same as that obtained in the centrifuge test (around 3Hz).

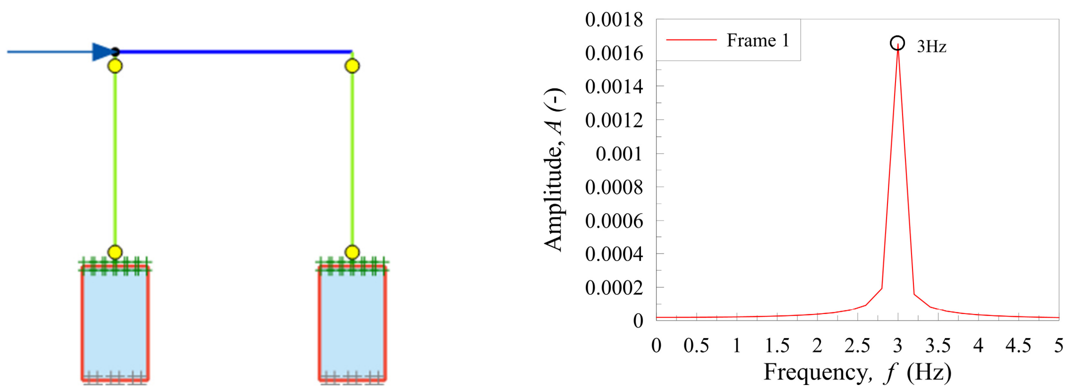

Figure 3. 46. (a) Hammer test carried out by FEM Plaxis 2D model, (b) Fourier Amplitude transform of free oscillations after the application of the horizontal force load.

Interface elements with properties derived from the adjacent soil were used with a value of R_{int} equal to 0.6 (Kulhawy *et al.* 1983, Di Donna *et al.*, 2015). In particular, the interface elements were extended beyond the volume occupied by the foundation to allow for relative displacements of the nodes at the edge of the foundation. The following calculation phases were carried out to reproduce the whole centrifuge test:

- Initialisation of the stress state (k_0 procedures);

- Series of multiple dynamic drained analysis in terms of effective stresses to reproduce the effect of the seismic signals applied in the centrifuge test;

As shown in Chapter 3.2.5, soil densification occurs as a result of different earthquakes. These densifications obviously result in soil stiffening that the HS_{SS} material model cannot predict. In fact, in HS_{ss}, the variation of pore index is not a state variable on which the stiffness of the soil depends (contrary to material models such as SaniSand and PM4sand). For this reason, since the relative density was about 65% (see Table 3. 11) in the natural earthquakes, the shear stiffness profile of Figure 3. 43 has been updated by considering the corrected density. Using the relation of Hardin and Black with the parameters fitted on centrifuge Hostun Sand and suggested by Hoque and Tatsouka, at 65% relative density, it was possible to find out the G_0 stiffness profile in the soil bank. From the G_0 stiffness profile it was possible to recalibrate the parameters of the HS_{ss} as already done at 55% relative density . Table 3. 18 e Table 3. 19 reported the updated parameter for HSss.

Table 3. 18. Mechanical Properties of Hostun Sand at 65% relative density

Soil name	γ	c'	φ'	Ψ	K_0
[-]	[kN/m^3]	[kPa]	[°]	[°]	[-]
Hostun Sand	15.22	1	40	10	0.36

Once again, the peak friction angle values refer to an average within the significant volume of the foundations estimated from the CPT at the end of the centrifuge test.

Table 3. 19. Stiffness parameters for Hostun Sand at 65% relative density with HSss material model

G_0^{ref}	m	E_{50}^{ref}	E_{oed}^{ref}	E_{ur}^{ref}	$\gamma_{0.7}$
[MPa]	[-]	[MPa]	[MPa]	[MPa]	[-]

153	*0.45*	45	45	135	0.2559E-3

It is possible to compare the stratrigraphic amplifications obtained in the centrifuge and by numerical modelling for sine wave trains Figure 3. 47, Figure 3. 48, Figure 3. 49, Figure 3. 50 and the natural earthquakes Figure 3. 51, Figure 3. 52, Figure 3. 53, Figure 3. 54 . The comparisons are between the middle row of piezo accelerometers, specifically ACC_{13}, ACC_{23}, ACC_{33}, ACC_{43} of Figure 3. 11 and the respective nodes in the numerical analysis.

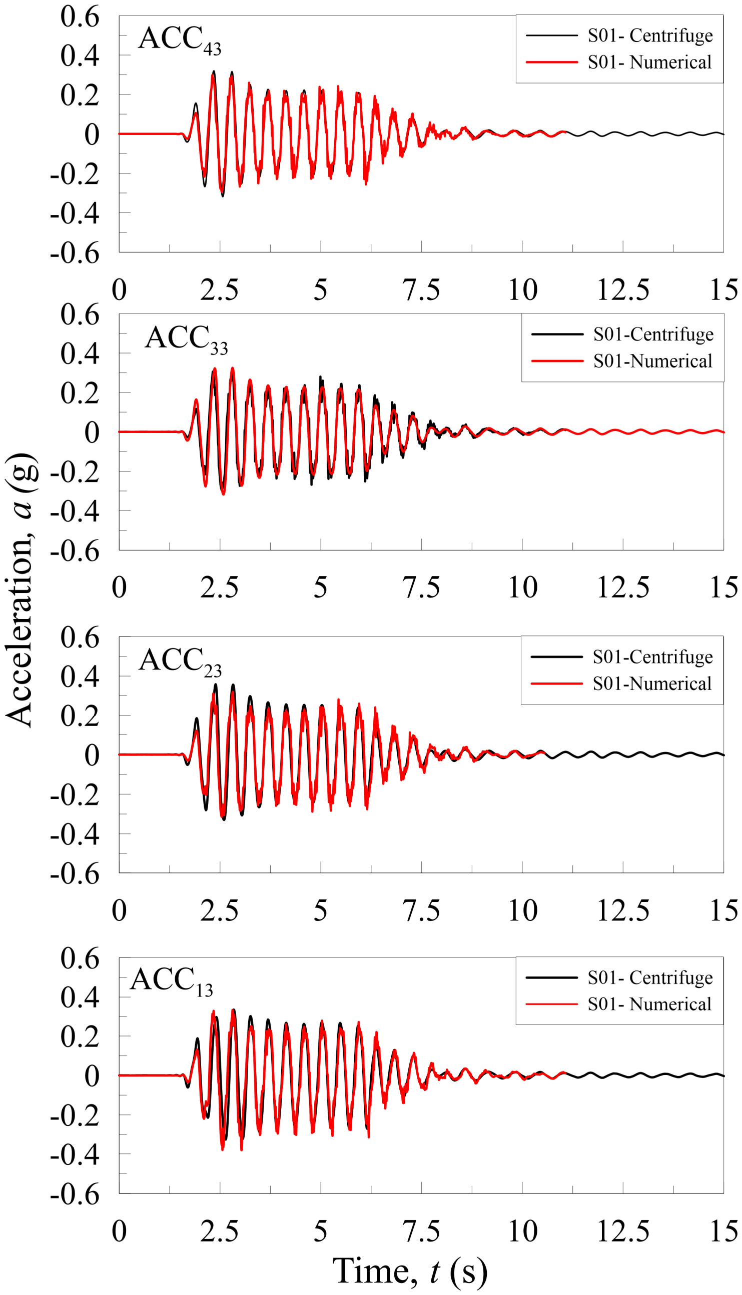

Figure 3. 47. Comparisons of accelerations per S01 sine wave in centrifuge and by numerical modeling.

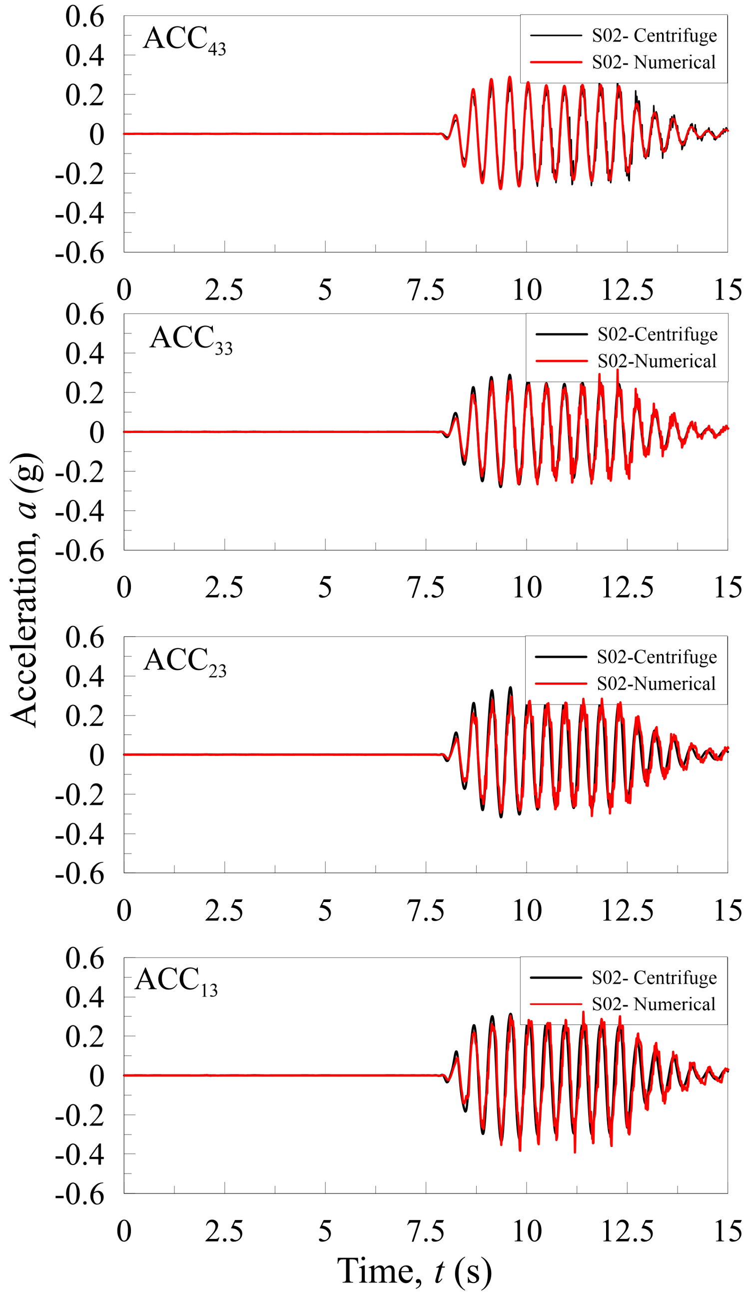

Figure 3. 48 Comparisons of accelerations per S02 sine wave in centrifuge and by numerical modeling.

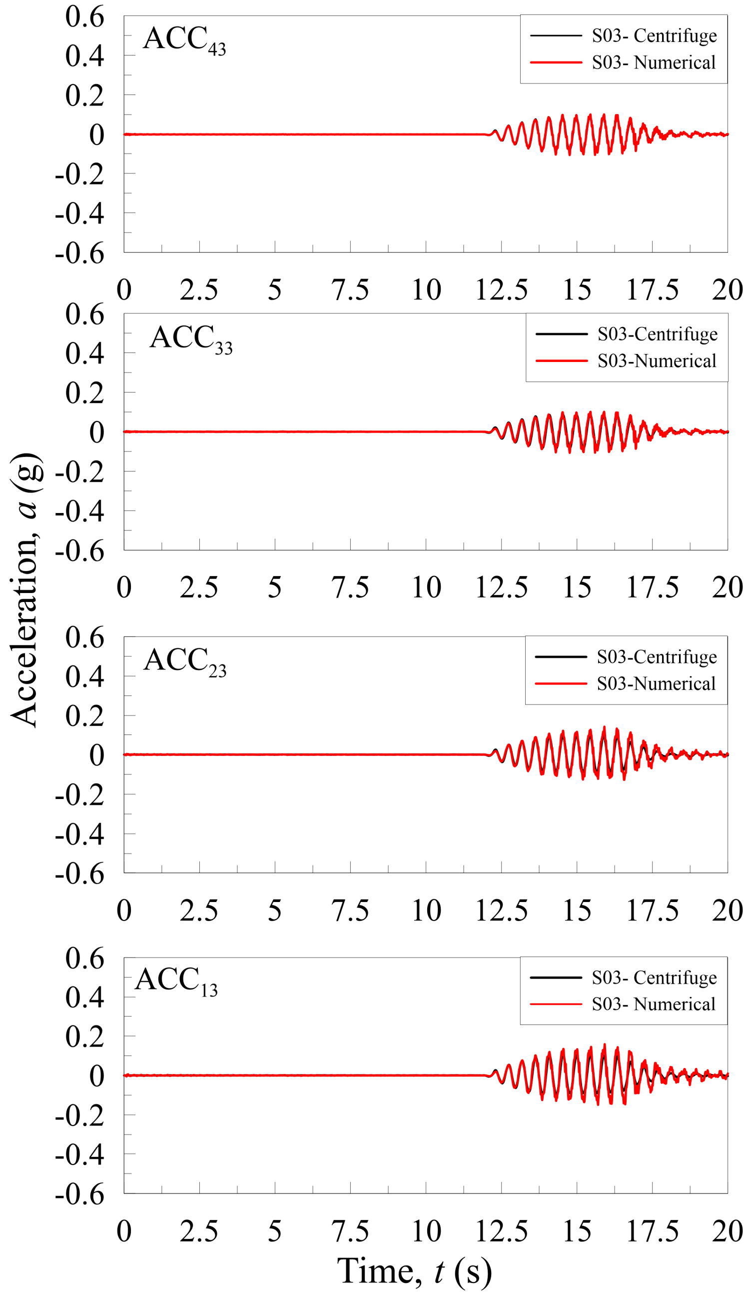

Figure 3. 49 Comparisons of accelerations per S03 sine wave in centrifuge and by numerical modeling.

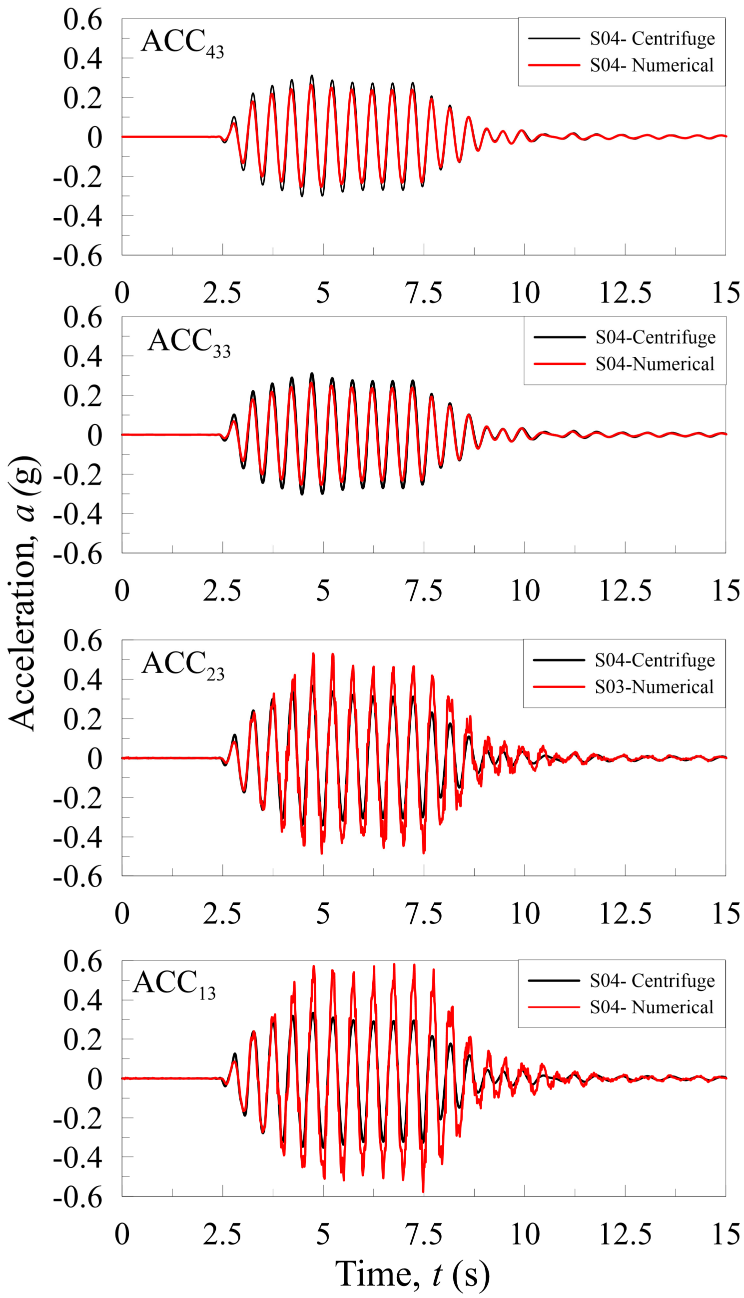

Figure 3. 50. Comparisons of accelerations per S04 sine wave in centrifuge and by numerical modeling.

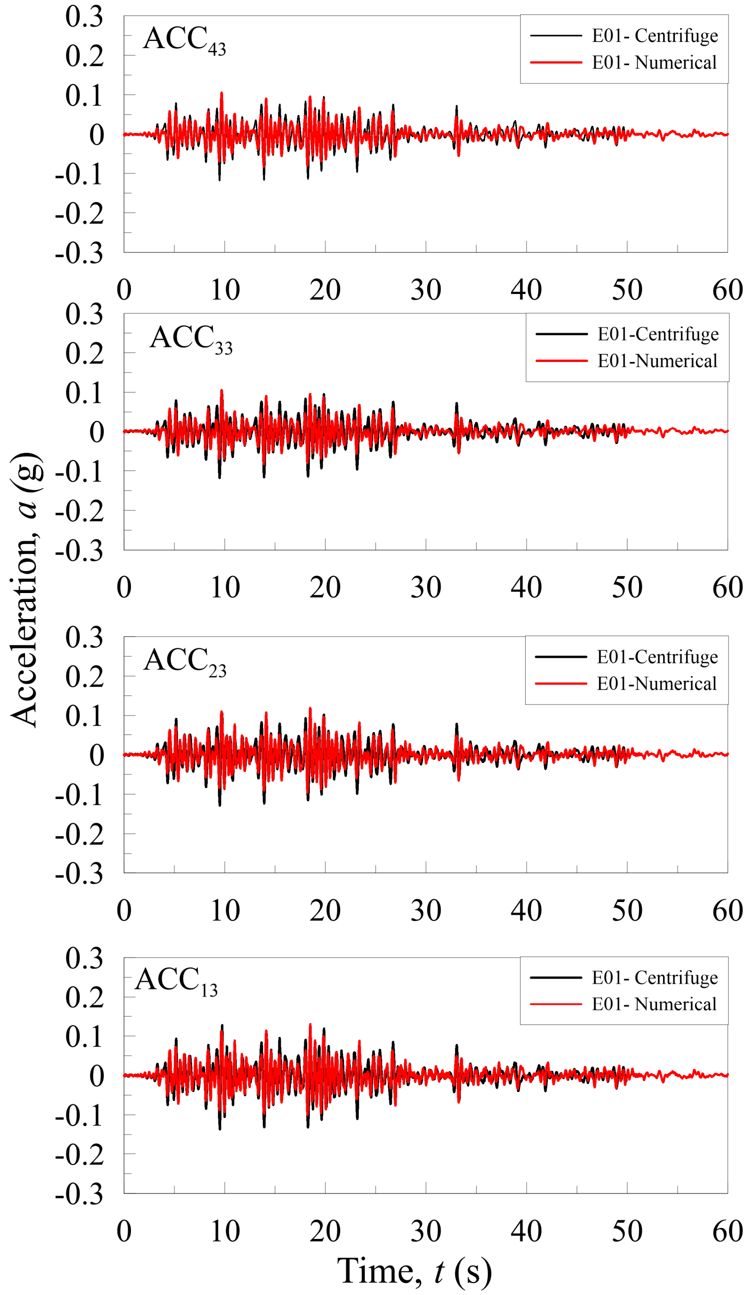

Figure 3. 51. Comparisons of accelerations per E01 earthquake in centrifuge and by numerical modeling.

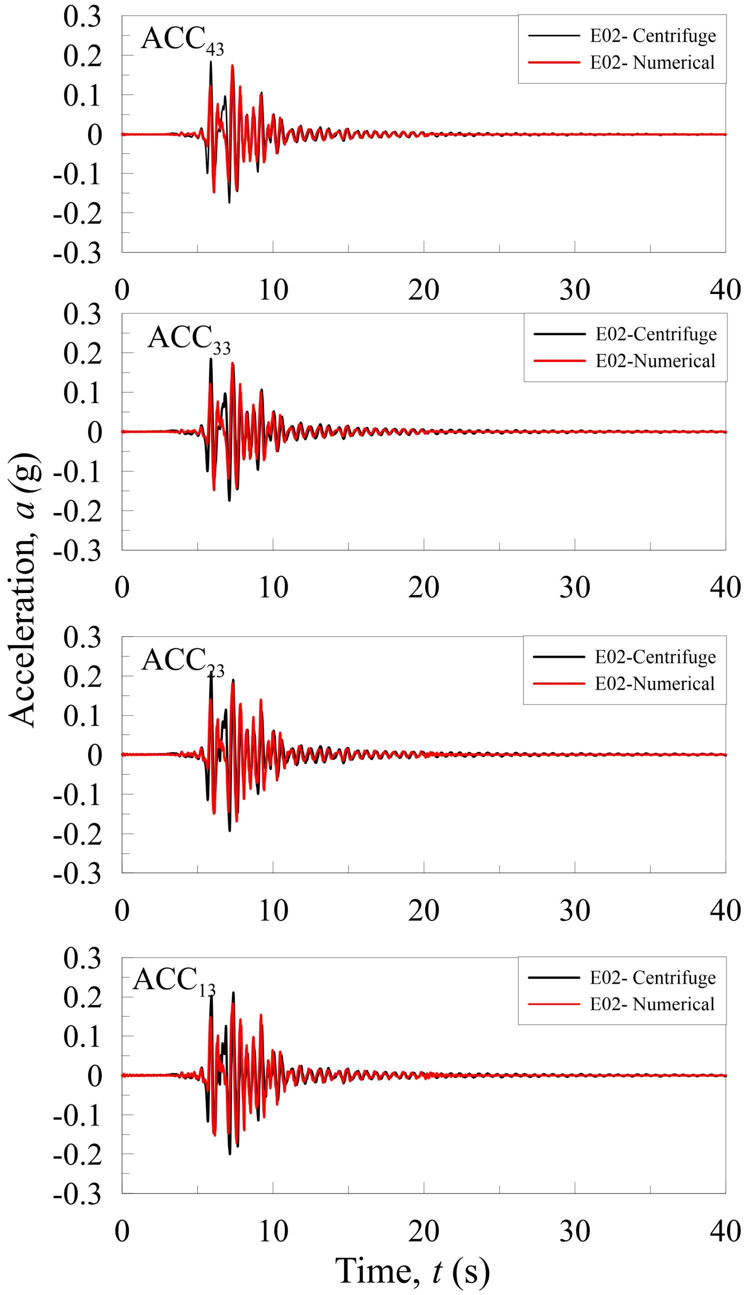

Figure 3. 52. Comparisons of accelerations per E02 earthquake in centrifuge and by numerical modeling.

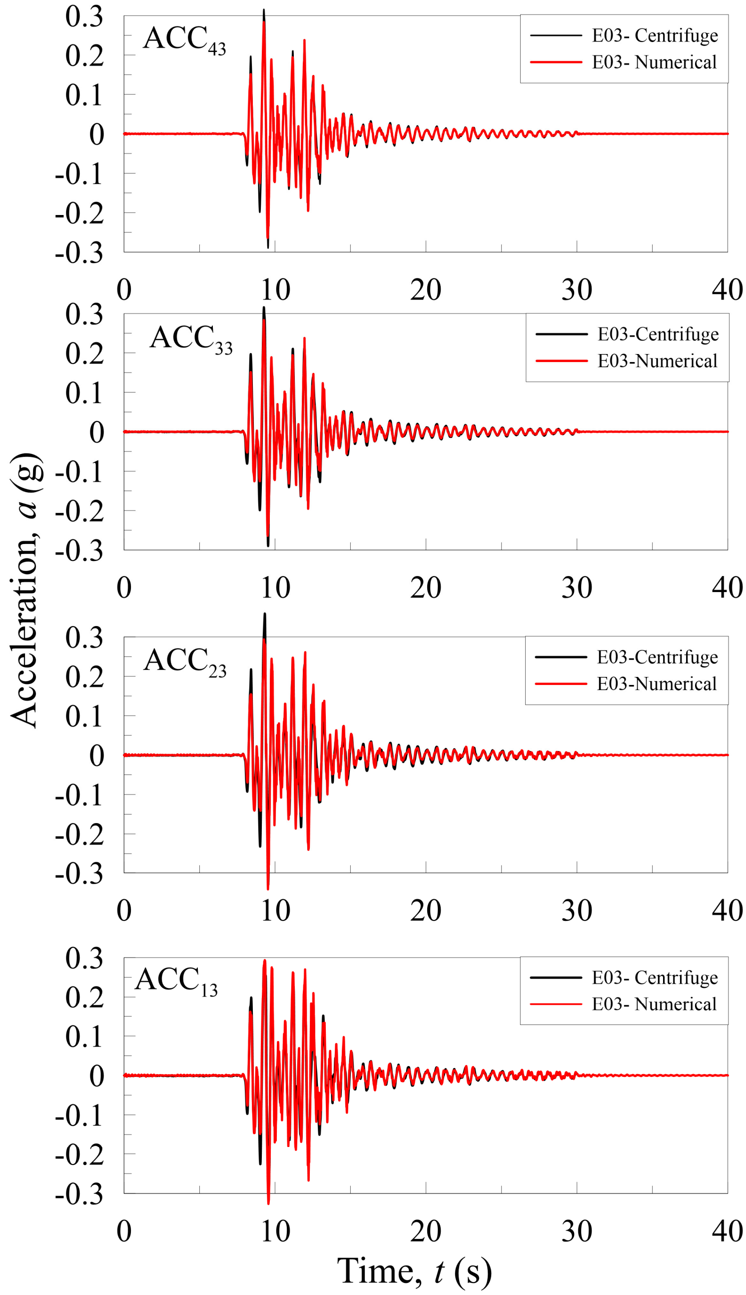

Figure 3. 53. Comparisons of accelerations per E03 earthquake in centrifuge and by numerical modeling.

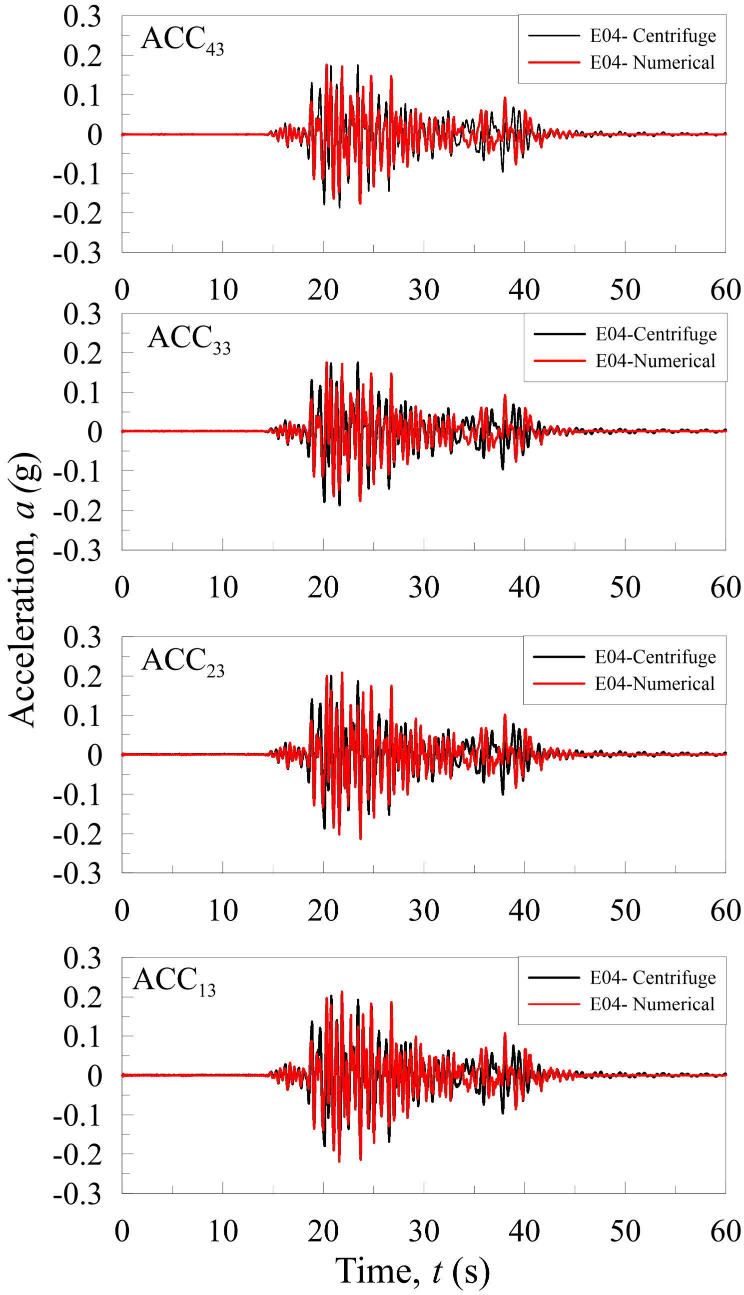

Figure 3. 54. Comparisons of accelerations per E04 earthquake in centrifuge and by numerical modeling.

The similarity of accelerograms between numerical and centrifuge modelling is remarkable. The small differences, specially in the spikes of the accelerogram signals, may be due to the necessity to use a Butterworth bandpass filter between 0.1Hz and 25Hz to the seismic accelerogram input before applying it to the numerical model base. This may result in the loss of amplitude in the spikes of accelerograms. Figure 3. 55 shows the PGA profile obtained in the numerical analisys up to the base of the structures.

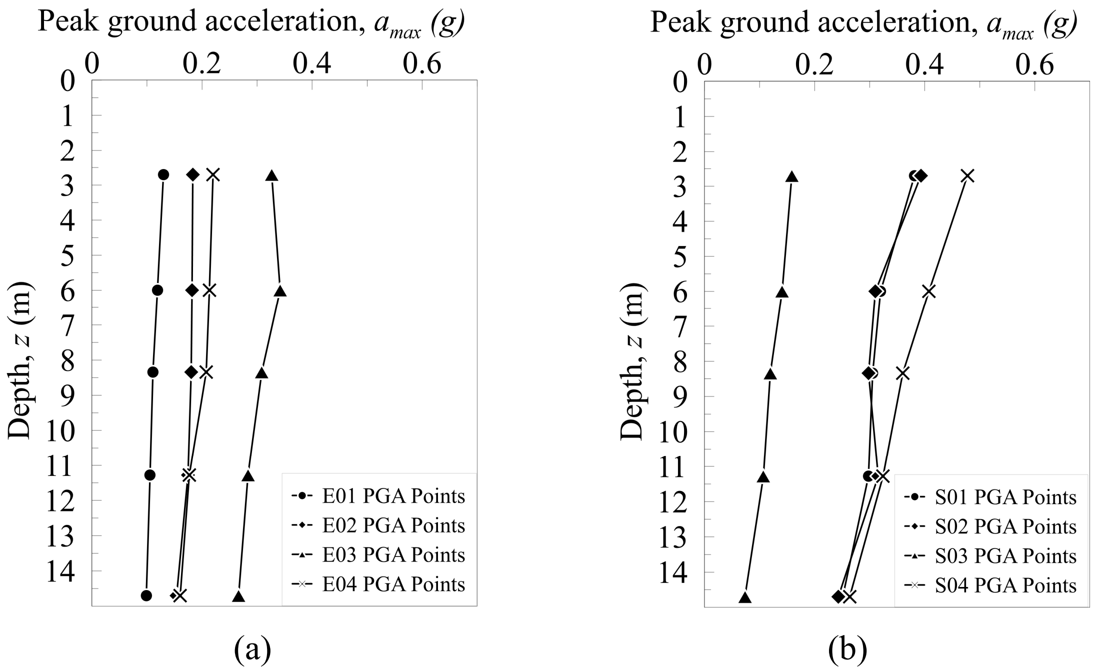

Figure 3. 55. PGA profile for natural earthquakes (a) and sinusoidal signals (b).

It is also possible to numerically calculate the period increase that is determined by the lateral disconnection technique through the use of the seismic signal called SS1, fired at the beginning of the centrifuge test. Following the same procedure conducted for the centrifuge test, sinesweep (SS1 in Table 3. 10) was applied to the numerical model base and from the ratio of the Fourier transforms between the foundation base and the ground floor, the period elongation related to the fixed base conditions of both structures is calculated.

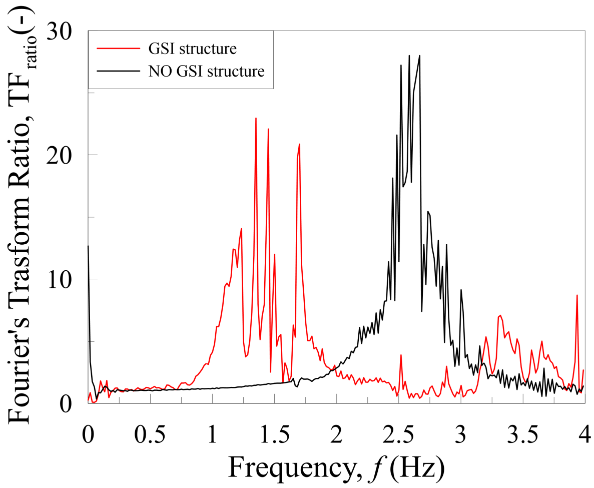

Figure 3. 56. Acceleration amplification function between the base of structure and the roof

It is possible to notice the big reduction of the accelerations amplitudes in the frequency range higher than 2*Hz* generated by the translation of the natural period of vibration for GSI structure. Slighlty greater period elongation can be seen in the numerical modelling compared to the centrifuge test for the NO GSI and GSI structure. In particular, in the centrifuge test the natural resonant frequency computing soil-structure interaction was around 1.6Hz while in the numerical model the natural resonant frequency seems to be concentrated around 1.40-1.45Hz while for the NO GSI structure, istead of 2.7Hz, the natural resonat frequency is around 2.4Hz-2.5Hz. This is likely due to localized densification that occurred exactly underneath the structures in the centrifuge test and that the material model HS_{ss} cannot accurately predict. However, even in this case a great similarity between the numerical and experimental results can be seen. It is important to underline that, as these are non-linear elasto-plastic dynamic analyses, it is very difficult to identify a precise value of the natural resonance frequency of the soil-structure system, as this varies as the stiffness properties of the soil change step by step. The indication of a single value of the natural period of vibration of the structure soil system is only intended to be a way of identifying a frequency where maximum amplification is expected for that specific seismic signal. In this sense, it is very likely that an earthquake with an intensity greater than the SS1 seismic signal or with a predominant frequency similar to that of the soil bank will generate a longer period elongation for both GSI and NO GSI structures because the primary nonlinearities (i.e., those generated by the earthquake itself in the soil) as well as secondary nonlinearities (i.e., those generated by soil structure interaction phoenomena) can vary the stiffness properties of the soils in the significant volume of soil.

Comparing the absolute floor accelerations between the two GSI and NO-GSI structures for the sinusoidal and earthquakes signals it is possible to understand the difference in period elongation between the the two structures (Figure 3. 57, Figure 3. 58. As done for the centrifuge test, in the following graphs, the length of the seismic acceleration in the real earthquakes signals has been reformulated focusing on the parts of interest. This makes the following graphs more understandable.

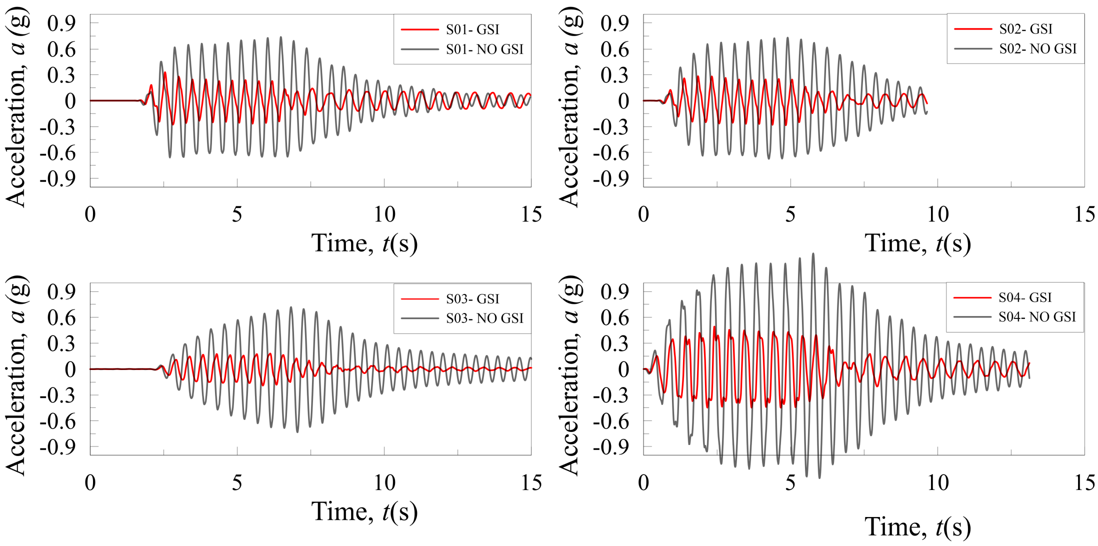

Figure 3. 57. Comparison of absolute acceleration on ground floor between NO GSI and GSI structures for sinusoidal signals.

Figure 3. 57 clearly shows the different resonant condition between the two structures during the sinusoidal signals. In particular, since the frequency of the sinusoids is very close to that of the NO GSI structure (2.2Hz is very close to the 2.40-2.5Hz frequency detected by SS1) there is a strong increase of accelerations due to resonance phenomena. On the other hand, for the GSI

structure, since the resonant frequency is much lower (around 1.40-1.45Hz) we can notice a much lower accelerations demand. Comparing these accelerations requests with those obtained in centrifuge (Figure 3. 24) the same effect can be seen. In fact, even in the centrifuge test, the accelerations demand for the NO GSI structure were greater than the GSI structure during the sinusoids. However, it is noticed that for the GSI structure there is a good agreement, while for the NO GSI structure there is a much higher acceleration demand in the numerical modelling. As already mentioned, this is due to the fact that the period elongation we had in the centrifuge for the NO GSI structure was less than that predicted by the numerical analysis (Figure 3. 56) and for this reason the frequency of the sinusoids is closer to that of the structure than happened in the centrifuge test. As already mentioned, this may be due to slightly different soil stiffness conditions around the structures than those in the model itself, which is obviously very difficult to calibrate or predict.

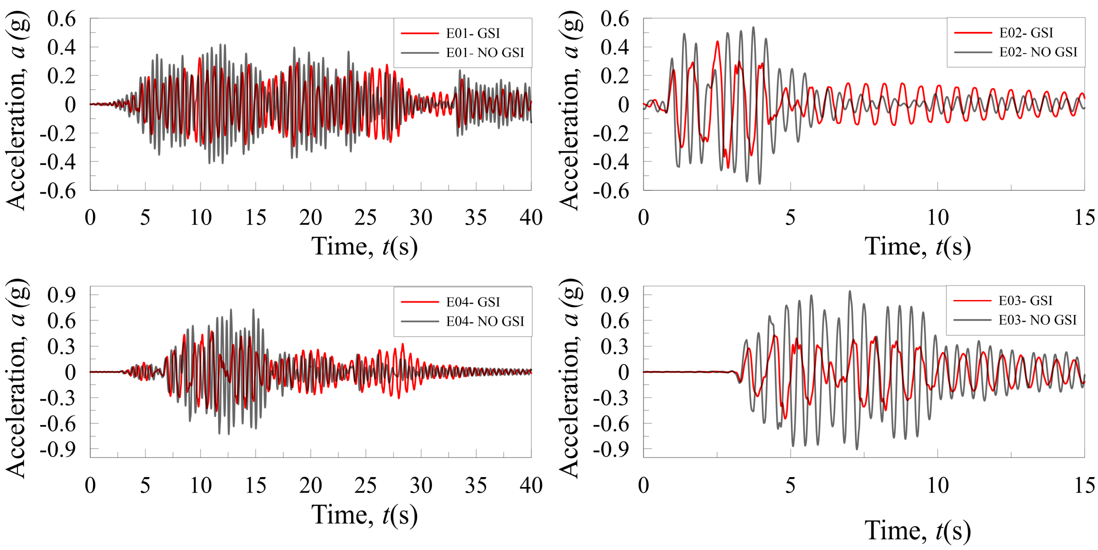

Figure 3. 58. Comparison of absolute acceleration on ground floor between NO GSI and GSI structures for real earthquakes.

The same considerations can be made for natural earthquakes (Figure 3. 58). In fact, also in this case (as in the centrifuge test) the acceleration demands were higher for the NO GSI structure. Once again, there are slightly higher acceleration demand for the NO GSI structure compared to the centrifuge test due to the different period lengthening.

The efficiency in terms of acceleration reductions (Figure 3. 59a) as well as the efficiency in terms of Arias Intensity reduction (Figure 3. 59b) is reported. Slighlty higher efficiencies can be seen related to the centrifuge test for both sine waves and natural earthquakes. However, it is still possible to see the same trend observed in the centrifuge test as the maximum acceleration of the seismic signal inceased.

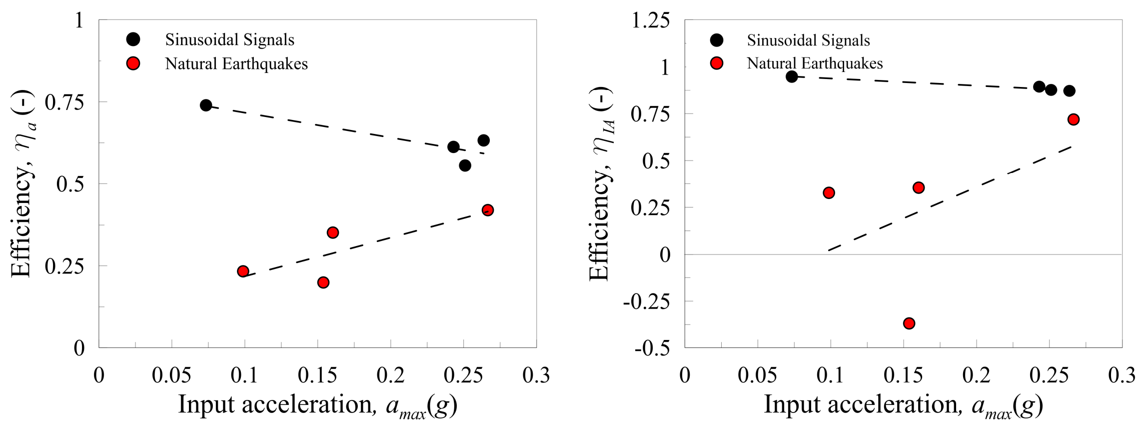

Figure 3. 59. Efficiency in terms of absolute accelerations reduction and IA reduction between the GSI and NO GSI structure

Focusing on the Kobe earthquake (the earthquake with the maximum PGA), it is possible to extrapolate some significant stress and strain patterns. Figure 3. 60, Figure 3. 61, Figure 3. 62, Figure 3. 63, Figure 3. 64 show the isolines of the degree of mobilisation of the shear resistance, τ_{rel}, and of the deviatoric deformation, γ_s, for the instant t in which the maximum displacement at structural floor is reached (t = 9.84sec for GSI structure and t=9.62sec for NO GSI) and at t=30sec which is the end of dissipation of the inertia forces (*i.e.* the end of the earthquake). The distribution of τ_{rel} between the two structures is completely different. It can be seen that for the GSI structure the maximum resistance of the soil at the base of the foundations is mobilised. This is generated by the rotations that the foundation undergoes during the earthquake. It is therefore possible to see a fully plasticised zone below the foundations. For the NO GSI structure, on the other hand, the achievement of the resistance of the soil occurs laterally to the foundations themselves rather than below them. This is generated by the fact that the lateral soil is able to fix the rotations of the foundations through the mobilisation of passive pressure. Similar considerations can be made when considering the deviatoric strain, γ_s. Below the foundations of the GSI structure there is an accumulation of deviatoric deformations reaching values of more than 1%. Such deviatoric deformations, below the foundation level, are not present for the NO GSI structure.

For GSI structure, at the end of the earthquake (*t*=30sec), the deviatoric deformations increased and spread below the foundation, reaching values greater than of 1 % (out of scale in the representation to allow observation of the other isolinea). The increase of the deformations with respect to the instant t = 9.84 s is due to the fact that this instant is at the beginning of the significant phase of the seismic input.

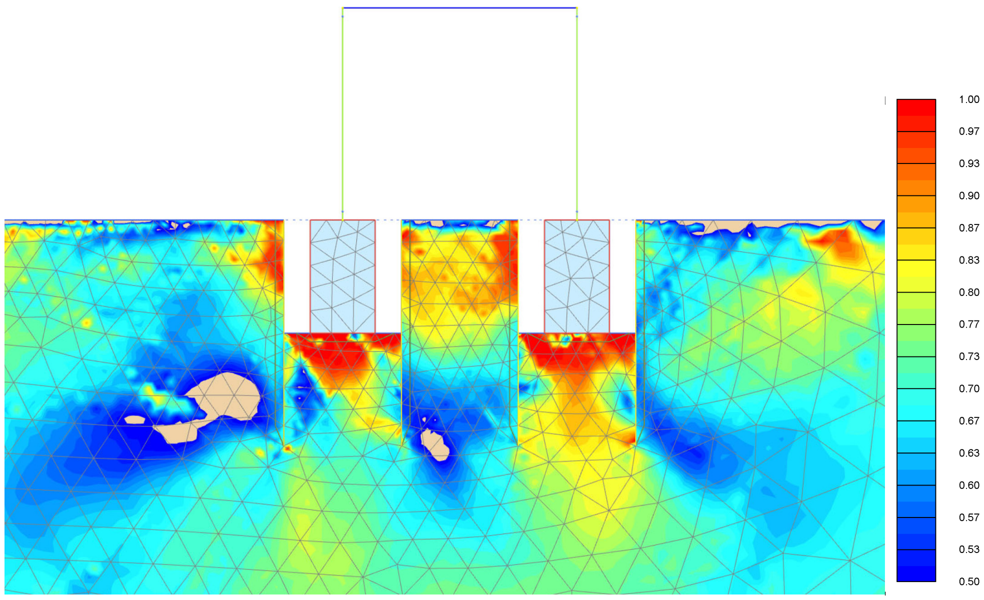

Figure 3. 60. Isolines of the shear strength mobilized, τ_{rel}, for GSI structure at the instant of time equal to 9.82sec during Kobe earthquake

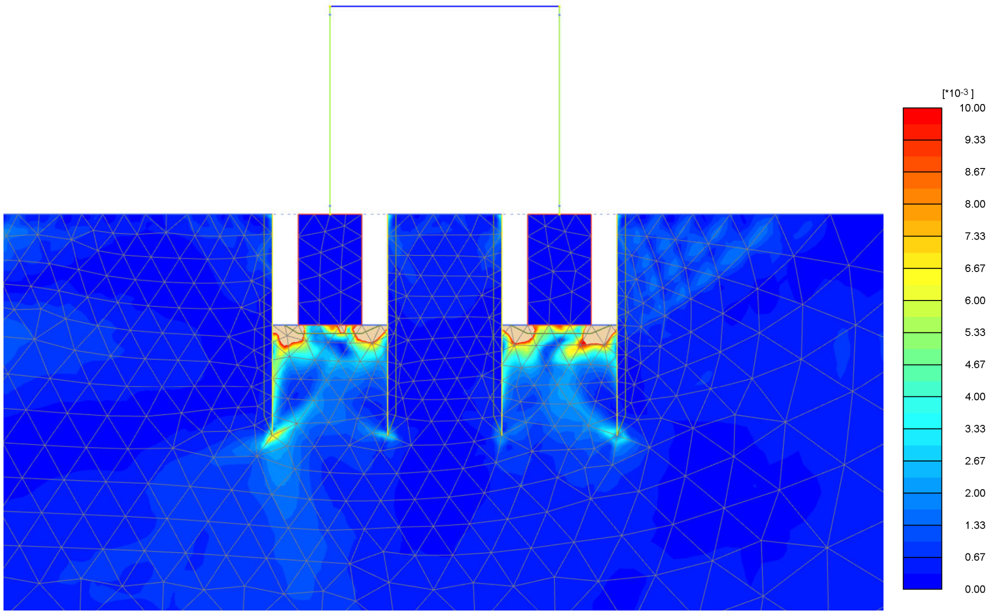

Figure 3. 61. Isolines of deviatoric strain, γ_s, for GSI structure at the instant of time equal to 9.82sec during Kobe earthquake

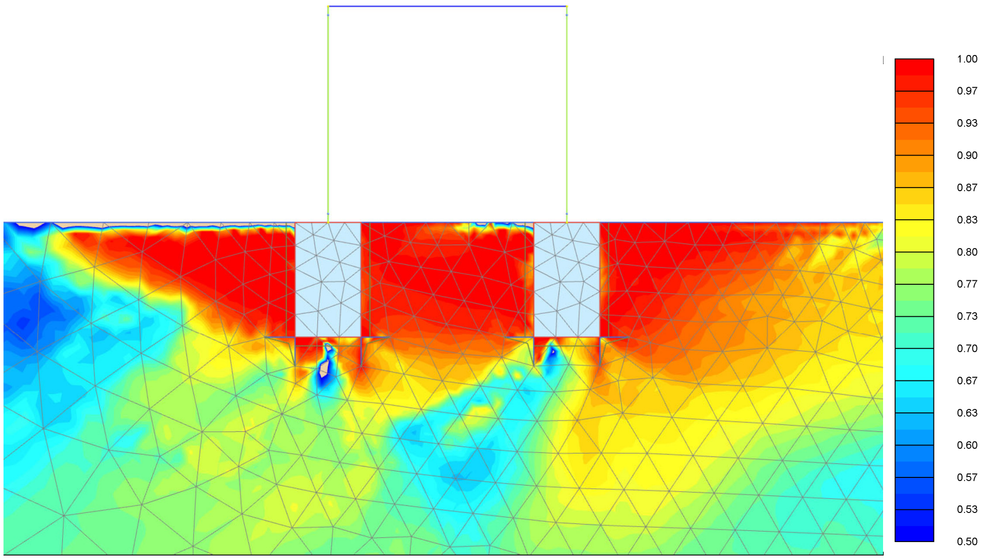

Figure 3. 62. Isolines of the shear strength mobilized, τ_{rel}, for NO GSI structure at the instant of time equal to 9.62sec during Kobe earthquake

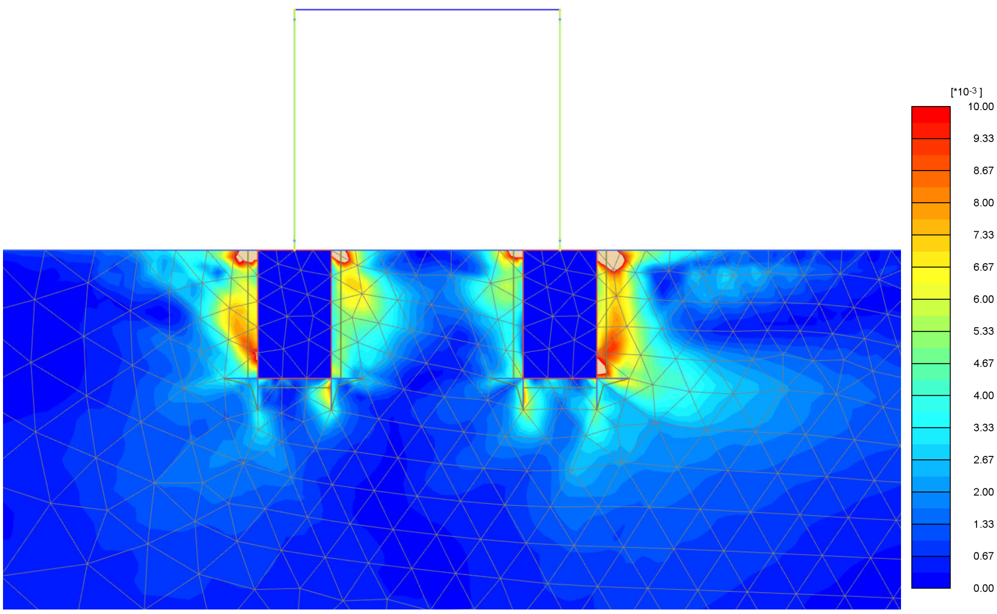

Figure 3. 63. Isolines of deviatoric strain mobilized, γ_s, for NO GSI structure at the instant of time equal to 9.62sec during Kobe earthquake

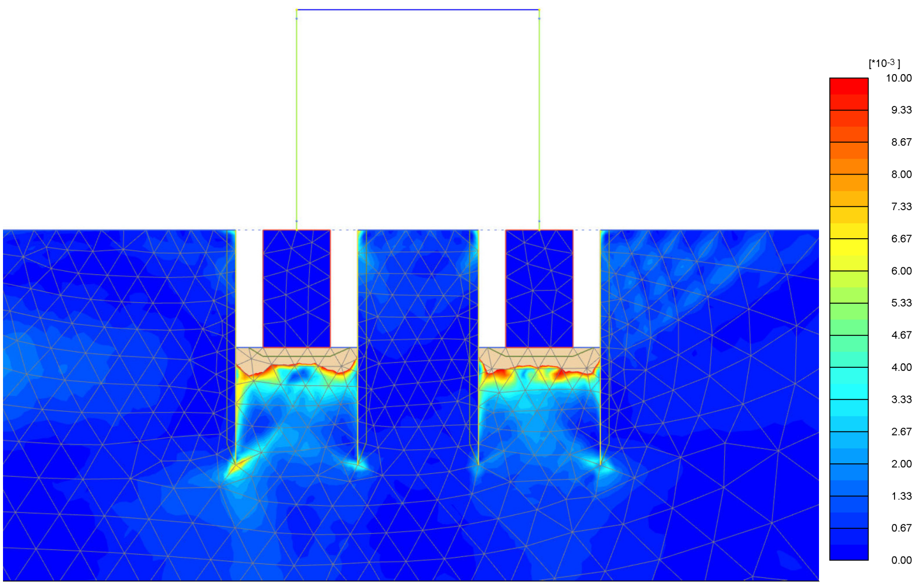

Figure 3. 64. . Isolines of deviatoric strain, γ_s, for GSI structure at the instant of time equal to 30sec during Kobe earthquake

As already shown in Figure 3. 28, the lateral disconnection technique reduces the structural damage (structural drift) mainly due to the increase of the global rotations of the building. The demand in terms of displacement of the disconnected building will be concentrated in rotational displacements (global tilts) that obviously do not generate distortions in the load-bearing elements. As already shown in Figure 3. 36, Figure 3. 65 shows the global rotations and displacements that the two frames undergo during natural earthquakes. It is clear that the global rotations are profoundly different between the two structures. In particular, the GSI structure undergoes global rotations equal to double and in some cases triple the NO GSI structure.

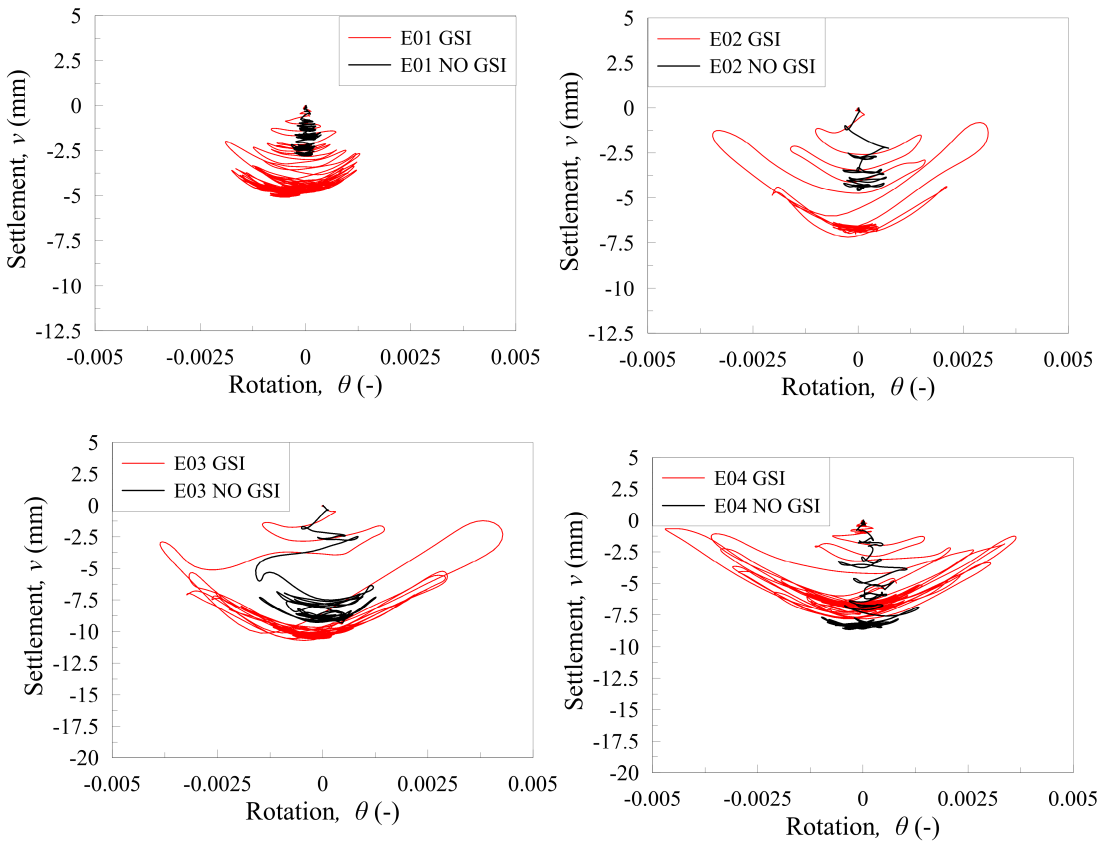

Figure 3. 65. Settlement rotation behaviour evaluated by numerical modelling

Considering the difficulty of evaluating the exact conditions of stiffness and strenght of the soil around the two structures because of local densification or reduction of effective ground contact foundation, which obviously affects the interaction between the soil and the structure itself, the results found are in substantial agreement with those evaluated in the centrifuge. In fact, also in this case, the settlements of the GSI structure are greater than those of the NO GSI structure, as well as the global rotations.

As the goal of this numerical back analysis is to extrapolate further information on lateral disconnection rather than simply replicate the centrifuge test conducted, the whole centrifuge test was reproduced numerically using the same medium (Hostun Sand) but with a much higher density (D_r= 85%). The G_0 stiffness profile was obtained using Hardin and Black's formulation for Hostun Sand with a density of 85%. Table 3. 20 and Table 3. 21 represent the parameters used for sand with 85% relative density. The procedure used to evaluate these parameters is similar to that already shown for evaluating the parameters of sand at 55% relative density and 65% relative density.

Table 3. 20. Mechanical properties of Hostun Sand at 85% relative density

Soil name [-]	γ [kN/m3]	c' [kPa]	φ' [°]	ψ [°]	K_0 [-]
Hostun Sand	16.02	1	42	12	0.33

Table 3. 21. Stiffness properties of Hostun Sand at 85% relative density

G_0^{ref} [MPa]	m [-]	E_{50}^{ref} [MPa]	E_{oed}^{ref} [MPa]	E_{ur}^{ref} [MPa]	$\gamma_{0.7}$ [-]
180	*0.45*	60	60	182	0.2076E-3

Figure 3. 66 summarises the stratrigraphic amplifications that occurred in the soil with a relative density equal to 85%.

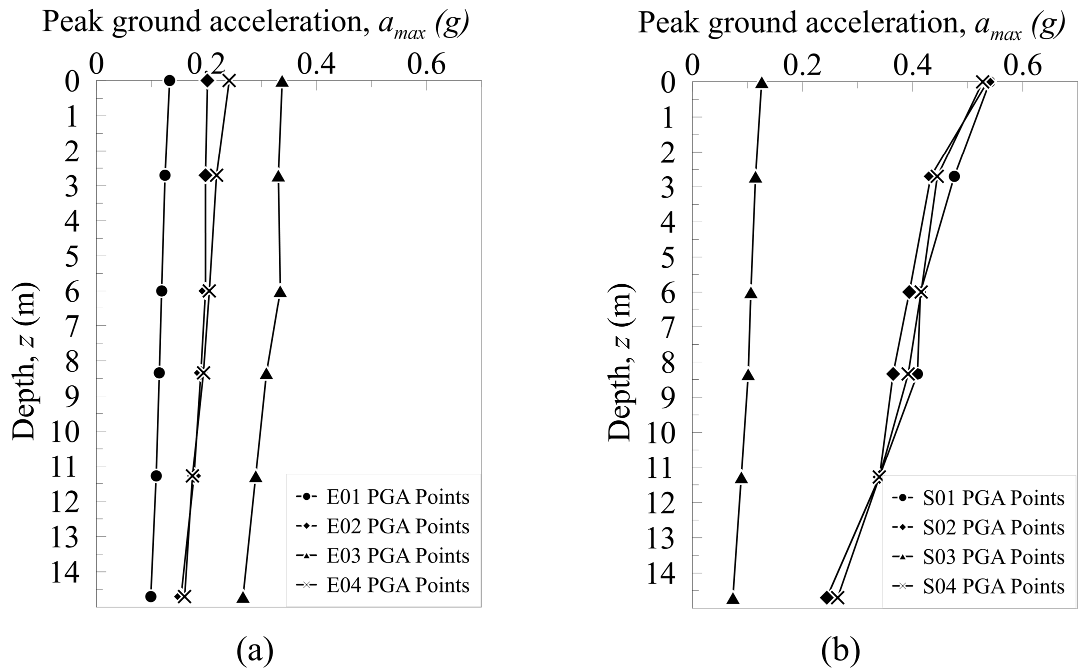

Figure 3. 66. Stratrigraphic amplification in the soil bank with a relative density of 85%; (a) real earthquakes; (b) sinusoidal signals

For natural earthquakes there are no significative differences in the local seismic response compared with the amplification evaluated at 65% relative density (Figure 3. 55a). Instead, for sinusoidal there are higher amplifications of the seismic signal at the base generated by the greater stiffness of the foundation soils.

Using sinesweep SS1, the period elongation of the two structures can also be known in this case (Figure 3. 67).

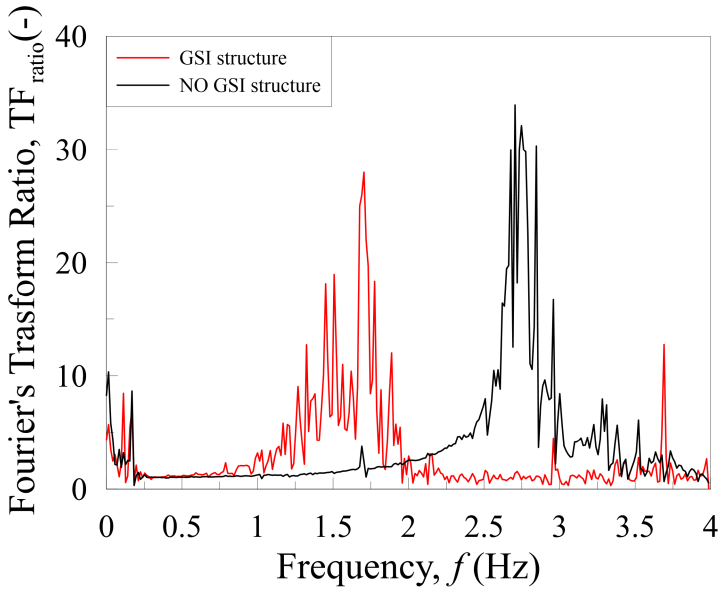

Figure 3. 67. Elongation of natural resonance period for GSI and NO GSI structure with 85% relative density.

Comparing Figure 3. 56 with Figure 3. 67 it is possible to make some considerations. For medium loose sand, the maximum amplifications is between 1.4Hz and 1.5Hz for the GSI structure while in this case they appear to be gathered around the 1.6-1.7Hz frequencies. For the NO GSI structure, on the other hand, the maximum amplification frequencies slip to higher values around 2.7Hz instead of 2.5Hz. The period elongation, as expected, seems to be lower when the soil stiffness is higher. It is also possible to note a greater similarity of the amplification functions with a relative density of 85% with those obtained from the centrifuge experiment. This is a further demonstration of the fact that there were localised densification phoenomena under the two structures during the centrifuge test. Figure 3. 68 and Figure 3. 69 show the total roof accelerations of the two structures for sinusoidal signals and natural accelerograms. Due to the higher acceleration amplifications generated by the dense soil for sinusoidal seismic signals, a higher acceleration demand can be observed for both the NO GSI and GSI structure related to Figure 3. 57. With regard to natural earthquakes, it is possible to notice a greater similarity in terms of amplitude between the accelerations affecting the GSI and NO GSI structures rather than Figure 3. 58. This occurs because the stiffening of the ground generates a lower period elongation for both structures and therefore the acceleration demand tends to be more similar.

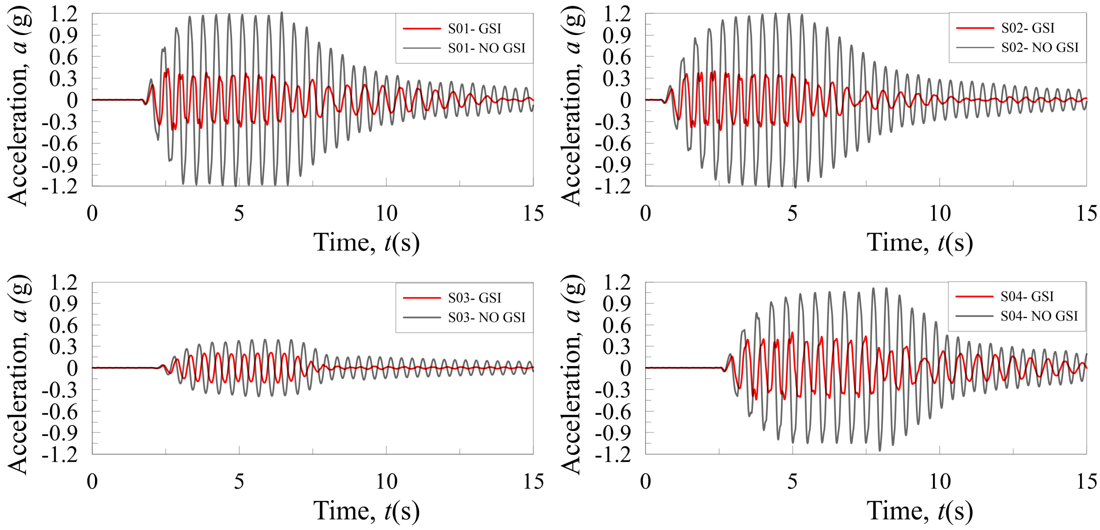

Figure 3. 68. Top GSI and NO GSI absolute acceleration during sinusoidal signals with relative density of 85%.

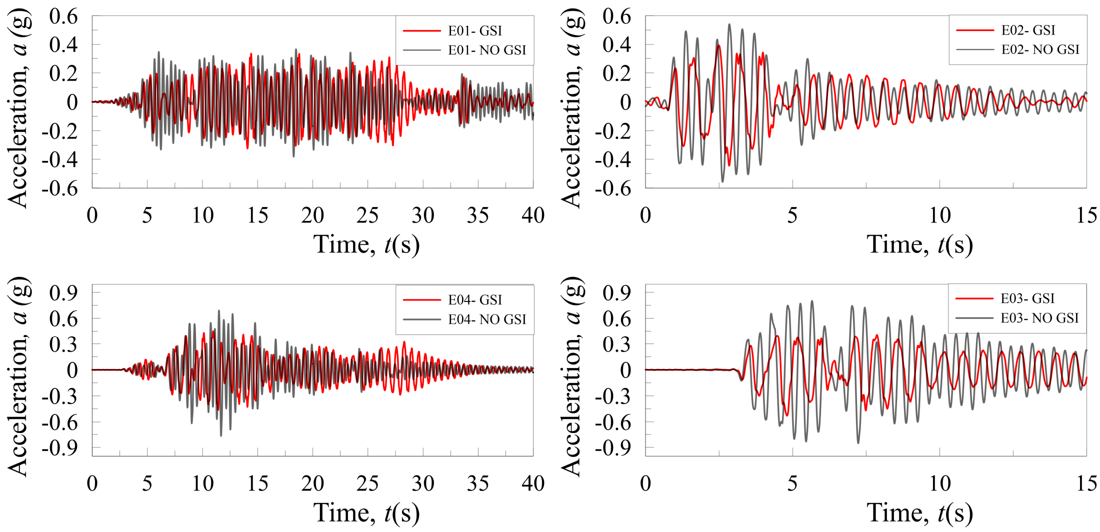

Figure 3. 69. Top GSI and NO GSI absolute acceleration during natural earthquakes with relative density of 85%.

As already done, it is possible to introduce some efficiency measures such as acceleration reduction and *IA* reduction in case of dense sand (Figure 3. 70).

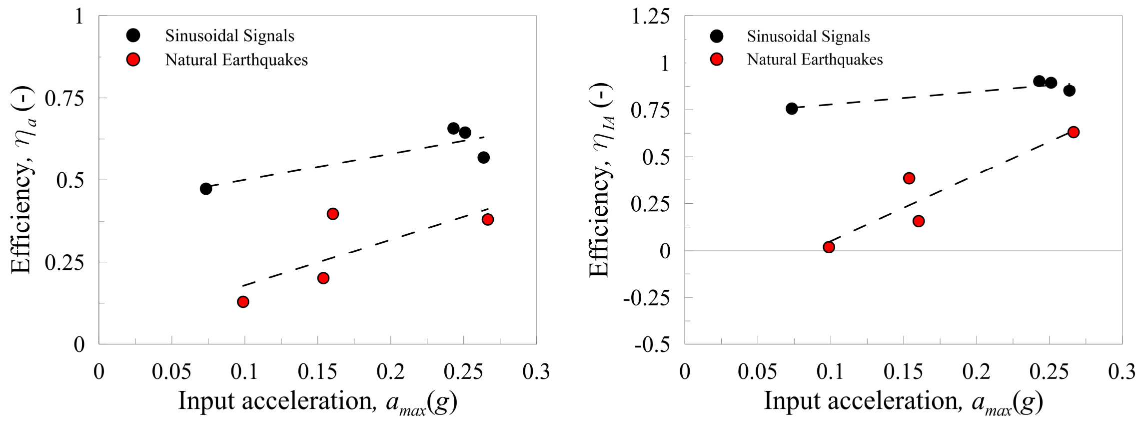

Figure 3. 70. Efficiency in terms of acceleration reduction (a) and IA reduction (b) for relative density of 85%.

A slight reduction in acceleration and *IA* efficiencies can be seen in the case of dense sand related to medium loose sand. As done in the case of medium loose sand, Figure 3. 71 shows the rotation-settlement behaviour of the foundations of the two buildings during the natural earthquakes.

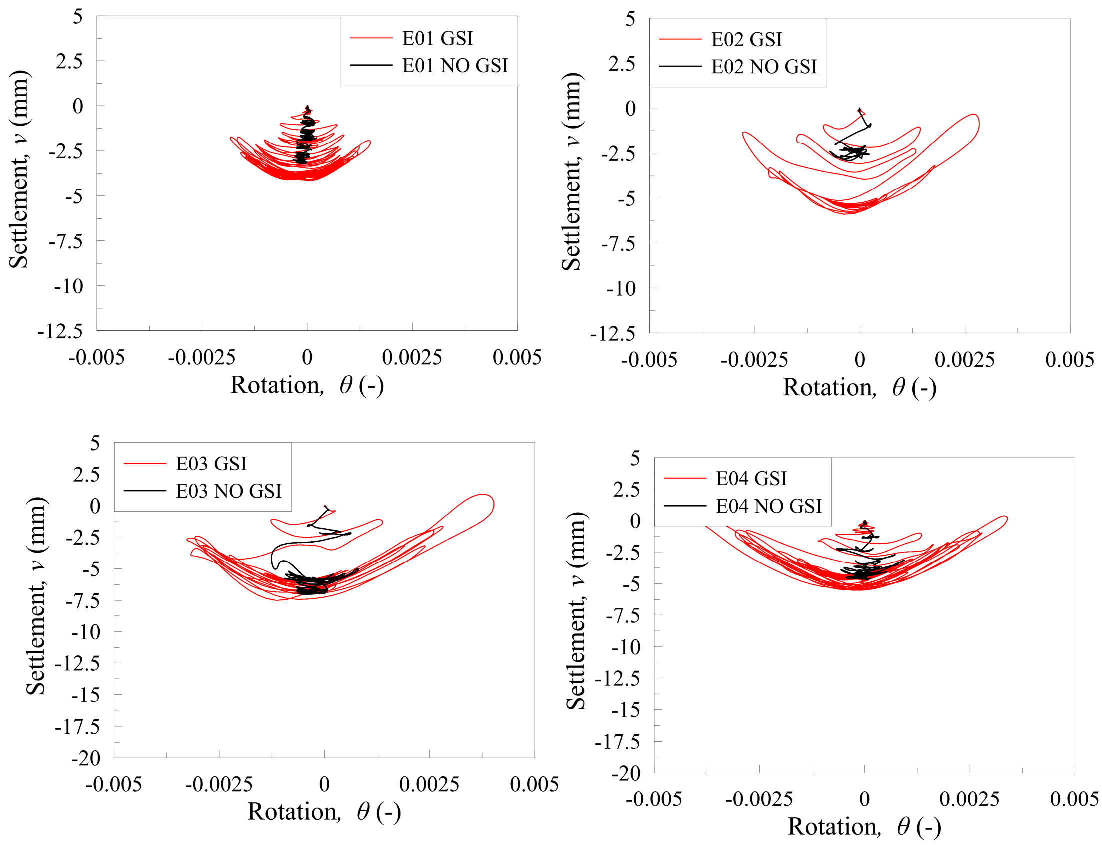

Figure 3. 71. Settlements-rotations behaviour for GSI and NO GSI structure in caso of 85% relative density.

Comparing Figure 3. 71 with Figure 3. 65 it is possible to see a slight reduction in overall global rotation and settlement in dense sand. This is due to the higher stiffness of the foundation soils, which reduces rotations in both structures. However, it should be pointed out that the increase in average soil stiffness in the significant volume of interest for the foundations (from 2.4m to 5m), with a relative density of 65% to 85%, is equal approximately to a 20% increase. The period elongation connected to the lateral disconnection increases with the ratio of structure to soil relative stiffness,$H_{str}/(Vs * T_{FB})$ (further details will be given in next paragrah). This dimensionless parameter is reduced by only 5% in the case of dense sand. This obviously justifies the fact that there are not very marked differences in the two cases.

At this point it is important to clarify the results found so far. The stiffness of the soil influences the period elongation and in particular, from the back-analysis, it results that the stiffer the soil, the lower the relative period elongations between the structure with and without lateral disconnection. The lateral disconnection technique bases its effectiveness precisely on its ability to distance the resonance period of the connected structure from the disconnected one. In this sense, the relative variation of the natural period between the two structures is the main form of efficiency of this technique. Small variations in period generated by this technique would not guarantee any particular form of advantage. On the contrary, in some cases just a 30%-40% natural period variation between the GSI and NO GSI structure can lead to significative benefits. However, depending on the seismic hazard, it is important to higlight that the lateral disconnection could be detrimental. Indeed, if the building with disconnected foundations has a natural period of vibration close to the peak of the acceleration spectrum there will be a worsening of the seismic vulnerability. It is therefore obvious that the effectiveness of this technique will depend not only on the ground and structural conditions in terms of stiffness and strength but also on the local seismic hazard. The results found thorught the numerical back analysis need to be further investigated since, as widely reported in the literature, it is not so much the stiffness of the soil as the relative structure to soil stiffness that influences the period elongation. This aspect open an important issue of the such thesis, namely “the influence of dimensionless parameters that control the effectivness of lateral disconnection”.

Before concentrating on this aspect, in the following section some information will be given about the reduction of static bearing capacity induced by lateral disconnection. Due to a number of theoretical aspects, later confirmed by analytical and numerical calculations, this aspect was considered to be of minor importance.

3.3.4. On the modification of static load bearing capacity and stability of cantilever walls.

In this small section, the calculation of the stability of the 4 cantilevel walls used to retain the soil during the centrifuge test and the variation of the bearing capacity of the foundations, following the lateral disconnection intervention, will be examined. In particular, the embedment of the cantilever walls was determined by simple stability calculations, using Blum’s method. In particular, the active earth pressure coefficient was computed using Rankine’s expression:

$$K_A = \frac{1 - \sin \varphi'}{1 + \sin \varphi'} \tag{3. 51}$$

and the passive earth pressure coefficient with the expression by Lancellotta (2002):

$$K_P = \frac{cos\delta}{1 - sin\varphi}\left[cos\delta + \sqrt{(sin\varphi')^2 - (sin\delta)^2}\right] e^{2\Theta tan\varphi'} \tag{3. 52}$$

where:

$$2\Theta = \sin^{-1}\left(\frac{sin\delta}{sin\varphi'}\right) \tag{3. 53}$$

With $\varphi' = 33°$ (friction angle at costant volume) and a friction angle at the interface between soil and wall, $\delta = \frac{\varphi'}{3} = 11°$. In these assumptions, an embedment depth equal to the retained height yields a safety factor against overturning, *F ≈ 1.5*.

Even in seismic conditions, a pseudo-static calculation carried out using a seismic coefficient $K_h = 0.25$ (corresponding to the strongest seismic signal applied to the model) and computing the active earth pressure coefficient with the theory by Monobe-Okabe (1926):

$$K_{AE} = \frac{\sin^2(\alpha + \varphi' - \psi)}{cos\psi \cdot \sin^2\alpha \cdot \sin(\alpha - \delta - \psi)\left[1 + \sqrt{\frac{\sin(\varphi' + \delta)\cdot\sin(\varphi' - i - \psi)}{\sin(\alpha - \delta - \psi)\cdot\sin(\alpha + i)}}\right]} \tag{3. 54}$$

and the passive earth pressure coefficient with the expression by Lancellotta (2007):

$$K_{PE} = \left[\frac{cos\delta}{\cos(i - \psi) - \sqrt{\sin^2\varphi' - \sin^2\delta)}} \times (cos\delta + \sqrt{\sin^2\varphi' - \sin^2\delta)}\right] e^{2\theta tan\varphi'} \tag{3. 55}$$

where:

$$2\theta = \sin^{-1}\left(\frac{sin\delta}{sin\varphi'}\right) + \sin^{-1}\left[\frac{\sin(i - \psi)}{sin\varphi'}\right] + \delta + (i - \psi) + 2\psi \tag{3. 56}$$

$\psi = \tan^{-1} K_h$, and i is the slope of the backfill, yields a safety factor against overturning just larger than 1, which proved sufficient to prevent the retaining plates from failing during seismic shaking.

Regarding the variation of the bearing capacity between the GSI and NO GSI structure, it should be noted that the 10 mm distance (0.6m at prototype scale) between the footings and the cantilever wall results from the compromise between practical aspects, such as *e.g.*, ease of placement of the model foundations, and geotechnical aspects, requiring limited removal of soil laterally to the foundations not to affect their bearing capacity. With reference to this last aspect, the Figure 3. 72 shows schematically a potential global collapse mechanism for a shallow foundation in sand (Vesic, 1973).

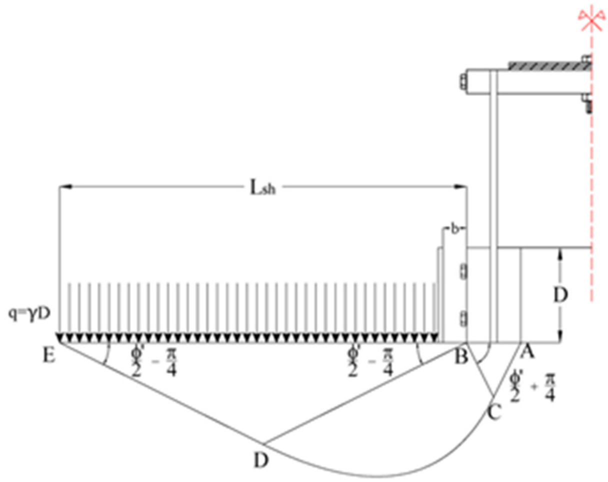

Figure 3. 72. Schematic representation of foundation collapse mechanism

The percentage reduction of the soil counterweight at foundation level due to the creation of the lateral disconnection can be computed as:

$$\frac{L_{sh} - b}{L_{sh}} \tag{3. 57}$$

where L_{sh} is the lateral extent of the global collapse mechanism and b is the width of the trench. Using a friction angle $\varphi' = 33°$, the corresponding computed reduction of bearing capacity (Terzaghi 1943) and safety factor are marginal, of the order of 6% (see Table 3. 22).

Table 3. 22. Value of the bearing capacity and static factor of safety for GSI and NO GSI foundation.

	φ' [°]	q [kPa]	q_{lim} [kPa]	FS [-]
GSI	33	133	1246	9.36
NO GSI	33	133	1326	9.96

To further investigate this last aspect, the laoding bearing capacity of both foundations (connected and disconnected) was also studied numerically. In particular, a force of increasing intensity was applied to both the foundations (Figure 3. 73) and consequently the displacements were obtained.

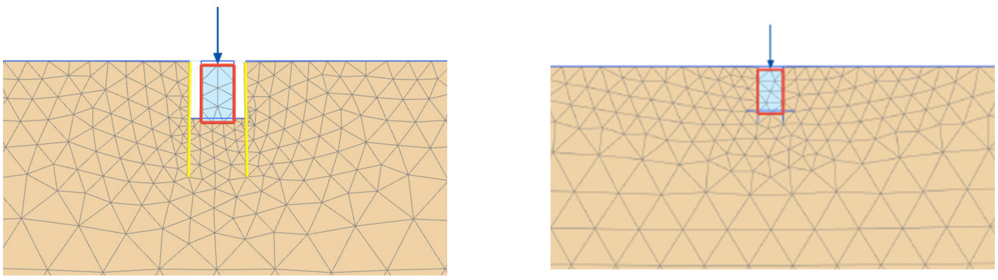

(a) (b)

Figure 3. 73. Numerical models to study the modification of vertical load static bearing capacity.

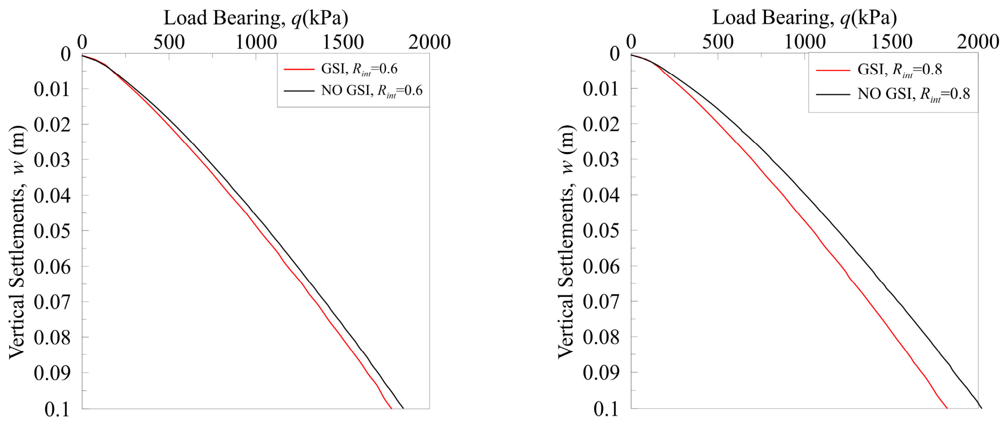

(a) (b)

Figure 3. 74. Vertical load-settlements behaviour in case of R_{int} =0.6 (a) and R_{int}=0.8 (b).

As can be seen from Figure 3. 74a the bearing capacity of the two foundations, connected and disconnected, differ by less than 10%. It can also be seen that the quality of the foundation-soil contact (which determines the value of R_{int}) influences the differences in the limit load between the two foundations (Figure 3. 74b). This is because, in the case of a poor foundation-soil contact (low value of R_{int} between *0.5* or *0.6*) the vertical tangential stresses at the foundation-soil interface have lower limit values and, therefore, the two bearing capacities values are more similar. However, it should be noted that, even in the case of perfect effective contact (R_{int} = 1), the value of the safety factor, for the disconnected foundation, is very high. Therefore, it is very unlikely that the lateral disconnection would compromise the static safety of a masonry building as the latter are generally characterised by very high safety factor values (FS>10).

3.4 A-dimensional factor controlling the lateral disconnection effectiveness

As shown in the paragraph 3.3.3, the lateral disconnection technique is more or less effective in lengthening the natural period of vibration depending on some significant dimensionless parameters. In this paragraph, through dimensional analysis, the main adimensional groups, governing the effect of lateral disconnection, were identified. This will clarify the circumstances where this intervention can generate significant anti-seismic benefits.

3.4.1. A brief introduction of Dimensional Anlysis

Dimensional analysis can provide a procedure for assessing the influence of the parameters of a system on its response, even if the equations connecting the parameters are not known. Dimensional analysis is widely applied for the design of experiments in several research fields (such as Idraulic, Astrophisic. ecc) because it can provide insight on the behavior of systems that require many parameters to be described. In particular the dimensional analysis can reduce the parameter space required to tune the system response by identifying how physical quantities relate to each other. The dimensionless response will then be a function of a set of dimensionless parameters. Such groups are found through the famous Buckingham's theorem. There is a vast literature concerning dimensional analysis, several books have been written from the mid-20th century until now (Langhar, 1951 ; Volker 2017). In the geotechnical field, however, dimensional analysis has not found much success. Kausel, for example, stated with regard to dimensional analysis in geotechnics:"*dimensional analysis can be of invaluable help in establishing the form of some physical phenomena, but it cannot guarantee that such formulas will be physically meaningfull.*".

In mathematical terms, a relationship between the response of a system, namely u, and the parameters and variables that influce such response can be expressed through the equation:

$$u = f(\bar{x}; \bar{q}) \text{ with } \bar{q} = (q_1, q_2, \dots, q_n)^T \text{ and } \bar{x} = (x_1, x_2, \dots, x_d)^T \quad (3.\ 58)$$

The vector $\bar{x}$ represents the independent variables of a system (e.g. in a dynamic problem the three spatial coordinates and time), $\bar{q}$ represents the n-physical parameters, and f represents a function that relate the response of the structure on these physical parameters and on the number *k* of these physical dimensions. For example, a kinematic problem can be expressed as a function of distance and time (*k*=2), a dynamic problem adds mass (*k*= 3). In order to use Buckinghma's theorem it is necessary to identify a dimensional basis; this basis is a set of k parameters (*i.e.* k elements in $\bar{q}$) whose physical units are independent of each other and can reproduce the physical units of all the parameters of the problem. Any physical unit of the problem can be hence generated through combinations of elements of the basis, and for each out-of-basis parameter one can obtain a combination of basis elements having the same physical unit, what is referred as its "characteristic value". The ratio between a parameter and its characteristic value yields a dimensionless (or nondimensional) group (of parameters), whereas the ratio between a variable and its characteristic value is likewise termed dimensionless variable. Assuming that the first *k* elements of the vector $\bar{q}$ are the dimensional basis, we will have that $\bar{q}_1, \bar{q}_2, \bar{q}_k$ are the dimensional basis and $\bar{q}_i$ is the first element that is not part of the basis. Returning to equation (3. 58), dividing by the characteristic value the left term, we will have the nondimensional term *U* istead of u. Since this term is dimensionless, so must be the terms on the right. The parameter space for this new equation will comprise $m = n - k$ dimensionless parameters. In mathematical terms this implies that:

$$U = \frac{u}{u_{ch}} = F(\bar{\pi}) \, with \, \bar{\pi} = (\Pi_1, \Pi_2, \dots, \Pi_m)^T \qquad (3.\ 59)$$

where $\bar{\pi}$ is the vector of m-dimensionless parameters constructed from the vector q of *n*-physical variables by solving $m = n - k$ dimensionless equations. The generic dimensionless group Π_i can be expressed by solving the following equation:

$$\Pi_i = \frac{(q_i)^{\alpha_i}}{(q_1)^{\alpha_1} \dots (q_1)^{\alpha_k}} \tag{3. 60}$$

The exponents α_i, $\alpha_1 \dots \alpha_k$ must ensure that the final result is a dimensionless group; for this reason these α may be integers or rational numbers. It can also be pointed out that adding a linearly dependent element (a combination of the original elements) to the $\bar{\pi}$ vector does not change the linear space that the vector span:

$$span(\Pi_1, \dots, \Pi_m) = span((\Pi_1, \dots, \Pi_m, \Pi_{m+1}) \tag{3. 61}$$

for *m+1* being a combination (product) of the other groups. Therefore, the new element can replace one of the *m* original elements of the basis and the span remains unaltered, as long as the new element does depend on the element it replaces. This property allows certain flexibility to consider nondimensional groups. Finally, the most important consideration when using dimensional analysis concerns the concept of *physically similar results*. If two systems differ because of the different terms composing the vector $\bar{q}$, but have identical terms composing the vector $\bar{\pi}$, then their nondimensional response will be identical. In this case the two systems are said to be *physically similar*. Thus, to better understand, the two different systems will have different realisations of equation (3. 58), but identical realisations of equation (3. 59).

3.4.2 Numerical and material model used in the dimensional analysis

Due to the fact that the application of dimensional analysis requires the identification of the physical variables that control the phenomenon being studied, it is preferable to first outline the geometrical as well as the material model adopted. The numerical analyses, aimed at identifying the natural period of vibration with soil-structure interaction, are conducted using the software Plaxis 2D. Figure 3. 75 generically shows the FEM model used.

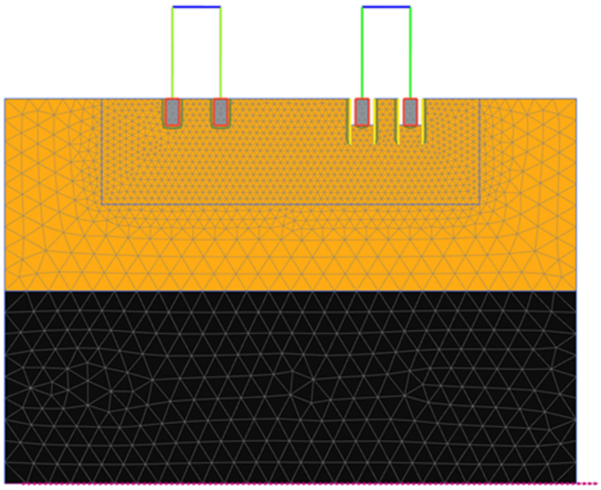

Figure 3. 75. Numerical model used to carry out the dimensional analysis

The two structural models, with and without lateral disconnection, were studied simultaneously within each analysis. The structural model used is a one-storey, one-bay building with discontinuous shallow foundations (*i.e.* SDOF system). The void generated by the lateral disconnection technique is supported by the presence of 4 small cantilevel walls, modelled as plate elements with very high lateral stiffness (*EI*), whose only task is to support the soil. The relative distance between the two structures and between the structures and the edges of the model, which is more than twice the width of the foundations, ensures that there is no interference. The columns and the beams of the structures are modelled as plate elastic elements. In order to generate the Grinter frames effect the structural crossbeam is characterised by a very high *EA* and *EI* (10^8kN/m and 10^9 kNm^2/m) values while the lateral stiffness of the columns is chosen, once the structural mass is fixed, to generate the desired structural period in fixed base condition. As the only objective of these analyses is to assess the period lengthening between the two structures, computing the soil-structure interaction, no internal damping is modelled in the frames. Therefore, only radiative damping will be present as an energy dissipation mechanism.

The soil is modelled as homogeneous visco-elastic as well as the structure. Since the depth of the bedrock is one of the parameters influencing the dynamic soil-foundation stiffness coefficients (Gazetas 1991), this was explicity modelled in the numerical model. The water table is not present.

The numerical procedure, to calculate the period elongation generated by the soil deformability on the two analysed structures, consists of several phases:

- In a static phase, application of an horizontal force on the roof of the two structures.
- In a dynamic phase, deactivation of the static force, and computation of the free oscillations generated.
- From the free oscillations, using the Fourier transform, it is possible to know the predominant period of the structure and therefore to know the period elongation with respect to the fixed base case $(\frac{\tilde{T}}{T_s})$.
- Finally it is possible to evaluate the relative period elongation between the two systems, with and without intervention, as: $\Delta = \frac{\tilde{T}_{disc} - \tilde{T}_{conn}}{\tilde{T}_{conn}}$; this value can be understood as an efficiency of the lateral disonnection.

As the free oscillations are produced by a static force applied within the mesh, it was preferred to use perfectly absorbent viscous contours on lateral boundaries (Lysmer and Kuhlemeyer, 1969).

3.4.3. Application of dimensional analysis on period elongation

As already stated, in order to delineate the dimensionless parameters that most influence the period lengthening produced by lateral disconnection, it is necessary to identify all the independent variables, q_i, as well as their physical dimensions able to influence it.

Parameters		Description of the variable
Variable	Dimension	
T_s	T	Fixed base period of the structure
H_s	L	Height of mass centroid in the first modal form for the fixed base structure
B	L	Width of single strip foundation

W	L	Base width of the building
D	L	Embedment of the foundation
d	L	Effective soil-foundation contact
m_s	ML^{-1}	Participating mass of the first modal form in plane cond.
v_f	-	Poisson coefficient of foundation material
p_t	ML^{-3}	Mass density of soil
p_f	ML^{-3}	Mass density of foundation
v_t	-	Possion coefficient of soil material
V_t	LT^{-1}	Shear waves velocity in the soil material
V_f	LT^{-1}	Shear waves velocity of the foundation material
H_b	L	Depth of the bedrock

The fundamental period of the structure, considering the soil-structure interaction ($\widetilde{T}$), can therefore be expressed as a function of the identified variables:

$$\widetilde{T} = f(T_s, H_s, B, W, D, d, m_s, v_f, p_t, p_f, v_t, V_t, V_f, H_b) \quad (3.62)$$

The number of variables identified is 14, while the number of independent units is 3 (mass, time, length). Therefore it would be possible to identify 14-3=11 dimensionless groups (Buckingham's Theorem). It is possible to identify the following dimensionless groups, using V_t, W, p_t as the dimensonally indipendent variable (dimensional base). It should be remembered that this choice is arbitrary and other bases can be chosen to obtain other significant dimensionless groups. A characteristic value for the resonance period of the structure is obviously given by the fixed base period T_s, so $U = \frac{\widetilde{T}}{T_s}$ is a dimensionless number representing the period elongation compared to the fixed base case. The dimensionless period lengthening, can, therefore, be expressed as a function of the following dimensionless parameters:

$$\frac{\widetilde{T}}{T_s} = f\left(\frac{T_s V_t}{W}, \frac{H_s}{W}, \frac{B}{W}, \frac{D}{W}, \frac{d}{W}, \frac{m_s}{p_t W^2}, \frac{p_f}{p_t}, v_f, v_t, \frac{V_f}{V_t}, \frac{H_b}{W}\right) \quad (3.63)$$

$$U = F(\Pi_1, \Pi_2, \Pi_3, \Pi_4, \Pi_5, \Pi_6, \Pi_7, \Pi_8, \Pi_9, \Pi_{10}, \Pi_{11}) \tag{3. 64}$$

As stated in Equation (3. 61), it is possible to manipulate these dimensionless groups, obtaining other dimensionless groups produced from the originals (for example, $\Pi_1' = \frac{\Pi_2}{\Pi_1} = \frac{H_s}{V_s T_s}$) . The following dimensionless groups, easier to understand, can be found:

$$\frac{\widetilde{T}}{T_s} = f\left(\frac{H_s}{V_t T_s}, \frac{H_s}{W}, \frac{B}{W}, \frac{D}{B}, \frac{d}{D}, \frac{m_s}{p_t W H_s}, \frac{p_f}{p_t}, v_f, v_t, \frac{V_f}{V_t}, \frac{H_b}{B}\right) \tag{3. 65}$$

At this point, it is appropriate to look briefly at each dimensionless parameter and explain its physical meaning:

- $\frac{H_s}{V_t T_s}$= is a very famous non-dimensional group representing the *structure-to-soil stiffness*. As mentioned in Chapter 2, the higher this parameter, the more the deformability of the soil influence the structure response.
- $\frac{H_s}{W}$ is the aspect ratio of the building.
- $\frac{B}{W}$ is the ratio between the width of the singular strip foundation and the widht of the building itself.
- $\frac{D}{B}$ is the ratio between the embedment of the foundation in the soil and the width of the singular strip foundation.
- $\frac{d}{D}$ is the ratio between the effective ground contact and the total embedmenet of the foundation.
- $\frac{m_s}{p_t W H_s}$ represents the ratio between the mass of the building in 2-D conditions and the mass of a characteristic volume of soil.
- $\frac{p_f}{p_t}$ is the ratio between the mass density of the foundation materia and the mass density of the soil material.
- v_f is the Poisson ratio of the foundation material.

- v_t is the Poisson ratio of the soil material.
- $\frac{V_f}{V_t}$ is the ratio between the ratio of the shear waves velocity in the soil and the shear waves velocoty in the foundation.
- $\frac{H_b}{B}$ is the ratio between the depth of the bedrock and the widht of the singular strip foundation.

The dimensionless period lengthening is therefore a function of 11 dimensionless parameters. It is obvious that an engineering problem governed by 11 dimensionless parameters is unmanageable and, for this reason, some of them will be neglected in the sensitivity analysis. For example, it is possible to neglect small variations in the Poisson's modulus of the soil considered (~ 0.2-0.3) and in the concrete of the foundation (~ 0.2), as these do not significantly affect the soil-structure interaction. Assuming infinitely stiff foundations, it is possible to neglect the parameter Π_{10} since it is much higher than unity in every possible scenario. It is possible to neglect the parameter Π_{11} because, except for particular cases of outcropping bedrock, this ratio is always higher than 10, as well as it is possible to neglect the variations of the parameter Π_7 because it rarely assumes values that are significantly different from unity. It is also possible to note that some of these parameters (i.e. Π_1, Π_6) coincide with those found by Veletsos (1974) and Bielak (1975) (respectively, structure-soil relative stiffness and structure to soil relative mass ratio).

3.4.4. Illustrative example and demonstration of physical similarity

Once the significant dimensionless parameters have been identified, in order to demonstrate the effectivness of the dimensionless groups found, it is possible to carry out parametrically similar numerical analyses. In particular, the following vector of dimensionless parameters has been fixed:

$$\pi = (\ 0.15, 0.85, 0.15, 1, 1, 0.24, 1.10, 0.2, 0.25, 20, 20) \qquad (3.\ 66)$$

Eight different numerical models with the same dimensionless parameters were therefore produced (Table 3. 23).

Table 3. 23. Numerical models made with identical dimensionless parameters but different physical dimensions.

Variables		Numerical models produced							
Name	Unit	I	II	III	IV	V	VI	VII	VIII
T_b	[s]	0.3	0.5	0.8	0.8	0.3	0.5	0.3	0.8
H_s	[m]	5.5	5.5	5.5	11	8.25	13.75	13.75	13.75
B	[m]	1	1	1	2	1.5	2.5	2.5	2.5
W	[m]	6.5	6.5	6.5	13	9.75	16.25	16.25	16.25
D	[m]	1	1	1	2	1.5	2.5	2.5	2.5
d	[m]	1	1	1	2	1.5	2.5	2.5	2.5
m_s	[kg]	16819	33639	61671	123343	25229	84097	42048	154179
v_f	-	0.2	0.2	0.2	0.2	0.2	0.2	0.2	0.2
p_t	[kg/m^3]	1911	3822	7008	3504	1274	1529	764	2803
p_f	[kg/m^3]	2102	4204	7708	3854	1401	1681	840	3083
v_t	-	0.25	0.25	0.25	0.25	0.25	0.25	0.25	0.25
V_t	[m/s]	122	73	44	91	183	183	305	114
V_f	[m/s]	2444	1466	916	1401	3666	3666	6111	2291
H_b	[m]	20	20	20	40	30	50	50	50

Table 3. 24 shows the value of the natural resonant period computing soil structure interaction for both structures while Figure 3. 76 shows the period lengthening related to the fixed base. Since the period variations between GSI and NO GSI structure and also the period elongation with respect to the fixed base case are practically identical in the 8 analyses, it is possible to state that the selected dimensionless parameters control the physical process analysed. It is important to underline that small discrepancies may be due to numerical aspects such as the axial stiffness of the columns which has not been included in the dimensionless parameter space.

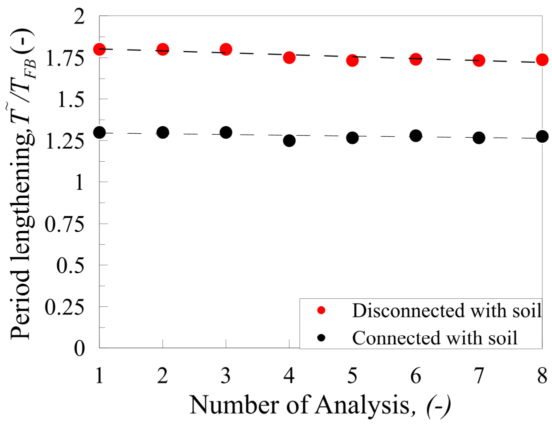

Figure 3. 76. Similar Period lengthening with dimensional analysis

Table 3. 24 Fundamental period values of the soil-structure system with indication of lateral disconnection efficiency

Numerical analysi [-]	$\tilde{T}_{disc}$ [s]	$\tilde{T}_{conn}$ [s]	$\Delta = \frac{\tilde{T}_{disc} - \tilde{T}_{conn}}{\tilde{T}_{conn}}$ [-]
I	0.54	0.39	0.38
II	0.9	0.65	0.38
III	1.44	1.04	0.38
IV	1.32	0.96	0.38
V	0.52	0.38	0.37
VI	0.87	0.64	0.36
VII	0.52	0.38	0.37
VIII	1.39	1.02	0.36

3.4.5. Sensitivity analysis

The previous paragraph has shown that the period variations between the two structures, with and without lateral disconnection, are the same as long as the dimensionless parameters are constant, confirming that in this case Buckingham's Theorem was correctly applied. In order to identify the most significant dimensionless parameters, it is possible to operate by varying each dimensionless parameter individually, and leaving the value of the others fixed (Figure 3. 77). In particular, each individual dimensionless parameter was varied up to a maximum of a 100%, increasing or decreasing, their initial value (see equation(3. 66) for the initial values). The graphs show the period variations between connected and disconnected structure (called Δ) for two different types of lateral disconnection interventions. The *"both sides"* case is the kind of lateral disconnection applied also in the centrifuge test and numerical back analysis. In this case, the disconnection occurs on both sides of the foundations (i.e. inside and outside the structure itself, on the left and on the right of each strip foundation). In the *"externally only"* case, on the other hand, the disconnection was generated only on the external side of the structure leaving the ground between the two adjacent foundations untouched. This solution has been introduced because it obviously represents a considerable technological simplification. For existing buildings, disconnecting the foundations even internally could be complicated but not impossible.

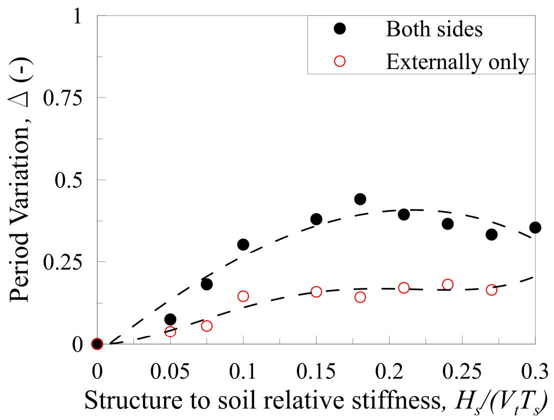

(a)

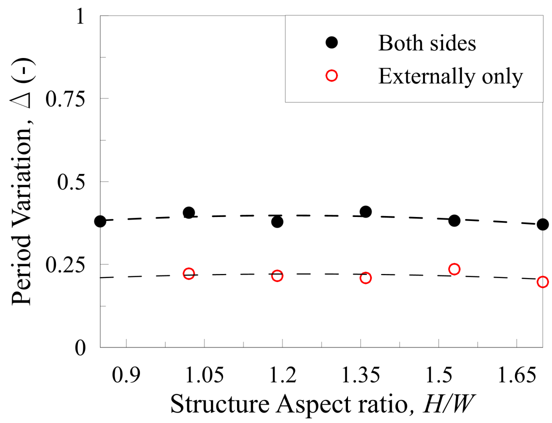

(b)

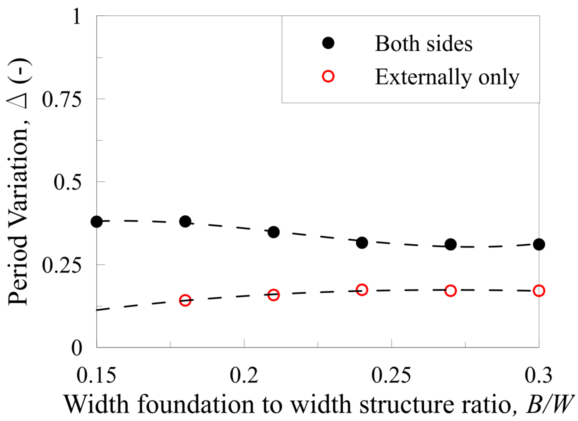

©

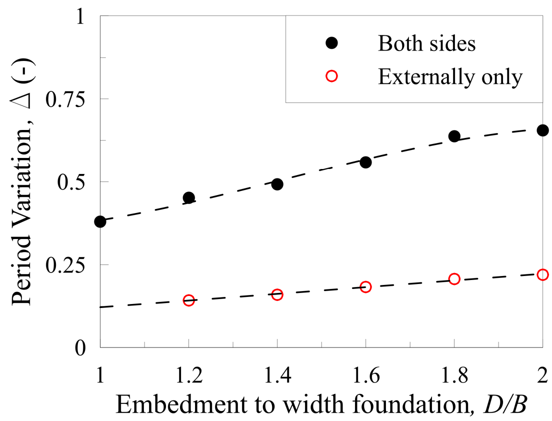

(d)

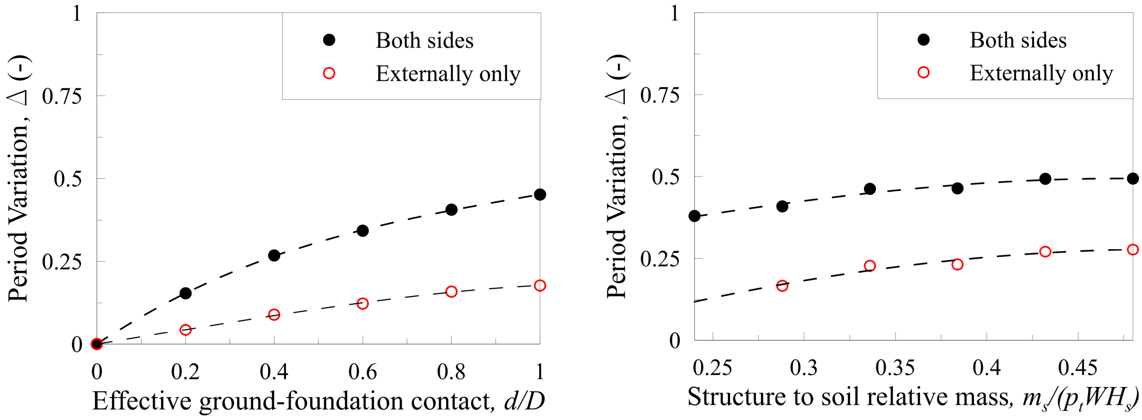

(e)

(f)

Figure 3. 77. Sensitivity analysis obtained by increasing or decreasing the dimensionless parameters up to a maximum of 100% of their initial value; (a) structure to soil stiffness ratio, (b) structure aspect ratio (c) width foundation to width structure ratio (d) Embedment to width foundation (e) Effective ground-foundation contact (f) Structure to soil relative mass

The graphs show that the disconnection generated only on the outer side of the structure, although easier to apply technologically, is less efficient than that on both sides of the foundations. For all dimensionless parameters, it is possible to state that the efficiency is almost halved if it is decided to operate only on the outer side of the foundations.

Some dimensionless parameters seem to have a relatively small influence on the period variations between the connected and disconnected structure. In particular, for the parameters Π_2, Π_3 the period variation trend seems to be almost independent from the variation of the dimensionless parameter considered (*i.e.* horizontal tangent). As far as the parameter Π_6 is concerned, i.e. the ratio between the mass of the structure and the mass of participating soil involved, a slight increase in the period variation can be observed as the parameter increases. This could indicate a greater efficiency of the technique for particularly massive structures related to the partecipating mass of soil.

In the engineering-significant range of 0.05-0.2 (NIST, 2012), the modification of the relative structure-soil stiffness (Figure 3. 77a) seems to significantly influence the period elongation between the two structures. In particular, the more rigid the structure is with respect to the soil, the more effective the disconnection will be. This is an interesting result since it is possible to understand that the applicability of this intervention, in contexts where the foundation soil is particularly rigid with respect to the structure, may be useless. This happens because the high stiffness of the soil below the foundations inhibits the global rotations of the structure more significantly than the lateral soil does and for this reason the two structures tend to have approximately the same period with and without intervention. Lateral disconnection, therefore, may give greater benefits, in terms of period extension, for rigid structures on deformable soils.

A further significant dimensionless parameter is the *D/B* ratio of the foundations. It is clear that this parameter affect a lot the effectivness of lateral disconnection. Very high values of this ratio indicate foundations with considerable embedment for which the removal of adjacent soil can have a significant effect. For values less than unity the relative period elongations are reduced and the lateral disconnection technique loses its effectiveness.

The effective lateral contact of the soil with respect to the total embedment (*d/D*) of the foundation is also particularly important. In fact, if for the connected structure the effective contact between the foundation and the ground is particularly low, the relative period variations were reduced. In case of *d/D*=0, indeed, there is zero lateral effective contact between the fondation and the ground and no period variations will be generate by the lateral disconnection. In general, the effective contact is never equal to unity (perfect contact *d/D*=1) but tends to be reduced by soil non linearities such as gapping.(Gazetas, 1991).

3.4.6. Parametric analysis on Lateral disconnection

From the dimensional and sensitivity analysis it was possible to reduce the number of variables in the problem connected to the elongation of period generated by the lateral disconnection. This is very important considering the labor that is required for the determination of a function. A function of one variable may be plotted as a single curve. A function of two variables is represented by a family curves (called a “chart”), one curve for each value of the second variable. A function of three variable is represented by a set of charts, one chart for each value of the third variable. A function of four variables is represented by a sets of charts, and so on. If, for example, five experimental points are required to plot a curve, twenty-five points are required to plot a chart of five curves, one hundred and twenty-five points are required to plot a set of five charts, etc. This situation quickly gets out of hand. The sensitivity analysis showed the importance of the different dimensionless groups keeping the value of others fixed. However, it is obvious that the value of the fixed parameters influences the period elongation to a greater or lesser extent. However, some dimensionless groups seem to have a very little influence on period lengthening between the GSI and NO GSI structure, and for this reason will be negletced in the following analysis. It was decided to focus on the reciprocal variations of the parameters Π_1, Π_4, Π_5 because, as suggested by sensitivity analisys, these parameters are the most important, governing the elongation of period between the NO GSI and GSI structure. It is clear that a slight influence of the other parameters will always be present (see Π_6 or Π_3 in Figure 3. 77), but this is very small compared to the three selected dimensionless groups. The structure to soil relative stiffness parameter, $\frac{H_s}{V_t T_s}$, was varied in the following range [0, 0.05, 0.1, 0.15, 0.2]. The $\frac{D}{B}$ parameter was varied in the following range [1.2, 1.4, 1.6, 1.8, 2]. The $\frac{d}{D}$ parameter was varied using the following vector [1, 0.6, 0.2]. A total number of 75 analyses was then performed.

Figure 3. 78 shows the period variations generated by the modification of the relative stiffness of the soil structure and the *D/B* ratio with a *d/D* value of 1.

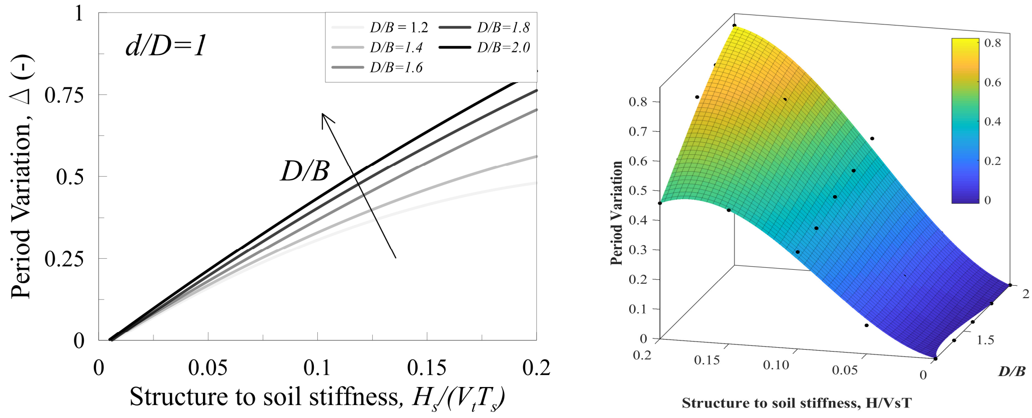

(a) (b)

Figure 3. 78 Changing structure to soil relative stiffness with embedment of foundation with a fixed value of effective ground contact (d/D=1); (a) two dimensional view, (b) tridimensional view.

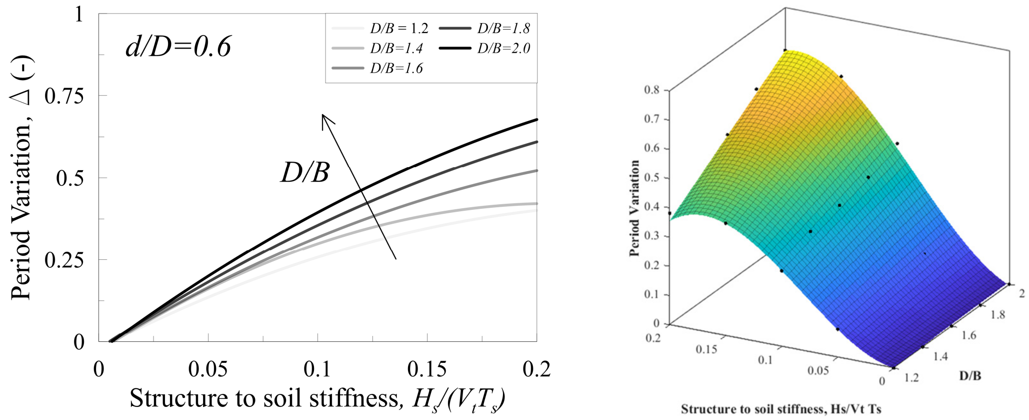

(a) (b)

Figure 3. 79. Changing structure to soil relative stiffness with embedment of foundation with a fixed value of effective ground contact (d/D=0.6); (a) two dimensional view, (b) tridimensional view.

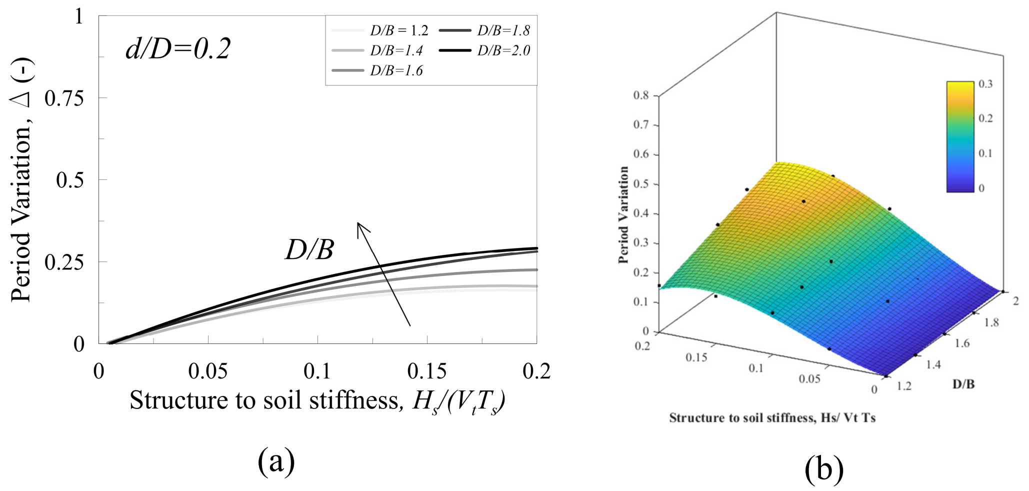

Figure 3. 80. Changing structure to soil relative stiffness with embedment of foundation with a fixed value of effective ground contact (d/D=0.2); (a) two dimensional view, (b) tridimensional view.

On the basis of these results, it is possible to introduce a very simplified formulation that makes it possible to estimate, in a preliminary way, the period increment that is able to determine the lateral disconnection on one bay one storey frame with two shallow strip foundations as function of $\frac{D}{B}$, $\frac{d}{D}$ and $\frac{H_s}{V_tT_s}$, under the assumption of visco-elastic soil:

$$\Delta = \frac{\tilde{T}_{disc} - \tilde{T}_{conn}}{\tilde{T}_{conn}} = \frac{d}{D}\left(0.13 \cdot \frac{D}{B} + 2.82 \cdot \frac{H_s}{V_tT_s} - 0.22\right) + 0.07 \cdot \frac{D}{B} + 0.61\frac{H_s}{V_tT_s} - 0.09 \qquad (3.\ 67)$$

In order to validate this formulation, the period elongations between GSI and NO GSI structure obtained in the 8 physically similar analyses (see Table 3. 24) were compared with those produced by the proposed simplified analytical formulation (Table 3. 25).

Table 3. 25. Comparison between the period elongations found in the visco-elastic finite element analysis and those obtained from the simplified formulation.

Numerical analysis	$\Delta_{num} = \frac{\tilde{T}_{disc} - \tilde{T}_{conn}}{\tilde{T}_{conn}}$ [-]	$\Delta_{ana} = \frac{\tilde{T}_{disc} - \tilde{T}_{conn}}{\tilde{T}_{conn}}$ [-]
I	0.38	0.40
II	0.38	0.40
III	0.38	0.40

IV	0.38	0.40
V	0.37	0.40
VI	0.36	0.40
VII	0.37	0.40
VIII	0.36	0.40

The comparisons between the period elongations found in the visco-elastic physically similar finite element analysis and those obtained from the simplified formulation shows a remarkable agreement. Certainly this formulation is affected by some semplification such as the use of a visco-elastic material model for the soil. However, with regard to primary non-linearities (i.e. those induced by the earthquake) it is possible to use an operational value of V_s determined by a local seismic response analysis in a significant volume of soil for the foundations, while with regard to secondary non-linearities (i.e. those induced by the soil-structure interaction such as gapping or sliding) it should be noted that they may only further increase this period increment value. In this sense, this formulation could only lead to an underestimation of the period increase and this would generally correspond to a cautelative procedure. Based on the local seismic hazard, if the estimated analytical elongation of period is sufficient to riduce seismic action, the effect of the disconnection could be be further investigated through non-linear analyses and complex numerical model.

3.5 Implementation of lateral disconnection on a real hazard scenario

In this chapter, a series of multiple real earthquakes have been selected considering a specific seismic hazard. These earthquakes were then applied to a single scenario to highlight the potentiality of such G.S.I technique.

3.5.1 Input motion Applied

The accelerograms were selected and scaled by using the software Rexel (Iervolino *et al.*, 2009) considering the Elastic Design Spectrum of L'Aquila centre (Italy) with a return period of 475 years. This value correspond to the life safety limit states as defined by the Italian Code (NTC, 2018). Since the earthquakes were selected on soil class A (rock) no deconvolution of the earthquakes is needed. Due to the fact that L'Aquila was one of the cities most devastated by earthquakes in the past, the frequency content and intensity of L'Aquila hazard was considered as a good reference to highlight the applicability of the proposed technique. All the informations about the selected earthquakes are reported in Table 3. 26 while Figure 3. 81 shows the spectra compatibility of L'Aquila design spectrum with the selected scaled earthquakes.

Table 3. 26. Main characteristics of the selected accelerograms, before scaled at the Aquila's PGA, for the earthquake analysis

Record (-)	Location (-)	Year (-)	M (-)	NERHP Site (-)	JB dist (km)	PGA (g)	Arias Intensity (m/s)
1	Campano Lucano	1980	6.9	A	25	0.06	0.06
2	Bingol	2003	6.3	A	14	0.51	1.99
3	South Iceland	2000	6.5	A	13	0.13	0.16
4	Mt. Vatnafjoll	1987	6.0	A	24	0.03	0.006
5	Golbasi	1986	6.0	A	29	0.03	0.01
6	Friuli	1976	6.5	A	23	0.35	0.79
7	South Iceland (aftershock)	2000	6.4	A	15	0.12	0.21

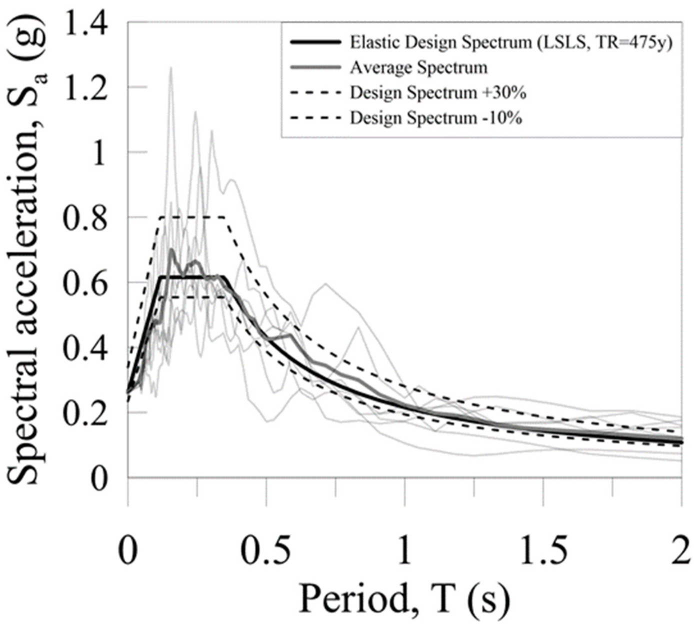

Figure 3. 81. Spectro compatibility of the selected earthquakes with elastic design spectrum of Aquila centre at life safety limit state.

3.5.2. Numerical Model

The structure is a linear elastic one bay one frame model laying on shallow strip foundations with a fixed base resonant period equal to 0.5sec. The foundations of the structures were modelled through the use of a non-porous linear elastic element volume with reinforced concrete properties (E=30000Mpa, v=0.2, γ=25kN/m3) while beam structural element were used to model the columns and crossbeams. The crossbeam length is equal to 5.00 meters while the distance between the strip shallow foundations (W) is equal to 6.36 meters. The SDOF model would represent the main dynamic and static properties of masonry structures. In particular, considering the Eurocode 8 formulation:

$$T_{\text{fixed\_base}} = C_{\text{t}} H^{0.75} \tag{3. 68}$$

where $T_{\text{fixed\_base}}$ is the fundamental period in seconds, H is the height of the building and $C_{\text{t}} = 0.05$ is a constant depending on the type of earthquake resistant structural system, it is possible to estimate the total height of the prototype structure and, assuming an interfloors height equal to 3meters, estimate the specific number of floors associated. Considering an unit load of 10kPa per floor it is possible to calculate the total mass to assign at the crossbeam and thus the stiffness of the column beam to ensure, respectively, the desired average bearing pressure on the soil and the fixed base period. The width of the strip footing shallow foundation (B) was fixed at 1.4 meter while the embedment of the foundation (D) was equal to 2.8m with a full effective contact d = 2.8m. Table 3. 27 shows all the properties of the modelled structure.

Table 3. 27. Parameters of the structures modelled

Parameter	Prototype
Nominal Bearing Pressure	150kPa
Foundations width	1.40m
Embedment foundation	2.80m
Natural frequency (fixed base)	2Hz
Superstructure Mass	30Mg/m

Foundation Mass	6.5Mg/m
Base Width	6.36m
Structural Height	9.5m
Geometrical Aspect Ratio	1.5
Lateral stiffness	4861 kN/m/m

Regarding the deformable soil, the properties of Hostun Sand were used. In particular, Hostun Sand was modelled using the material model defined in Plaxis as Hardening Soil Small Strain. The imposed relative density value for the investigated soil bank is Dr=65%. For this reason, the parameters given in Table 3. 18 and Table 3. 19 can also be used here. The numerical analysis were carried out by the use of the software Plaxis 2D. The finite element model is presented in Figure 3. 82.

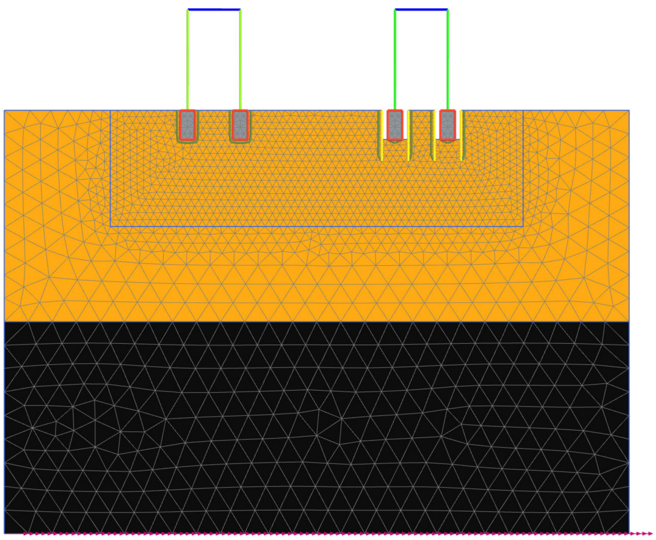

Figure 3. 82. Numerical model used to investigate the effectivness of lateral disconnection on real seismic hazard scenario

The model has a width dimension of 60m and a total depth of 40meters. The width of the deformable soil is fixed at 20meters while 20 meters of bedrock are included in the model to ensure no significative interference between the bottom base and the soil layer. The ground water is absent. Standard boundary conditions were applied during the initial (static) stage, that is zero horizontal displacements along the lateral boundaries and fixed nodes at the base of the grid. During the dynamic analysis, the seismic inputs were applied to the bottom nodes of the mesh. In order to take into account the finite stiffness of the underlying bedrock, and to reproduce the upward propagation of shear waves within a semi-infinite domain, the outcrop input accelerations were halved to compute the corresponding upward-propagating wave motion and applied to the bottom nodes together with adsorbing viscous dashpots. Free-field boundary conditions were applied along the lateral sides of the mesh. The element size of the soil has been taken always smaller than one-tenth of the wavelength associated with the highest frequency component of the input wave containing appreciable energy (Kuhlemeyer & Lysmer, 1973). For this reason, the discretization was carried out using 7872 tetrahedral elements with 15 nodes each. Both the structures, with and without the lateral disconnection, have been studied in the same numerical model. The relative distance between the two structures (13meter) and between the structures and lateral boundaries of the models (16meters) ensures no significant interaction.

3.5.3. Results and Interpretation

Figure 3. 83a represents the PGA profile with depth for the 7 spectrum compatible earthquakes. It can be seen that the maximum accelerations at the base of the structures vary from a minimum of 0.3g to a maximum of 0.4g between the different earthquakes. The first resonance frequency of the modelled soil bank, averaged over all investigated earthquakes, is about 3Hz.

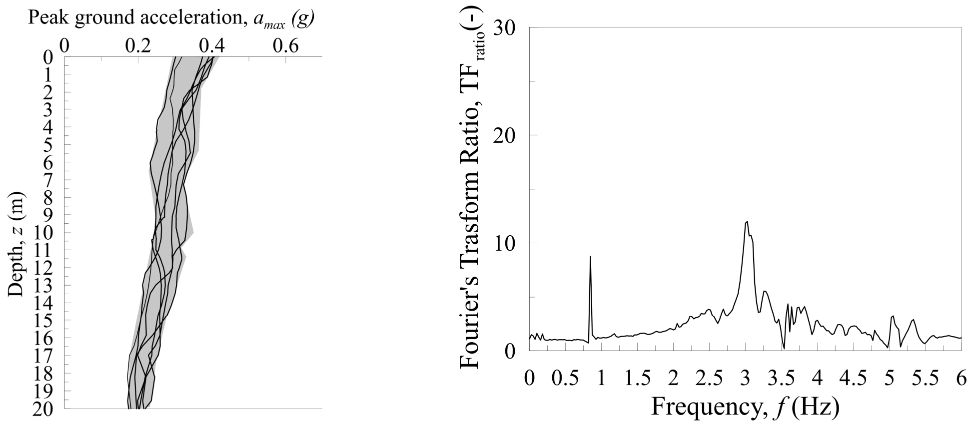

(a) (b)

Figure 3. 83. PGA amplification profile for 7 spectro compatible accelerograms, (b) mean amplification function between bottom base and surface of the model.

In order to highlight the variations in the resonance frequency of the two structures, generated by the lateral disconnection, during the different selected earthquakes, Figure 3. 84 represents the amplification function between the base of the two structures and the roof.

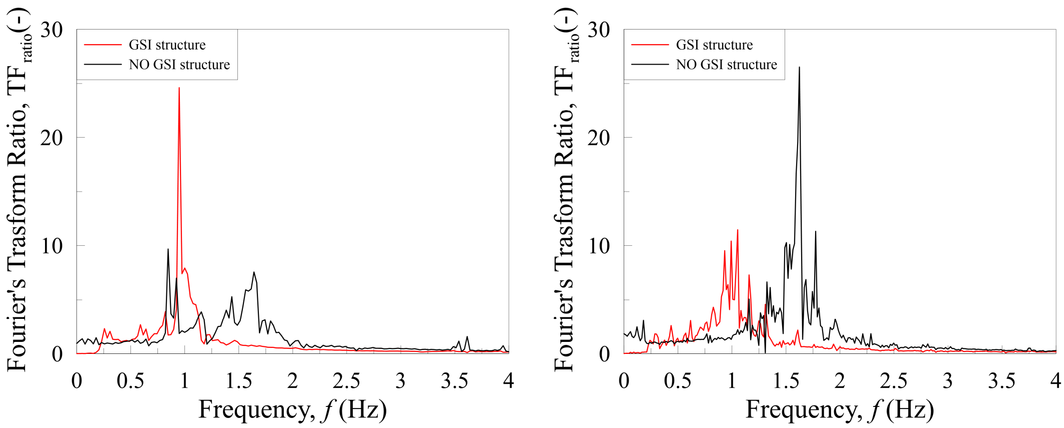

(a) (b)

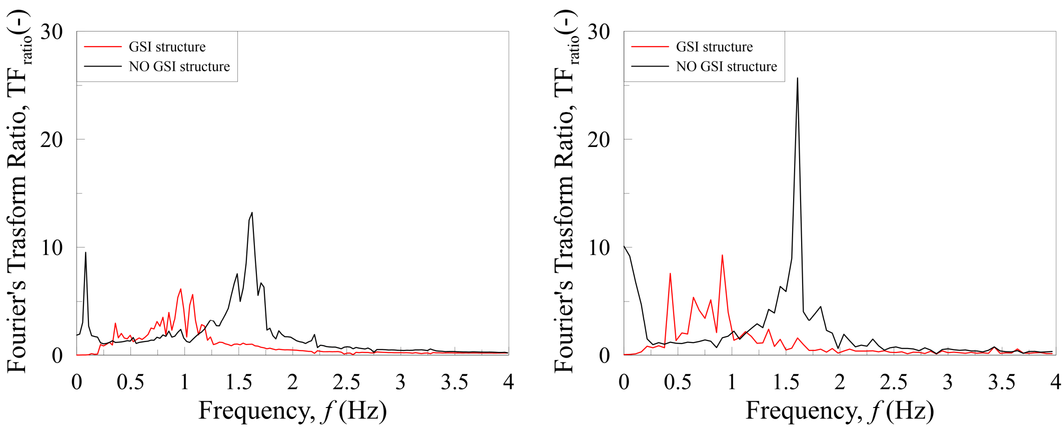

(c) (d)

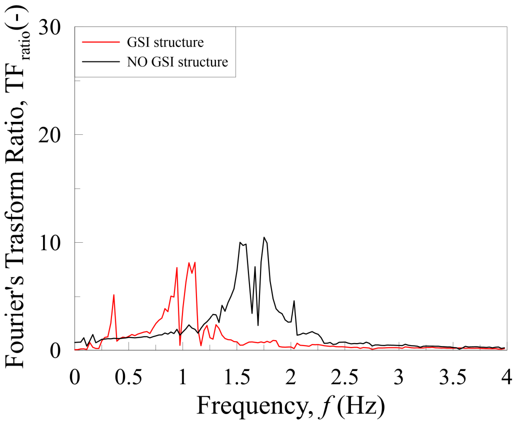

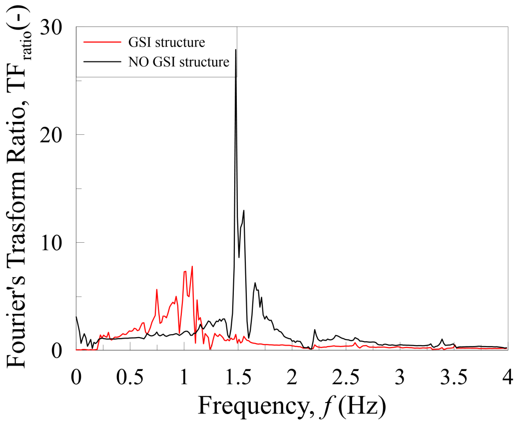

(e) (f)

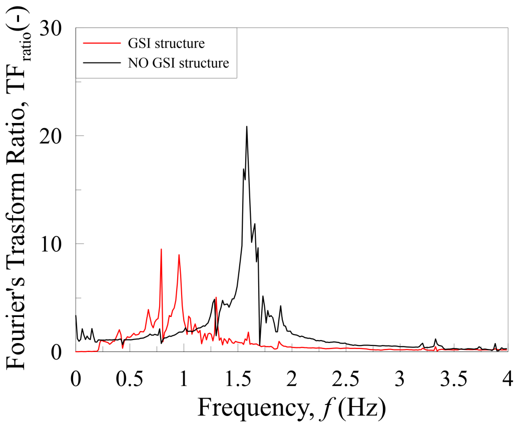

(g)

Figure 3. 84. Acceleration amplification function between the bottom base of the structures and the roof: (a) Bingol, (b) Campano Lucano, (c) Friuli, (d) Golbasi, (e) Mt. Fnajoll, (f) South Iceland, (g) South Iceland Aftershock

Disregarding small variations between the different earthquakes, it is possible identify the resonance frequency of the GSI structure (about 1Hz) and the one of the No GSI structure (about 1.6Hz) ($\Delta = \frac{\tilde{T}_{disc} - \tilde{T}_{conn}}{\tilde{T}_{conn}} = 0.6$). Using the simplified formulation (3. 67) with the parameters in Table 3. 27 and a reduced average value of the shear wave velocity roughly equal to 150m/s (estimated from the numerical analysis between 2.4metres and 5metres below the foundation) the period variation (Δ) is 0.52. As already mentioned, the analytical formulation tends to underestimate the period variation values by not taking into account the secondary non-linearities (gapping, sliding).

It is possible to use some synthetic parameters representing the efficiency of the disconnection technique such as the maximum accelerations (Figure 3. 85a), Arias Intensity (AI) (Figure 3. 85b), as well as mean structural displacements reduction efficiency (Equation (3. 20) (Figure 3. 85c).

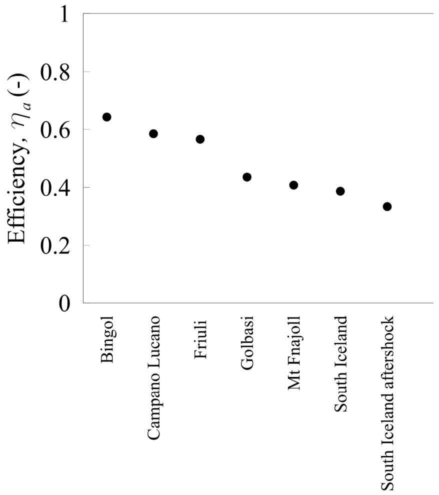

(a)

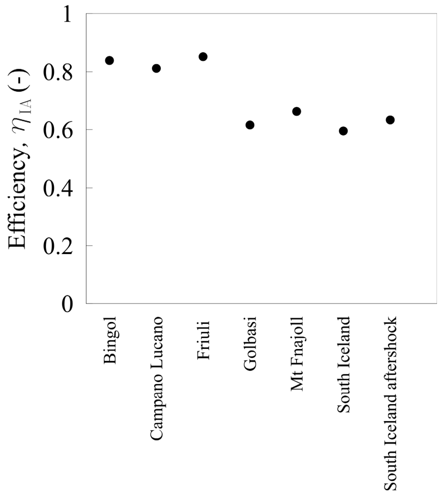

(b)

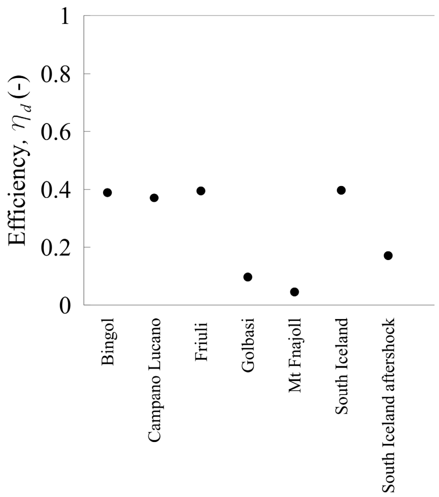

(c)

Figure 3. 85. Efficiency parameters for reduction of total accelerations (a), reduction of Arias Intensity (b), reduction of mean structural drifts (c).

References

Alpan, I. (1970). “The geotechnical properties of soils”. *Earth-Science Reviews*. **6**(5):49-62

Augenti, N., Parisi, F. (2019). Teoria e tecnica delle strutture in muratura. *Ulrico Hoepli Editore*

Benz, T. (2006). “Small-Small Stiffness of Soils and its Numerical Consequences*”. PhD Thesis,,* Institut für Geotechnik der Universitä, Stoccarda.

Bielak, J., (1975). “Dynamic behavior of structures with embedded foundations,” *Earthquake Engineering and Structural Dynamics*. 3:259-274.

Bolton, M. (1986). “The strength and dilatancy of sands”. *Geotechnique*, **36**(1):65-78.

Boussinesq J. (1885). “Application des potentiels à l’ètude de l’equilibre et du mouvement des solides elastiques”. Gauthier-Villard, Paris.

Brinkgreve, R. B. J., Engin, E., Swolfs, W. M. (2013). “PLAXIS 3D”. Reference Manual.

Brinkgreve, R. B. J., Kappert, M. H., Bonnier, P. G. (2007). Hysteretic damping in a small - strain stiffness model”. *Proceedings of Numerical Models in Geomechanic*s. NUMOG X, Rodi, Pande & Pietruszczak, Taylor & Francis Group, 737-742.

Brinkgreve, R.B.J., Swolfs, W.M., Engine, E. (2011). «PLAXIS user’s manual »

BS EN 1998-1. (2004). “Design of Structures for Earthquake Resistance”. Eurocode 8. 3:57.

Charles, J. A., Skinner, H.D. (2004). “Settlement and tilt of low-rise buildings”*. Proceedings of the Institution of Civil Engineers, Geotechnical Engineering* **157** (GE2), 65–75

Cremer, C., Pecker, A., Davenne, L. (2001). “Cyclic macro-element for soil-structure interaction: material and geometrical non-linearities”. *Int. J. Numer. Anal. Methods Geomech*. **25** :1257–1284.

D.M. 17.01.2018. Nuove Norme Tecniche per le Costruzioni.

Di Donna A., Ferrari A., Laloui L. (2016). “Experimental investigations of the soil–concrete interface: physical mechanisms, cyclic mobilization, and behaviour at different temperatures”. *Canadian Geotechnical Journal*. **53**(4): 659-672. https://doi.org/10.1139/cgj-2015-0294

Duncan, J. M., Chang, C. Y. (1970). “Nonlinear analysis of stress and strain in soil”. *Journal of the Soil Mechanics and Foundations Division*. **96**:1629-1653.

Flavigny, E., Desrues, J., Palayer, B. (1990). “Le sable d’Hostun”. *Revue Française de Géotechnique*. **53**:67–70.

Gajan, S., Kutter, B. (2008). “Capacity, settlement, and energy dissipation of shallow footings subjected to rocking”. *J. Geotech. Geoenviron. ASCE*. **134**(8):1129–1141.

Gazetas, G. (1991). “Formulas and charts for impedances of surface and embedded foundations”. *J Geotech Eng, ASCE*. **117**(9):1363–81.

Gerolymos, N., Gazetas, G. (2006). “Winkler model for lateral response of rigid caisson foundations in linear soil”. *Soil Dynamics and Earthquake Engineering*. **26**:347-361.

Ghosh, B., Madabhushi, G. (2002). “An efficient tool for measuring shear wave velocity in the centrifuge”. *Proc. Int. Conf. on Phys. Modelling in Geotechnics, R. Phillips, P. J. Guo, and R. Popescu, eds., Balkema, Rotterdam, Netherlands*. 119–124.

Hardin, B., Black, W. (1969). “Closure to vibration modulus of normally consolidated clays”. *J Soils Mechanics and Foundation Division ASCE.* **95**(6):1531-1537.

Hardin, B., Drnevich, V. (1972). “Shear modulus and damping in soils: measurement and parameter effects”. *J. Soil Mech. Found. Div. ASCE*. **98**(6):603–624.

Hardin, B.O., Black, W.L. (1968). “Vibration modulus of normally consolidated clay” *Journal of the Soil Mechanics and Foundation Division*. **94**(2):353-369.

Heron, C.M. (2013). “The dynamic soil structure interaction of shallow foundation on dry sand beds”. *PhD Thesis, University of Cambridge*.

Hoque, E., Tatsuoka, F. (2000). “Kinematic elasticity of granular material”. *ISRM International Symposium, Melbourne, Australia*.

Iervolino I., Galasso, C., Cosenza, E. (2009). REXEL: computer aided record selection for code-based seismic structural analysis. *Bulletin of Earthquake Engineering*. **8**:339-362. DOI 10.1007/s10518-009-9146-1

Jiang, X., Yan, Z. (1998). “Earthquake response analysis of building-foundation-building interaction system”. *Journal of vibration engineering*. **11**(1).

Kottke, A.R., Wang, X., Rathje, E.M. (2019). “Technical Manual for Strata”. *Geotechnical Engineering Center, University of Texas, Austin (USA)*.

Kuhlemeyer, R.L., Lysmer, J. (1973). “Finite Element Method Accuracy for Wave Propagation Problems”. *Journal of Soil Mechanics & Foundations*. *Div. ASCE.* **99**(5):421–427.

Kulhawy, F. H., Trautmann, C. H., Beech, J. F., O'Rourke, T. D., McGuire, W., Wood, W. A., Capano, C. (1983). “Transmission line structure foundations for uplift compression loading”. Final report. United States

Lancellotta, R. (2002). *Analytical solution of passive earth pressure*. Géotechnique, **52** (8), 617–619.

Lancellotta, R. (2007). *Lower-bound approach for seismic passive earth resistance*. Geotechnique **57** (3), 319–321.

Langhaar, H.L. (1951). “Dimensional analysis and theory of models”. *Wiley.* New York.

Lenza, P., Ghersi, A. (2011). Edifici in muratura. *Dario Flaccio Editore*

Madabhushi, G., Haigh, S.K., Houghton, N.E., Gould, E. (2012). “Development of a servo-hydraulic earthquake actuator for the Cambridge Turner beam centrifuge”. *International Journal of Physical Modelling in Geotechnics*. **12**(2):77-88. https://doi.org/10.1680/ijpmg.11.00013

Madabhushi, G., Houghton, N.E., Haigh, S. (2006). “A new automatic sand pourer for model preparation at University of Cambridge”. *6th Int. Conf. Physical Modelling in Geotechnics*. 217-222.

Masing, G., (1926).“Eigenspannugen und Verfestigung beim Messing“. *In: Proceedings of the 2nd International Congress of Applied Mechanics*. Zurich. **100**:332-335.

Mononobe, N., Matsuo, M. (1929). “On the Determination of Earth Pressures during Earthquakes”. *Proceedings World Engineering Congress*, **9**, 179-187.

National Institute of Standards and Technology (NIST). (2012). “Soil-structure interaction for building structures”. Report No. NIST GCR 12-917-21. Gaithersburg, MD, U.S.: Prepared for U.S. Department of Commerce.

Negro, P., Paolucci, R., Pedretti, S., Faccioli, E. (2000). “Large scale soil-structure interaction experiments on sand under cyclic loading”. *In 12th World Conference on Earthquake Engineering*.

Paolucci, R., Figini, R., Petrini, L., Vecchiotti, M. (2011). “Accounting for non-linear dynamic soil-structure-interaction in the displacement-based seismic design”. *In 5th International Conference on Earthquake Geotechnical Engineering, Santiago, Chile*.

Pender, M. (2010). “Integrated earthquake resistant design of structure-foundation systems”. *In 5th International Conference on Recent Advances in Geotechnical and Earthquake Engineering and Soil Dynamics*.

Robertson, P. Campanella, R. (1983). “Interpretation of cone penetration tests. part I: Sand”. *Can Geotech J.* **20**(4):718-33.

Roscoe, K. H, Burland, J. B. (1968). “On the generalized stress-strain behaviour of "wet" clay”. *In: Heyman & Leckie, Engineering Plasticity*, Cambridge Univeristy.

Rowe, P. W. (1962). “The stress - dilatancy relation for static equilibrium of an assembly of particles in contact”. *In: Proceedings of the Royal Society of London: a methematical, physical and engineering sciences*. **269**(1339):500-527.

Santos, J. A., Correia, A. G. (2001). “Reference threshold shear strain of soil. Its application to obtain a unique strain - dependent shear modulus curve for soil”. *Proceedings of the 15th International Conference on Soil Mechanics and Geotechnical Engineering*, Istanbul, Turchia. **1**:267-270.

Schneider, J.A., Lehane, B.M. (2006). “Effects of width for square centrifuge displacement piles in sand”. *Proc. 6th Int. Conf. Physical Modelling in Geotechnics*. **2**: 867–873

Schofield, A. N. (1980). “Cambridge geotechnical centrifuge operations”. *Géotechnique*. **30**(3):227–268.

Skempton A.W., Macdonald D.H. (1956). “The allowable settlements of buildings”. *Proceedings of the Institution of Civil Engineers*. **5**(6):727-768

Somma, F., Bilotta, E., Flora, A., Viggiani, G.M. (2021). “Centrifuge Modeling of Shallow Foundation Lateral Disconnection to Reduce Seismic Vulnerability”. *Journal of Geotechnical and Geoenvironmental Engineering.* ASCE. **148**(2). doi: 10.1061/(ASCE)GT.1943-5606.0002746

Steedman, R., Madhabushi, G. (1991). “Wave propagation in sand medium”. *In Proceedings of the 4th International Conference on Seismic Zonation. Earthquake Engineering Research Institute*.

Terzaghi K. (1943). “Theoretical Soil Mechanics”. *Wiley*, New York.

Trifunac, M.D., Brady, A.G. (1975). “A study of the duration of strong earthquake groundmotion”. *Bull. Seismol. Soc. Am*. **65**(3):581–626.

Tsang, H.H. (2009). “Geotechnical seismic isolation”. *Earthquake engineering: new research. Nova Science Publishers*. 55–87.

Veletsos, A.S., Meek, J.W. (1974). “Dynamic behavior of building-foundation systems”. *Earthq Eng Struct Dyn*. **3**(2):121-38.

Vesic A.,S. (1973). “Analysis of ultimate loads of shallow foundations”. *J. Soil Mech. Found*. **99** (1), 45-73.

Volker, S., Bernhard, W., Hassan, G. (2017). “Dimensional analysis for engineers”. *Springer*

4. SAP-SAND MIXTURE AS SEISMICALLY ISOLATING BARRIERS

In this chapter the technique called "*SAP-sand mixture as seismically isolating barriers*" will be studied by means of experimental, numerical and analytical approach.

4.1 Introduction

Seismic isolation with traditional structural techniques is hardly implementable on existing structures. Recent results have shown that if a continuous barrier having a low dynamic impedance is created in the soil beneath the structure, both the absolute acceleration and structural displacement demands are significantly reduced without any direct intervention on the structure itself. Since seismic hazard depends, among other factors, on the deformability of the soil underlying the structure, an artificial modification of the mechanical properties of this part of the subsoil may be used to properly modify the seismic structural demand. The use of soft or stiff anti-seismic thin barriers in the ground was first investigated by Kirtas (Kirtas *et al*. 2009; Kirtas *et al*. 2009) and later considered by other authors. In particular, Nappa *et al*. (2016) and Flora *et al*. (2018) studied soft buried barriers having different geometrical schemes, analysing their behaviour through centrifuge tests and numerical modelling (Figure 4. 1a). The most effective anti-seismically scheme consists in the creation of a lower horizontal layer having reduced shear stiffness and four lateral vertical barriers having reduced normal stiffness (Figure 4. 1b).

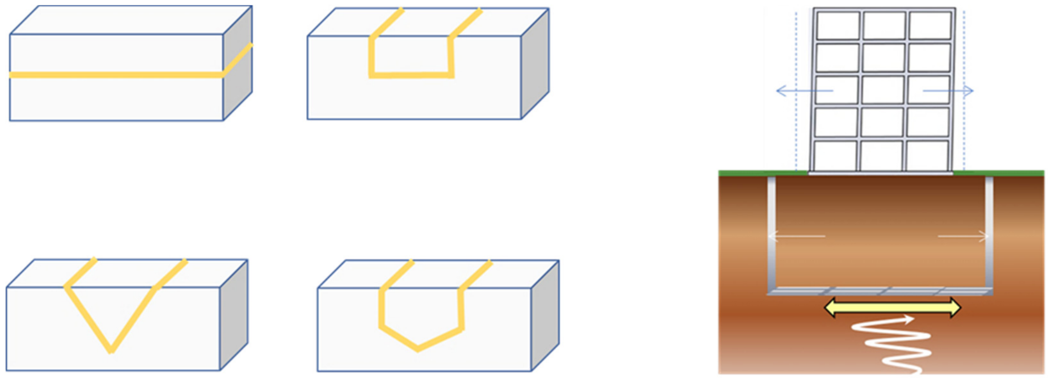

(a) (b)

Figure 4. 1. Geotechnical Seismic Isolation schemes using soft barriers: (a) different geometric layouts; (b) Schematic view of the layout with a base horizontal layer and side vertical ones (soft caisson).

In such a way, the bounded mass of soil may be added to that of the foundation, contributing, along with the reduced stiffness of the bounding soft barrier, to the system period elongation. Among other possible technologies, the use of Super Absorbent Polymers (SAP), for the creation of the base soft layer, is attractive. SAP is a granular material whose grains have the capacity of retaining huge amounts of water, becoming highly deformable jelly balls when hydrated (Figure 4. 2b).

(a) (b)

Figure 4. 2. Super absorbing polymer: (a) SAP in the dry/powder state; (b) hydrated SAP

Different kinds of SAP exist, depending on the use for which they are conceived. In fact, their capacity to absorb and retain water can be engineered. Being environmentally friendly, for instance, they are often used in agriculture to slowly release water. In the application considered in this research (and only in the case of applications over the ground water level), SAP has to be engineered to release water at the slowest possible rate, in order to keep, for the longest possible time, its peculiar jelly-like behaviour, that implies an extremely low shear stiffness (in the extreme case of a 100% SAP assembly, the mechanical behaviour tends to that of water, and thus the shear stiffness reduces to extremely low values). In any case, rehydration is extremely simple to perform on site, thus making the engineering use of this material feasible and reliable. The present chapter starts with an in-depth examination of the dynamic properties of SAP-sand mixtures through laboratory tests.

4.2 Experimental characterization of SAP-Sand Mixture

Due to the low shear stiffness of the sand-SAP mixture, the shear strains developed in the soft barrier during a seismic event are expected to be very high. For this reason, the dynamic characterization of these mixtures was carried out in a wide strain range: at very small strain levels, shear stiffness was explored with bender elements (*BE*) under isotropic confining conditions; at high or very high shear strain levels cyclic simple shear (*CSS*) tests were used to investigate the non-linear behaviour of the analysed mixtures. The shear modulus reduction and damping curves have been identified for different percentages of SAP in the SAP-sand mixtures, considering also the reference case of pure sand (*i.e.* SAP=0%), which was investigated through a resonant column (*RC*) test.

Even though *BE* tests are common, their interpretation is still a matter of discussion. Many authors have dealt with the difficulties of the interpretation of results (Viggiani and Atkinson 1995; Brignoli *et al.* 1996; Jovičić *et al.* 1996; Arulnathan *et al.* 1998; Greening *et al.* 2003; Greening and Nash 2004; Leong *et al.* 2005). Near-field effects (Sánchez-Salinero *et al.* 1986, Mancuso *et al.*, 1989; Pennington, 1999), transducer resonance and overshooting (Jovičić 2004; Lee and Santamarina 2005), electrical noise and grounding/shielding issues (Brignoli *et al.*, 1996; Lee and Santamarina 2005) can significantly affect the first arrival of the shear (S) waves at the receiver. Indeed, there is no consolidated procedure to interpretate BE tests in literature yet, and whatever procedure is adopted, some degree of judgment is required (Da Fonseca *et al.* 2009).

The interpretation of *CSS* and *RC* tests is straighter forward (e.g., Hardin and Drnerich, 1972). A critical aspect of the interpretation of cyclic tests at large strains (>1%) is that, often, the shear hysteretic loops are not symmetric. This has no specific effect on the peak to peak secant shear modulus, while it largely affects the value of the damping ratio, whose value is conventionally quantified using standard formulations based on the assumption of symmetric loops (e.g. ASTM- D3999). If the true shape is far from being symmetric, the conventional damping formulation can lead to an overestimation of the damping ratio. Then new formulations must be used (Kumar *et al.*2018, ASTM D5311–11), as will be shown in the following.

The primary purpose of this laboratory investigation is to have a detailed characterization of the dynamic behaviour of SAP-sand mixtures, to be used in the evaluation of the seismic performance of soft buried barriers as GSI systems. Since previously published numerical analyses (Flora *et al.* 2018) were carried out in the simplified hypothesis of a linearly elastic behaviour of the soft barriers with no damping, it is expected that the new experimental results presented in this paper will allow the use of more sophisticated material models and therefore more refined analyses, thus leading to more realistic predictions of GSI systems created with SAP-sand mixtures.

4.2.1. Material charateristics and specimen preparation

The sand used in this study is Hostun HN31 sand, with specific gravity G_s = 2.65, maximum and minimum void ratio $e_{max} = 1.011$ and $e_{min} = 0.555$, and critical state friction angle $\varphi_{cv} = 33°$ (Flavigny *et al.*, 1990). The Hostun Sand is made by high siliceous amount (SiO_2 >98%) and, as it is possible to see by optical microscope image, the grain shape varies from angular to sub-angular (Figure 4. 3a) The grain size distribution (Figure 4. 3b) confirms that it is a medium-fine sand with a uniformity coefficient (*Cu*) equal to 1.3.

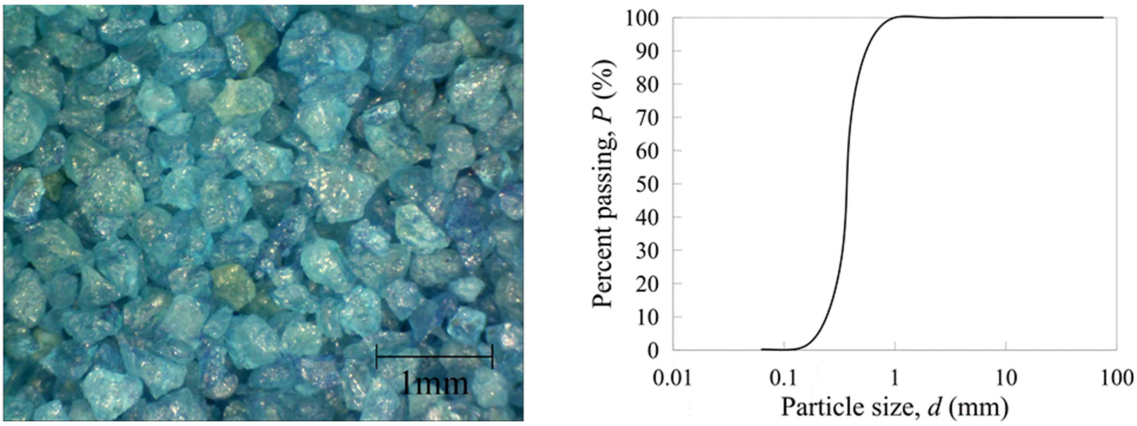

(a) (b)

Figure 4. 3. Physical properties of Hostun Sand: (a) picture with an optical microscope; (b) grain size distribution.

As previously shortly mentioned, SAP is a synthetic powder material. The one used in this research is able to absorb distilled water up to 240 times (1:240) his own initial weight.

In the physical identification of SAP-sand mixtures and in the interpretation of the experimental results, the following assumptions were made:

1. the sand grains have infinite shear and bulk stiffness. Thus, they neither change their volume nor their shape during shearing, and the volumetric changes of the pure sand samples are only a consequence of particles re-arrangements;

2. After hydration, SAP particles are incompressible (i.e. have an extremely high bulk stiffness) but can easily change shape (i.e. have a very low shear stiffness);

3. SAP-sand mixtures have a homogeneous spatial distribution of SAP particles (as shown in the following, the consistency of this hypothesis depends on the size of the SAP grains which in turn depends on the amount of hydration);

The effect of mixing sand and SAP largely depends on the relative amounts. For low percentages of SAP, it is expected that the grains tend not to become part of the micromechanical structure of mixture, and can be seen as essentially filling the existing voids. Because of this, when in low percentages, SAP can be expected to have a minor effect on shear stiffness. Theoretically, the maximum volume of SAP to be added to have the above-mentioned behavior (*i.e.* only filling the voids) is equal to the volume of the voids themselves. Likely, it will be a lower volume, as it is physically impossible that the SAP particles arrange in this very peculiar pattern.

For percentages of SAP higher than this limit, its grains inevitably take part to the mixture microstructure, thus modifying significantly the stress chains properties. As a consequence, a much more relevant effect is expected in terms of shear stiffness decrease and damping ratio increase.

The relative density selected in this study for the sand is D_r=0.7, corresponding in this case to a void ratio e=0.69. Figure 4. 4 summarizes the different compositions of the SAP-sand mixtures studied in this work, where SAPXX indicates the percentage of SAP by volume with respect to the total volume.

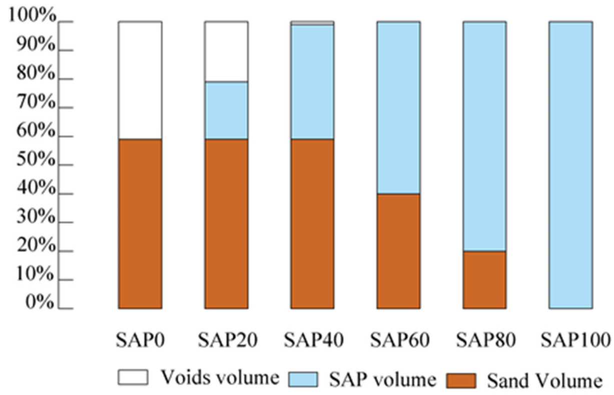

Figure 4. 4. Scheme of volume percentage of SAP for each studied specimen.

Table 1 summarizes the dynamic tests carried out for each SAP-sand mixture. In particular, *BE* tests were carried out at confining pressures of 10, 55, 150 kPa, while the *CSS* and the *RC* tests were carried out only for a confining stress of 55kPa. In order to understand the influence of the hydration percentage of SAP on dynamic mixture properties, the *BE* test at 55 kPa of confining pressure was carried out twice, once using a hydration ratio of 1:150 (smaller SAP grains) and once of 1:240 (bigger SAP grains). In all the other cases the SAP hydration ratio was fixed to 1:150.

Table 4. 1. Summary of tests carried out on different SAP-sand mixtures.

SAP-sand mixture	% SAP by volume (%)	B.E. tests	C.S.S. tests	R.C. test
Sand	0	•		•
SAP40	40	•	•	
SAP60	60	•	•	
SAP80	80	•	•	
SAP100	100	•		

4.2.1 Bender element (*BE*) tests

The bender element tests were carried out in a conventional triaxial cell (Figure 4. 5).

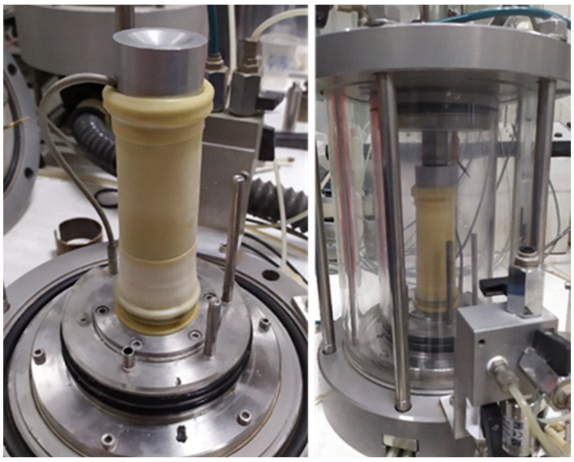

Figure 4. 5. Bender element triaxial cell used.

Reconstituted specimens, 38mm in diameter and 76mm high, were prepared inside the triaxial cell by constipation of the sand-SAP mixtures by using a split mold. The bender elements protrude 1.5 mm into each end of the specimen. For this reason, the effective length of the specimen, to be used in the evaluation of shear waves velocity, has been computed as the difference between the total length of the specimen after the consolidation and two times the bender element length protruding inside the sample. In order to have a clear reading of the single sine wave's arrive at the receiver, each test was performed following three simple rules:

1) swiping the input sine waves pulse frequency to maximize the output amplitude, which happens in correspondence of the resonant shear frequency of the specimens.

2) avoiding electrical crosstalk due to electromagnetic coupling through the soil.

3) avoiding near field effects using a ratio $n = L/\lambda$ between 2 and 9 (Wang *et al.* 2007, Lee *et al.* 2005), where L is the effective length of the sample and λ is the wavelength of the sine pulse.

A low pass filter was used to clean the signal trace from annoying high frequencies, having care of not modifying the output Fourier Spectrum. The travel time of the shear waves in the specimen was obtained by using a Cross

Correlation (*C.C.*) procedure (Viggiani, 1995) between the transmitter (input) and the receiver (output) signal track. The estimated travel time was then compared with the time distance between the input and the first, second and third deflection of the output. In most cases, the *C.C.* travel time corresponds to the time delay between the start of input and the second deflection of the output signal track, confirming the indications by Brignoli *et al.* (1996) and Viggiani *et al.* (1995). Figure 4. 6 shows the input and output signal traces as the input frequency changes with 1:240 hydrated SAP, while in Figure 4. 7 the SAP was hydrated at 1:150; in both cases, an isotropic confining pressure of 55 kPa was applied.

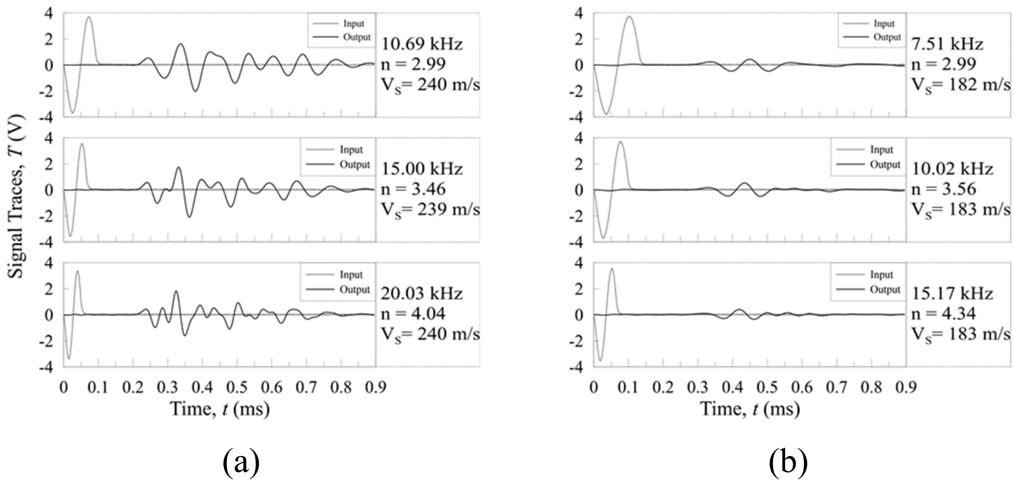

Figure 4. 6. – Input and output signal track with SAP hydration ratio equal to 1:240 at a confining pressure of 55kPa with indication of the input frequency, $n = \frac{L}{\lambda}$ *and* V_s*: (a) SAP40 and (b) SAP60.*

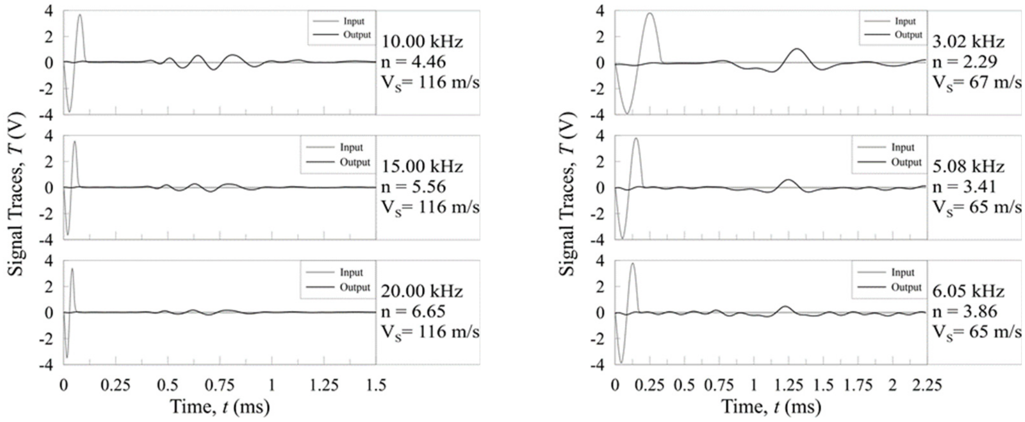

(a) (b)

Figure 4. 7. Input and output signal track with SAP hydration ratio equal to 1:150 at a confining pressure of 55kPa with indication of the input frequency, $n = \frac{L}{\lambda}$ *and* V_s*: (a) SAP40 and (b) SAP60.*

As expected, the higher the percentage of SAP, the lower the shear wave velocity in the sample. Interpreting the results of all *BE* tests, the value of shear waves velocity could be expressed as a function of the SAP percentage in the specimen. The following best fitting correlation results in this case:

$$V_s = V_{s,0} * \frac{1}{1+\left(\frac{SAP\%}{A}\right)^B} \quad (4.\ 1)$$

where $V_{s,0}$ is the shear waves velocity of the pure sand, at the considered confining pressure, $SAP\%$ is the volume percentage of SAP in the mixture, *A* and *B* are non-dimensional coefficients that depend on the confining cell pressure and have been evaluated by best fitting using as non-linear least square method.

Figure 4. 8a shows the shear waves velocity reduction as a function of the SAP percentage at 55kPa of confining pressure with SAP hydration ratio equal to 1:240, while Figure 4. 8b shows the different value of V_s at 10, 55, 150 kPa of confining pressure with hydration ratio equal to 1:150.

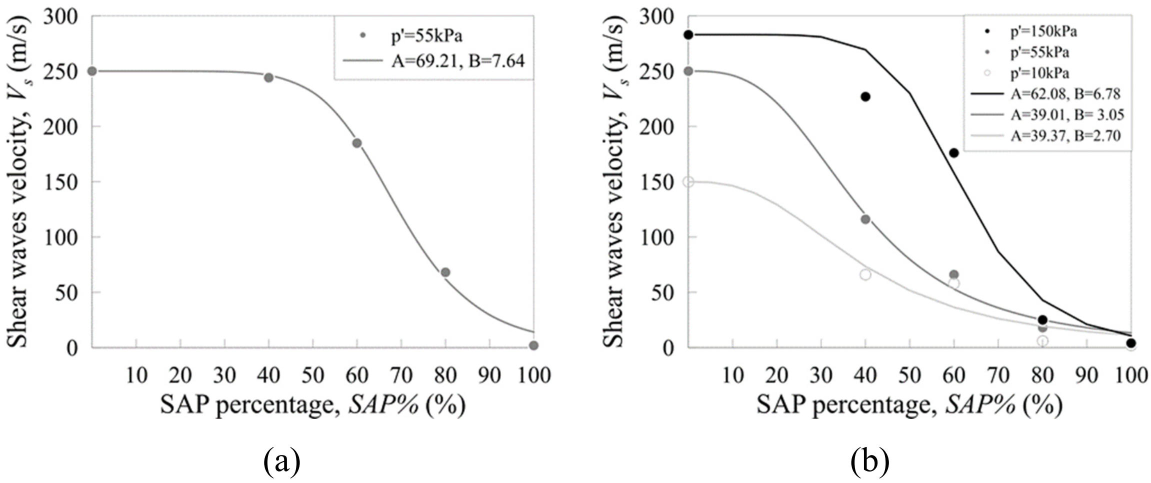

Figure 4. 8. Shear waves velocity reduction as function of the SAP percentage: (a) Confining pressure equal to 55kPa, and hydration ratio 1:240; (b) Confining pressure equal to 10, 55, 150 kPa and hydration ratio 1:150.

The results clearly highlight the role of SAP in reducing the shear stiffness of the mixture. Especially for high SAP content (>60%), the reduction of the shear wave velocity is very high (>70% on average). Comparing the curves regarding differently hydrated SAP (1: 240-1: 150), at a confinement pressure of 55kPa, it is also possible to see a different behaviour of the shear waves velocity reduction curve. In particular, for a less hydrated SAP (1:150), at SAP percentage of 40%, the shear waves velocity has already significantly decreased, while for the mixture with more hydrated SAP (1:240) and the same percentage, it is still almost equal to that of clean sand. This can be explained, from a micromechanical point of view, by considering that a more hydrated SAP, with the same overall volume of polymer introduced into the soil, is made by a lower number of bigger particles, thus resulting in a less homogeneous micromechanical fabric; conversely, a less hydrated SAP will have smaller and more uniformly diffused particles within the soil. In this latter case, therefore, the SAP particles will likely be able to break the shear stress chains more effectively. Even though this effect of hydration is general, its quantitative effect is strictly related to the kind of SAP and sand used, and thus cannot be generalized. Figure 4. 9 reports a schematic representation of this micromechanical interpretation.

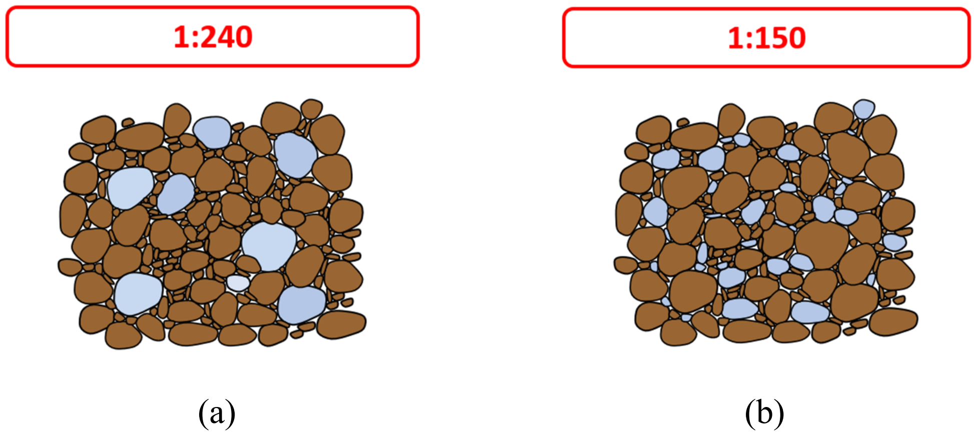

Figure 4. 9. Schematic drawing of the SAP-soil mixture with different hydration ratios at the same overall percentage: (a) high hydration raio (1:240) with SAP particles as isolated inclusions; (b) low hydration ratio (1:150) with SAP particles more homogeneously distributed within the mixture mass.

As already mentioned, the non-dimensional coefficients *A* and *B* depend on the confinement pressure. By evaluating these coefficients for three different confining pressures, the following best fitting general expressions of A and B as functions of the confining stress p' (Figure 4. 10) are herein proposed:

$$A = 40.4 - 12.4\left(\frac{p'}{p_{ref}}\right) + 17.9\left(\frac{p'}{p_{ref}}\right)^2 \tag{4. 2}$$

$$B = 2.74 - 0.68\left(\frac{p'}{p_{ref}}\right) + 2.25\left(\frac{p'}{p_{ref}}\right)^2 \tag{4. 3}$$

where p_{ref} is equal to *100kPa.*

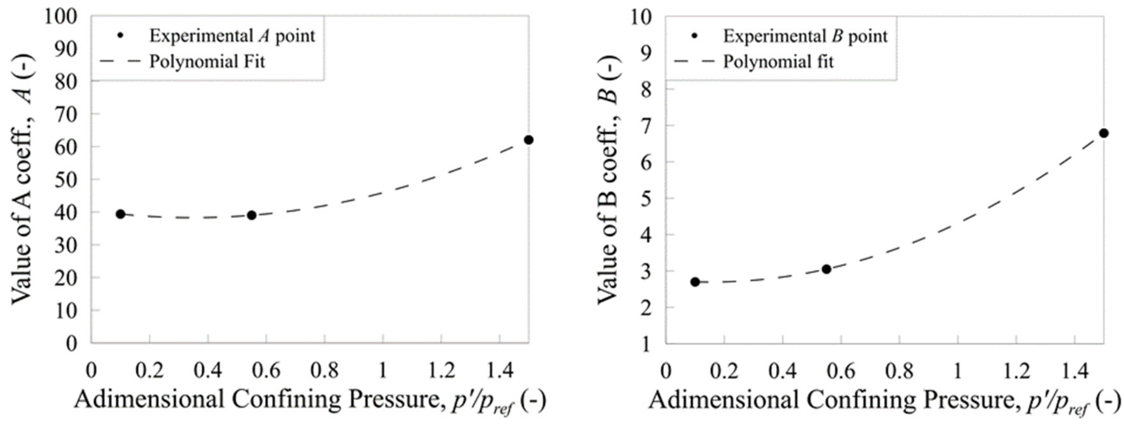

(a) (b)

Figure 4. 10. Values of the non-dimensional coefficients A and B for different confining pressure p': (a) evaluation of A; (b) evaluation of B.

4.2.2 Resonant column test (*RC*)

A resonant column test was carried out to obtain the variation of the normalized shear modulus, G/G_0, and the damping ratio, ξ, with shear strain, γ, required to characterize the non-linear behaviour of the pure clean sand. To be consistent with the other dynamic tests, the sand was compacted by moist tamping in layers, inside split mold, having a diameter of 50mm and a height of 100mm, at a relative density of 70% and then tested under an isotropic confining pressure of 55kPa. From the frequency response curve, the maximum shear modulus (G_0) was calculated, while the damping (ξ) was estimated using the half-power bandwidth method. These experimental points were then interpreted with the MKZ model by Matasovic and Vucetic (1993). Figure 4. 11a and Figure 4. 11b show, respectively, the normalized shear modulus and the damping experimental points of the pure clean Hostun sand, analytically fitted by the MKZ model. Different considerations will be made in the following section by comparing the behavior of the clean sand with the SAP-sand mixtures one.

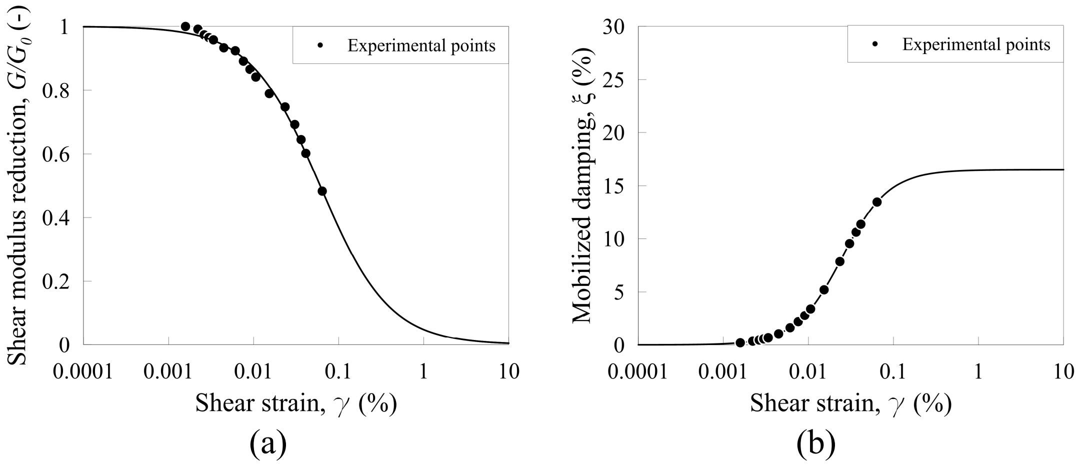

Figure 4. 11. Experimental results of the RC test on clean Hostun Sand: (a) shear modulus reduction curve; (b) mobilized damping curve.

4.2.3 Simple Cyclic shear tests (*CSS*)

Three drained cyclic simple shear tests were performed in strain-controlled mode on different SAP-sand mixtures, as reported in Table 4. 1. The different SAP-sand mixtures were compacted in layers by moist tamping. The specimen has a diameter equal to 70mm and a height of 26mm. The investigated range of shear deformations goes from around 0.1% to 10% of the initial specimen height. For each level of deformation, 5 shear cycles, at 1Hz frequency, were applied. This is the highest possible frequency in the used simple shear device, and was adopted being close to the typical range of the main frequencies of earthquakes (which usually lies between 1Hz to 2Hz). Figure 4. 12 shows the non-linear hysteretic loops for different SAP-sand mixtures presented in Table 4. 1, increasing the amplitude of the shear strains.

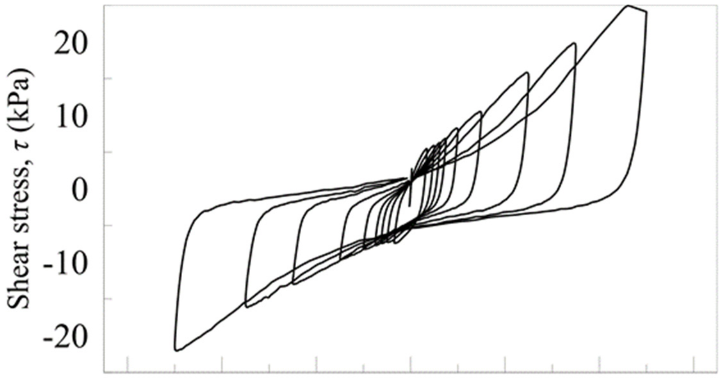

(a)

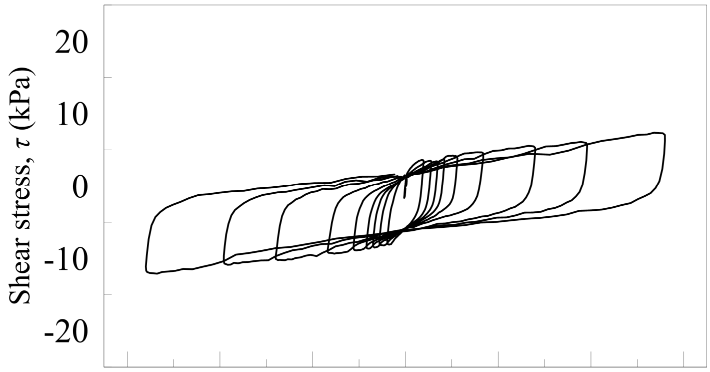

(b)

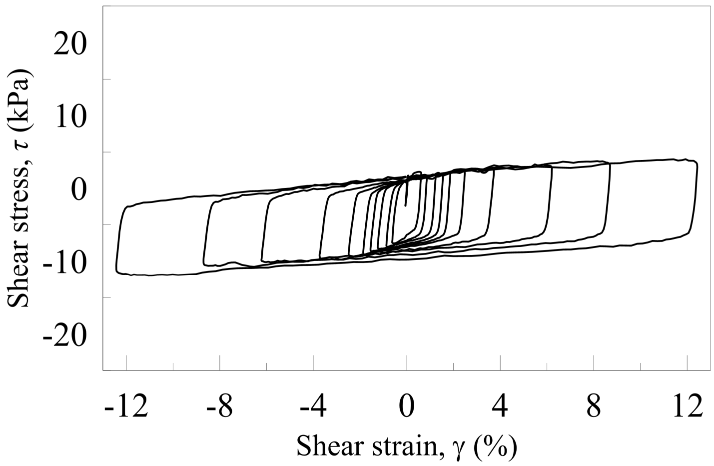

(c)

Figure 4. 12. . Experimental stress-strain loop found through the CSS tests for different SAP-sand mixtures : (a) SAP40; (b) SAP60; (c) SAP80.

As typical, the secant shear modulus was calculated using equation (4. 4):

$$G_{sec} = \tau_{pp}/\gamma_{pp} \qquad (4.\ 4)$$

Where τ_{pp} is the peak to peak stress value and γ_{pp} the peak to peak strain value in each cycle. The evaluation of the damping mobilized with shear strain is influenced by the loop asymmetry and, for this reason, different procedures were adopted to compute the experimental damping points (Figure 4. 13).

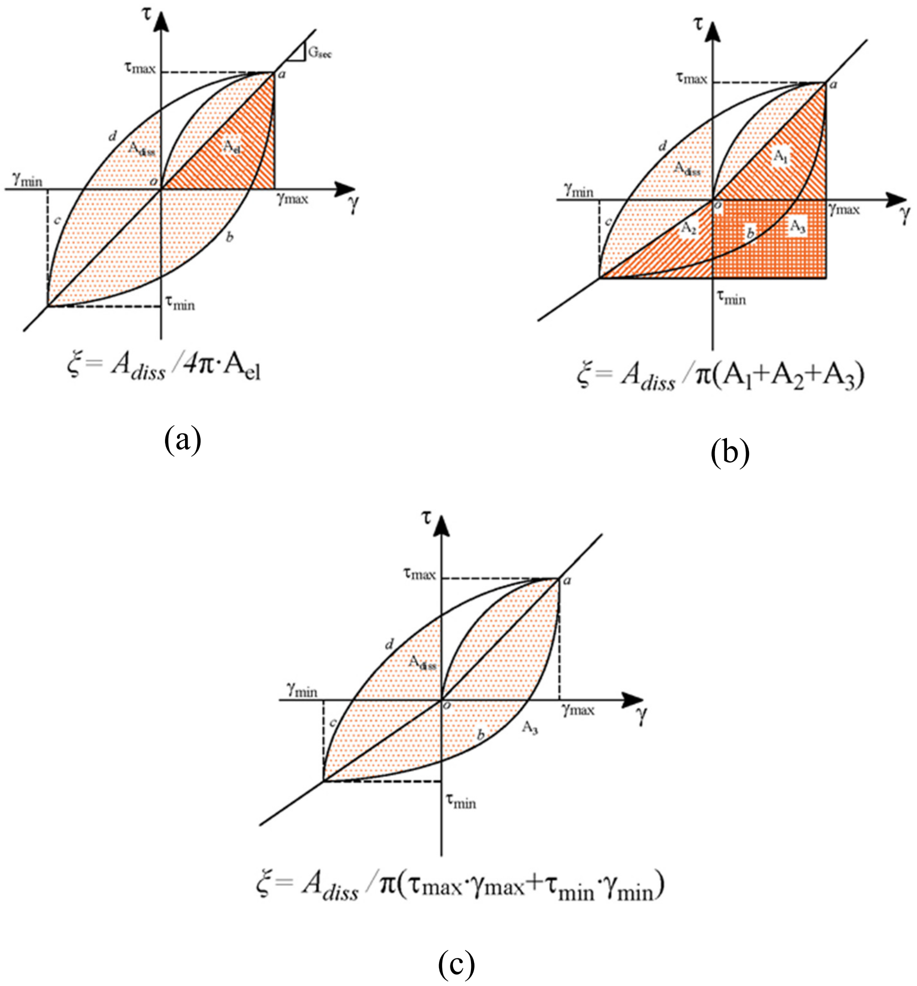

Figure 4. 13. Different procedure to compute the damping mobilized with shear strain: (a) Classical ASTM method for symmetric shear strain loop; (b) Formulation proposed by Kumar et al. (2018) for asymmetric loops; (c) Modified ASTM method for asymmetric loops.

In particular, due to the asymmetric nature of the shear-strain cycles, the procedure proposed by Kumar *et al.* 2018 and the one indicated by the modified ASTM (ASTM D5311) have been adopted. Figure 4. 14 shows the damping values obtained using these two procedures, analytically fitted by the MKZ model.

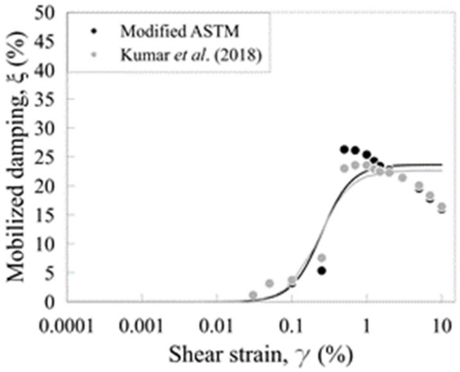

(a)

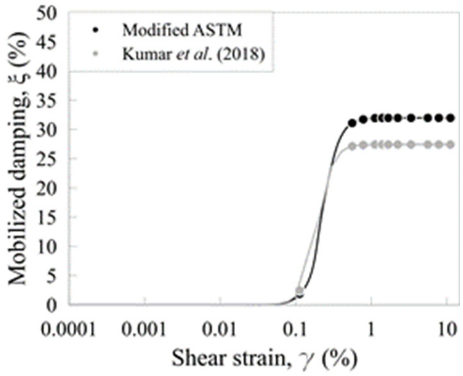

(b)

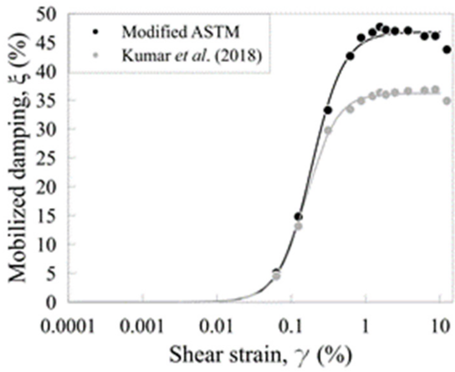

(c)

Figure 4. 14. Damping curves for different SAP-sand mixtures: (a) SAP40; (b)SAP60; (c) SAP80.

The damping values found trough Kumar *et al.*'s procedure are generally lower than those found via the modified ASTM procedure (-15% on average), with differences that increase with the increase in SAP percentage. This is due to the different method used to compute the elastic energy introduced in the system. Considering that damping accounts for the hysteretic dissipation of energy and is therefore a beneficial material property to reduce seismic actions, it can be concluded that the procedure proposed by Kumar leads to a conservative estimate of the damping values. It is also extremely interesting to highlight that, at high shear strain levels occurred in SAP-sand mixtures, extremely high values of damping are mobilized, confirming the attitude of SAP-sand mixtures to be used in geotechnical seismic isolating (GSI) systems. In fact, the mobilized damping increases from around 5% at medium shear strain range (0.1%) to 25, 35, 45% at a high shear strain range (>1%), respectively for SAP40, SAP60, SAP80. Figure 4. 15 compares the mobilized damping in the pure clean sand with the one found in the SAP-sand mixtures. The maximum sand damping value is tripled using the SAP80 mixture, while it is doubled in the case of the SAP60 mixture.

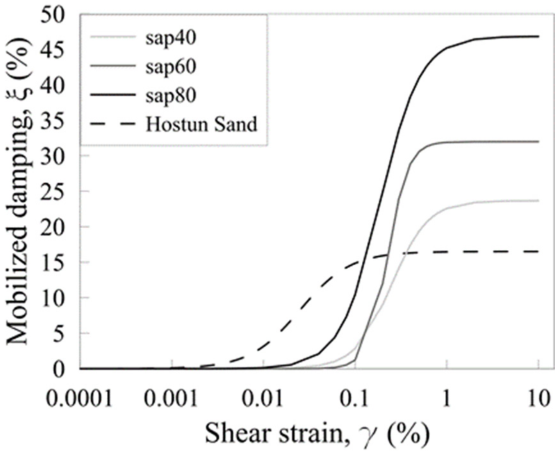

Figure 4. 15. Comparison between the mobilized damping in pure sand and the one mobilized in the different studied mixtures

By combining the results of the BE tests (conventionally assumed to be related to a mobilized value of the shear strain γ=0.0001%) with those of the *CSS* tests, it is then possible to find the decay curve of the shear modulus for the different studied mixtures (Figure 4. 16). Once again, the experimental results are fitted with the MKZ model.

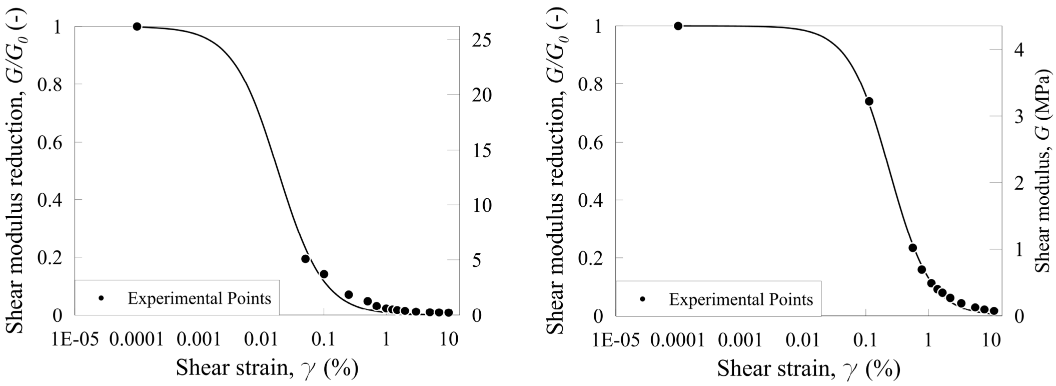

(a) (b)

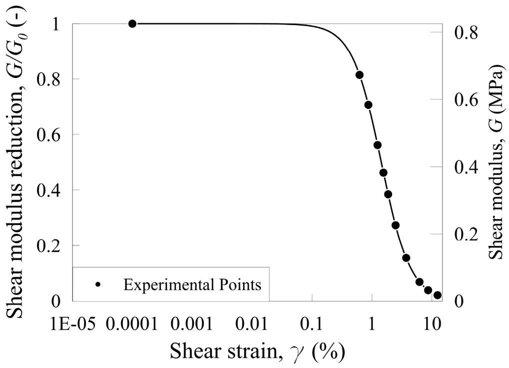

(c)

Figure 4. 16. Shear modulus reduction curves obtained combining the BE tests and CSS test: (a) SAP40; (b) SAP60; (c) SAP80

Figure 4. 17 summarizes the effect of adding SAP to the selected sand, in terms of shear stiffness reduction.

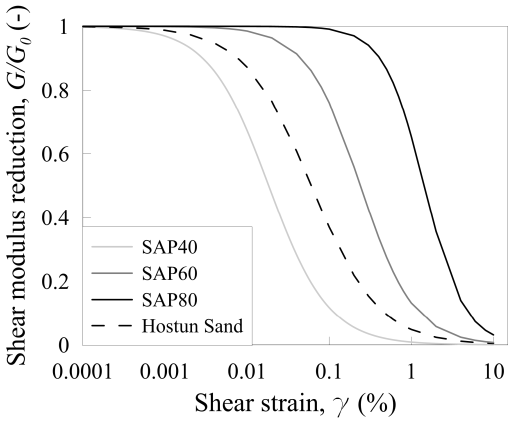

Figure 4. 17. Shear modulus decay curves for sand, SAP40, SAP60 and SAP80 mixtures.

It is worth mentioning that Figure 4. 17 also highlights that the addition of the jelly particles of SAP increases the linear range, which stretches to the high value of $\gamma \approx 0.1\%$ for the SAP80 mixture.

4.3 Monodimensional Analysis

In order to highlight the beneficial effect of anti-seismic soft barriers, a series of one-dimensional seismic response analyses were carried out by varying the sand-SAP properties (i.e. considering different relative percentages of the two components) and the depth of the soft layer in the ground. A visco-elastic non-linear equivalent model was used by means of the code STRATA (Kottke *et al.*, 2019). The depth of the deformable soil is fixed at 30m. The bedrock has been modelled as a visco-elastic half space with a damping ratio of 0.5%. The small strain shear stiffness with depth was modelled using the formulation suggested by Hardin and Drenevich (1972):

$$G_0 = A \cdot \frac{(2.17-e)^2}{1+e} \cdot \left(\frac{p'}{p_{ref}}\right)^m \tag{4. 5}$$

The parameters of eq. (4. 5) were calibrated on the results obtained on Hostun Sand by Hoque and Totquoka (2000) at a relative density of 70%: A =80, m =0.47, e =0.692 and p_{ref}=100kPa. The increasing stiffness profile with depth was simulated, in the numerical model, by discretizing the soil layers meter by meter. A barrier of SAP-sand mixture (considering the two cases SAP60 and SAP80) having a thickness of 1 m was placed at different depths (5, 10, 15, 20m). The shear wave velocity in the SAP-sand mixtures was evaluated using equation (4. 1), considering the influence of the mean pressure at the specific depth where the mixture was placed. The estimated non-linear properties found through the aforementioned laboratory tests, $G/G_0(\gamma)$ and $\xi(\gamma)$, of both Hostun sand and SAP-sand mixtures, were assigned in the numerical model. A series of spectra compatible earthquakes, on soil class type A (rock), were selected and applied at the bottom base of the numerical model, considering the specific seismic hazard of the city of L'Aquila (Italy) at the life safety limit state (as defined by the Italian building code, N.T.C. 2018) (Figure 4. 18).

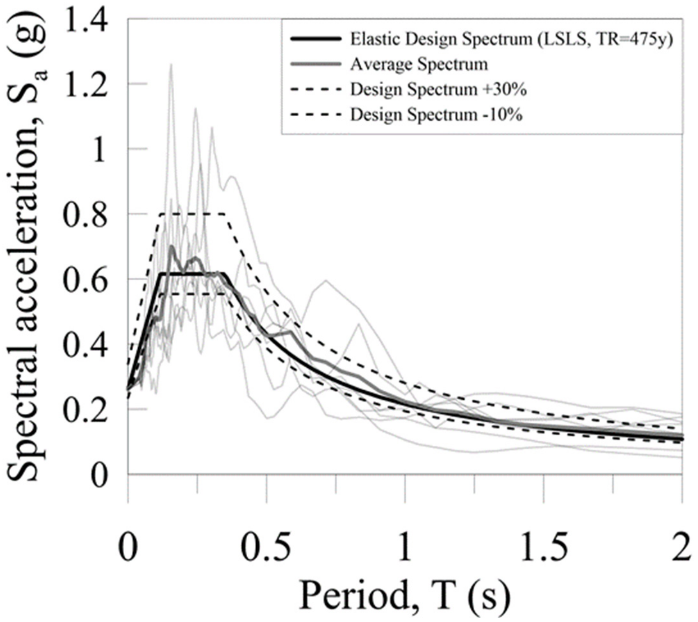

Figure 4. 18. Spectro compatibility of the selected earthquakes with elastic design spectrum of Aquila centre at life safety limit state.

Table 4. 2 reports the main dynamic features of the selected earthquakes.

Table 4. 2 Characteristics of the earthquakes used in the monodimensional analysis.

Location	T_d (sec)	T_m (sec)	I_A (m/s)	$T_{5\text{-}95}$ (s)
Bingol	0.16	0.33	0.51	4.56
Campano Lucano	0.10	0.49	1.27	40.33
Friuli	0.26	0.39	0.42	4.3
Golbasi	0.26	0.72	0.50	11.85
Mt. Fnajoll	0.20	0.59	0.40	7.96
South Iceland	0.24	0.47	0.63	4.45
South Iceland After	0.30	0.58	0.89	5.33

The frequency and amplitude content of the selected earthquakes reflects the typical high seismic hazard in the Italian Apennines where soft barrier interventions could be performed. The anti-seismic effectiveness of the soft layers is analysed comparing the dynamic behaviour of the soil bank with and without the soft barrier. The case in which the soft SAP-sand barrier is introduced is referred to by the acronym GSI (Geotechnical Seismic Isolation).

Three efficiency parameters such as *PGA* efficiency, $E_{PGA}= (PGA- PGA_{GSI})/ PGA$), Arias Intensity Efficiency, $E_{IA}= (IA- IA_{GSI})/ IA)$ and Housner Intensity Efficiency, $HI= (HI-HI_{GSI})/HI)$ have been used, to show the potentiality of this technique. Figure 4. 19 shows the effect of inserting a soft layer characterized by SAP60 by varying its depth while Figure 4. 20 shows the effect of inserting a soft layer made by SAP80.

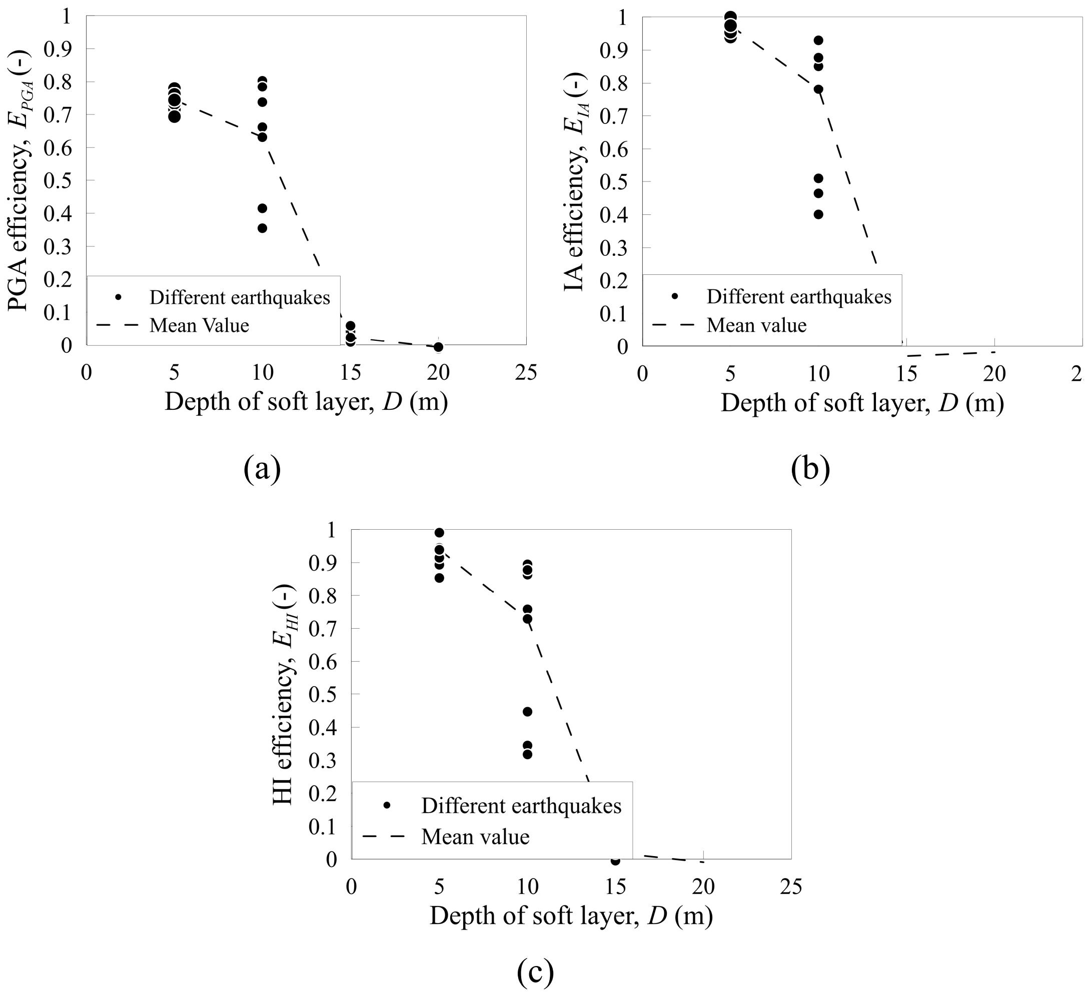

Figure 4. 19. Efficiency parameters for soft barriers made by SAP60 varying the depth of the soft layer: (a) Peak Ground Acceleration efficiency; (b) Arias Intensity efficiency; (c) Housner Intensity Efficiency.

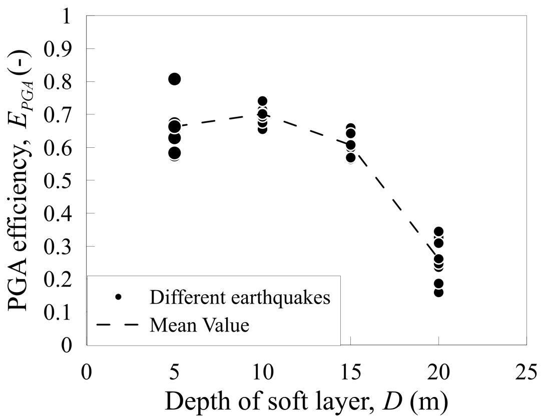

(a)

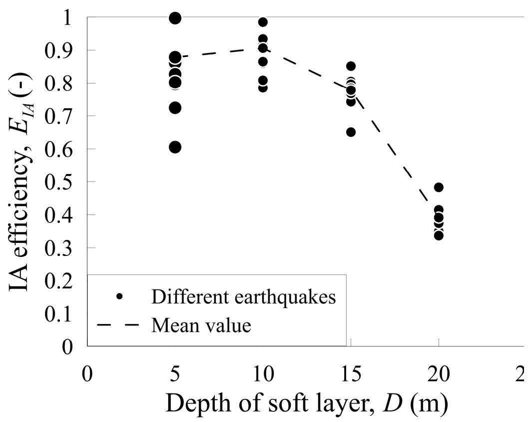

(b)

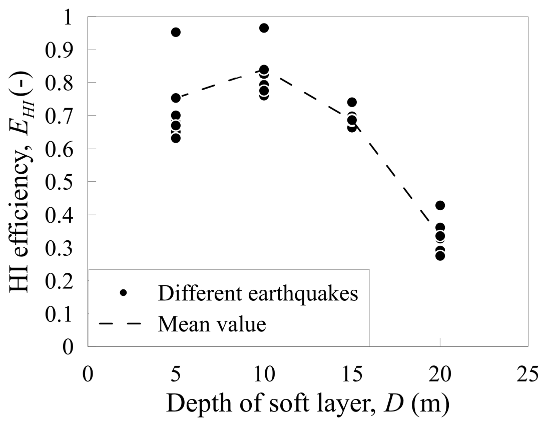

(c)

Figure 4. 20. Efficiency parameters for soft barriers made by SAP80 varying the depth of the soft layer: (a) Peak Ground Acceleration efficiency; (b) Arias Intensity efficiency; (c) Housner Intensity Efficiency.

The effectiveness of the barrier, up to 15 meters of treatment depth, is particularly high, reaching values higher than 0.7 for the shallowest depth (5m). In this 1D analysis, the deeper the barrier the lower its anti-seismic efficiency. Deepening the soft layer, the dynamic impedance contrast between the soil and soft layer is reduced and for this reason the maximum shear strains in the soft layer are lower (Figure 4. 21a) generating less mobilized damping and shear modulus reduction in the soft layer (Figure 4. 21b,c).

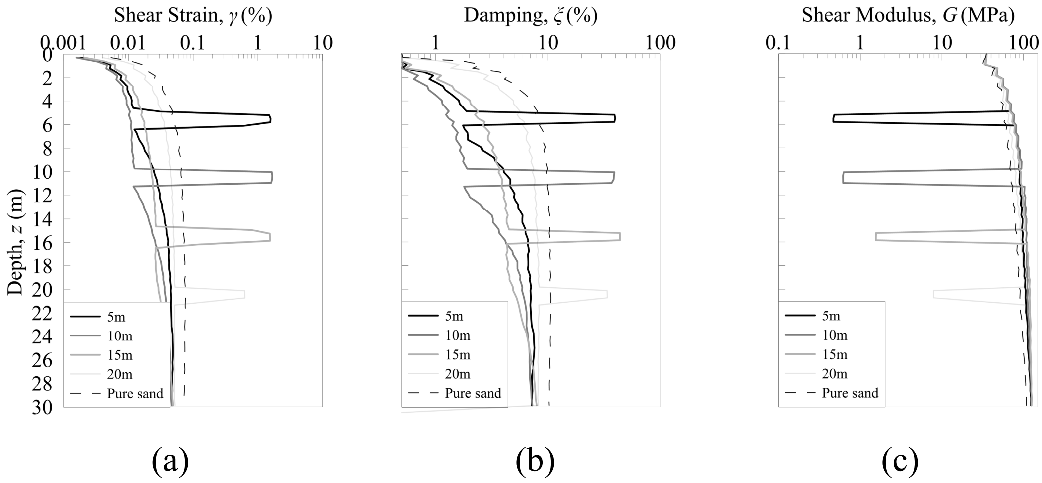

Figure 4. 21. Different damping and stiffness properties for different depths of the soft layer SAP80: (a) Maximum shear strain mobilized as mean of overall earthquakes; (b) Mean damping mobilized in the soil bank; (c) Mean shear modulus mobilized in the soil bank.

However, as it is possible to see in Figure 4. 8b, the influence of confinement pressure on shear modulus of SAP-sand mixtures is less marked for high SAP volume content in the soil (≥80%). Hence the dependence of the effectiveness of the technique on the depth tends to decrease by increasing the volume percentage of SAP in the soil. The parametric analysis also indicates (as obvious) that the higher the SAP content in the barrier, the higher its anti-seismic efficiency.

The main dynamic effect of inserting a soft layer in the soil is the reduction of the natural fundamental frequency of the soil bank (Figure 4. 22a). The first average fundamental frequency of the soil bank considered is around 2Hz, while it is reduced to values even lower than 1Hz with the soft layers. For this reason, soft barriers can be extremely effective for protecting low-period buildings, while they can be ineffective or even detrimental for high-period buildings. In the cases reported in Figure 4. 22b the efficiency in terms of acceleration spectrum reductions (E_{PSA}= *(PSA(T)- PSA_{GSI}(T)/ PSA(T))* is less than unity starting from periods higher than 1sec (for a depth of the barrier of 15 m).

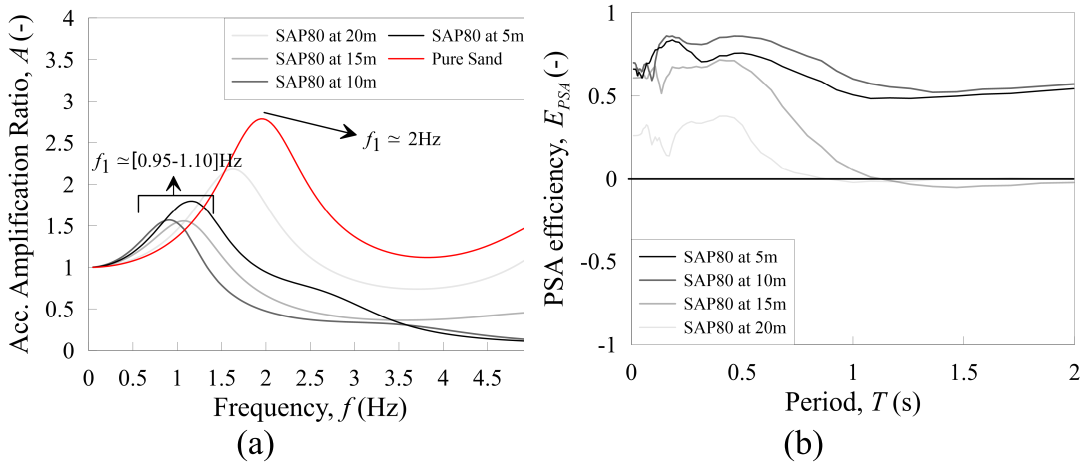

Figure 4. 22. Effect of the insertion of the soft layer: (a) Acceleration amplification ratio between the bedrock and the top surface; (b) Pseudo Spectral acceleration efficiency.

The filtering effect of the barrier confirms to be excellent, especially for the shallower positions. However, even though the dynamic impedance ratio decreases with depth (and so does the isolating efficiency) it must be highlighted that the soil mass above the soft horizontal barrier, adequately confined by additional vertical soft barriers, can be considered as an additional structural mass. As a consequence, it has a beneficial effect on the elongation of the natural period of the structure to be protected, that may partially compensate the reduced filtering effect of shear waves of the deeper barriers. In order to analyse the effects of creating an isolated volume of soil, called a 'soft caisson', it is necessary to carry out two-dimensional analyses. With this it will be possible to model the exact shape of the horizontal as well as vertical soft barriers and considering effects that one-dimensional analyses cannot capture.

4.4 Bidimensional Analysis and soft caisson effect

Two-dimensional analyses were carried out by using Plaxis 2D. The goal of these analyses is to calculate the resonance period of the caisson system created by the soft barriers as function of the aspect ratio and thickness of the barriers. For this reason, a big volume of soil with a depth of 30meters was modelled in which the vertical and horizontal soft barriers were inserted. As done for the one-dimensional analyses, it was decided to use Hostun Sand with a relative density of 70%. The material model used for sand is the Hardening Soil Small

Strain which is able to predict the increase in soil stiffness with the confinement pressure. In order to evaluate the same increase in stiffness produced in the mono-dimensional analysis by Eq. (4. 5), the following strength and stiffness parameters were selected using a best fitting procedure (*i.e.* same procedure of Chapter 3.3.2).

Table 4. 3. Strenght parameters used for numerical analysis with HSss

Soil name	γ	c’	φ'	Ψ	K_0
[-]	[kN/m^3]	[kPa]	[°]	[°]	[-]
Hostun Sand	15.37	1	40	10	0.36

Table 4. 4. Stiffness parameters used for numerical analysis with HSss

G_0^{ref}	m	E_{50}^{ref}	E_{oed}^{ref}	E_{ur}^{ref}	$\gamma_{0.7}$
[MPa]	[-]	[MPa]	[MPa]	[MPa]	[-]
128	*0.49*	35	35	105	0.27E-3

In order to clearly read the resonance frequency of the caisson system, instead of an earthquake signal, a frequency sine-sweep signal was applied at the base of the model. This frequency sweep, artificially created, has a length of 30 seconds and reaches a maximum of 10Hz by increasing the frequency linearly (Figure 4. 23). In order not to induce plasticization in the soil model the amplitude of this sine-sweep is very low (0.1m/s^2).

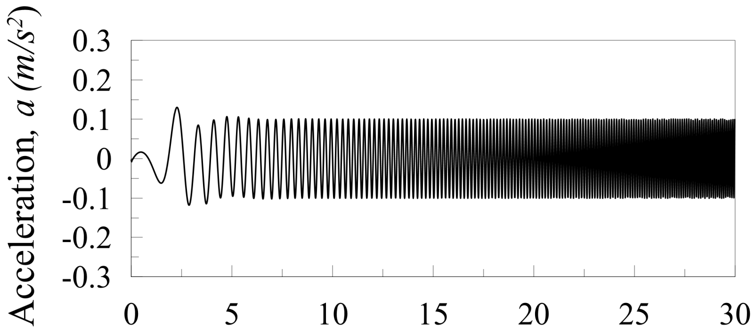

Figure 4. 23. Sinesweep up to 10Hz applied at the base of the numerical model.

Free field numerical boundary conditions were applied on the lateral sides of the model to reproduce the mono-dimensional propagation of the sine-sweep in the soil at a considerable distance from the soft caisson. As the goal of these analysis is only the calculation of the soft caisson resonant period, an infinitely rigid bedrock constraint condition was implemented at the base of the model. In addition to the soil and the soft caisson, it was decided to model the presence of a simple structure within the soft caisson itself. The modelling of the structure is important because, as will be seen later, it constitutes an additional mass to the isolated soil volume which can slightly modify the resonance period of the soft box itself. The modelled structure has the following characteristics:

Table 4. 5. Properties of the modelled structure in two-dimensional analyses

Parameter	Prototype
Nominal Bearing Pressure	95kPa
Foundations width	1.40m
Natural frequency (fixed base)	3.33Hz
Superstructure Mass	18.71Mg/m
Foundation Mass	8.44Mg/m
Base Width	7.5m
Total Height	10m
Geometrical Aspect Ratio	1.3
Lateral stiffness	8976 kN/m/m
Damping ratio	5%

In the following analyses, the soft caisson was modelled by placing the horizontal barrier at the following depths 10-15 meters because they were considered to be acceptable for technological installation purposes and not affecting the significant load volume of the structure. The aspect ratio of the soft caisson (*i.e.* ratio of the width of the caisson to its depth) was then varied, for each depth investigated, up to a maximum of B/H=6 where B and H are, respectively, the width and height of soft caisson. The thickness of the horizontal barrier (t_h) is equal to 1m while the ones of the vertical barriers (t_v) were changed from 1 to 2 meters. Thickness of 1m for the lower horizontal barrier is certainly an upper limit, while for vertical barriers a thickness of 2m is easily achievable technologically. Further information about the technological feasibility of such configurations will be given in Chapter 4.8. It was decided to use the properties of SAP80 to create the horizontal barrier. This choice is motivated by the high anti-seismic efficiency that has been evaluated in the one-dimensional analysis of this mixture. Furthermore, it is very difficult the possibility of creating a homogeneous barrier characterized only by SAP (*i.e.* SAP100) due to difficulties linked to its injection. The equivalent linear properties used for SAP80, at the different depths, are derived from the one-dimensional analyses already carried out and therefore consider the level of shear deformation and damping achieved during the strong seismic events considered (Table 4. 6).

Table 4. 6. Equivalent properties of stiffness and damping for the lateral and horizontal barriers.

Depth barrier, H [m]	Shear waves velocity, V_s [m/s]	Specific weight, γ_{SAP80} [kN/m^3]	Poisson Ratio, ν [-]	Damping mobilized, ξ [%]
10	21	12,94	0.49	38
15	34	12,94	0.49	43

Damping values were assigned to the SAP layer through the dual control frequency approach. In particular, the first control frequency (f_1) was set equal to the first natural frequency of vibration of the soil while the second control frequency (f_2) was set equal to 3 times f_1. The value of the Poisson's modulus was calculated from the V_p values calculated by Nappa *et al.* (2016b) for SAP80. Therefore, these properties create an horizontal barriers characterized by very low shear stiffness and high volumetric and edoemetric stiffness. With regard to the properties of the vertical barriers, it should be remembering the importance to have a low volumetric/edoemetric stiffness. Since the shear waves generated by an earthquake will normally impact the vertical barriers, these must be particularly deformable in such direction. When choosing materials for vertical barriers, it is therefore important to select a compressible and lighweight materials such as peat, polystyrene, air-filled balloons (Massarsch 2004, 2005) or rubber-soil. Ideally an open vertical trench would provide the most effective isolation. However, in practice, the walls of an open trench could suffer instability and to solve this problem it is possible to fill such trench. A material that is relatively soft compared with the surrounding soil, yet is sufficiently stiff to balance the confining pressure of the soil, may fit the purpose of isolation preventing instability at the same time. Because of the very high volumetric/edometric stiffness the use of high percentages of SAP (like SAP100%) is not suitable for the creation of vertical barriers. For this reason, it was decided to use the properties of SAP80 at 10 meters depth with Poisson's modulus equal to 0.3. This change in Poisson's modulus can be achieved by simply blowing air into the mixture in order to create small bubbles in suspension and this effect was confirmed by the parameters find by Nappa *et al.* (2016) in her centrifuge test for SAP100%. The creation of these bubbles means that the material is no longer incompressible and therefore the volumetric stiffness decreases drastically. Several full-scale experiments show this peculiarity of SAP, which may also be used for human vibration-induced isolation with a proper calibration (Nappa, 2019). The technique of air sparging has already been studied and analyzed in detail, especially to mitigate the risk of liquefaction (Astuto, 2021). The presence of only a few air bubbles (i.e. a degree of saturation just a bit lower than 100%) can significantly reduce the volumetric stiffness and so the compression waves velocity of the equivalent fluid (water+bubbles). The specific amount of air to be injected into the SAP to reduce its volumetric stiffness to a predetermined value is beyond the scope of this work. However, it was realized that the SAP mixtures properties can be engineered for the specific case also for the vertical barriers.

Figure 4. 24, represents, as an example, the numerical model used to analyse the dynamic behaviour of the soft caisson with aspect ratios of 2 and 6 and horizontal barriers placed at a depth of 10 meters.

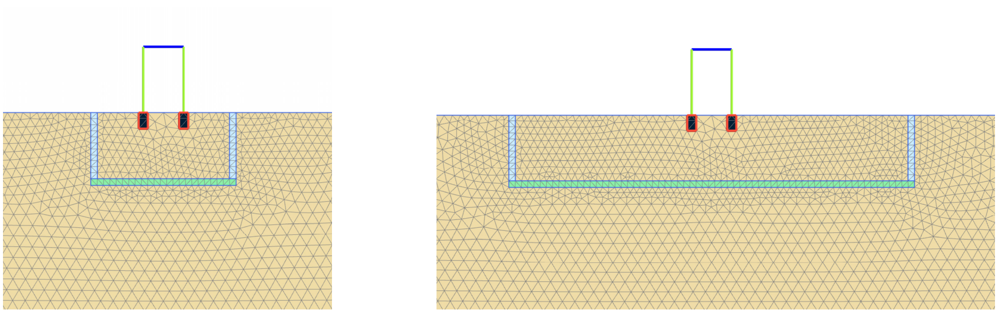

(a) (b)

Figure 4. 24. Different soft caisson dimensions: (a) aspect ratio equal to 2, (b) aspect ratio equal to 6 with both thickness of barriers equal to 1 meter.

In order to calculate the period elongations generated by the presence of the soft box, the amplification function between the model base and the surface was calculated. This amplification function was also calculated in the case of pure sand only, thus, returning the natural frequencies of the soil bank without intervention. Figure 4. 25 shows the amplification function in the case of a caisson with a height of 15m and aspect ratios of 1, 2 and 4 comparing with the resonance periods of the ground without intervention.

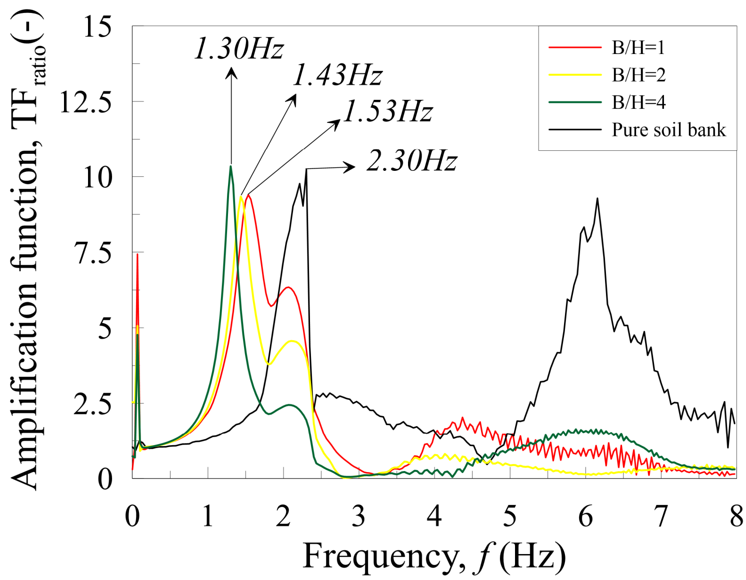

Figure 4. 25. Amplification function for sinesweep signal up to 10Hz in case of soft caisson with height 15m and aspect ratio of 1-2-4.

As already assessed with one-dimensional analyses, the natural resonance periods of the soil bench are completely shifted towards lower values. This can be extremely beneficial, especially for structures with a low resonance period such as masonry buildings. It is also evident from Figure 4. 25 that the resonance period of the caisson increases as the size of the caisson, and hence the *B/H* soft caisson aspect ratio, increases too. However, the natural periods lengthening, obtained in the case of two-dimensional analyses (Figure 4. 25), are smaller than in the case of one-dimensional (Figure 4. 22a). In fact, in one-dimensional analyses, the soft caisson system can be idealized by an aspect ratio, *B/H,* very high and, for this reason, the period elongation effect is maximized. Indeed, the caisson system can be modelled as a one degree of freedom system, characterized by a mass equal to the mass of the incorporated soil (plus the mass of the structure), and by a stiffness given by the sum of the lateral stiffnesses of the lower and lateral barriers (Figure 4. 26).

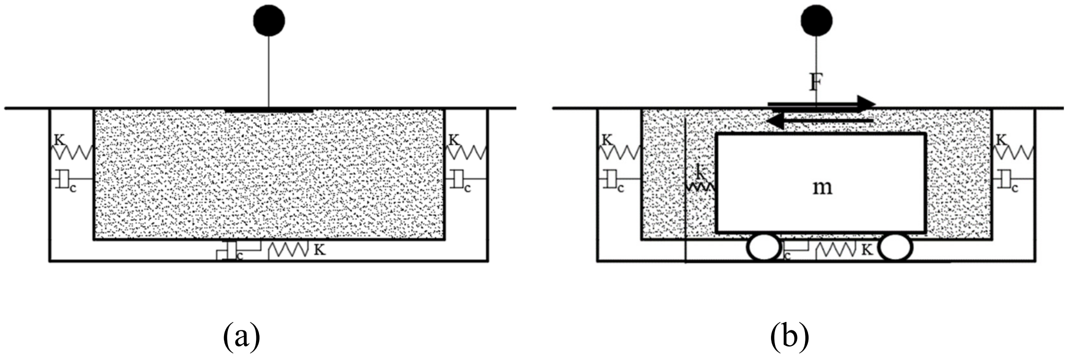

Figure 4. 26. Schematic representation of the dynamic "soft caisson" system: (a) static condition (b) dynamic condition.

The following graphs show the value of the first natural period of the caisson as a function of aspect ratio and height of the soft caisson (10 and 15meters).

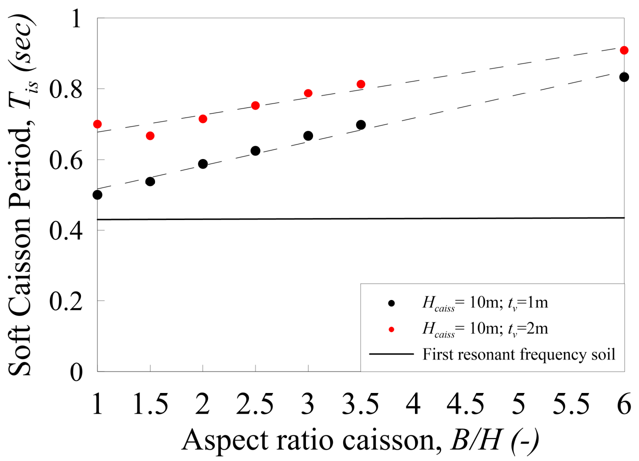

(a)

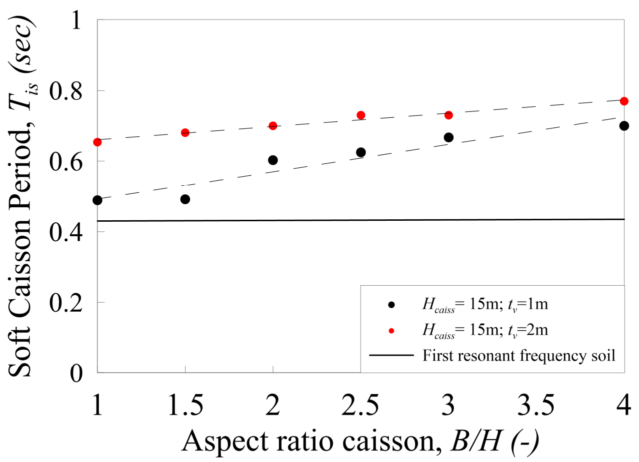

(b)

Figure 4. 27. Values of the resonance period of the caisson system as the form factor increases: (a) height of caisson equal to 10meters (b) height of caisson equal to 15 meters.

As can be seen from Figure 4. 27a, the caisson system for high aspect ratio (*B/H*) values is able to double the natural period of vibration of the soil bench (0.43 sec). It is also possible to note that, comparing the systems with same aspect ratio, slightly lower values of resonant period can be found in case of deeper horizontal barriers. This is generated by the increase in shear stiffness of SAP80 with depth, as shown in Table 4. 6.

4.5. Implementation of soft barriers on a real hazard scenario

As already done for the lateral disconnection technique, the soft barriers were investigated in a real seismic hazard scenario. The 7 spectrum-compatible accelerograms selected correspond to those used for the one-dimensional analyses (already showed in Figure 4. 18 and Table 4. 2) while the soil was modelled with HS_{ss} with the parameters reported in Table 4. 3 and Table 4. 4. (same soil and same increases in stiffness as in the mono-dimensional analysis). The modelled structure corresponds to that used in the parametrical two-dimensional analyses (Table 4. 5). Based on the excellent period elongations (up to about 0.9sec) obtained from the two-dimensional analyses (Figure 4. 27), with horizontal barriers at 10 metres depth and aspect ratio of 6, it was decided to use this shape of soft caisson with the thickness of the lateral barriers equal to 2meters and its related properties. In order to highlight the seismic improvement generated by the soft barrier, the direct analyses with soil-structure interaction were also calculated without the presence of the soft barriers as benchmarks example. The numerical model with soft barriers (GSI model) are shown in Figure 4. 28 while the benchmark model (NO GSI model) is practically the same but without the presence of the soft barriers

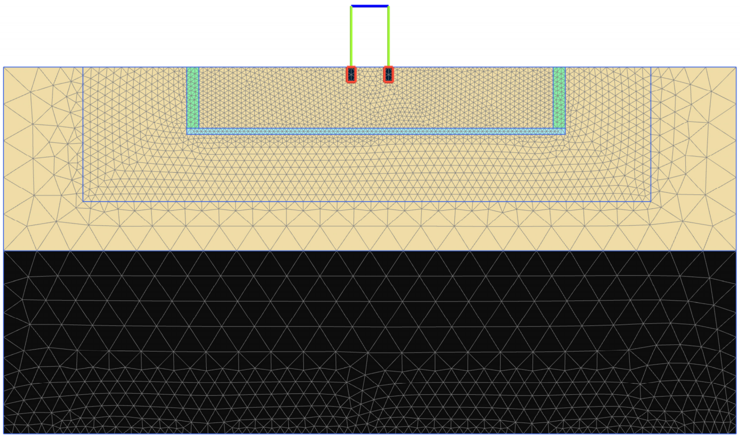

Figure 4. 28. Two-dimensional numerical model with presence of soft barriers with aspect ratio equal to 6

The model has a width dimension of 120m and a total depth of 60meters. The width of the deformable soil is fixed at 30meters while other 30 meters of bedrock are included in the model to ensure no significative interference between the bottom complaint base and the deformable soil layer. The ground water is absent. This has no effect on the effectiveness of the soft caisson but, as will be described later, can greatly influence the choice of SAP injection technique. Standard boundary conditions were applied during the initial (static) stage, that is zero horizontal displacements along the lateral boundaries and fixed nodes at the base of the mesh. During the dynamic analysis, the seismic inputs were applied to the bottom nodes of the mesh. In order to consider the finite stiffness of the underlying bedrock, and to reproduce the upward propagation of shear waves within a semi-infinite domain, the outcrop input accelerations were halved to compute the corresponding upward-propagating wave motion and applied to the bottom nodes together with adsorbing viscous dashpots (complaint base). Free-field boundary conditions were applied along the lateral sides of the mesh. The element size of the soil has been taken always smaller than one-tenth of the wavelength associated with the highest frequency component of the input wave containing appreciable energy (Kuhlemeyer & Lysmer, 1973). For this reason, the discretization was carried out using 5933 tetrahedral elements with 15 nodes each. The 30 meters relative distance between the lateral barriers and side model boundaries of the models ensures no significant interaction. As can be seen from Figure 4. 29, the presence of the soft barriers drastically modifies the accelerations between the bedrock and the surface. In particular, it can be seen that in the soft layer there is a decrease in peak accelerations. This is due to the fact that high shear deformations are generated in the soft barrier.

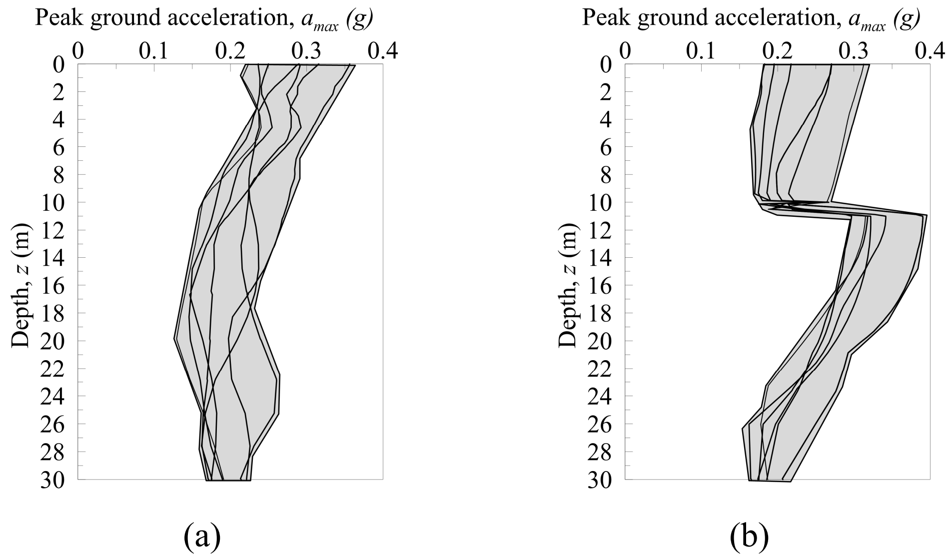

Figure 4. 29. Maximum PGA profile with depth; (a) without soft barrier intervention, (b) with soft barrier intervention

As already stated, a very important information, in the design process of soft caisson, is the estimation of its natural period of vibration. In fact, a resonance period far enough away from the earthquake predominant period and from the resonance period of the structure will generate large reductions in accelerations. This last aspect is very important and, as will be show clearer in Chapter 4.7, corresponds to the design strategy of the soft caisson sizes and properties. In order to calculate the caisson natural period of vibration, as already done, the acceleration amplification function between the bedrock and a node inside the soft caisson can be used. Figure 4. 30 shows this amplification function for natural earthquakes with and without the soft barriers.

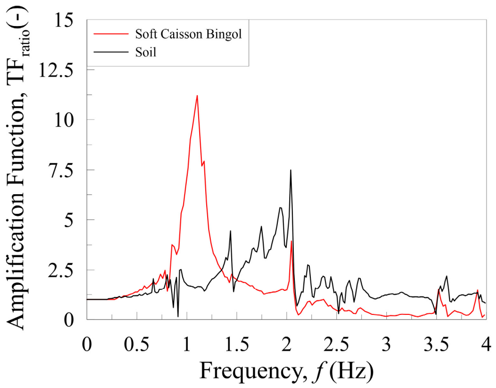
Soft Caisson Bingol
Soil
Amplification Function, TF_{ratio}(-)
Frequency, f (Hz)

(a)

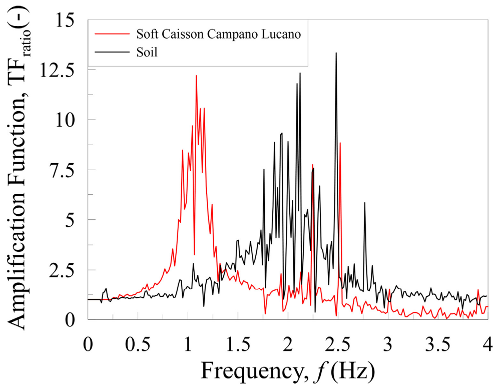
Soft Caisson Campano Lucano
Soil
Amplification Function, TF_{ratio}(-)
Frequency, f (Hz)

(b)

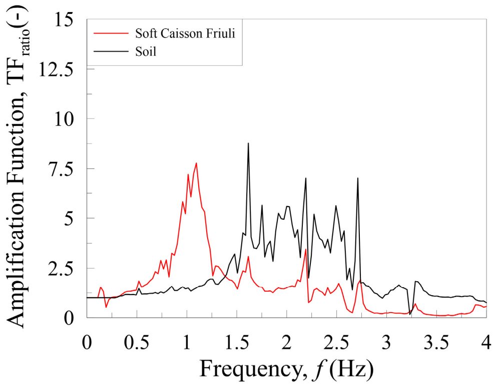
Soft Caisson Friuli
Soil
Amplification Function, TF_{ratio}(-)
Frequency, f (Hz)

(c)

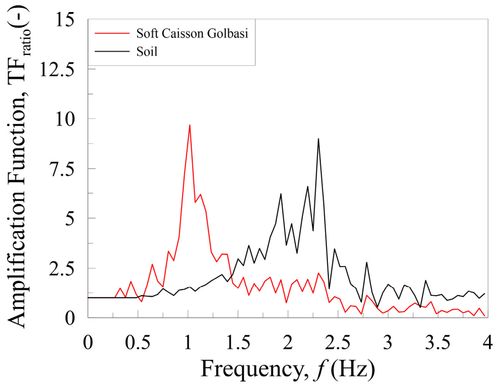
Soft Caisson Golbasi
Soil
Amplification Function, TF_{ratio}(-)
Frequency, f (Hz)

(d)

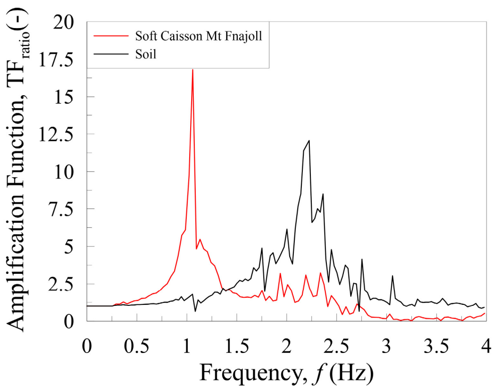
Soft Caisson Mt Fnajoll
Soil
Amplification Function, TF_{ratio}(-)
Frequency, f (Hz)

(e)

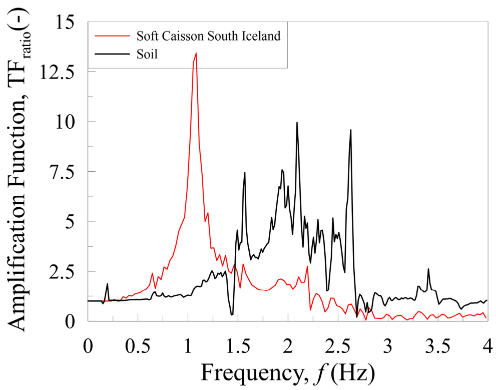
Soft Caisson South Iceland
Soil
Amplification Function, TF_{ratio}(-)
Frequency, f (Hz)

(f)

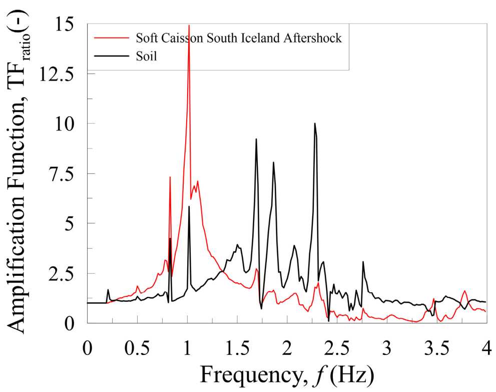
Soft Caisson South Iceland Aftershock
Soil
Amplification Function, TF_{ratio}(-)
Frequency, f (Hz)

(g)

Figure 4. 30. Acceleration Amplification Function to detect the resonant period of the soft caisson: (a) Bingol, (b) Campano Lucano, (c) Friuli, (d) Golbasi, (e) Mt Fnajoll, (f) South Iceland, (g) South Iceland Aftershock

A resonance frequency of the soft box in the range of 1-1.10Hz (period 0.9-1.0 sec) can be estimated whereas, without the soft barriers, the first natural frequency of pure soil was approximately equal to 2Hz. In this case, it can therefore be seen that the soft caisson is able to double the natural period of vibration of the soil bed. This contributes significantly to the reduction of seismic actions on the analysed structure as it moves the resonance frequency of the structure away from the resonance frequency of the soil bed. To better understand this concept, it is possible to calculate the efficiency in terms of reductions in Pseudo Acceleration at the base of the structure. This efficiency parameter, calculated as $E_{PSA}= (PSA(T)- PSA_{GSI}(T)/ PSA(T),$ will show for which values of resonance period of the hypothetical structure there will be reductions in acceleration.

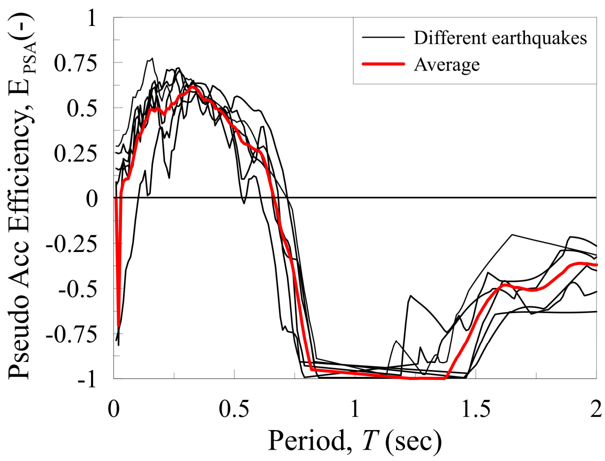

Figure 4. 31. Efficiency PSA(T) parameters for different natural earthquakes.

It can be seen that for structures with a resonance period up to 0.7 sec there will be a reduction in acceleration, whereas from 0.7 sec onwards the intervention will lead to an increase in acceleration on the structure. This leads to an obvious but essential consideration. The soft barriers technique in the ground is able to protect the generic structure from seismic actions, provided the caisson is adequately designed in its geometry and mechanical properties. However, the application of this technique in engineering practice will be more effective for low to medium rise structures such as masonry buildings, while it could be detrimental for high period structure such as tall structure. Again, the effectiveness of the soft barriers have to be analysed case by case.

It is also possible to calculate the period elongations for the building, generated by the deformability of the ground, using the amplification function between the base of the structure and the roof. Figure 4. 32 show the amplification function for Campano Lucano and Friuli earthquakes being representative of all other earthquakes.

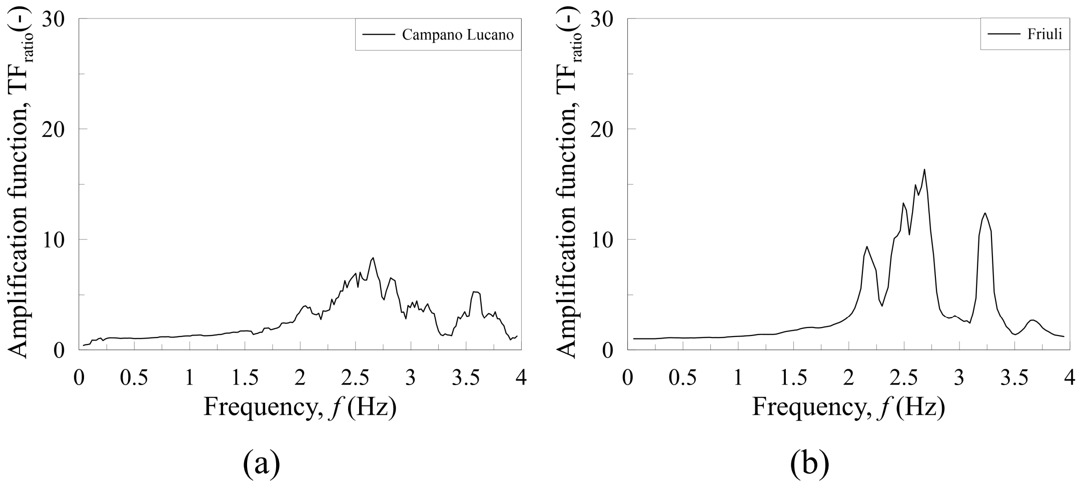

Figure 4. 32. Amplification function between the base of the structure and the roof to detect the natural resonant frequency with soil structure interaction; (a) Campano Lucano (b) Friuli.

It can be seen that the resonant frequency of the soil-structure system is about 2.6-2.7 Hz (or 0.37 second).

Other different efficiency parameters can be introduced to quantify the benefits of this technique such as effectiveness in terms of acceleration reductions, or in terms of Arias Intensity reduction.

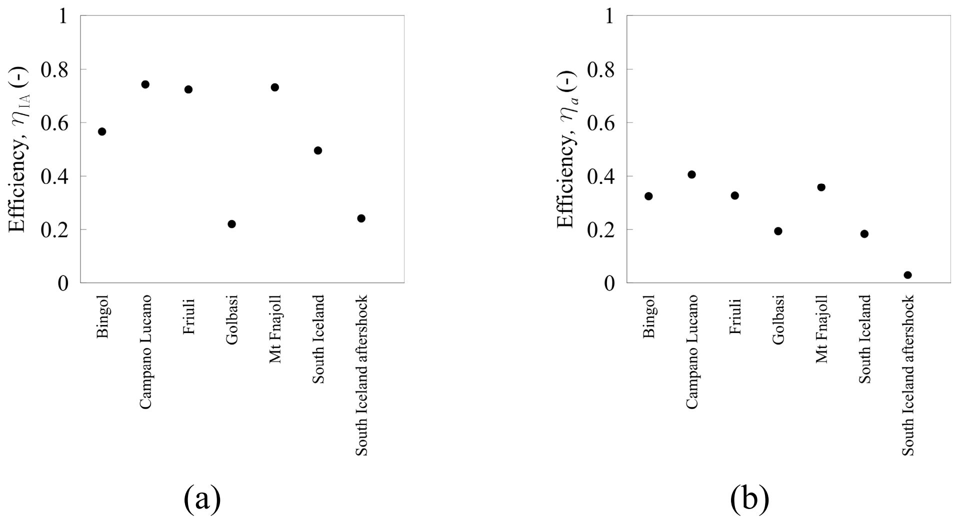

Figure 4. 33. Efficiency parameters such as: (a) Arias Intensity and (b) Maximum Acceleration Efficiency.

The effectiveness of the technique is remarkable, contributing in some cases to a reduction of up to 40% in maximum accelerations and 80% in Arias intensity. It should also be noted that this technique, unlike lateral disconnection, can be adapted to achieve the required level of safety. In this sense, a soft box design of different sizes would have led to different acceleration demands.

4.6 Simplified dynamic system

As already mentioned in the paragraph 4.4, the caisson system can be studied, from a dynamic point of view, as a one degree of freedom system moving horizontally under seismic actions. Flora *et al.*(2018) found that the following formulation allows to estimate the resonant frequency of a rectangular soft caisson:

$$f_{IS} = \frac{1}{2\pi} \cdot \left[\frac{1-\xi^2}{\rho}\left(\frac{2E_g}{S_1 B} + \frac{G_g}{S_2 H}\right)\right]^{0.5} \tag{4. 6}$$

Where:

- ρ is the soil density of the isolated volume;
- ξ is the mobilezed damping in the barriers;
- E_g is the normal stiffness of the vertical barriers; in particular E_g refers to the relevant compressive stiffness, that may be the oedometer one if

the ratio *B/S* is high and confinement is provided, or the Young modulus in all other cases;

- G_g is the shear stiffness of the horizontal barrier;
- S_1 and S_2 are the thickness of the lower and side barriers respectively

The proposed formulation allows to estimate, in a simplified way, the resonant period of the caisson without the presence of the structure; by manipulating the formulation it is possible to introduce a further formulation, which allows to consider the real mass of the soft caisson as the sum of the mass of the soil and the mass of the structure (m_{str}):

$$f_{IS} = \frac{1}{2\pi} \cdot \left[\frac{1-\xi^2}{(\rho HB+m_{str})}\left(\frac{2E_gH}{S_1}+\frac{G_gB}{S_2}\right)\right]^{0.5} \tag{4. 7}$$

In order to validate the effectiveness of this expression, the values of the period derived from the numerical analyses were compared with those derived from the analytical formulation.

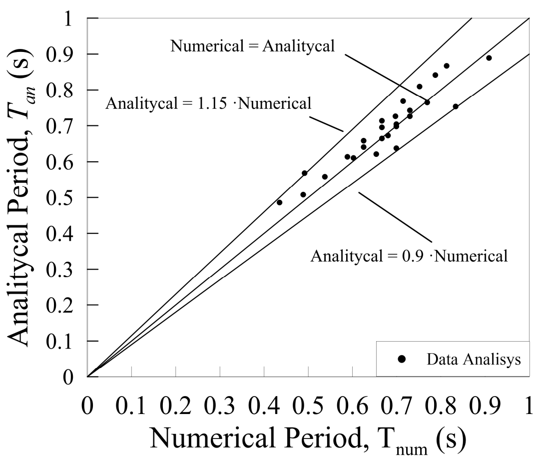

Figure 4. 34. Comparison between the analytical period estimation and numerical period estimation

The comparison shows reliable results with small differences between 10 and 15%. The similarity between the analytical and numerical periods makes it possible to recognize that the estimation of mass and stiffness of the caisson system is acceptable and, for this reason, allows also the structure to be modelled with its proper mass and stiffness. In particular, the dynamic system (soft caisson + structure) could be simplified with two concentrated masses in series:

1. The mass of the soil plus the mass of the foundation: it moves together with the ground (as a single unit of mass) due to the rigidity of the ground compared to that of the barriers and provides the input to the superstructure mass. It is assumed that the soil and foundation vibrate together, as SSI stiffness will be much greater than that of the soft material.
2. The top-structure mass→ it moves due to the movement of the lower mass

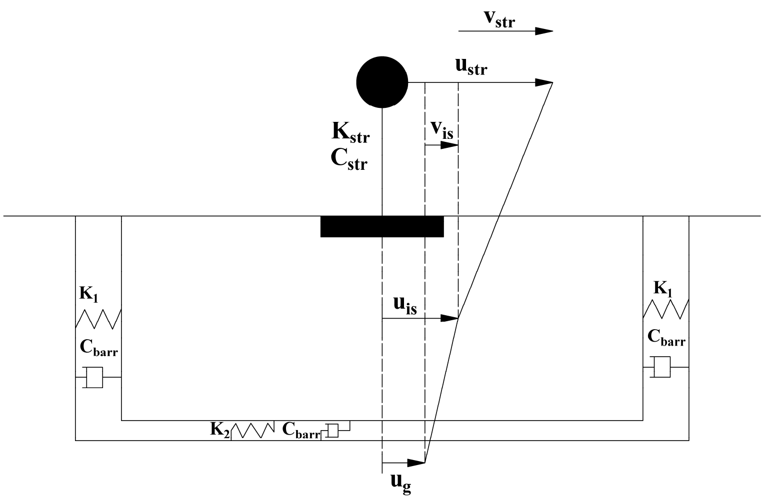

Figure 4. 35. Dynamic system with two discrete masses and 2 degrees of freedom.

As shown in Figure 4. 35, a simple mass-spring model is created to reproduce the effect of the soft caisson. Spring stiffness (k_{barr}) for the soil-caisson system, due to the horizontal soft layer, $k2$, passing shear waves (Equation (4. 9)) and soft walls, $k1$, passing compression waves (Equation (4. 8)), is estimated as being (Equation (4. 10)):

$$k1 = \frac{2 \cdot E_g \cdot H}{S_2} \qquad (4.\ 8)$$

$$k2 = \frac{G_g \cdot B}{S_1} \tag{4. 9}$$

$$K_{barr} = k1 + k2 \tag{4. 10}$$

While the dashpot, C_{barr} is equal to:

$$C_{barr} = \frac{2k_{barr}\xi_{IS}}{\omega_{IS}} \tag{4. 11}$$

Where ξ_{IS} is the equivalent damping mobilized in the barriers and $\omega_{IS} = \frac{2\pi}{T_{is}}$. Regarding the spring that connect the foundation with the superstructure, it is simple to realise that m_{str} is the first modal participating mass of superstructure, while K_{str} is the structural stiffness in a fixed base condition. As already mentioned, the foundation ground stiffness is much greater than the stiffness of the barriers and for this reason the increase in period given by the SSI can be neglected. However, if the soil-structure interaction is particularly relevant ($\frac{H_{str}}{V_S T_{FB}} > 0.10$ as suggested by NIST, 2012) the value of K_{str} can be reduced by using the theory of the replacement oscillator and a value of K_{eq} can be used. According to Wolf (1985) if K_r denotes the stiffness of the soil-foundation system referring only to the rotational mode, an equivalent fixed-base system of stiffness K_{eq} can be introduced (Figure 4. 36), as:

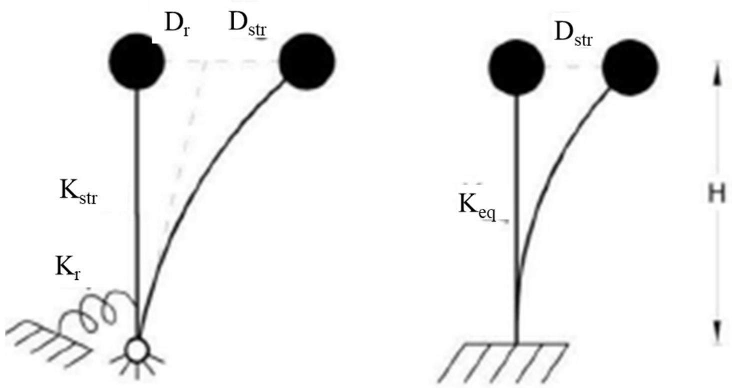

Figure 4. 36. Replacement oscillator

$$K_{eq} = \frac{K_{str}D_{str}}{D_{str}+D_r} = \frac{K_{str}}{1+\frac{H^2K_{str}}{K_r}} \tag{4. 12}$$

in which K_{str} and K_r are the stiffnesses of the structure and the foundation respectively; D_{str} stands for the structural horizontal displacement; D_r for the lateral displacement due to the rotational capability of the foundation and H for the height of the equivalent SDOF. The procedure to evaluate the stiffness of the structural elements K_{str} is well established while it is possible to estimate $K_r$with the solution proposed by Gazetas (1991).

The value of C_{str} is equal to:

$$C_{str} = \frac{2k_{str}\xi_{str}}{\omega_{str}} \tag{4. 13}$$

The equations of the coupled horizontal motions suitable for the idealized GSI system can be expressed as follows (Figure 4. 35):

$$m_{IS}\ddot{u}_{IS} + m_{str}\ddot{u}_{str} + C_{bar}\left(\dot{u}_{IS} - \dot{u}_g\right) + K_{barr}\left(u_{IS} - u_g\right) = 0 \tag{4. 14}$$

$$m_{str}\ddot{u}_{str} + C_{str}(\dot{u}_{str} - \dot{u}_{IS}) + K_{str}(u_{str} - u_{IS}) = 0 \tag{4. 15}$$

Assuming relative displacements as Lagrangian:

$$v_{str} = u_{str} - u_{IS} \tag{4. 16}$$

$$v_{IS} = u_{IS} - u_g \tag{4. 17}$$

The equations of motion become:

$$(m_{IS} + m_{str})\ddot{v}_{IS} + m_{str}\ddot{v}_{str} + C_{barr}\dot{v}_{IS} + K_{barr}v_{IS} = -(m_{str} + m_{IS})\ddot{u}_g \tag{4. 18}$$

$$m_{str}\ddot{v}_{IS} + m_{str}\ddot{v}_{str} + C_{str}\dot{v}_{str} + K_{str}v_{str} = -m_{str}\ddot{u}_g \tag{4. 19}$$

And, in matrix form:

$$[M]\cdot\{\ddot{v}\}+[C]\{\dot{v}\}+[K]\{v\}=-[M][R]\,\ddot{u}_g \qquad (4.\ 20)$$

With $[R]=[1{,}0]^T$, $[v]=[v_{IS},v_{str}]^T$.

The system can be solved, step by step, using Newmark's method with a numerical code in Matlab. It is also possible to derive some remarkable dynamic information by manipulating equations (4. 18) and (4. 19). Dividing the eq. (4. 18) by the total mass $M=m_{IS}+m_{str}$ and the eq. (4. 18) by the structural mass, m_{str}, and introducing the mass ratio gamma $\gamma=\frac{m_{str}}{M}$:

$$\gamma\ddot{v}_{str}+\ddot{v}_{IS}+2\xi_{IS}\omega_{IS}\dot{v}_{IS}+\omega_{IS}^2 v_{IS}=-\ddot{u}_g \qquad (4.\ 21)$$

$$\ddot{v}_{IS}+\ddot{v}_{str}+2\xi_{str}\omega_{str}\dot{v}_{str}+\omega_{str}^2 v_{str}=-\ddot{u}_g \qquad (4.\ 22)$$

Introducing the circular frequency:

$\omega_{IS}^2=\frac{K_{barr}}{m_{IS}+m_{str}}$ and $\omega_{str}^2=\frac{K_{str}}{m_{str}}$

And the critical damping ratio:

$\xi_{IS}=\frac{c_{barr}}{2M\omega_{IS}}$ and $\xi_{str}=\frac{c_{str}}{2m_{str}\omega_{str}}$

Solving the eigenvalue problem for the coupled system of the two previous equations leads to the evaluation of the two frequencies of the DDOF system:

$$\omega_1^2=\frac{1}{2(1-\gamma)}\left\{\omega_{IS}^2+\omega_{str}^2-\sqrt{(\omega_{IS}^2+\omega_{str}^2)^2+4\gamma\omega_{IS}^2\omega_{str}^2}\right\} \qquad (4.\ 23)$$

$$\omega_2^2=\frac{1}{2(1-\gamma)}\left\{\omega_{IS}^2+\omega_{str}^2+\sqrt{(\omega_{IS}^2+\omega_{str}^2)^2+4\gamma\omega_{IS}^2\omega_{str}^2}\right\} \qquad (4.\ 24)$$

Putting $\varepsilon=\frac{\omega_{IS}^2}{\omega_{str}^2}$, the first of the above expressions gives:

$$\omega_1^2=\frac{\omega_{str}^2}{2(1-\gamma)}\left\{\varepsilon+1-\sqrt{(\varepsilon-1)^2+4\gamma\varepsilon}\right\} \qquad (4.\ 25)$$

Considering that, for an effective geotechnical seismic isolation, it is necessary that $\omega_{IS} \ll \omega_{str}$ and therefore $\varepsilon \ll 1$, developing in series the quantity in brackets up to the terms ε^2, we obtain:

$$\omega_1^2 \cong \frac{\omega_{str}^2}{2(1-\gamma)}\{2(1-\gamma)\varepsilon - 2\gamma(1-\gamma)\varepsilon^2\} \tag{4. 26}$$

Or:

$$\omega_1^2 \cong \frac{\omega_{IS}^2}{2(1-\gamma)}\{2(1-\gamma) - 2\gamma(1-\gamma)\varepsilon\} = \omega_{IS}^2(1-\gamma\varepsilon) \tag{4. 27}$$

The second frequency it is therefore obtained as:

$$\omega_2^2 \cong \frac{\omega_{str}^2}{(1-\gamma)}(1+\gamma\varepsilon) \tag{4. 28}$$

Once the eigenvalues are known, the two modal vectors are also deduced. Developing in series and using the same approximations, we obtain:

$$\varphi_1 = \begin{bmatrix} 1 \\ \varepsilon \end{bmatrix}; \varphi_2 = \begin{bmatrix} 1 \\ -[1-(1-\gamma)\varepsilon]/\gamma \end{bmatrix}$$

The first modal component is related to v_{IS} and the second to v_{str}; moreover, it is observed that in the first mode the second component is negligible compared to the first. A representation of the modes is given in Figure 4. 37:

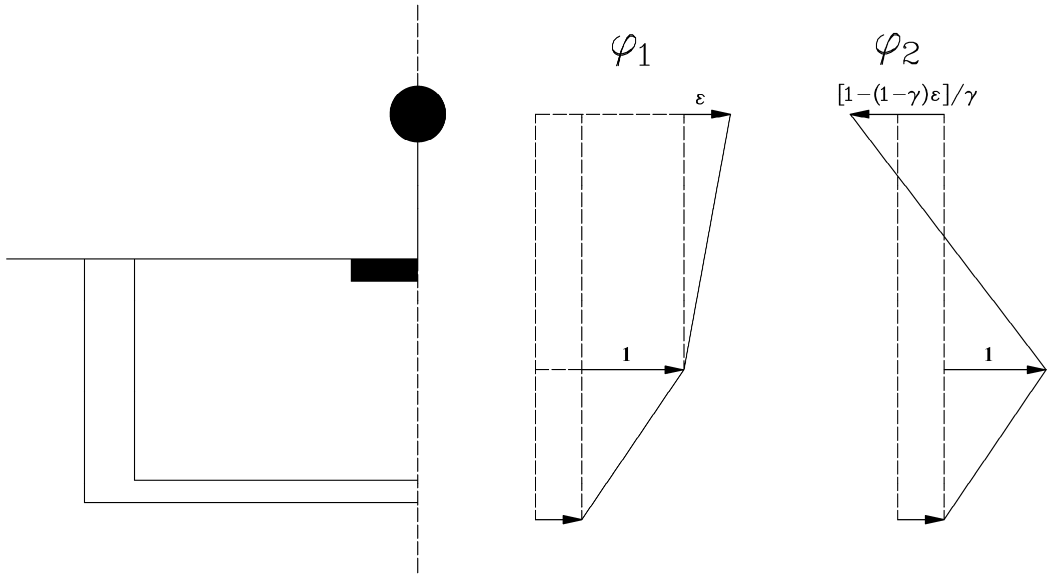

Figure 4. 37. Soft caisson vibration modes with structure.

The modal masses, neglecting terms of degree greater than one, are given by the following expressions:

$$M_1 = \varphi_1^T[M]\varphi_1 = M[1\ \varepsilon]\begin{pmatrix}1 & \gamma\\ \gamma & \gamma\end{pmatrix}\begin{bmatrix}1\\ \varepsilon\end{bmatrix} = M(1+2\varepsilon\gamma) \tag{4. 29}$$

$$\begin{aligned} M_2 &= \varphi_2^T[M]\varphi_2 \\ &= M[1\quad -[1-(1-\gamma)\varepsilon]/\gamma]\begin{pmatrix}1 & \gamma\\ \gamma & \gamma\end{pmatrix}\begin{bmatrix}1\\ -[1-(1-\gamma)\varepsilon]/\gamma\end{bmatrix} \\ &= \frac{M(1-\gamma)(1-2(1-\gamma)\varepsilon)}{\gamma} \end{aligned} \tag{4. 30}$$

The modal participation coefficients are :

$$L_1 = \frac{\varphi_1^T[M][R]}{M_1} = 1-\gamma\,\varepsilon$$

$$L_2 = \frac{\varphi_2^T[M][R]}{M_2} = \gamma\,\varepsilon$$

It is noted that, due to the assumption on ε, $L_2 \ll L_1$; therefore, the contribution of the second mode on the seismic response of the system is negligible compared to that of the first one.

In order to validate the simplified dynamic system, the total accelerations produced at the centre of gravity of the isolated volume (5-meter depth) in the numerical analyses with Plaxis 2D were compared with those produced by the dynamic system with 2 degrees of freedom (Figure 4. 38). The parameters reported in Table 4. 7 were set in order to reproduce exactly the same parameter used in the numerical analyses performed by Plaxis 2D. As already mentioned, the height of the soft box is 10 metres and the width is 60 metres (*B/H=6*), the thickness of the lower barrier is 1 metre and that of the side barriers is 2 metres.

Table 4. 7. Parameter for isolated soil volume and structure in the 2 degree of freedom dynamic system.

Shear modulus for horizontal barrier, G_g [kN/m²]	Young modulus for vertical barriers, E_g [kN/m²]	Density of soil, ρ [kg/m³]	Structural mass, m_{str} [kg/m]	Structural stiffness, K_{eq} [kN/m/m]
581	1512	1566	26727	6000

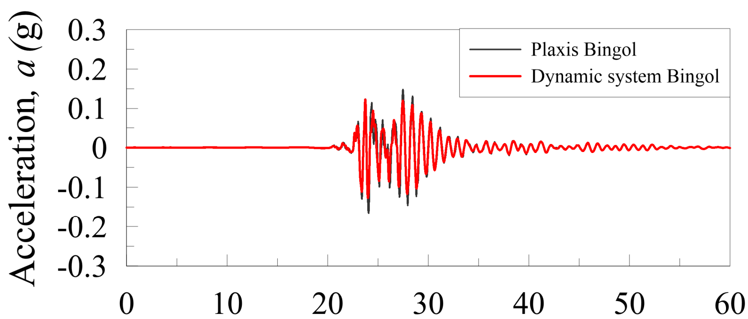

(a)

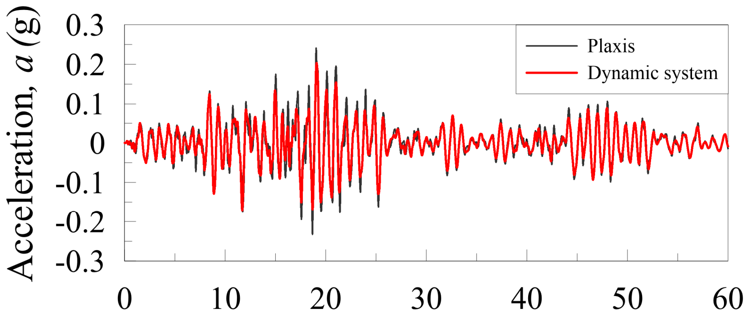
Acceleration, a (g)
0.3
0.2
0.1
0
-0.1
-0.2
-0.3
0
10
20
30
40
50
60
Plaxis
Dynamic system

(b)

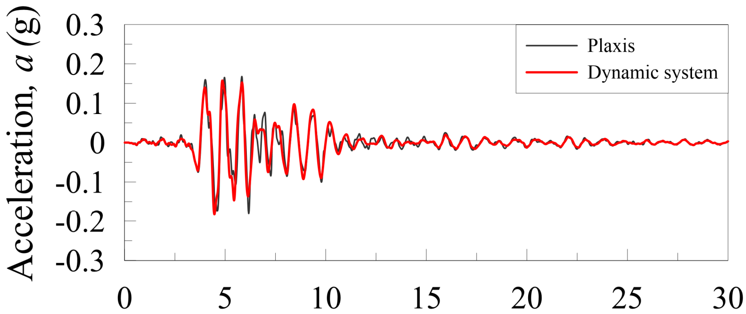
Acceleration, a (g)
0.3
0.2
0.1
0
-0.1
-0.2
-0.3
0
5
10
15
20
25
30
Plaxis
Dynamic system

(c)

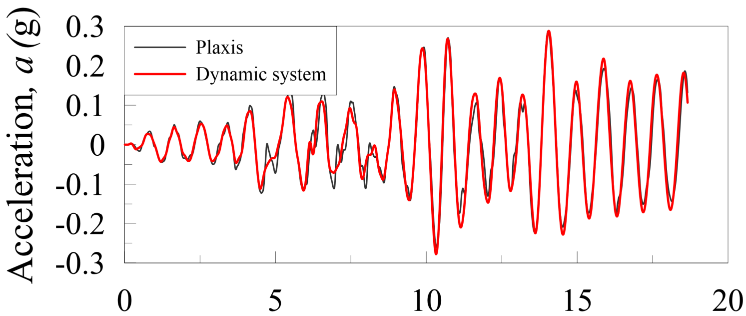
Acceleration, a (g)
0.3
0.2
0.1
0
-0.1
-0.2
-0.3
0
5
10
15
20
Plaxis
Dynamic system

(d)

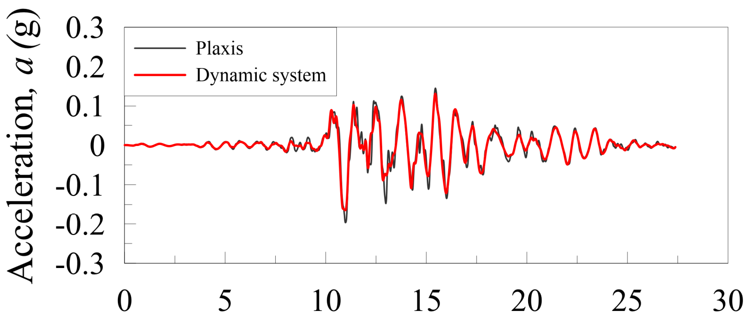
Acceleration, a (g)
0.3
0.2
0.1
0
-0.1
-0.2
-0.3
0
5
10
15
20
25
30
Plaxis
Dynamic system

(e)

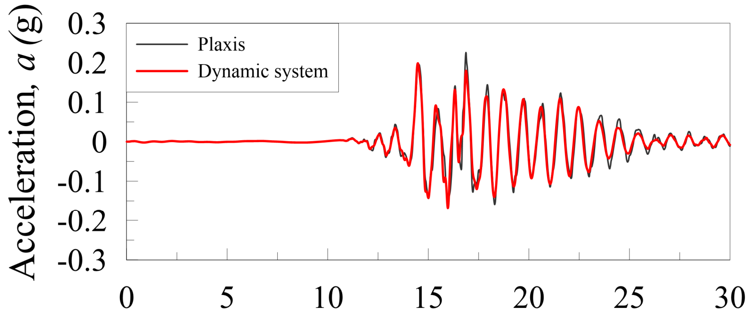

(f)

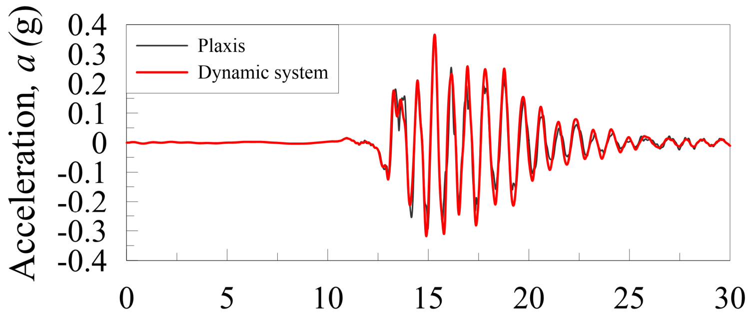

(g)

Figure 4. 38. Comparison between the absolute accelerations recorded at the centre of gravity of the caisson system with Plaxis 2D and via the dynamic system implemented in Matlab for (a) Bingol, (b) Campano Lucano, (c) Friuli, (d) Golbasi, (e) Mt Fnajoll, (f) South Iceland, (g) South Iceland Aftershock.

Figure 4. 39 shows, instead, the comparison between the total accelerations on the roof of the structure obtained through Plaxis 2D and through the dynamic system implemented in Matlab.

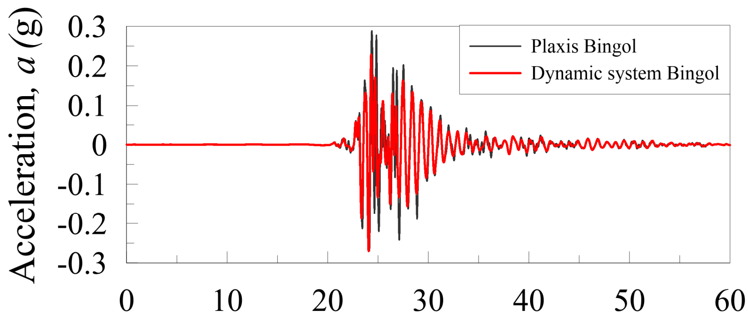

(a)

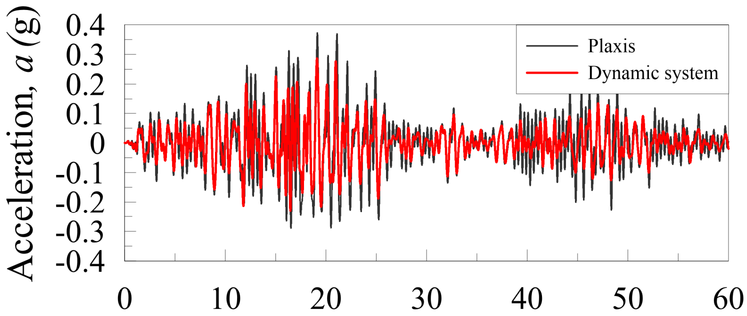
Acceleration, a (g)
Plaxis
Dynamic system
0.4
0.3
0.2
0.1
0
-0.1
-0.2
-0.3
-0.4
0
10
20
30
40
50
60

(b)

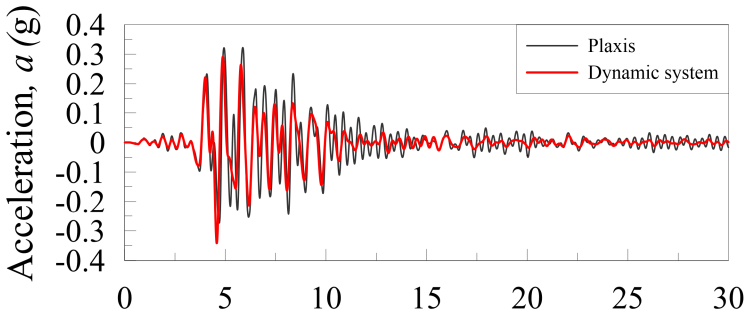
Acceleration, a (g)
Plaxis
Dynamic system
0.4
0.3
0.2
0.1
0
-0.1
-0.2
-0.3
-0.4
0
5
10
15
20
25
30

(c)

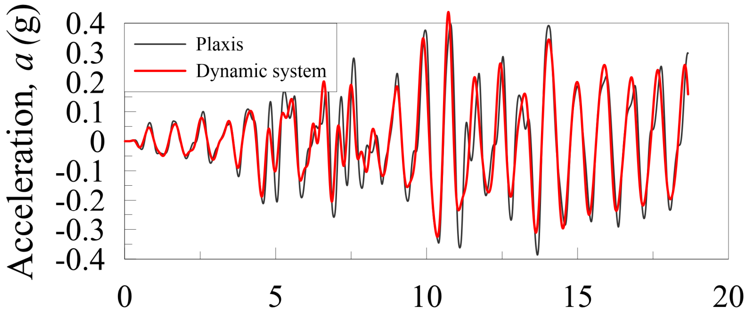
Acceleration, a (g)
Plaxis
Dynamic system
0.4
0.3
0.2
0.1
0
-0.1
-0.2
-0.3
-0.4
0
5
10
15
20

(d)

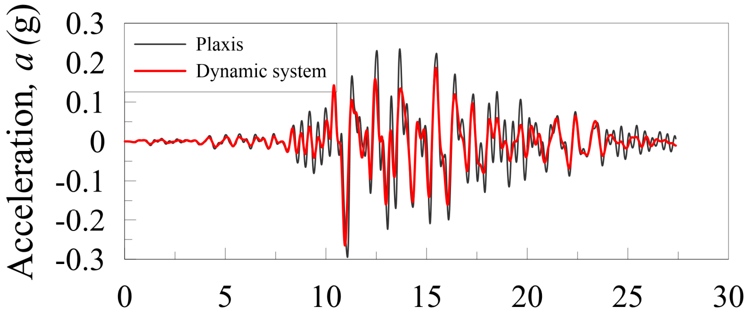
Acceleration, a (g)
Plaxis
Dynamic system
0.3
0.2
0.1
0
-0.1
-0.2
-0.3
0
5
10
15
20
25
30

(e)

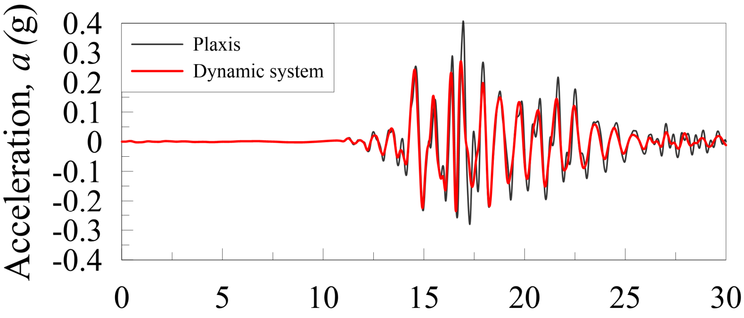

(f)

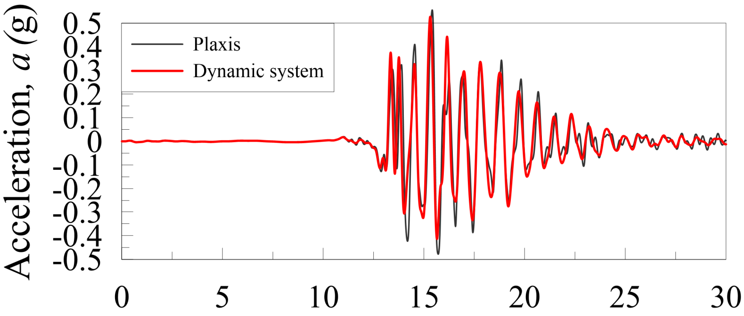

(g)

Figure 4. 39. . Comparison between the absolute accelerations recorded at the roof of the structure with Plaxis 2D and via the dynamic system implemented in Matlab for (a) Bingol, (b) Campano Lucano, (c) Friuli, (d) Golbasi, (e) Mt Fnajoll, (f) South Iceland, (g) South Iceland Aftershock.

The results between the finite element modelling and the dynamic system modelling show substantial agreement, suggesting the possibility of using this tool to have a preliminary estimate of the effects of the soft caisson in a design process with a real seismic hazard.

In particular, this simplified modelling will allow the preliminary dimensioning of the caisson system to maximise its anti-seismic effects. Further finite element or finite difference modelling can then be carried out to refine the design of the caisson.

4.7. Design approach

At this point it seems necessary to outline the design strategy for such an intervention that can be used in any seismic hazard condition or local stratigraphy.

Considering the particular local seismic hazard and the desired safety limit state, the first step in designing the soft caisson system is to perform a local seismic response analysis. This analysis can be carried out with different levels of complexity according to the different lithological complexities of the soil. In most cases, a mono-dimensional equivalent visco-elastic analysis may be sufficient to reliably identify the amplifications produced by the soil and the mean acceleration response spectrum at the surface of soil bank. Using the mean acceleration response spectrum, it will be possible to select the target period of the soft caisson. The target period of the soft caisson should be about 40-50% greater than the period related to the peak of the mean response spectrum. To be more precise, through the acceleration response spectrum, it is necessary to identify the range of periods in which the maximum accelerations occurs and, then, select a soft caisson period of vibration far from the peak of the mean acceleration response spectrum (as much as possible). This is the most important design phase and may even lead to the exclusion of this type of intervention. In fact, if the acceleration response spectrum, deriving from the local seismic response, has its peak values located at high values of the period (*i.e.* 1 second), the intervention with soft barriers may not be suitable for this particular situation, as it may generate a dangerous resonance situation between the frequency contents of the accelerograms and those of the soft box. In this case it is wiser to proceed towards other types of intervention. The identification of the target period of the caisson can also be performed using the elastic design spectrum (without resorting to spectro-compatible accelerograms and local seismic response analysis). By means of stratigraphic and lithographic coefficients, depending on the particular seismic hazard and the equivalent shear wave velocity, a linearized elastic design spectrum can be constructed. However, this simplified approach is not recommended for the obvious simplifications inherent in such a procedure.

Once the target period of the caisson has been set, it is possible to use the simplified DDOF dynamic system. The delineated dynamic system makes it possible to quickly run several attempts to identify the ideal width, depth and thickness of the barriers as well as the percentage of SAP-sand to be used (SAP70-SAP80-SAP90) and the relative properties. Once the pre-dimensioning of the caisson system is complete, it is then possible to validate the designed system using finite element or finite difference numerical model. The design of the caisson system can therefore be considered complete if the total absolute acceleration or other efficiency parameters on the structural system considered leads to acceptable safety levels. If this is not the case, it is possible to vary some of the properties of the barriers to achieve higher isolation efficiencies. Figure 4. 40 summarises the described design strategy.

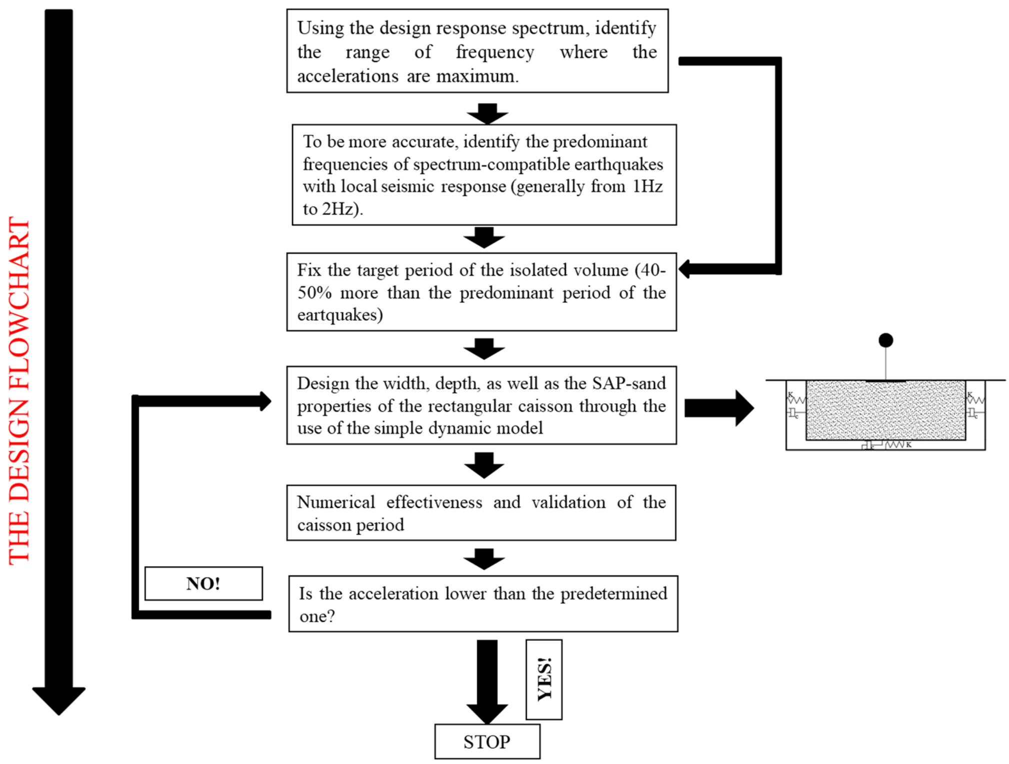

Figure 4. 40. Strategy for the design of soft barriers in the soil with the different steps to follow.

4.8 Some aspects of soft barrier installation techniques

One of the most important aspects of soft anti-seismic barriers concerns their implementation in the soil. For this reason, a number of possible installation procedures is presented here. The aim of this chapter is to provide the reader a range of possible strategies, which can then be validated through full-scale experiments in future work perspective. These strategies have been identified with the experience of the world's leading soil improvement company Keller Holding thorught several meetings.

While the vertical barriers are easy to implement by means of techniques based on soil removal, such as those used to create trenches, the most delicate aspect is the generation of the lower horizontal barrier. It is important to remember that the implementation of the horizontal barrier, able to close the soft box at the bottom, is absolutely necessary for the effectiveness of this technique. It is therefore necessary to distinguish two different application scenarios. In the case where the lower soft barrier is built below the water table level, it is possible to use SAP in the powder (non-hydrated) state. For this reason, through the execution of deep dry soil mixing, it would be possible to mix the dry SAP with the soil at specific depth and therefore, being below the water table, the latter will be naturally hydrated. Such a technique would be possible by performing numerous vertical deep soils mixing drillings which, performed in series, would create a uniform horizontal layer of SAP. Some of Keller's machines may be suitable for this purpose. In particular, Figure 4. 41 shows a specific machine supplied by Keller which allow to drill small holes and, once the depth of interest has been reached, treat areas with a larger diameter. This would make it possible to drill holes with the minimum possible disturbance in the soil and then treat larger areas at depth required. Using Dry Soil Mixing the prerequisite for the chemical reactions, is that the soil is obviously immersed in the water table or that it has a sufficient moisture level for the complete development of the hydration reactions. However, this idea would be inapplicable where the water table is particularly deep.

Perforation diameter from 15 to 30 cm
Diameter of columns from 60 to 71.5cm

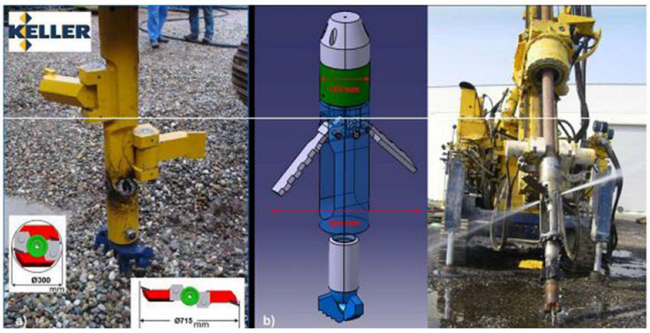

Figure 4. 41. Dry deep soil mixing machine

In case of no water table, injections of hydrated SAP were considered. However, as suggested by the Keller group, the horizontal lower soft barrier would be more easily created if it were confined below and above by a very thin rigid material like a cemented ground. This would allow the SAP gelatinous material to be injected at high pressures and with greater certainty of the treatment area. Injecting hydrated SAP at very high pressures would destroy the soil matrix, creating SAP-soil zones with even very high percentages of SAP by volume (greater than 60-70%) without the possibility of SAP to branching out or dispersing into external soil areas. The upper and lower confinement of the soft barrier can be achieved through the execution of Lamellar Jet Grouting. Lamellar Jet Grouting is a popular technology that allows the creation of thin strips of cemented material (20-30 cm thick). In particular, the lamellar jet grouting, being carried out by means of vertical and horizontal telescopic rods, can be performed with full control and monitoring and could also deal with areas of soil underneath buildings. It is also possible to inject the horizontal SAP through the execution of a work stabilised trench at one side of the building. Part of this trench may become the vertical barriers later on. Infact, as the depths of the horizontal barrier are quite small (not more than 15 metres) it is possible to create a side trench to work at the level of the horizontal barrier. In this way the jet grouting and SAP injections could be performed horizontally. This is similar to the no-digging or trenchless technologies allow underground pipes and cables to be laid or existing underground pipelines to be partially or totally restored or replaced without open trenching, avoiding tampering with the surface (roads, railways, airports, forests, rivers and canals, areas of high environmental value, historic squares, etc.). The possibility of making the horizontal SAP layer in this particular way was called 'jet grouting-SAP-jet grouting sandwich' because of its particular shape. As it was not possible to carry out full-scale tests to validate the feasibility of this idea, it is not possible to confirm its total applicability. However, the effect of the creation of lamellar jet grouting, below and above the horizontal soft barrier, has been studied from a numerical point of view. For this reason, the effects of the modified soft caisson (with jet grouting) was analysed comparing the acceleration produced in the model, during the Bingol earthquake (Table 4. 2), with the no jet grouting case. Figure 4. 42 shows the system designed using the Jet-SAP-Jet sandwich.

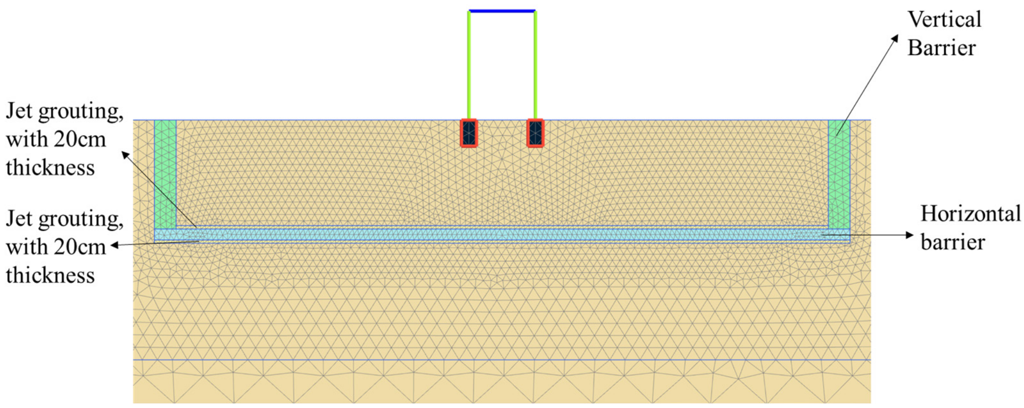

Figure 4. 42. Numerical model with implementation of the Jet-SAP-Jet sandwich system

To derive the properties in terms of stiffness and strength of jet grouting, reference was made to a work of Toraldo *et al.* (2018). Typical values of resistance parameters for jet grouting can be seen in Table 4.8. In particular,

Table 4.8 shows the values of friction angle and cohesion evaluated by triaxial tests on jet grouting samples at different cell pressures. It is clear that jet grouting produces a completely different material from the sand.

Table 4. 8. Mohr–Coulomb parameters and compressive strengths for different jet-grouted materials

Reference [-]	Soil type [-]	φ [-]	c [MPa]	q_c (at σ_c=0kPa) [MPa]	q_c (at σ_c=200kPa) [MPa]
Bzòwka (2009)	Sandy	58.2	2.3	16.1	18.4
Croce & Flora (1998)	Silty Sand	26.1	3.2	10.3	10.6

A further essential aspect is the predominant role of cohesion on total strength. In fact, the results produced for zero confinement and 200kPa confinement show a very limited contribution given by the frictional resistance. For this reason, jet grouting is usually characterised by the presence of only cohesion and neglecting the frictional component. The uniaxial resistance (q_u) can be related to the cohesion (c) and the angle of friction (φ) by the following relationship:

$$q_u = \frac{c}{\alpha} \quad (4.\ 31)$$

Where

$$\alpha = \frac{1}{2 \cdot \tan\left[\left(\frac{\pi}{4}\right) + \left(\frac{\varphi}{2}\right)\right]} \quad (4.\ 32)$$

Furthermore, in some cases, jet grouting layers may be subject to tensile stress. Based on a comprehensive experimental observation on different jet-grouted soils, Van der Stoel (2001) suggests the tension cut-off is expressed by the following functions of the uniaxial compressive strength for granular soils:

$$f_t = -0.3q_u^{0.8} \tag{4. 33}$$

Regarding the stiffness of jet-grouting, the literature includes numerous examples (see Table 4. 9) where authors suggest linear relationships between the secant or tangent Young's moduli computed at different strain levels and the uniaxial compressive strength obtained in the same test (Equation (4. 34)).

$$E_0 = \beta q_u \tag{4. 34}$$

Table 4. 9. Relation between Young's modulus and q_u from literature

Reference [-]	Definition of *E* [-]	Soil type [-]	β
Nanni *et al.* (2004)	Tangent unspecified	Gravel and sand	440-1000
Croce *et al.* (1998)	Tanget unspecified	Sandy gravel	210-670
Corce & Flora (1998)	Secant at $\varepsilon_a =$ 0.01%	Silty sand	220-700

A value of β equal to 564 has been selected (Toraldo, 2018). Using a mono-fluid technology, a compressive strength of $q_u = 15MPa$ was selected. From this, a set of stiffness and strength parameters is derived (Table 4. 10):

Table 4. 10. Stiffness and strength parameters for Lamellar Jet Grouting

Coesion, c [MPa]	Young Modulus, E [GPa]	Tensile Strength, f_t [MPa]	Poisson ratio, ν [-]
3.75	8.46	2.61	0.3

Figure 4. 43a shows the accelerations within the isolated volume (at a depth of 5m) for the case with and without sandwich while Figure 4. 43b shows the respective accelerations on the roof of the structure.

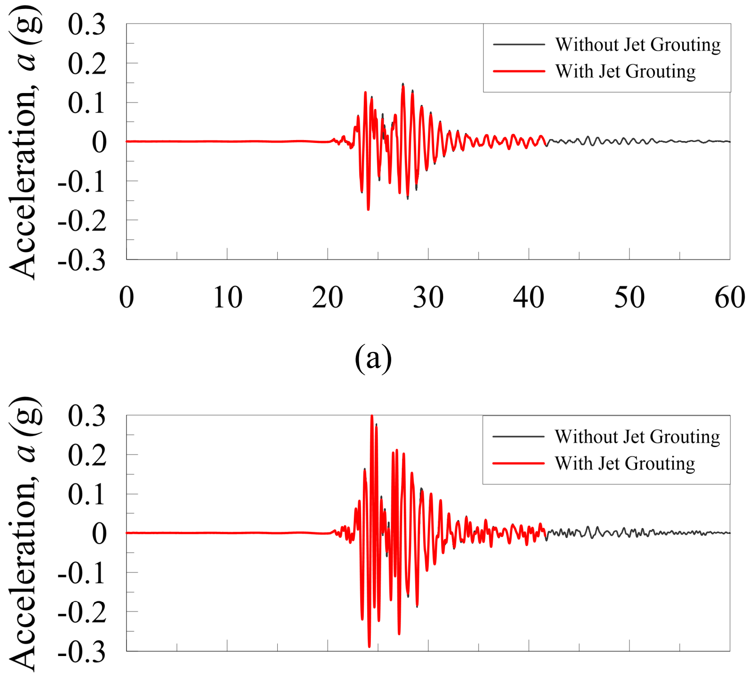

(b)

Figure 4. 43. Comparisons of accelerations recorded in the isolated volume with and without jet grouting (a) and at the roof of the structure with and without jet grouting(b).

It is clearly evident that the presence of jet grouting does not alter the functioning of the soft caisson system and does not compromise its efficiency. However, such a system can offer considerable advantages from the point of view of the technology applicability.

References

Arulnathan, R., Boulanger, R. W., Riemer, M. F. (1998). “Analysis of Bender Element Tests,” *Geotech. Test. J.* **21**(2):120-131

ASTM D-3999. (2003). “Standard test methods for the determination of the modulus and damping properties of soils using the cyclic triaxial apparatus”. ASTM, West Conshohocken.

ASTM D5311–11. (2013). “Standard test method for load controlled cyclic triaxial strength of soil”. ASTM, West Conshohocken

Astuto, G. (2021). “Bio-Induced Partial Saturation as a Liquefaction Mitigation Technique”. *PhD Thesis*. University of Naples Federico II

barriers. *Bull Earthq Eng*. https://doi.org/10.1007/s10518- 016-9912-9

Brignoli, E. G. M., Gotti, M., Stokoe, K. H., II. (1996). “Measurement of Shear Waves in Laboratory Specimens by Means of Piezoelectric Transducers,” *Geotech. Test. J.* **19**(4):384-397

Croce, P., Flora, A. (1998). Effects of jet grouting in pyroclastic soils. *Rivista Italiana di Geotecnica.* **32**(2):5–14

Da Fonseca, A., Ferreira, C., Fahey, M. (2009). “A Framework Interpreting Bender Element Tests, Combining Time-Domain and Frequency-Domain Methods”. *Geotechnical Testing Journal.* **32**(2):91-107

Flavigny, E., Desrues, J., Palayer, B. (1990). “Le sable d’Hostun”. *Revue Française de Géotechnique*. **53**:67–70.

Flora, A., Lombardi, D., Nappa, V., Bilotta, E. (2018). “Numerical analyses of the effectiveness of soft barriers into the soil for the mitigation of seismic risk”. *Journal of Earthquake Eng*. **22**(1):63–93.

Gazetas, G. (1991). “Formulas and charts for impedances of surface and embedded foundations”. *J Geotech Eng, ASCE*. **117**(9):1363–81.

Greening, P. D., and Nash, D. F. T. (2004). “Frequency Domain Determination of G0 Using Bender Elements”. *Geotech. Test. J.* **27**(3):288-294

Greening, P. D., Nash, D. F. T., Benahmed, N., Viana da, Fonseca A., Ferreira, C. (2003). “Comparison of Shear Wave Velocity Measurements in Different Materials Using Time and Frequency Domain Techniques” *Proceedings of Deformation Characteristics of Geomaterials*, Lyon, France, 22–24 September, Balkema, Rotterdam, pp. 381–386.

Hardin, B., Drnevich, V. (1972). “Shear modulus and damping in soils: measurement and parameter effects”. *J. Soil Mech. Found. Div. ASCE*. **98**(6):603–624

Jovičić, V. (2004). “Rigorous Bender Element Testing”. *Workshop on Bender Element Testing of Soils*, University College, London.

Jovičić, V., Coop, M. R., Simic, M. (1996). “Objective Criteria for Determining Gmax from Bender Element Tests” *Geotechnique*. **46**(2):357-362.

Kirtas, E., Pitilakis, K. (2009). “Subsoil interventions effect on structural seismic response. Part II: parametric investigation”. *Journal of Earthquake Engineering.* **13**(3):328–344.

Kirtas, E., Rovithis, E., Pitilakis, K. (2009). “Subsoil interventions effect on structural seismic response. Part I: validation of numerical simulations”. *Journal of Earthquake Engineering*. **13**(2):155–169

Kottke, A.R., Wang, X., Rathje, E.M. (2019). “Technical Manual for Strata”. *Geotechnical Engineering Center*, University of Texas, Austin (USA).

Kuhlemeyer R.L., Lysmer J. (1973). “Finite Element Method Accuracy for Wave Propagation Problems”. *Journal of Soil Mechanics & Foundations*, Div. ASCE **99**(5):421–427

Kumar S.S., Krishna A.M., Dey A. (2018). “Dynamic properties and liquefaction behaviour of cohesive soil in northeast India under staged cyclic loading”. *J Rock Mech Geotech Eng*. **10**:958–967

Lee, J. S., Santamarina, C. (2005). “Bender Elements: Performance and Signal Interpretation,” *J. Geotech. Geoenviron. Eng.* **131**(9):1063:1070.

Leong, E. C., Yeo, S. H., Rahardjo, H. (2005). “Measuring Shear Wave Velocity Using Bender Elements,” *Geotech. Test. J.* **28**(5):488-498.

Mancuso, C., Simonelli, A. L., Vinale, F. (1989.) “Numerical analysis of in situ S-wave measurement,” *Proceedings 12th Int. Conf. on Soil Mechanics and Foundation Engineering*, Rio de Janeiro, Brazil. **1**:277–280.

Massarsch, K.R. (2004). “Mitigation of Traffic-induced Ground Vibrations”. *Proc. 11th international conference on earthquake geotechnical engineering, pp.22–31. Berkeley, California (USA).*

Massarsch, K.R. (2005). “Vibration isolation using gas-filled cushions”. *Proc. Sessions of the Geo-Frontiers Congress, Austin, Texas (USA).*

Matasovic N., Vucetic M. (1993). “Cyclic characterization of liquefiable sands” *Journal of Geotech. Eng*. ASCE **119**:1805-1822.

Nanni, E., Oberhuber, J. & Froldi, P. (2004). “L’utilizzo della metodologia jet grouting per l’ampliamento e la ristrutturazione di edifici esistenti (in ambito urbano)”. *Proceedings of the 22nd national geotechnical conference*, Palermo, Italy, pp. 403–407 (in Italian).

Nappa V, Bilotta E, Flora A. (2016). “Soft barriers for the mitigation of seismic risk”. *Proc Eng.* **158**:404–409.

Nappa, V., Bilota E., Flora A. (2019). “Experimental and Numerical Investigation on the Effectiveness of Polymeric Barriers to Mitigate Vibrations”. *Geotech Geol Eng.* **37**:4687–4705.

Nappa, V., Bilotta, E., Flora, A., Madabhushi, G. (2016). “Centrifuge modelling of the seismic performance of soft buried barriers”. *Bullettin of Earthquake Engineering* **14**:2881–2901. org/10.1016/j.proeng.2016.08.463

National Institute of Standards and Technology (NIST). 2012. “Soil-structure interaction for building structures”. Report No. NIST GCR 12-917-21. Gaithersburg, MD, U.S.: Prepared for U.S. Department of Commerce.

Pennington, D. S. (1999). “The Anisotropic Small Strain Stiffness of Cambridge Gault Clay,” PhD Thesis, University of Bristol, UK.

Sánchez-Salinero, I., Roesset, J. M., Stokoe, K. H., II. (1986). “Analytical Studies of Body Wave Propagation and Attenuation”. *Geotechnical Report No. GR86–15*, Civil Engineering Department, University of Texas at Austin.

Toraldo, C., Modoni. G., Ochmański, M., Croce P. (2018). “The characteristic strength of jet-grouted material”. *Géotechnique.* **68**(3):262-279

Van der Stoel, A. E. (2001). “Grouting for pile foundation improvement”. PhD thesis, Delft University Press, Delft, the Netherlands.

Viggiani, G., and Atkinson, J. H. (1995). “Interpretation of Bender Element Tests,” *Geotechnique*, **45**(1):149-154.

Wang, Y. H., Lo K. F., Yan, W. M., Dong, X. B. (2007.) “Measurement biases in the bender element test”. *Journal of Geotechnical and Geoenvironmental Engineering*, ASCE. **133**:564-574.

Wolf, J. P. (1985).” Dynamic Soil-Structure Interaction”. *Englewood Cliffs*, N. J., U.S.A.: Prentice Hall.

5. A NUMERICAL EXAMPLE OF THE GSI TECNIQUES TO THE MONUMENTAL STRUCTURE OF TOWER T19 OF THE WALLS OF CONSTANTINOPLE

In this chapter, the techniques described in Chapters 3 and 4 will be applied to a real case study. In particular, a rigorous numerical analysis will characterise the condition in which the Tower 19, part of the defensive walls of Constantinople, was stood before it was affected by the 1999 Kocaeli earthquake that almost completely destroyed it. Tower19 will be analysed in its *"as-is"* condition. Then it will be evaluated, in a deterministic way, what would have happened using geotechnical seismic isolation techniques. The effects of soil-structure interaction on the Tower19 have already been studied in previous work focusing on a decoupled approach (Flora *et al.* 2021). Based on a considerably increased level of knowledge, regarding both the geometric and material properties of the Tower and soil, this chapter updates all the results found by means of mono-dimensional and three-dimensional analysis and introduces the effects of lateral disconnection and soft barriers geotechnical seismic isolation techniques.

5.1 Introduction

"That city, placed at the junction of two seas and two continents, seemed like a diamond set between two sapphires and two emeralds, to form the most precious stone in a ring of universal empire"

Osman's Dream of Costantinople 1380

The walls of Constantinople or Theodosian Walls are an impressive piece of Byzantine military architecture, the largest in the Byzantine Empire. They surrounded and protected the city of Constantinople (modern-day Istanbul) and are considered one of the most impressive and complex military constructions of antiquity. Even during the last siege by the Turks, the specially designed cannons were not fully effective in breaching the Byzantine walls. The walls of Constantinople were built from the time that the city was founded as the new capital of the Roman Empire (324 AD). Throughout the more than thousand-year history of the Byzantine Empire, the walls were continually fortified until the city fell to the Ottoman Turks (Tuesday 29 May 1453). Constantinople has been the city that has endured the most sieges in the history of the world, capitulating only twice: once in 1204 when it was sacked by the Crusaders and the second and final time in 1453.

Initially, the walls of Constantine were built to protect the city from potential attacks from both land and sea. Later, the Byzantine Emperor Arcadius, seeing that the city was expanding, ordered the architect Flavius Antemius to build a new wall, which was constructed in the 5th century during the reign of Theodosius II. These new walls were so powerful that they were considered impregnable. They saved Constantinople many times from sieges by Arabs, Russian, and Bulgarians. Only gunpowder and cannons made the fortifications obsolete, resulting in three sieges by the Ottomans; the first two were repulsed, but the third was successful for the Ottomans, who conquered Constantinople, and, thus, ended the thousand-year old Eastern Roman Empire.

The walls of Constantinople were kept intact even at the beginning of the Ottoman rule, until in the 19th century when parts of the walls were dismantled to enlarge the old boundaries of the medieval city. Despite the subsequent lack of maintenance, many parts of the walls have survived and are still visible today.

Figure 5. 1 shows the process of enlargement of the city of Byzantium with the consequent construction of new walls.

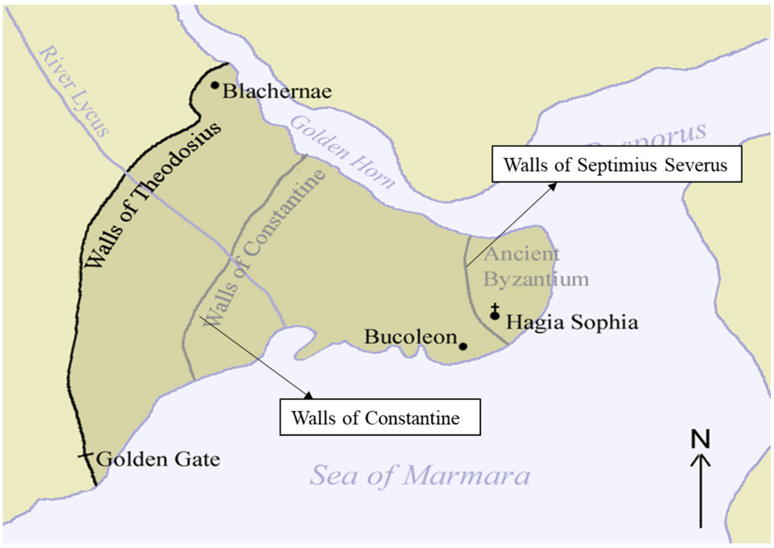

Figure 5. 1. Enlargement of the city of Byzantium resulting in the modification of the protective walls (from Turnbull, 2012).

It can be seen that the city was initially defended by a relatively small walls dating from the period of emperor Septimius Severus (2nd-3rd century AD). When Constantine I moved the capital of the Roman Empire from Rome to Byzantium, which he refounded under the name of "Nova Roma", he greatly expanded the new city and provided it with a new wall of about 2.8 km at west of Severus wall, incorporating an even larger territory. Constantine's walls consisted of a single wall, reinforced with towers at regular intervals. In 408, Emperor Theodosius II began the construction of a new city wall, about 1,500 m west of the centre, extending 5,630 m between the Sea of Marmara and the village of Blacherne near the Golden Horn. The construction of the new city wall began when the emperor was seven years old, although the walls became known as Theodosian Walls. The walls were completed in 413. **Of considerable importance is the fact that on 6 November 447 a strong earthquake destroyed a large part of the walls and towers.** Theodosius II, then, ordered the reconstruction of such walls and, in addition, a second outer row of walls was added, with a large open moat in front of the walls. In its final configuration Figure 5. 2, on the land side the system consisted of two closely spaced defensive lines: an *inner wall*, with a maximum height of 12 m, and an *outer wall*, with a lower height, each one fortified by towers placed at some tens of meters apart.

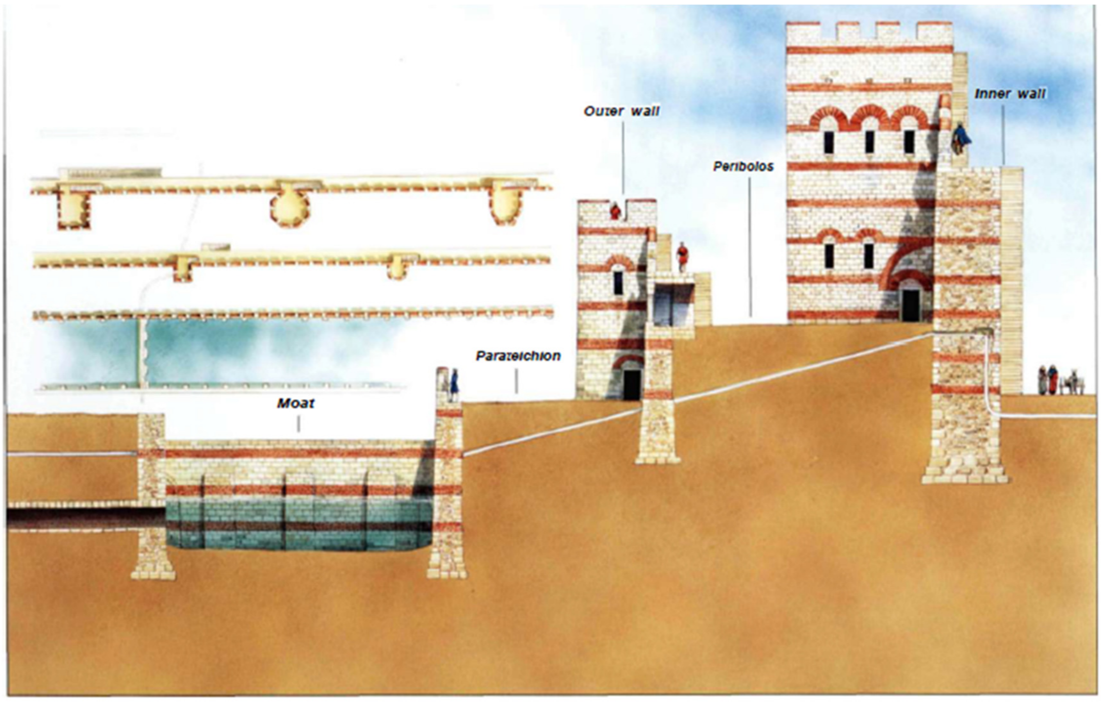

Figure 5. 2. A view of the Theodosian defence system consisting of an inner wall with towers, an outer wall with as many towers, and a moat (from Turnbull 2012).

The city walls were reinforced with 96 towers, square or octagonal or hexagonal, these towers were between 18 and 22 metres high, they were placed at 55 metre intervals. Each crenellated tower had a terrace at the top, its interior was usually divided by a floor into two sections. The lower chamber, which opened out to the city, was used for storage, while the upper section could be entered from the walkway wall, which had slits for seeing and firing projectiles, access to the wall was then provided by large ramps along the interior. Figure 5. 3 shows an axonometric view of a generic tower. The tower shown in Figure 5. 3, as shown later, is practically identical to the Tower19 which will be studied in this thesis.

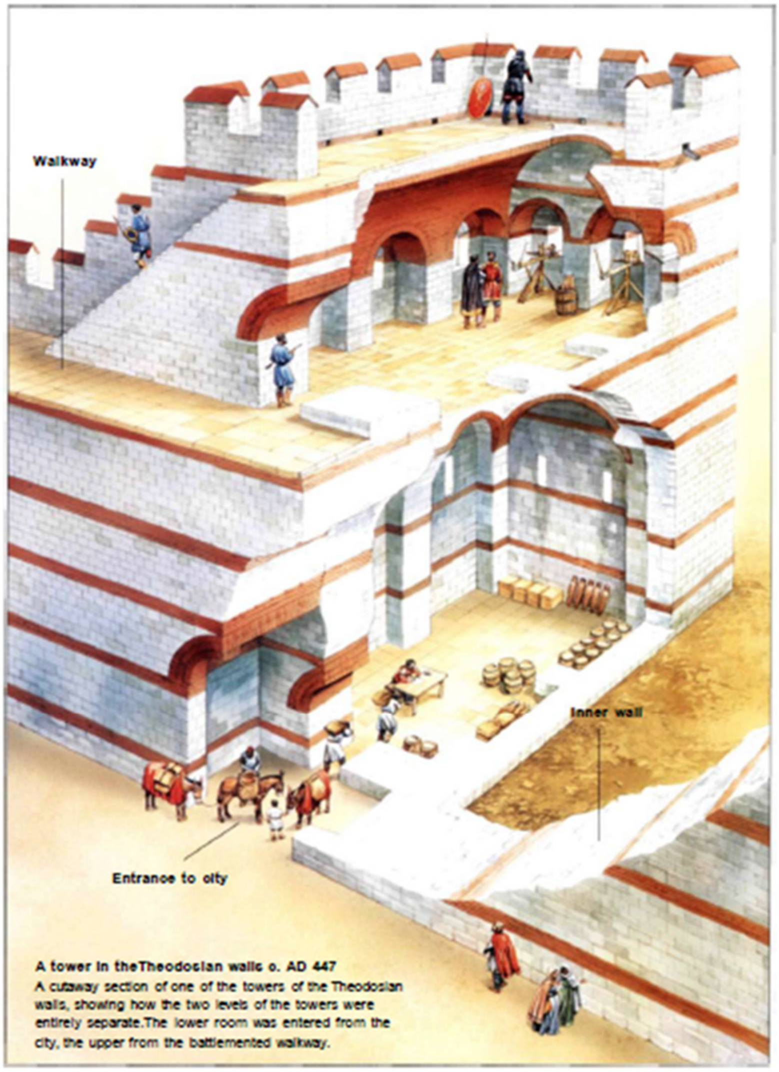

Figure 5. 3. An axonometric view of a square tower (identical to the one that will be modelled) (from Turnbull 2012).

As well as being protected by land walls, sea walls were also built. Ancient Byzantium certainly had sea walls, but the date of construction of the medieval ones is uncertain, though usually also attributed to Constantine. The sea wall is architecturally similar to the land wall, but with a simpler structure, consisting of a single wall and a lower height. Later, long floating chains were also laid between the Golden Horn and the Galata peninsula to prevent foreign ships from entering the harbour without permission. Figure 5. 4a shows a google maps image of the Tower19 while Figure 5. 4b shows the impressive entire system of walls that protected the city of Byzantium with the location of the Tower19 under study.

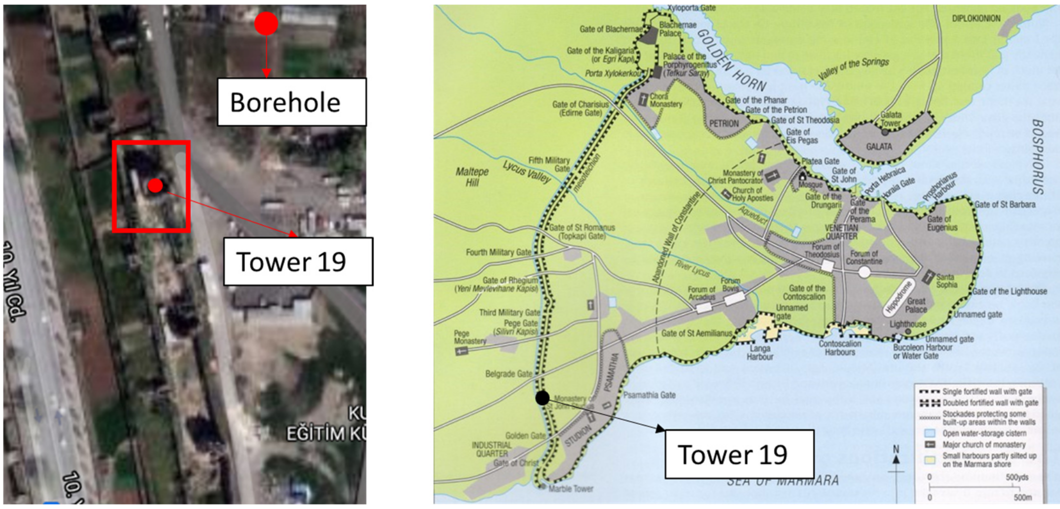

(a) (b)

Figure 5. 4. (a) An image taken from Google Maps with the position of the Tower and the nearest stratigraphic survey, (b) the complete defence system of the city of Constantinople (from Turnbull 2012)

The Istanbul area (and Turkey in general) has a very high seismic hazard. Figure 5. 5 shows the date and epicentres of the most violent earthquakes to date.

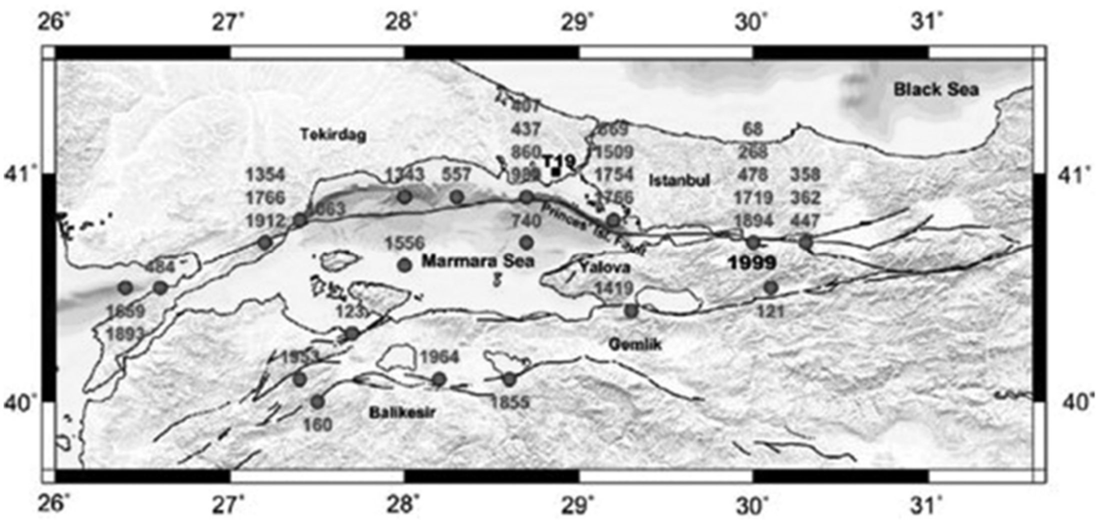

Figure 5. 5. Map of Turkey with location and date of major seismic events.

The strong Kocaeli- Adapazari earthquake of 447, for instance, resulted in the partial collapse of 57 towers and large sections of the walls, and also the subsequent major earthquakes (1509, 1719, 1754, 1766 and 1894) caused significant damages to the walls and towers (Ispir et al. 2014). Repairs were therefore undertaken on numerous occasions, as testified by the inscriptions commemorating the emperors or their servants who undertook the restoration works.

5. 2 Influence of SSI on Tower19

As reported in Figure 5. 4a and Figure 5. 4b the Tower 19 (T19) is located on the south side of the land walls, close to the Marmara Sea and between the Belgrade and Golden Gates (coordinates: 40.99811651299815, 28.921048767990584). It is one of the tallest towers of the walls and was almost totally destroyed by the Koacaeli earthquake (1999). To date, the tower has been partially rebuilt; in particular, the lower part of the tower is still characterised by the original Byzantine style of masonry, while the upper central part is in the Ottoman style. Recent restoration work has completed the tower in the Byzantine style. Figure 5. 6 represent the current half-destroyed situation of Tower 19.

(a)

(b)

(c)

Figure 5. 6. (a) Front view of Tower 19 (b) Side view of Tower 19, (c) Rear view of Tower 19

In order to model the tower accurately, various historical sources were consulted. In particular, reference was made to the Restitution-Report concerning all towers between No. 15 and 19. Fortunately, these reports had several elevations and sections of Tower 19 and it was possible to extrapolate the exact dimensions of the Tower itself (Figure 5. 7-Figure 5. 8).

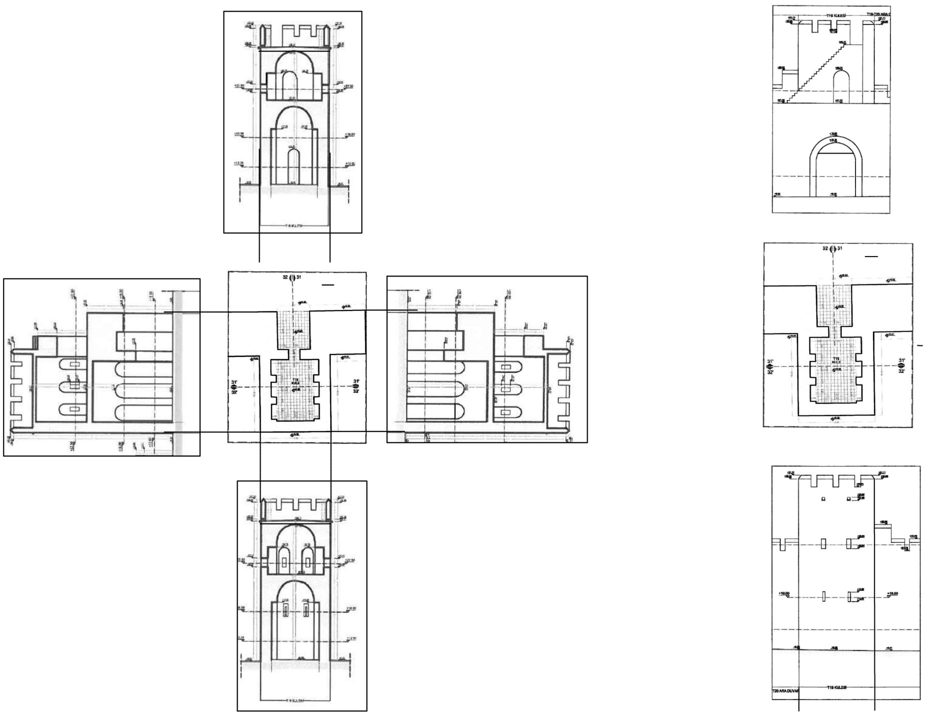

(a) (b)

Figure 5. 7. (a) Vertical sections of Tower 19. (b) Front and rear elevations of Tower 19.

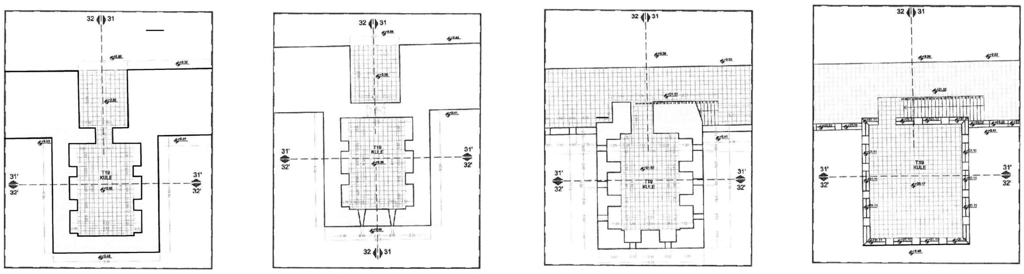

Figure 5. 8. Horizontal sections of Tower 19 at different heights.

The tower was modelled using Autocad3D software (Figure 5. 9)

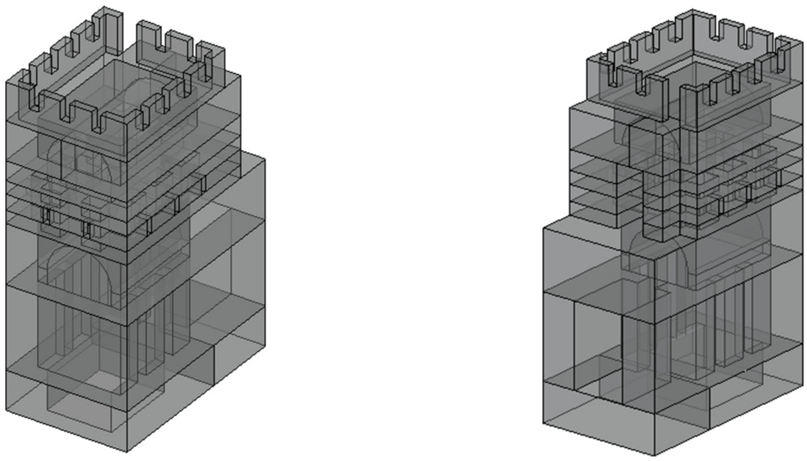

(a) (b)

Figure 5. 9. (a)Front view of Tower19 as modelled in Autocad3D, (b) rear view of Tower19 as modelled in Autocad3D

In particular, the structure was modelled as an aggregate of several superimposed volumes. These volumes were imported into Plaxis 3D and a very fine mesh was created. In particular 7131 element volume with 10 nodes each.

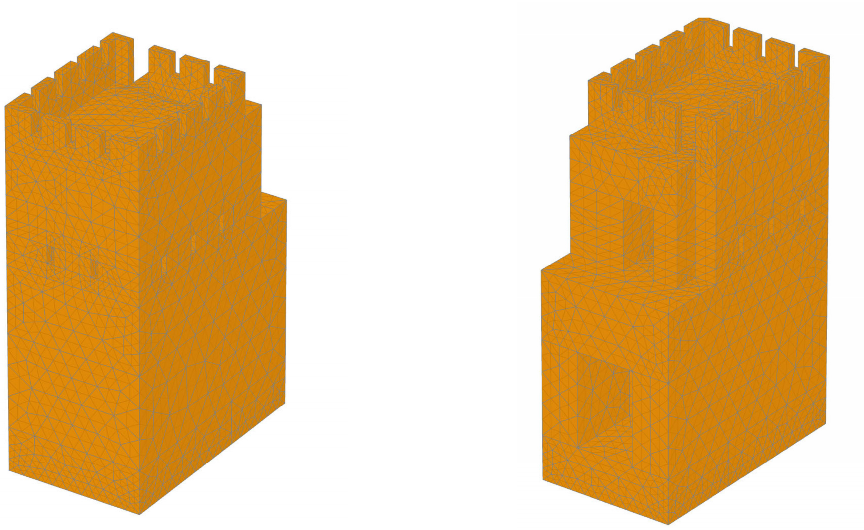

Figure 5. 10. 3D Plaxis finite element modelled tower

The modelled structure does not present major geometrical simplifications. In particular, the two main vaults have been explicitly modelled with their exact dimensions (between ground floor and first floor and between first floor and roof). The correct modelling of the span, rise and thickness of vaults is extremely important in predicting the behaviour of masonry structures. In fact, the vaults, with their geometries, determine the seismic and static actions that are applied on the load bearing walls. The numerous small arch structures and the external stair to the roof were not modelled. The height of the tower between the foundations base level and the roof is 21.65m (without considering the height of the defence wall on the roof). The height of the foundations is 3 metres. The direction parallel to the vaults will be indicated as Y-direction (long side of the Tower) and the direction orthogonal to the vaulting frame will be indicated as X-direction (short side of the Tower). There are very little informations about the material properties of Tower19, specially just before the Kocaeli earthquake (1999). For this reason, it was decided to use linear visco-elastic models as preliminary step. Subsequently, non-linear modelling of the Tower was carried out. The visco-elastic model is able to show the areas where the highest concentrations of stresses (especially tensile stresses) are generated, but not to follow the redistribution of these stresses as a result of possible plasticisations. In particular, the variation of the Young's modulus of the masonry (E_m) may significantly determine the variation of the natural period of vibration of the tower itself. An equivalent homogenised model was considered for masonry according to the available level of knowledge and to the purpose of analysis. Consistently, with the previously mentioned distinction, two kinds of masonry were considered in Table 5. 1: The Ottoman one (masonry M1), which is the least stiff and lightest; the original Byzantine one (masonry M2), which is stiffer and heavier than the Ottoman one; due to the lack of information related to the particular quality of the masonry of the tower 19 these values are selected from modern guidelines (IBC and Eurocode 6). These chosen values are typical of these historical masonries (Lourenco Paulo 1998; Lourenco 2002).

Table 5. 1. Masonry properties for Tower 19.

Masonry Type	Young Modulus, E_m [MPa]	Unit weight, γ_m [kN/m^3]	Possion Modulus, v [-]	Damping ratio, ξ [%]
Ottoman (M1)	900	15	0.2	5
Original Byzantine (M2)	1600	16	0.2	5

5.2.1 Modal Analysis of Tower19

In order to characterise the dynamic properties of Tower 19 in fixed base conditions, two different software were used: *Plaxis3D* and *SAP2000*. Plaxis 3D does not allow to conduct a modal analysis with identification of participating masses and modal shapes while SAP2000, solving the problem in terms of principal coordinates, provides exactly such results. Wanting to study the tower through a direct approach, which involved modelling the ground and the tower in the same numerical model, it was necessary to use both software to get as much information as possible and manage the outputs. Although it is not possible to perform a modal analysis through Plaxis3D, it is still possible to use some strategies to identify the natural vibration periods of the modelled structure. In fact, in a three-dimensional model, in a fixed base condition, it is possible to calculate the natural resonant periods in X and Y direction through the application of sine-sweep at the model base. Figure 5. 11a shows the sinesweep applied at the base and Figure 5. 11b shows the Fourier transform.

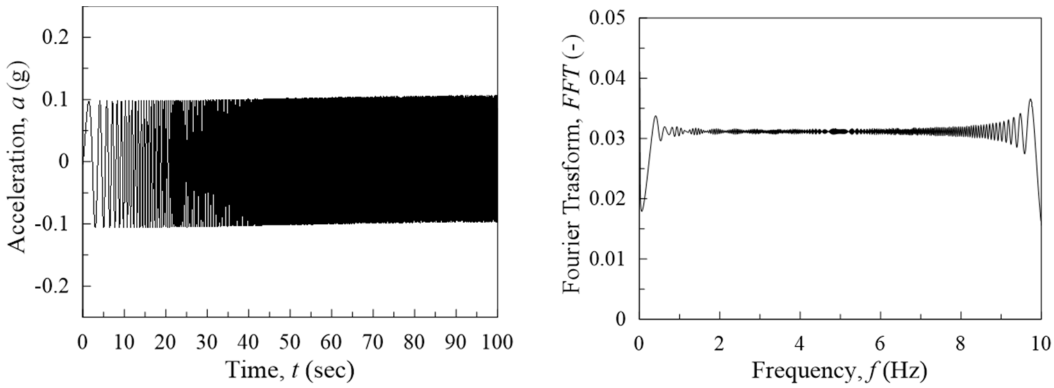

(a) (b)

Figure 5. 11. (a) Sinesweep in accelerations applied to the base of the tower, (b) Fourier transform of Sinesweep

Figure 5. 12 shows the fixed base model implemented in Plaxis3D with the application of the sinesweep in Y and X direction;

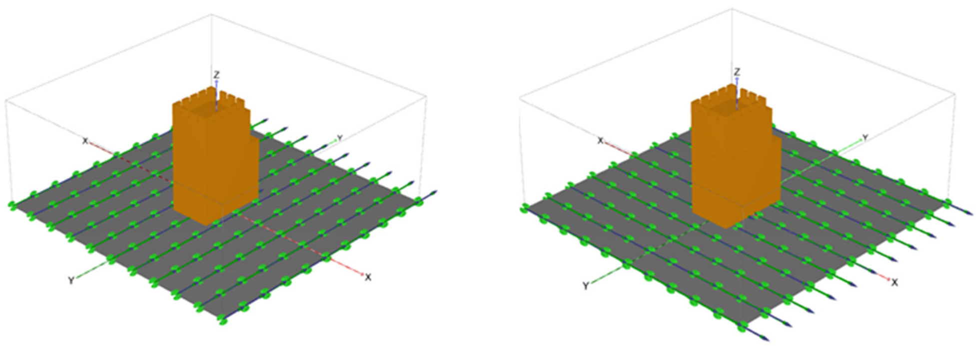

(a) (b)

Figure 5. 12. Numerical fixed base model in Plaxis 3D; (a) Y direction, (b) X direction

Figure 5. 13 shows the absolute accelerations, generated by the application of sinesweep at the base, on the roof of the structure in the X and Y direction with M1 masonry properties. From these it is possible to use an amplification

function to calculate the natural vibration periods of the structure in both directions (Figure 5. 14).

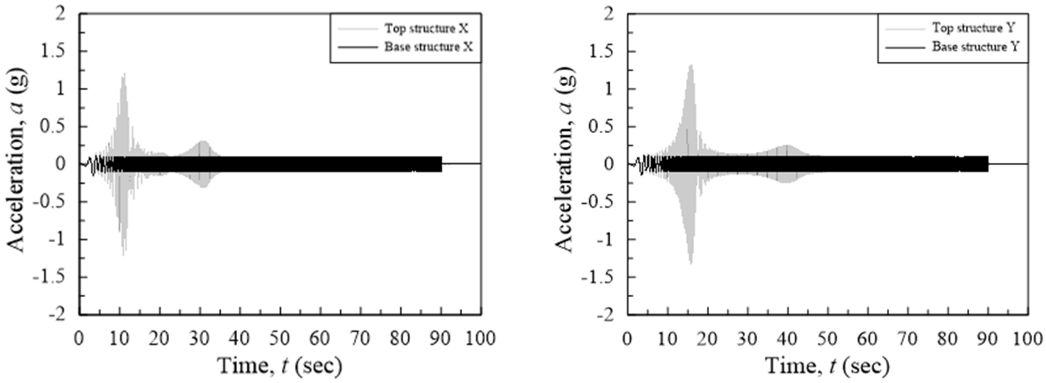

(a) (b)

Figure 5. 13. Absolute Top Acceleration generated by the sine-sweep in X direction (a) and Y-direction (Y).

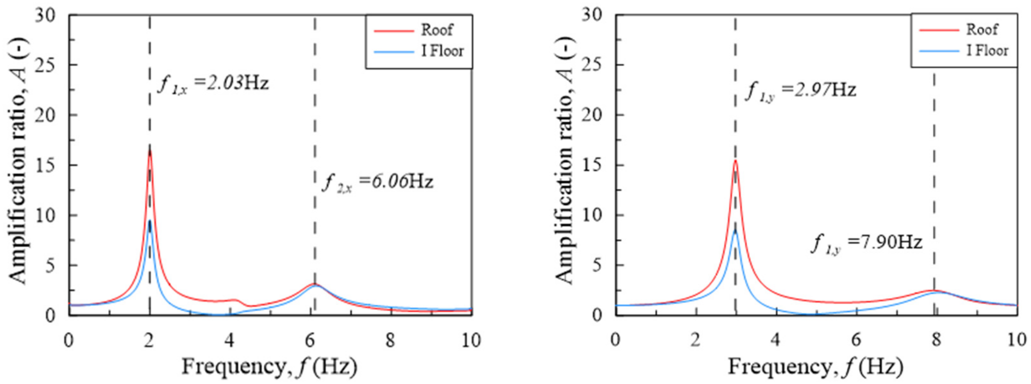

(a) (b)

Figure 5. 14. Amplification acceleration function in X direction (a) and Y-direction (b) with M1 masonry properties.

The same procedure can be applied in the case of towers with M2 properties providing the natural vibration periods shown in Figure 5. 15.

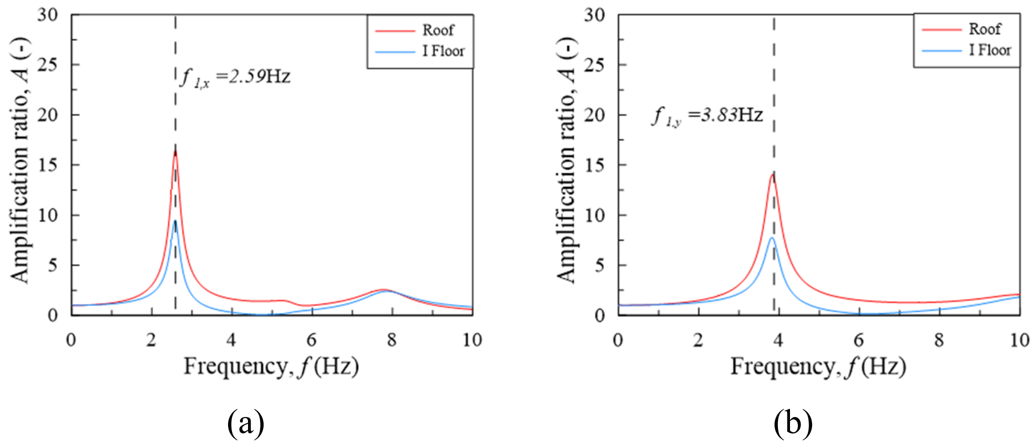

Figure 5. 15. Amplification acceleration function in X direction (a) and Y-direction (b) with M2 masonry properties.

The same modelling of the tower was also carried out in SAP2000 using brick elements. The modelling in SAP allows the calculation of the periods associated with all the vibration modes and the participating masses (Figure 5. 16a and b) as well as the different modal shapes (Figure 5. 17 shows the first modal form dimensioned with respect to the maximum displacement on the roof).

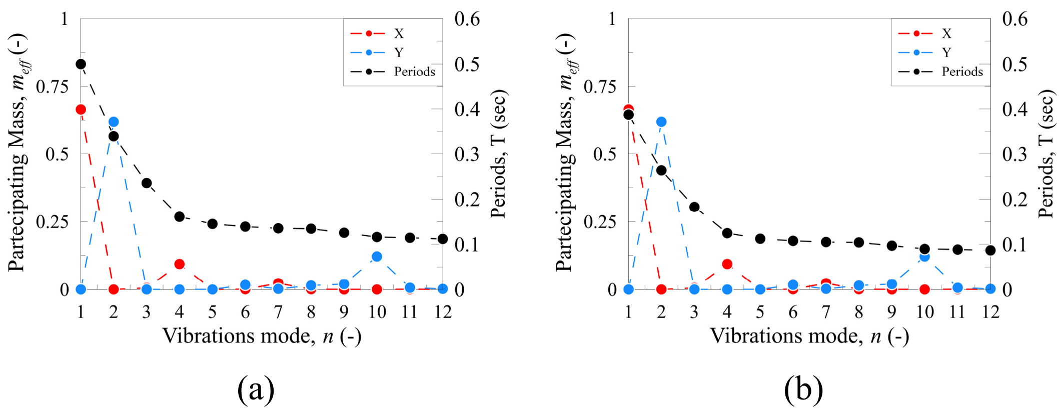

Figure 5. 16. Participating masses and periods associated with the various vibration modes for M1 (a) and M2(b)

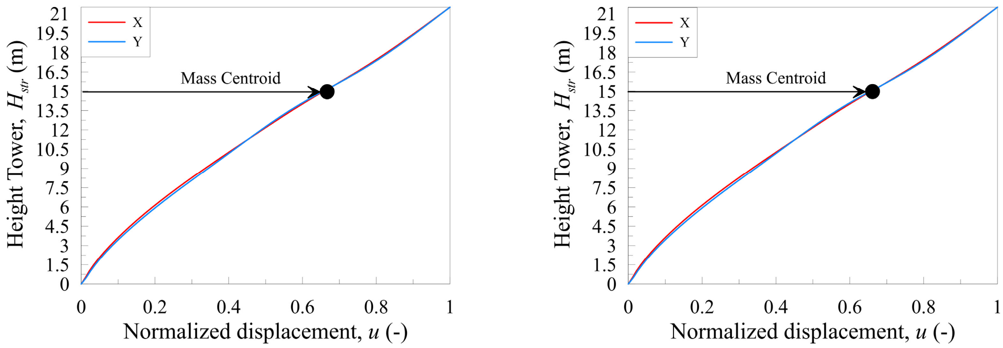

(a) (b)

Figure 5. 17. I modal shapes with the indication of the mass centroid for M1(a) and M2(b)

Modal analysis using Plaxis 3D and SAP2000 identifies exactly the same vibration periods. The participating mass (effective mass) associated with the first mode of vibration is 66% in the X-direction and 62% in the Y-direction (for both M1 and M2). The total mass of the Tower is 3097Mg with M1 masonry properties and 3306Mg with M2. The centroid of the masses of the structure associated with the first mode of vibration is located at a height of approximately 15 metres. Table 5. 2 summarizes all the relevant information related to the isolated Tower.

Table 5. 2. Dynamic Properties of the isolated tower

Structures	I mode (in X) (sec)	II mode (in Y) (sec)	Effective mass (I mode) (Mg)	Effective mass (II mode) (Mg)
M1	0.49	0.33	2044	1920
M2	0.39	0.26	2181	2049

It is also very important to study the effect of the longitudinal wall adjacent to Tower 19. This longitudinal wall can significantly alter the vibration periods found depending on the quality of the tower-wall contact and, therefore, the soil-foundation-structure interaction. Assuming the contact between the tower and the wall as a simple lateral restrain, no major alterations to the natural vibration periods will be generated. On the other hand, assuming the contact as an interlocking (*i.e.* Tower and Wall modelled as a single block unit) profound alterations in the evaluated periods will be generated. What kind of contact there was at the time of the Kocaeli earthquake is impossible to know. However, there are a number of reasons for believing that the most correct way of modelling such an adjacent wall is by simple lateral restrain:

1) The historian Turnbull (Turnbull, 2012), discussing on the different towers, states: "*Although lying along the wall, the towers were part of the same construction, but* ***were built as separate structures. This ensured that different rates of settlement would not cause them to break apart***". This seems to be very logical if one reflects on the fact that a possible siege could have brought down the walls and, therefore, the towers would also have suffered enormous distortions if they had been rigidly connected to the wall. On the other hand, the towers, built as isolated structures, would certainly have suffered less from the traumas that the walls were forced to endure.
2) After more than a thousand years, it is very difficult to conceive that the contact, existed at the time of the Kocaeli earthquake between the walls and the Tower, was *" rigidly connected"*. Especially if one reflects on the number of earthquakes that these structures have suffered. It is more logical to idealize a simple contact between the wall and the tower certainly capable of preventing movement in a direction parallel to the wall.
3) As will be seen later, modelling the tower as an isolated structure or as a structure with a disconnected wall (*i.e.* no perfectly bound between walls and Tower) generates enormous stresses on the tower itself due to a series of resonance phenomena. These effects are drastically reduced if the wall is modelled as perfectly bounded at the structures. Since many towers of the walls of Constantinople were severely damaged during the Kocaeli earthquake and also during many other earthquakes, it is much more logical to foresee that the most severe scenario (tower with disconnected wall) occurred.

In this respect, Figure 5. 18 shows the numerical model of Tower with the presence of the wall as a single unit block and with the disconnection.

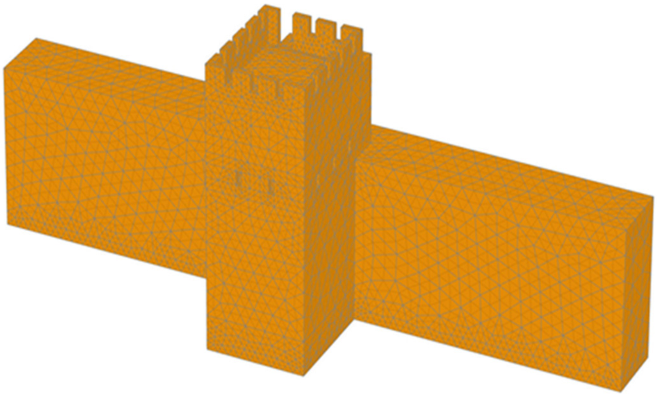

(a)

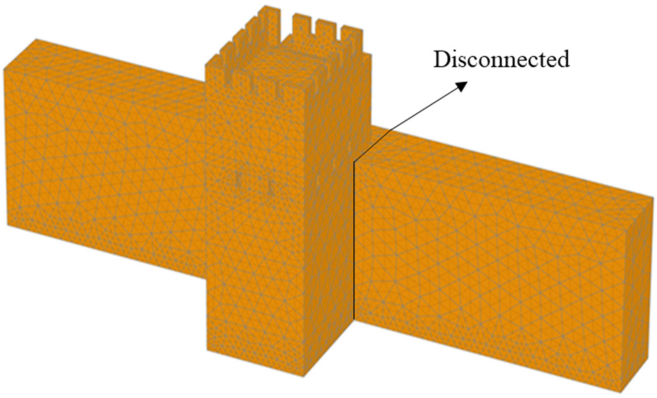

(b)

Figure 5. 18. Different modelling of the wall: (a) perfect contact with the tower, (b) simple support with the tower.

Figure 5. 19 and Figure 5. 20 show the natural resonance frequency of Tower with the presence of the wall modelled as disconnected or connected. As already mentioned, modelling the wall as a simple support, there are very slight variations in period (only in X-direction, from 0.49 sec to 0.46sec for M1 masonry properties and from 0.39sec to 0.36sec for M2 masonry properties).

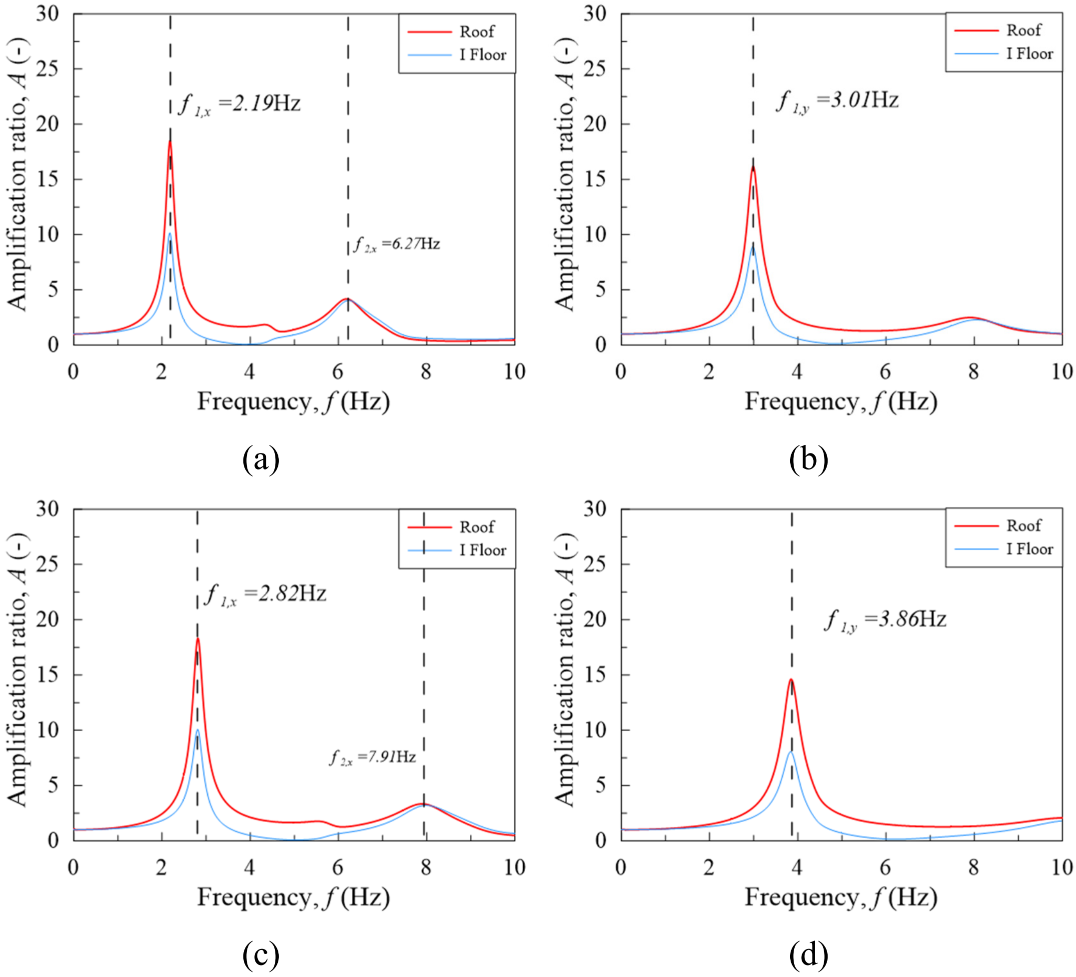

Figure 5. 19. Acceleration Amplification function, in the case of disconnected walls from tower, for M1 in X direction (a) and Y-direction (b); for M2 in X direction (c) and Y-direction (d);

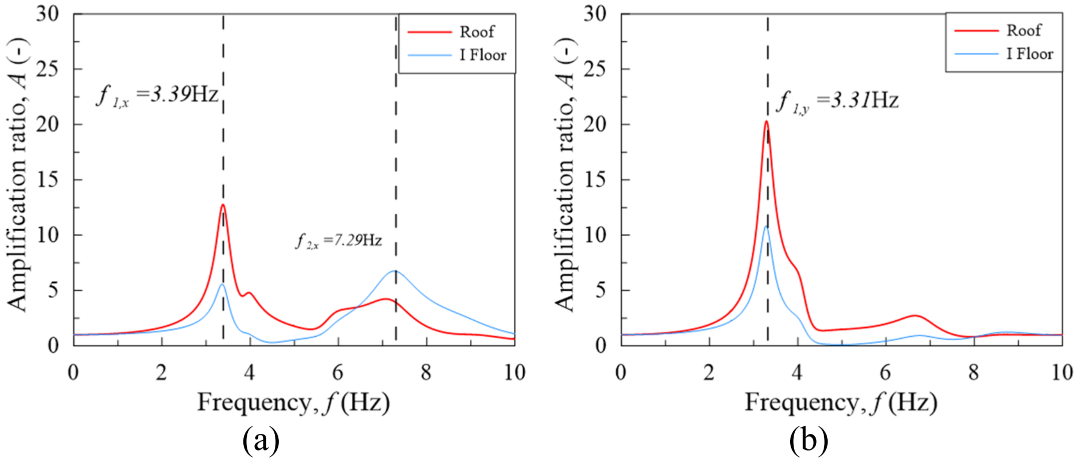

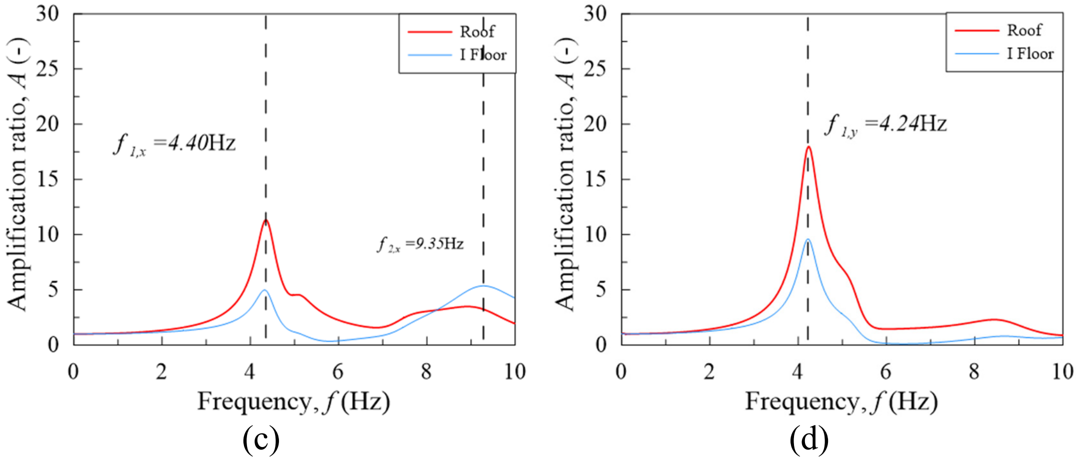

Figure 5. 20. Acceleration Amplification function, in the case of connected walls from tower, for M1 in X direction (a) and Y-direction (b); for M2 in X direction (c) and Y-direction (d);

It can be seen that, modelling the tower and the wall as a single block, the first period in X-direction is equal to that in Y-direction (0.29sec for M1 and 0.23sec for M2). The presence of the wall, rigidly connected to the tower, significantly lowers the natural periods of vibration with predictably significant effects on soil-structure interaction.

5.2.2 Geotechnical characterisation of the site

The municipality of Istanbul carried out an extensive microzoning of the area of interest (south of Istanbul including the area around the Theodosian wall). In particular, using the borehole closest to Tower 19 (Figure 5. 4a, the borehole is around 100 metres away from the Tower), it was possible to extrapolate the stratigraphy and the shear wave velocity V_s beneath the Tower19 (Figure 5. 21).

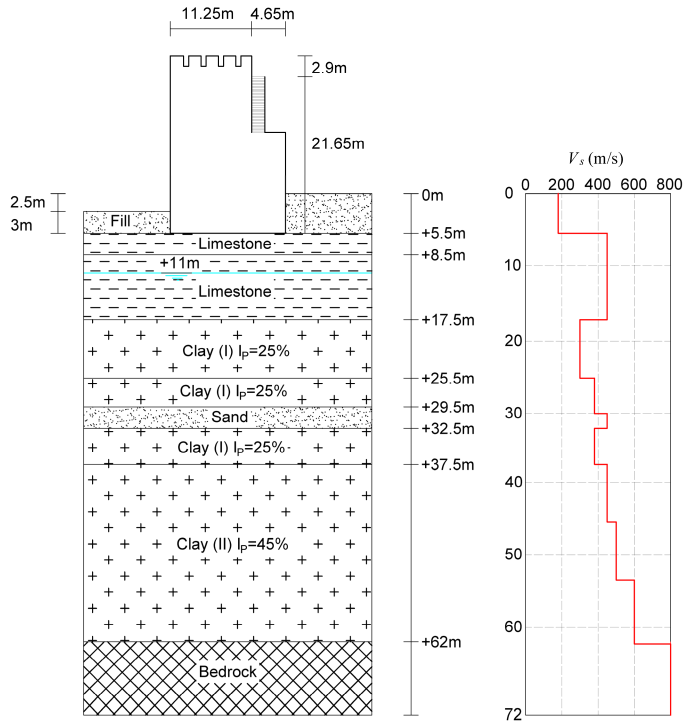

Figure 5. 21. Stratigraphy below the Tower showing the shear waves velocity in the ground.

The water table is at 11 m of depth. The embedment of the foundations is of 3 meters. More precisely, the ground level presents a 2-meters discontinuity between the left and right sides of the Tower. For this reason, it is possible to state that the base of the tower is below the ground level by 5.5m on the right side and 3m on the left side (see Figure 5. 6b and Figure 5. 6c). The foundation base level was deduced from simple considerations. Experienced builders such as the Romans would never have founded their structures on a filler material but on a rigid material such as limestone. The fact that the base of the tower and wall rests on limestone, as will be seen later, will have a significant effect on soil structure interaction.

The stratigraphy consists of the following layers: at the top, there is a fine grained made soil (from 0m to 5.5m depth), overlaying a weathered limestone with thin clayey interlayers (from 5.5m to 17.5m), which was used as the foundation base for the inner defensive wall and tower. Below the limestone there is a thick layer of highly plastic clay (from 17.5m to 37.5m) separated by a thin layer of sand (from 29.5m to 32.5m). This clay layer rests on a further thick layer of hard claystone/siltstone up to 62 meters of depth where the seismic bedrock was placed. The low-strain stiffness, G_0, has been calculated as $G_0 = \rho \cdot V_s^2$, where ρ is the density of the various layers. The non-linear and dissipative behaviour of the soils was modelled using literature curves, as laboratory tests were not available. For the clayey formations, the curves proposed by Vucetic and Dobry (1991) have been selected as a function of the soil plasticity index (I_P = 25% for Clay (I) and I_P = 45% for Clay (II)), while the mean curves for sand proposed by Seed and Idriss (1970) have been adopted for the sandy layers. Finally, the weathered limestone has been modelled using the mean shear modulus and lower damping ratio curves for sand proposed by Seed and Idriss (1970), as suggested for this type of soils by Park (2010) on the basis of experimental findings (Figure 5. 22).

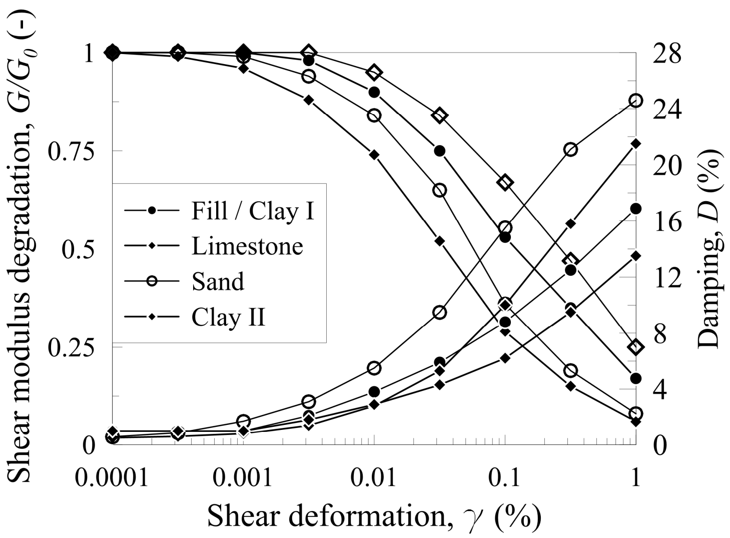

Figure 5. 22. Shear modulus reduction and damping ratio curves adopted for the different soil layers.

Based on the macrozonation done by Ince (2008), it is possible to identify the depth of the bedrock throughout the Istansbul Peninsula as well as the equivalent shear wave velocity of the first 30 metres of ground surface. The depth of the bedrock assessed by the micro-zonation study coincides with that identified by the stratigraphic surveys for the Tower19.

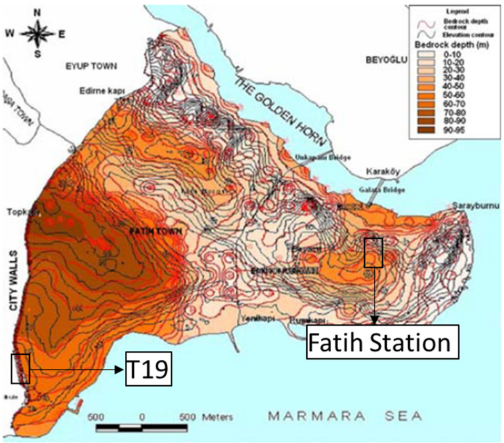

(a)

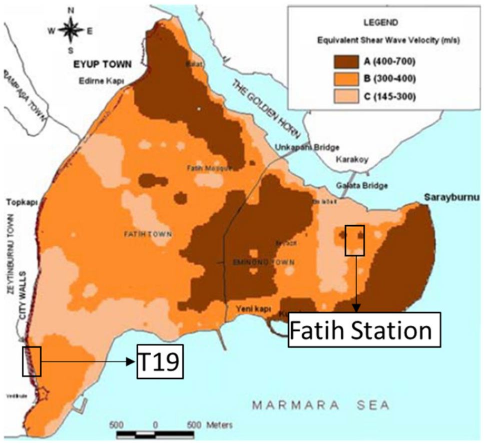

(b)

Figure 5. 23. (a) Depth to bedrock map of the historical peninsula, (b) Site classification according to equivalent shear wave velocity for the historical peninsula (modified from Ince, 2008).

The outcrop motion of the 1999 Kocaeli earthquake was recorded at the Fatih station (around 5km away from T19 Tower), founded on a class B soil (EC8, 2004). The seismic signal from the Kocaeli earthquake (1999), to be applied at the bedrock of the Tower19, was evaluated in the aforementioned study (Flora *et al.* 2021). Figure 5. 24 shows the accelerogram applied to the base of the model, while Table 5. 3 shows the most important information regarding this seismic signal.

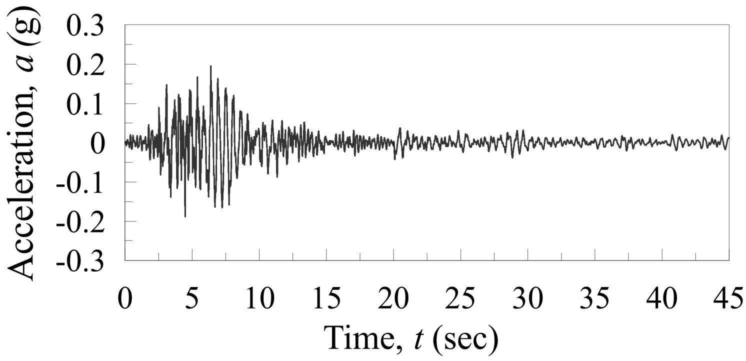

Figure 5. 24. Kocaeli earthquake to be applied used in seismic analysis.

Table 5. 3. Dynamic input motion features

a_{max} (g)	a_{min} (g)	f_d (Hz)	f_m (Hz)	IA (m/s)	T_{5-95} (sec)
0.195	0.188	1.85	2.09	0.710	17.42

5.2.3 Monodimensional Analysis with STRATA

The one-dimensional local seismic response was performed through the use of STRATA software. The deconvoluted seismic motion was applied to the bedrock modelled as a visco-elastic layer with shear wave velocity of 800m/s and 0.5% damping. The modelled soil bank has a depth of 62 metres (the surface ground level is set from the right side of the Tower). The properties shown in Figure 5. 21 and Figure 5. 22 were used for the one-dimensional study. Maximum acceleration profile, shear deformations, shear stiffness and mobilized damping are shown in Figure 5. 25.

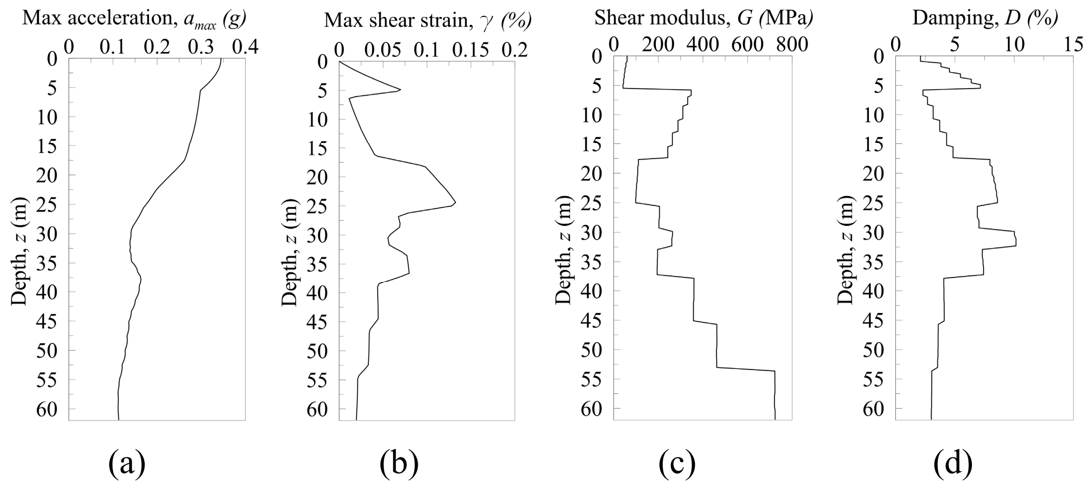

Figure 5. 25. Results of the dynamic analysis in terms of vertical profile of maximum acceleration (a), shear strain (b), shear modulus (c) and damping ratio (d).

It is also possible to find the natural vibration periods of soil by means of the amplification function, as well as the acceleration response spectrum at the foundation level (5.5m depth) and at the bedrock (Figure 5. 26).

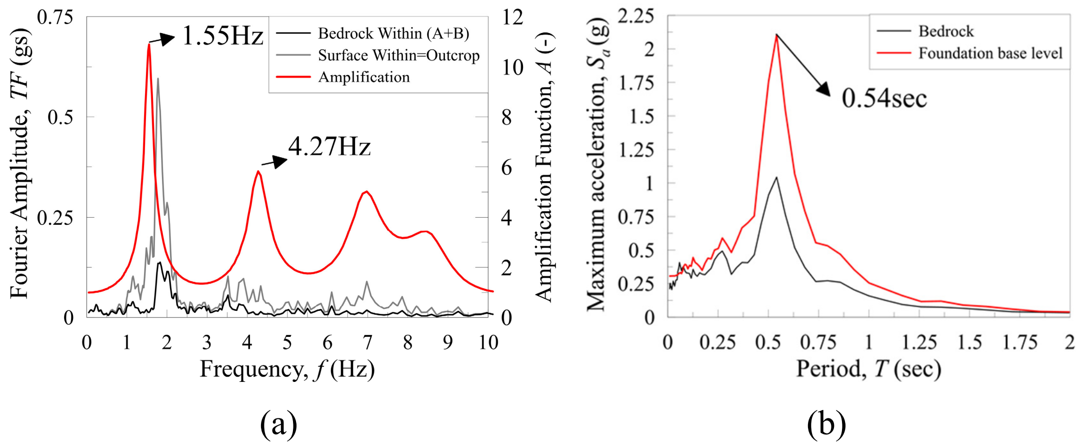

Figure 5. 26. Fourier (a) and acceleration (b) response spectra predicted compared with the input motion applied at the base (bedrock) of the soil profile.

Some important considerations can be made from the one-dimensional analyses. The dominant frequency of the earthquake is very close to the first natural frequency of the soil bank. This generates a very strong resonance phenomenon that results in a maximum acceleration at ground level of 0.34g, and 0.30g at the base of the Tower (5.5 metres depth). The acceleration spectrum presents a single hump with very high absolute acceleration demand values (approx. 2g). During the Kocaeli earthquake, near Tower19, structures with a period close to

0.54sec were affected by huge actions that inevitably led to damaged or collapse. The collapse of a very large number of Towers during the Kocaeli earthquake may be a clear evidence that these Towers had predominant periods close to 0.54. The resonance period values of the Tower with fixed base and disconnected wall (0.49sec and 0.46sec for M1 masonry properties) could represent the most likely scenario occurred. In the next chapter the effect of the soil-structure interaction on the dynamic behaviour of the towers will be studied through the coupled approach.

5.2.4 Visco elastic FEM geotechnical modelling of soil column.

In order to study the soil-structure interaction with the Plaxis 3D visco-elastic numerical model, firstly, the propagation of the seismic signal in the three-dimensional model of soil was calculated. This is important as it ensures that propagation of the seismic waves in the three-dimensional column soil is well simulated. The width of the deformable soil is 62 meters (same of mono-dimensional analysis) while 60 meters of bedrock are included in the model to ensure no significative interference between the compliant bottom base of the model and the soil deformable layer. The water table is at 11 metres of depth. Standard boundary conditions were applied during the initial (static) stage, that is zero horizontal displacements along the lateral boundaries and fixed nodes at the base of the mesh. During the dynamic analysis, the seismic inputs were applied to the bottom nodes of the mesh in terms of accelerations. In order to consider the finite stiffness of the underlying bedrock, and to reproduce the upward propagation of shear waves within a semi-infinite domain, the outcrop input accelerations were halved to compute the corresponding upward-propagating wave motion and applied to the bottom nodes together with adsorbing viscous dashpots (complaint base). Free-field boundary conditions were applied along the lateral sides of the mesh. The element size of the soil has been taken always smaller than one-tenth of the wavelength associated with the highest frequency component of the input wave containing appreciable energy (Kuhlemeyer and Lysmer, 1974). For this reason, the discretization was carried out using 61566 elements with 10 nodes each. The dimension of the model in Y and X direction is equal to 80 metres.

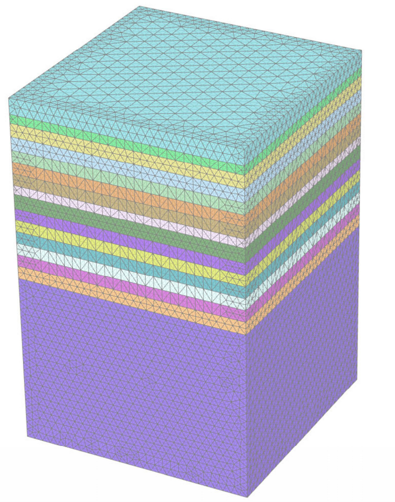

Figure 5. 27. Soil column for local seismic response analysis using the finite element method.

As already mentioned, in this analysis, the structure is not modelled. The soil is assimilated to a linear visco-elastic medium characterised by the operational values of the shear modulus *G* and the damping ratio as assessed by analyses using the equivalent linear method (Figure 5. 25c and Figure 5. 25d). Regarding the assignment of equivalent damping, it should be remembered that the Plaxis uses the dual control frequency approach. Once the two target damping values from the equivalent visco-elastic analysis have been set, the first frequency (f_1) corresponds to the first natural frequency of the soil (1.55Hz) while the second frequency is equal to the odd integer greater than the ratio $f_p/f_1 = 1.19 \rightarrow 3$ (Hudson, Idriss & Beirkae (1994), Hashash & Park (2002)). This approach, in this case, generated more similarities with one-dimensional propagation than that suggested by Amorosi, Boldini & Ellia (2010). Figure 5. 28 shows the comparison between the amplification function obtained by FEM modelling and that obtained by STRATA at ground level and at depth of 5.5m (foundation base level).

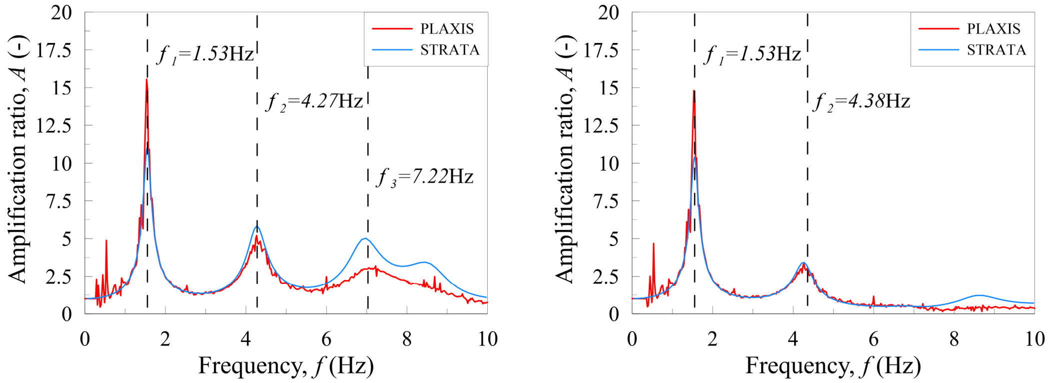

(a) (b)

Figure 5. 28. Comparison between the amplification functions using finite element model and STRATA: (a) at ground level, (b) at foundation level.

It can be seen that the resonance frequencies of soil are identical between STRATA and Plaxis3D. The small differences, only at a single peak frequency value, are due to the different way in which damping is considered in the two numerical model (STRATA and Plaxis). Figure 5. 29 shows the identical acceleration spectrum at ground surface and foundation level obtained from the two models.

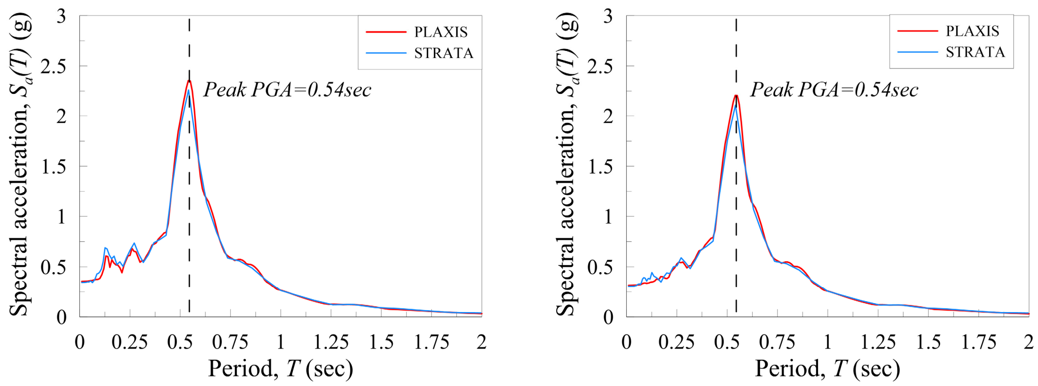

(a) (b)

Figure 5. 29. Acceleration response spectrum between Plaxis and STRATA at ground surface (a) and base foundation level (b).

Finally, comparing the accelerograms obtained at ground level and at foundation level (Figure 5. 30) by the two-calculation software (Plaxis and STRATA), we can conclude that the propagation in the three-dimensional FEM model shows a considerable degree of affinity with that obtained through the equivalent visco-elastic analyses.

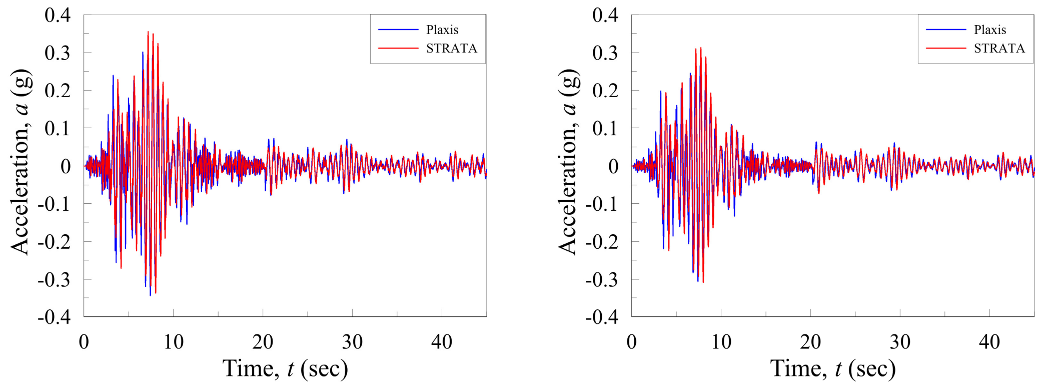

(a) (b)

Figure 5. 30. Comparison of the accelerations recorded by FEM and STRATA at ground level (a) and at foundation level (b).

5.2.5 Soil structure interaction with visco-elastic FEM 3D model

As the geotechnical 3D model is calibrated, it is possible to include the Tower19 to study the effect of SSI on the structural response. As already mentioned in Chapter 5.1.2, several possible scenarios have been studied in order to evaluate, in the most reliable way, the behaviour of the Tower19 and the wall. Therefore, three different structural models with soil-structure interaction was studied:

1) Isolated tower (M1 and M2 masonry properties);

2) Tower with wall as simple lateral restrain (M1 and M2 masonry properties);

3) Tower with wall as a single block unit (M1 and M2 masonry properties);

Isolated Tower19

The Tower19 was imported into the plaxis3D finite element numerical model. The foundation of Tower19 as already mentioned rests on the limestone layer. This will have considerable effects on the SSI, since the limestone is very stiff and the effect of SSI is expected to be very limited. The numerical model (Tower + Soil) is characterised by 68679 elements with 10 nodes. The distance of the tower from the domain boundaries (greater than 2 times the width of the structural base) ensures that there is no interference (Jiang and Yan, 1998). In order to correctly model the effects of the SSI, the mesh was refined considerably in the area around the Tower and below the Tower (distance between nodes less than 0.5m). Figure 5. 31 shows an axonometric view of the 3D model with isolated Tower and a top view of the model.

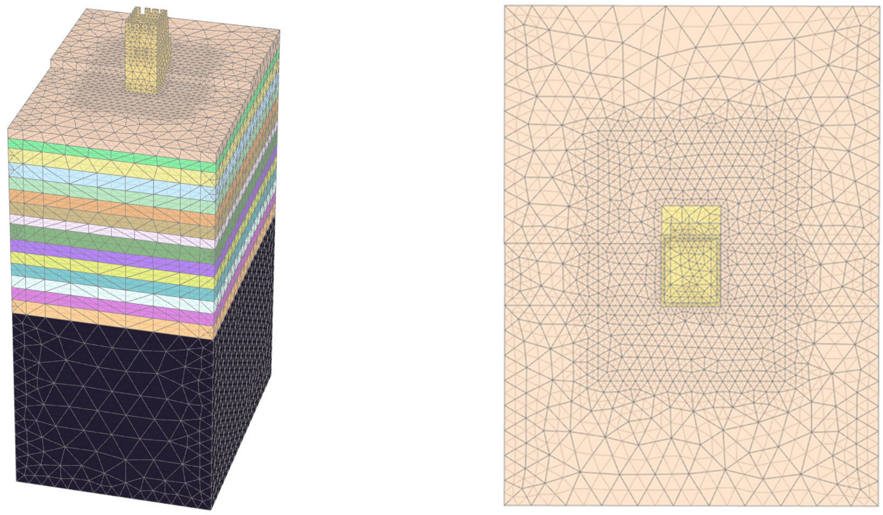

(a) (b)

Figure 5. 31. Axonometric view of numerical 3D model with Isolated Tower and plan view of the numerical model (b).

The properties of the various soil layers as well as the boundary conditions and the seismic input signal are identical to those used in the previous paragraph. The seismic signal was applied separately first in the X-direction and then in the Y-direction of the model. In the next subsections, the results in terms of the period lengthening generated by the soil and the displacement demand in terms of structural drift will be shown for M1 and M2 Masonry properties.

M1 Masonry Properties

Using the acceleration amplification function between the foundation base level (top limestone level layer) and the roof of the structure (and/or the I floor) it is possible to compute the natural resonant frequency of the structure with soil-foundation-structure interaction.

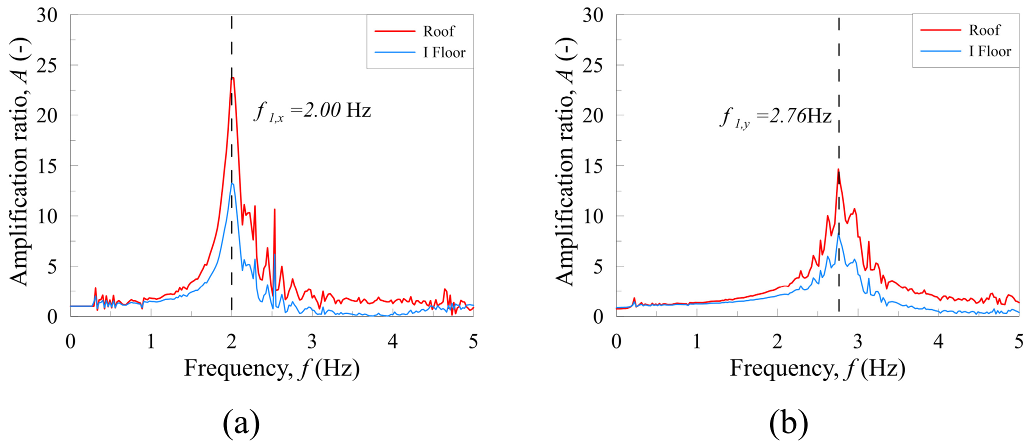

Figure 5. 32. Acceleration amplification function for M1 masonry properties with earthquake in X-direction(a) and Y-direction (b).

Comparing the amplification function in Figure 5. 32 with Figure 5. 14 (fixed base) it can be seen that the period elongation given by the soil is very low (in X-direction from 0.49sec to 0.50sec and in Y-direction from 0.33 to 0.36). It is important to note that in the X-direction the tower has a resonance period, with soil-structure interaction, very close to the acceleration peak of Figure 5. 29. For this reason, the isolated tower will be subjected to an enormous seismic demand. It is possible to calculate the demand in terms of global roof structural displacements by subtracting from the total displacement of the roof the displacement recorded at the foundation base and the rigid rotation (tilt rotation) undergone by the Tower. Figure 5. 33 shows the structural drifts recorded in X and Y direction for this isolated tower model.

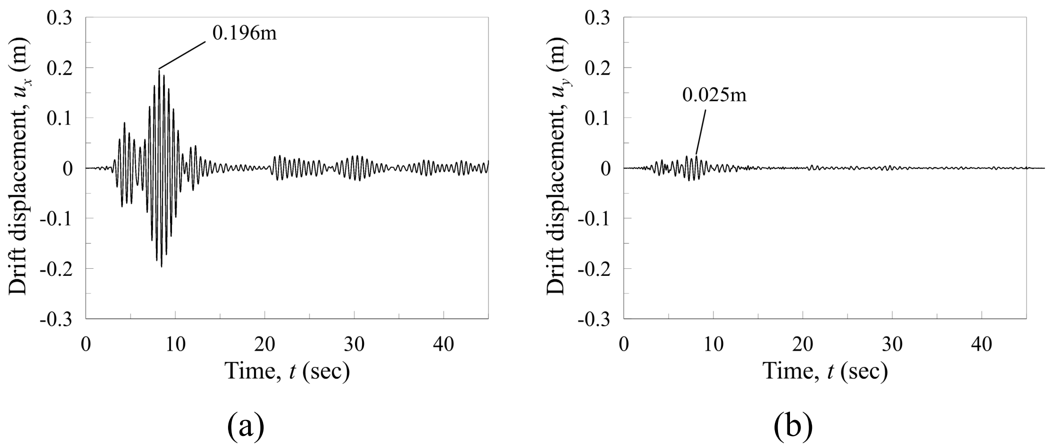

Figure 5. 33. Structural drift demand in fixed base condition and complaint base condition in X-direction (a) and Y-direction with M1 masonry properties.

It is clear that the demand in terms of structural displacements in the X-direction is enormous and may have led to the collapse of the Tower19.

M2 Masonry Properties

As in the case of M1 masonry, it is possible to calculate the period elongation with the acceleration amplification function between base and roof of the structure for M2 masonry structure (Figure 5. 34).

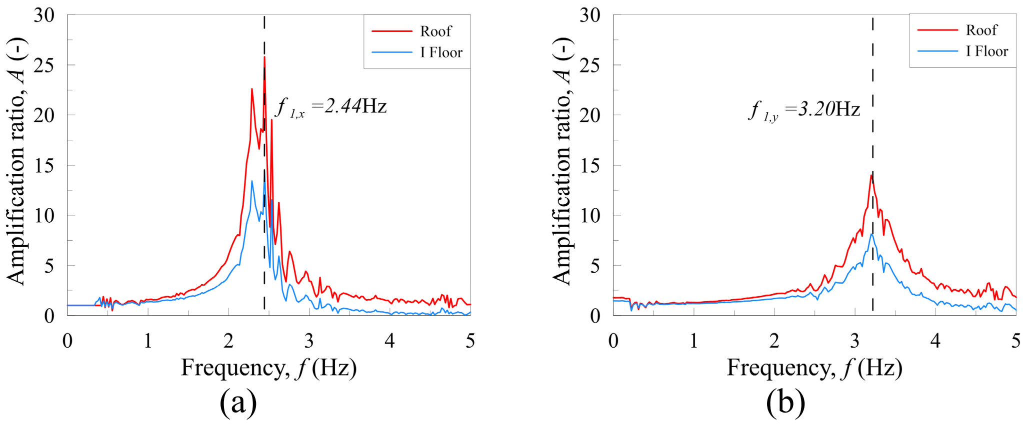

Figure 5. 34. Acceleration amplification function for M2 masonry properties with earthquake in X-direction(a) and Y-direction (b).

Comparing the amplification function in Figure 5. 34 with Figure 5. 15 (fixed base) it can be seen that the period elongation given by the soil is still low (in X-direction from 0.39sec to 0.41sec and in Y-direction from 0.26 to 0.31). The higher stiffness of the M2 structure results in slightly higher period elongation related to M1 masonry. This is because as the structure to soil relative stiffness increases ($H_{str}/(V_s T_{FB})$), the period elongations increase (Veletsos, 1974). Figure 5. 35 shows the structural drifts recorded in X and Y direction for this isolated tower model.

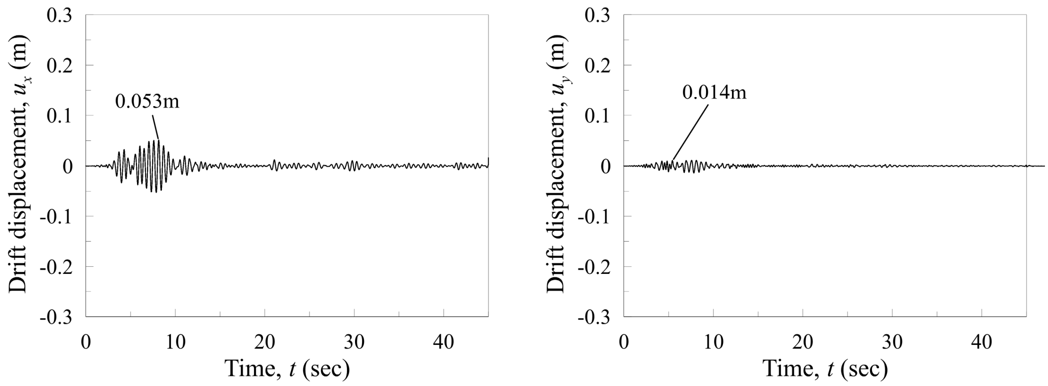

(a) (b)

Figure 5. 35. Structural drift demand in complaint base condition in X-direction (a) and Y-direction with M2 masonry properties.

The structural displacements are lower than in the M1 case, but they are still quite high and may affect the stability of the tower (particularly in the X direction).

Tower with Wall Disconnected

The numerical model (Tower + Wall + Soil) is represented in Figure 5. 36

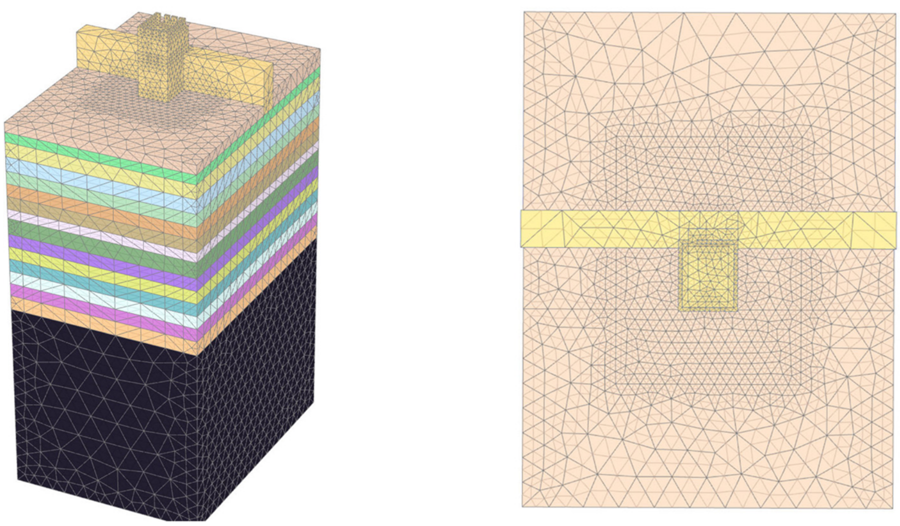

(a) (b)

Figure 5. 36. Axonometric view of numerical 3D model with Tower and Wall and plan view of the numerical model (b).

As already mentioned, the boundary conditions, the properties of the various layers and their thicknesses are identical to those used in the geotechnical soil column modelling.

M1 Masonry Properties

As expected, the modelling of the Tower with the Wall in simple contact generates great similarities with the case of the Isolated Tower. As done previously, the amplification function between the base of the tower and the roof was calculated to know the elongations of periods generated by the deformability of the ground (Figure 5. 37).

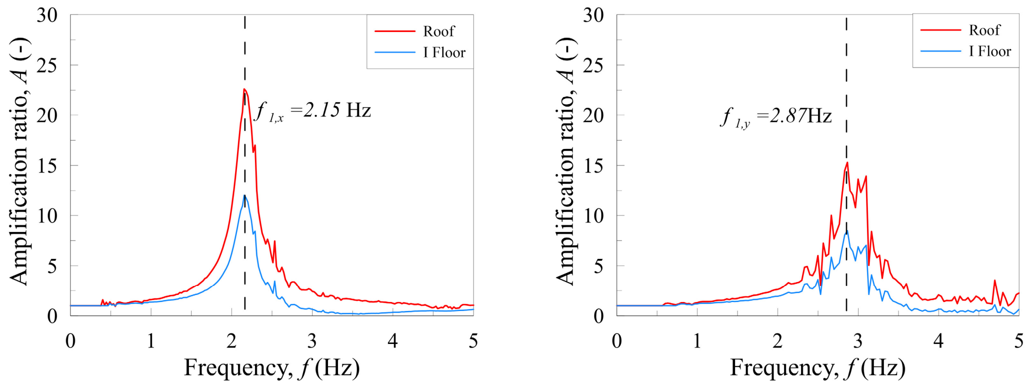

(a) (b)

Figure 5. 37. Acceleration amplification function for M1 masonry properties with disconnected walls with earthquake in X-direction(a) and Y-direction (b).

Comparing the values of natural resonant period in fixed base condition with those obtained in Figure 5. 37, it is possible to see a period elongation in X - direction from 0.46sec to 0.47sec and in Y-direction from 0.33sec to 0.35sec.

Figure 5. 38 shows the values of the structural drifts in this case as well.

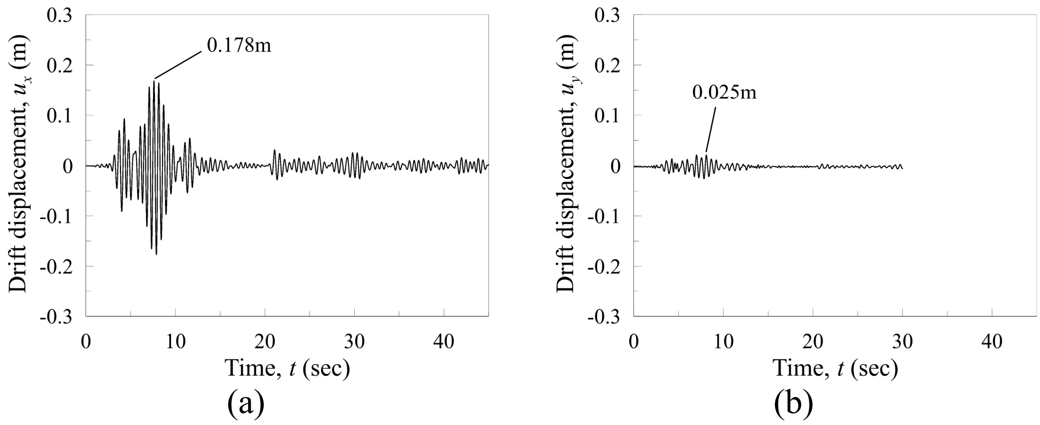

Figure 5. 38. Structural drift demand in complaint base condition in X-direction (a) and Y-direction with M1 masonry properties with disconnected walls.

M2 Masonry Properties

The same considerations can be made for M2 masonry (Figure 5. 39).

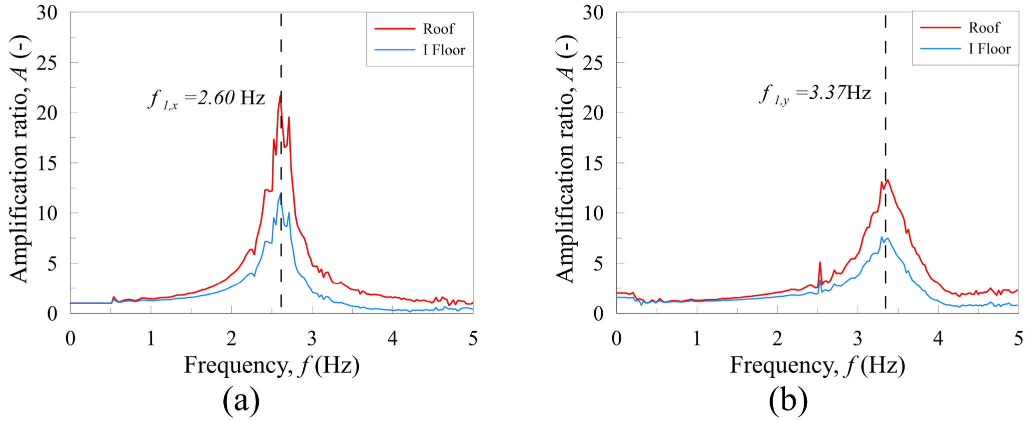

Figure 5. 39. Acceleration amplification function for M2 masonry properties with disconnected walls with earthquake in X-direction(a) and Y-direction (b).

In this case the period elongation is from 0.35sec to 0.38sec for the X direction and from 0.26 to 0.30 for the Y-direction. Figure 5. 40 shows the values of the structural drifts in this case as well.

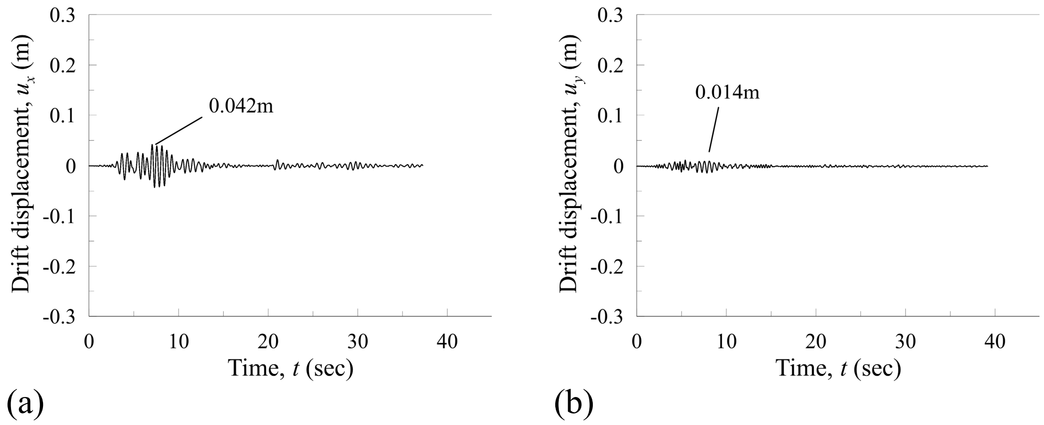

Figure 5. 40. Structural drift demand in complaint base condition in X-direction (a) and Y-direction with M2 masonry properties with disconnected walls.

Tower with Wall Connected

M1 Masonry Properties

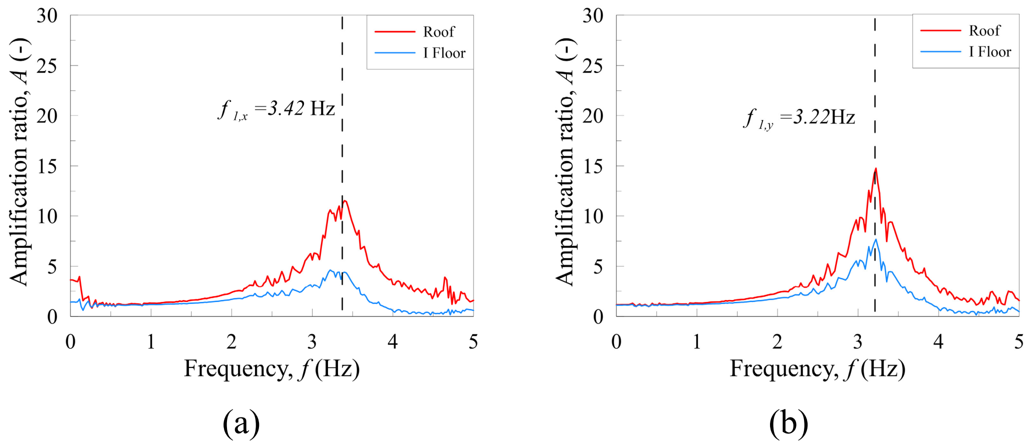

Figure 5. 41. Acceleration amplification function for M1 masonry properties with connected walls with earthquake in X-direction(a) and Y-direction (b).

The period elongation is from 0.29sec to 0.29sec for the X direction and from 0.30 to 0.31 for the Y-direction. Figure 5. 42 shows the values of the structural drifts in this case as well.

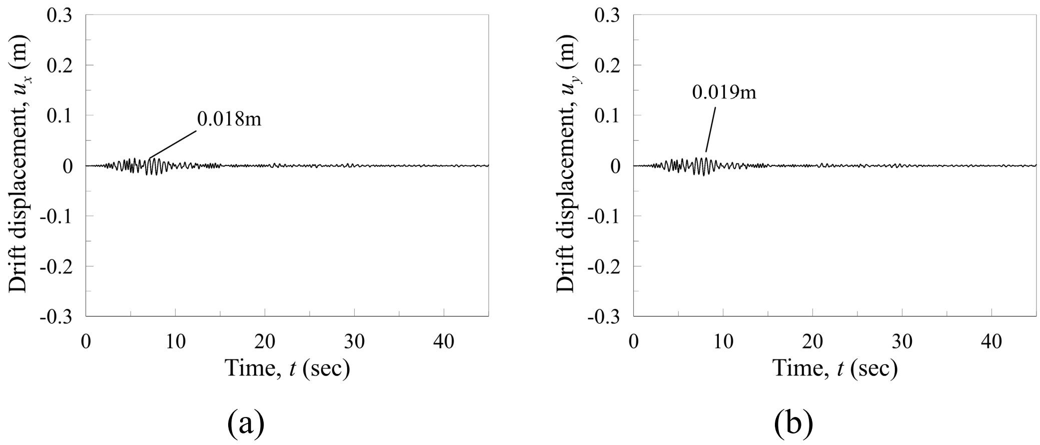

Figure 5. 42. Structural drift demand in complaint base condition in X-direction (a) and Y-direction with M1 masonry properties with connected walls.

M2 Masonry Properties

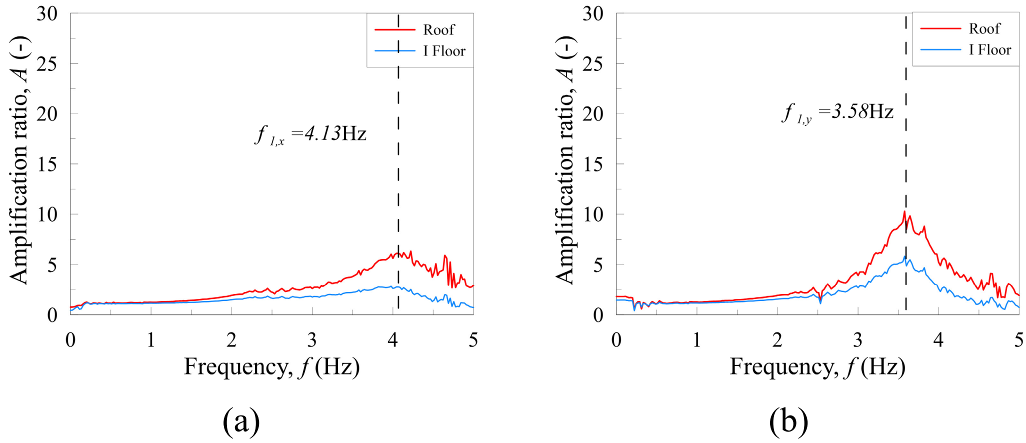

Figure 5. 43. Acceleration amplification function for M2 masonry properties with disconnected walls with earthquake in X-direction(a) and Y-direction (b).

The period elongation is from 0.23sec to 0.24sec for the X direction and from 0.23 to 0.28 for the Y-direction. Figure 5. 44 shows the values of the structural drifts in this case as well.

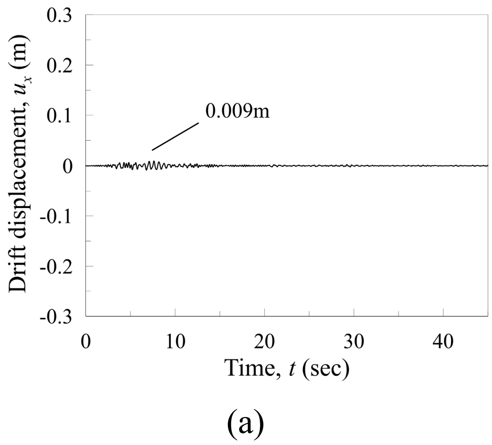

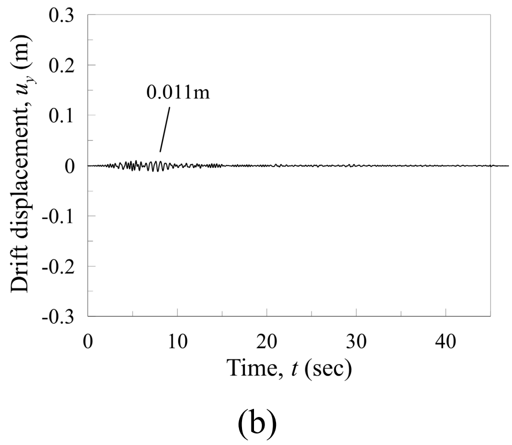

Figure 5. 44. Structural drift demand in complaint base condition in X-direction (a) and Y-direction with M2 masonry properties with connected walls.

It is possible to summarise all the values of the natural vibration periods in Table 5. 4 and with Soil structure interaction (Table 5. 5).

Table 5. 4. Natural period of vibration in fixed base condition for different configuration of structural model

	FIXED BASE CONDITION					
	Isolated Tower		With Wall Disconnected		With Wall Connected	
	T_x (sec)	T_y (sec)	T_x (sec)	T_y (sec)	T_x (sec)	T_y (sec)
M1	0.49	0.33	0.46	0.33	0.29	0.30
M2	0.39	0.26	0.35	0.26	0.23	0.23

Table 5. 5. Natural period of vibration with soil-structure interaction for different configuration of structural model

	COMPLAINT BASE					
	Isolated Tower		With Wall Disconnected		With Wall Connected	
	T_x (sec)	T_y (sec)	T_x (sec)	T_y (sec)	T_x (sec)	T_y (sec)
M1	0.50	0.36	0.46	0.35	0.29	0.31
M2	0.41	0.31	0.38	0.30	0.24	0.28

It is clearly evident that the periods elongations due to the soil-structure interaction are generally low. Infact, due to the presence of the limestone as foundation soil, the relative structure to soil stiffness is rather low in the visco-elastic analysis. In order to confirm this, the Foundation Input Motion, calculated from the FEM analysis in the different configurations (*i.e.* Isolated Tower, Connected Walls, Disconnected Wall), was applied at the base of the structure in fixed base conditions. To this end, Table 5. 6 shows the maximum drift values recorded in the various configurations with SSI while Table 5. 7 shows the drifts with fixed base conditions.

Table 5. 6. Demand in terms of structural drift in complain base condition for different configuration of structural model

	COMPLAINT BASE					
	Isolated Tower		With Wall Disconnected		With Wall Connected	
	$u_{d,x}$ (m)	$u_{d,y}$ (m)	$u_{d,x}$ (m)	$u_{d,y}$ (m)	$u_{d,x}$ (m)	$u_{d,y}$ (m)
M1	0.196	0.025	0.178	0.025	0.018	0.019
M2	0.053	0.014	0.042	0.014	0.009	0.011

Table 5. 7. Demand in terms of structural drift in fixed base condition for different configuration of structural model

	FIXED BASE					
	Isolated Tower		With Wall Disconnected		With Wall Connected	
	$u_{d,x}$ (m)	$u_{d,y}$ (m)	$u_{d,x}$ (m)	$u_{d,y}$ (m)	$u_{d,x}$ (m)	$u_{d,y}$ (m)
M1	0.181	0.024	0.180	0.024	0.016	0.022
M2	0.041	0.018	0.033	0.014	0.008	0.011

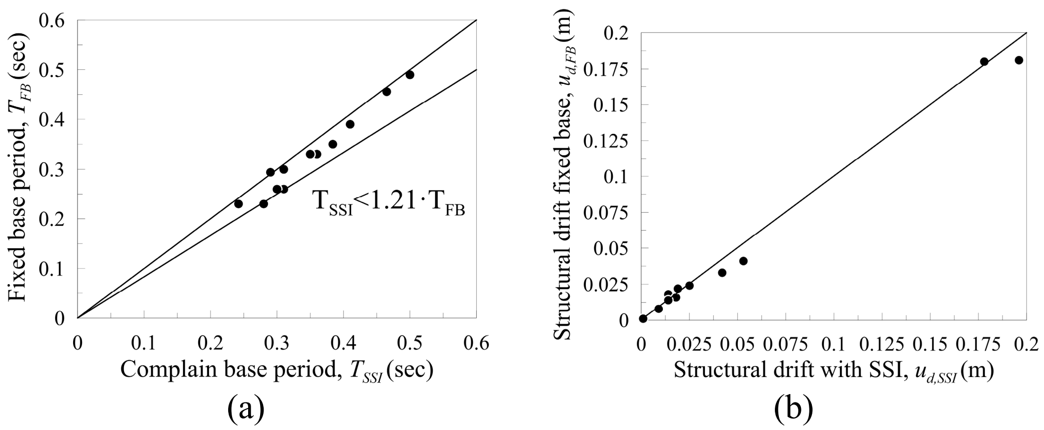

Figure 5. 45. (a) Comparison between the natural resonant period in fixed base condition and with soil structure interaction; (b) comparison of fixed base and complaint base structural drifts

It can be seen that the effect of the soil-structure interaction produces modest period elongations (Figure 5. 45a). Due to the low deformability of the soil, the structural drifts between the fixed base condition and the complaint base condition are also similar (Figure 5. 45b). The results found up to this point can be summarised as follows:

1. The significance of the SSI is modest. This is determined by the fact that the foundation of the structure rests on limestone, a very rigid material.
2. The effects of SSI, although modest, are generally detrimental. SSI leads the structure to a period closer to the peak of the acceleration spectrum and therefore to greater demands in terms of accelerations and displacements.
3. The most realistic configurations are those of Isolated Tower or Tower with Disconnected Wall. In these two configurations the demands in terms of structural drift are an order of magnitude higher than in the Connected Tower. This happens because of an evident resonance phenomenon between the period of the Tower and the predominant period of the seismic signal at the base of the structure. Empirical evidence shows that the Towers have been heavily damaged by various historical earthquakes. The modelling of the damage scenario leads to believe in the behaviour of Tower as isolated or Tower with Disconnected Wall.
4. In all configurations, the resonance periods with soil-structure interaction lie to the left of the peak of the acceleration spectrum. This is very important from the perspective of the lateral disconnection technique. The period increase generated by this technique must be able to overcome the peak. This, due to the stiffness of the limestone, may not be possible.
5. Considering the level of knowledge of the materials of the Tower as well as the degree of constraint with the wall, the numerical modelling of the Tower19 and the identification of collapse reason can only be a deductive process (from the general to the particular). Turnbull states: *" In AD 447, only 34 years after their construction, the greater part of the new walls, including 57 towers, was flattened by a series of mighty earthquakes*" and, again "Most *of the damage the walls sustained came from the effects of weather or earthquakes, not war. The walls were so strong that little battle*

damage was sustained until very late in their history when gunpowder was employed". The reason for this strong propensity of the towers to collapse under seismic actions is certainly to be found in resonance structural phenomena.

5.3. Lateral Disconnection

In this paragraph the effect of the lateral disconnection technique will be described for the case of isolated tower. It is clear that this intervention needs to separate the tower from the wall in order to generate the gap between the foundations and the adjacent ground. The disconnection will be made only along the outer perimeter of the foundation. In terms of a real application, it is possible to fill the space, generated by the gap, with a very light and deformable material such as polystyrene. The externally generated gap (0.5m width) is able to disconnect the foundations up to their laying level and not affecting the bearing capacity (see Chapter 3). The embedment of the foundations is approximately 3 metres on the front side and 5.5 metres on the back side. The disconnection eliminates the confinement effect given by the soil up to the foundation base, thus, reducing both the rotational and translational stiffness of the soil-foundation system. However, it is important consider that the rotational and translational stiffness value is also determined by the stiffness of the ground beneath the foundation. Even if the elimination of the lateral soil reduces the translational and rotational stiffness of the soil-foundation interface, it can still have a very high value and not result in a significant period elongation. It is possible to make some simple considerations on the basis of the parametric analyses conducted in Chapter 3. The relative period elongation with respect to the connected case is directly proportional to the dimensionless factor $H_{str}/(V_s T_{FB})$. Chapter 3 has shown that for values less than 0.10 such period elongations are rather small and less than 25 %. In the Isolated Tower configuration, this dimensionless parameter is equal to approximately to 0.07 in the X-direction and 0.10 in the Y-direction for M1 masonry and 0.08 and 0.12

for M2 masonry (with H_{str} =15m in Figure 5. 17, fixed base period in Table 5. 4, and V_s in Figure 5. 21). The period elongations are also proportional to *D/B*; this value is less than unity on both sides of the structure. All of this information suggests that lateral disconnection may not be beneficial in this case. Lateral disconnection was carried out for both M1 and M2 masonry properties.

M1 Masonry Properties

As mentioned in Chapter 3, it is necessary to calculate the natural period of vibration of the disconnected structure in order to highlight the beneficial effects produced by lateral disconnection. Through the acceleration amplification function it is possible to know this period lengthening (Figure 5. 46).

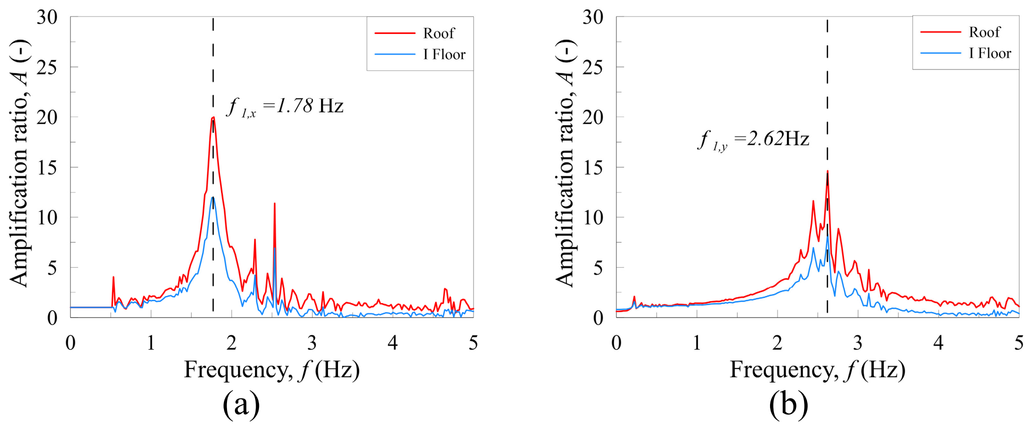

Figure 5. 46. Acceleration amplification function for M1 masonry properties with lateral disconnection tecnique in X-direction(a) and Y-direction (b).

As can be seen, the lateral disconnection technique is able to lengthen the natural period of vibration. In particular, in the X-direction, compared to the fixed base case, T_{FB}=0.49sec, the period shifts to T_{LD} = 0.56sec (14% increase). In Y-direction the period shift from 0.33sec at fixed base condition to 0.38sec with lateral disconnection (15% increase). Compared to the fixed-base case, it can be stated that the technique leads to an increase in the natural vibration period of about 15% in both directions (compared to the period with soil-structure interaction about 12% in X-direction and 6% in Y-direction). These period extensions unfortunately do not allow the peak of the acceleration spectrum to be exceeded, but rather lead to even higher stress values in the structural elements.

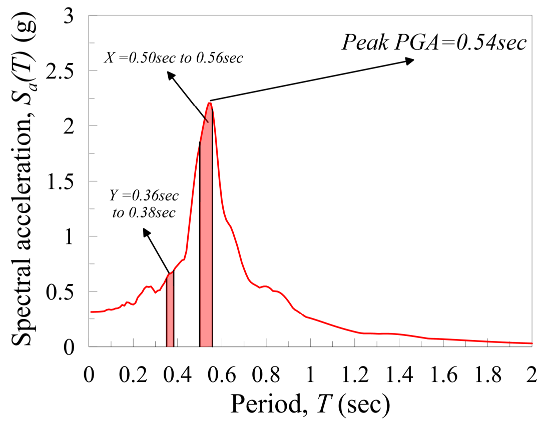

Figure 5. 47. Periods elongation and effects in terms of absolute total acceleration demand.

Calculating the structural displacements, as done above, it can be seen that the effect of lateral disconnection is detrimental and not beneficial (Figure 5. 48).

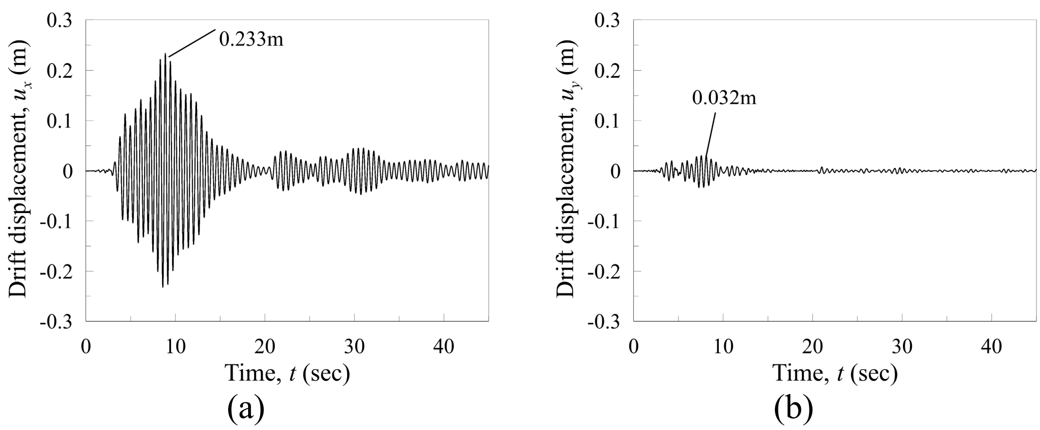

Figure 5. 48. Structural drift demand in complaint base condition with lateral disconnection in X-direction (a) and Y-direction with M1 masonry properties.

M2 Masonry Properties

The same considerations can be made in the case of M2 masonry (Figure 5. 49).

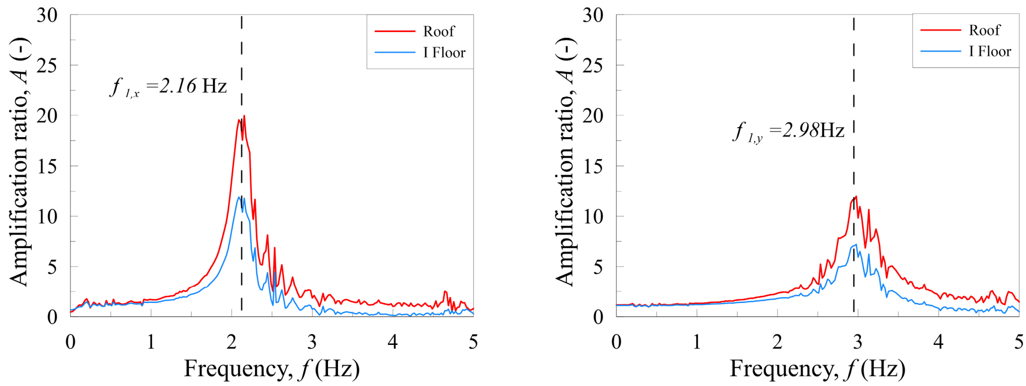

(a) (b)

Figure 5. 49. Acceleration amplification function for M2 masonry properties with lateral disconnection tecnique in X-direction(a) and Y-direction (b).

The first natural period of vibration of 0.39sec in fixed base condition translate to 0.46sec in X-direction and from 0.26sec to 0.33sec in Y-direction with 18% increase in X and 27% in Y. Related to the first natural period of vibration with soil structure interaction these percentages obviously decrease (12% in X-direction and 6% in Y-direction). Once again, the period lengths are not high enough to allow a benefit in terms of reductions in seismic actions (Figure 5. 50).

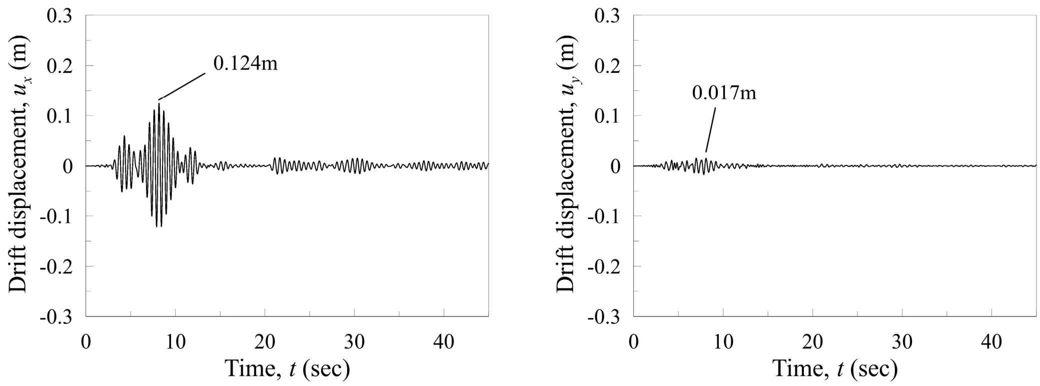

(a) (b)

Figure 5. 50. Structural drift demand in complaint base condition with lateral disconnection in X-direction (a) and Y-direction with M2 masonry properties.

5.3.1 Lateral disconnection inside the limestone layer

The lateral disconnection up to the foundation level does not seem to provide any beneficial result but instead contributes to further increasing the seismic actions on the structure. This aspect, already pointed out in Chapter 3, is a delicate issue of this technique. Being based on a simple removal of soil adjacent to the foundations, there may be cases where the intervention does not give any form of contribution and may be ineffective. It is reiterated that a careful analysis of the soil-structure interaction and the study of the local seismic response must always be carried out to assess the effectiveness of this technique.

However, the natural stratigraphic condition of the ground below the tower allows for a further modification of the soil-structure interaction. In fact, the tower is founded on limestone, a rocky material that can be cut vertically up to a certain depth depending on its properties in terms of cohesion and friction angle. It was decided to make a further vertical cut in the limestone of approx. 7.5m and 0.5m width. Please note that the total thickness of the limestone layer is 12m. This gap is an extension of the one already made in the first soil layer. This strategy is obviously a modification of the classical lateral disconnection technique described in the previous chapters and is presented in this thesis as a demonstration of the multiple different ways that can be followed to create a different soil-structure interaction and, thus, to modify the seismic actions affecting the structure. As already mentioned, in this case, it is only the presence of rock below the foundation that allows such an operation. In different stratigraphic conditions the static safety factor could be unacceptable. The removal of the soil below the foundation for a 7.5m section has two main effects:

- A further reduction in the rotational and translational stiffness of the soil-foundation interface; this occurs because the significant volume of soil involved in the various foundation motion (see Figure 2. 18) changes drastically as stresses can only spread inferiorly and not laterally (due to the gap). The absence of continuous rock below the foundations inevitably reduces the rotational stiffness of the soil-foundation interface.
- A change in the foundation input motion (FIM).

Regarding the second point, Figure 5. 51 shows the relative acceleration spectrum in X and Y-direction at the base of the foundation level.

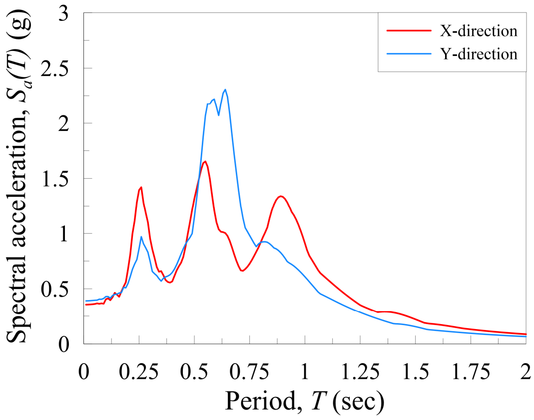

Figure 5. 51. Acceleration response spectrum in X and Y direction with lateral disconnection inside the limestone layer.

It is possible to see that this type of intervention not only changes the soil-structure interaction, but also the FIM. In fact, especially in the X direction, where the notched limestone column has a thickness of 9.35m, additional resonance peaks arise (probably coinciding with the translational resonance of the notched rock block). In the Y direction, however, the situation is more similar to that previously shown.

M1 Masonry Properties

As has been done several times before, it is possible to know the resonance periods of the tower in the X and Y direction with soil-structure interaction by means of the amplification function between the base of the foundation and the roof (Figure 5. 52).

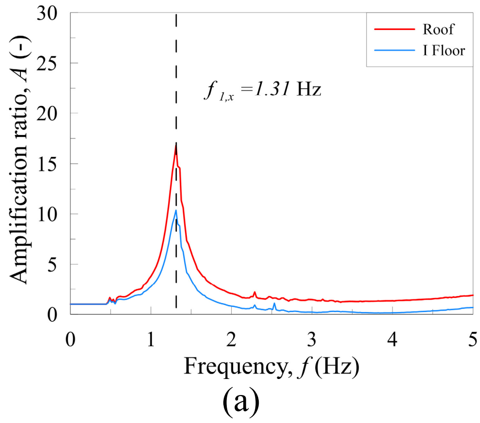

Figure 5. 52. Acceleration amplification function for M1 masonry properties with lateral disconnection technique up to limestone in X-direction(a) and Y-direction (b).

In the X-direction the natural resonance period is about 0.76sec (35% higher than the resonant period in case of lateral disconnection up to foundation level and 52% higher than *"as is"* soil-structure interaction condition). In Y-direction the resonance period is about 0.53sec (39% higher than the resonant period up to foundation level and 47% higher than real soil-structure interaction condition). These variations clearly produce different demands in terms of structural displacements (Figure 5. 53). In particular, in the X-direction a reduction of the peak drift displacement of about 56% occurred, while in Y an increase of 61%. Although, in one direction there is an increase in displacement structural demand, the most critical and dangerous condition was in X-direction. In X-direction, the displacement demand was significantly reduced. Depending on the displacement capacity of the tower masonry (information that can only be estimated due to the lack of a material characterisation of the tower), the displacement requirements in X and Y could be met.

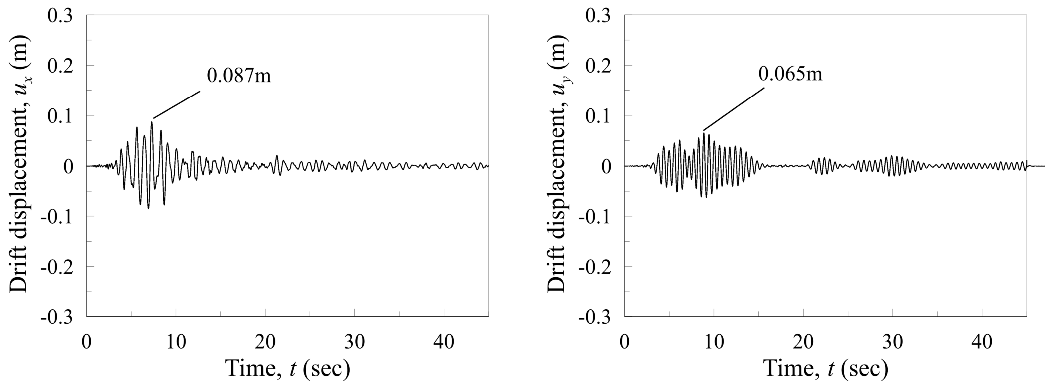

(a) (b)

Figure 5. 53. Structural drift demand in complaint base condition with lateral disconnection up to limestone in X-direction (a) and Y-direction with M1 masonry properties.

M2 Masonry Properties

Figure 5. 54 shows the resonant period elongations for the M2 masonry tower.

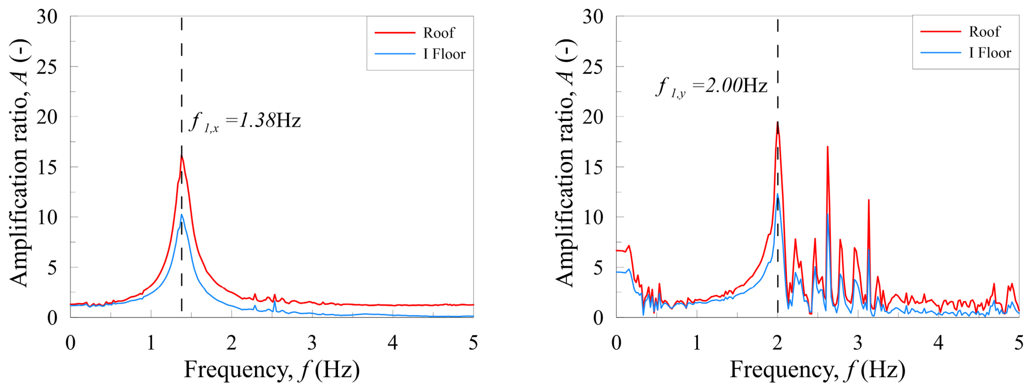

(a) (b)

Figure 5. 54. Acceleration amplification function for M2 masonry properties with lateral disconnection technique up to limestone in X-direction(a) and Y-direction (b).

Still large period elongations can be seen here. In X-direction the resonant period shift from 0.39sec to 0.72sec (84% increase). In Y-direction from 0.31sec to 0.5sec (61% increase). Structural drifts are also significantly altered in this case. In particular, for the M2 masonry the intervention is still detrimental in both directions. In X direction we have an increase in structural displacement of 18% while in Y-direction it is 228%.

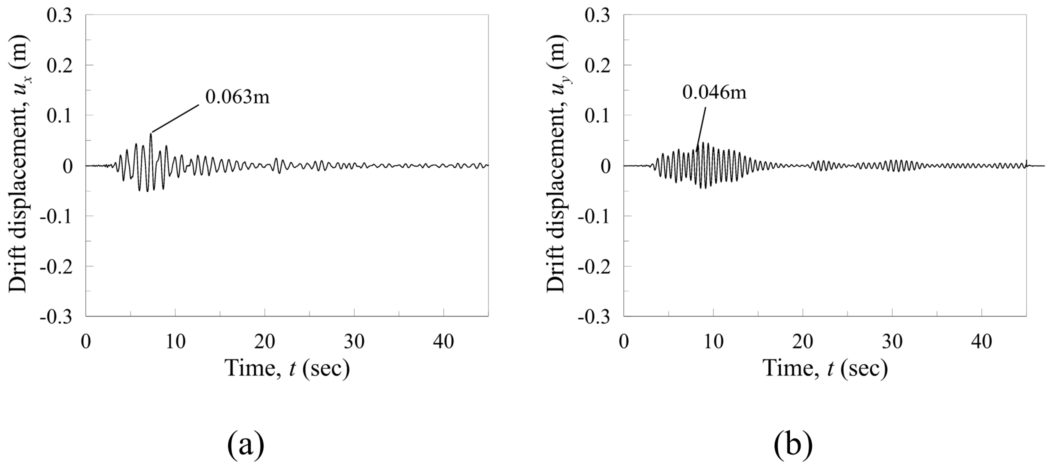

Figure 5. 55. Structural drift demand in complaint base condition with lateral disconnection up to limestone in X-direction (a) and Y-direction with M2 masonry properties.

It is clear that the disconnection inside the limestone can only be considered acceptable if the masonry material is the M1 type (poorer and lighter). It is worth nothing to mention the complexity of this case study both for the lack of knowledge of the materials (which leads to perform analyses with very different possible materials) and for the particular condition of the Tower's resonance period (exactly on the left of the peak of the acceleration spectrum for both masonry properties). This acceleration peak is also very complex to overcome due to the stiffness of the limestone layer.

5.4 Soft barrier

Both the idea of lateral disconnection up to the base of the foundation and within the limestone showed strong limitations for this case study. The only scenario where there is an advantage is the M1 masonry with disconnection up to the limestone layer. This prompts us to make a consideration: not all GSI strategies can be used in every case.

In this paragraph the idea of soft barriers as seismically isolated barriers will be implemented for the isolated Tower19. Once again, the isolated Tower configuration is the most critical ones. The natural stratigraphy of the soil beneath Tower19 allows the horizontal SAP layer to be injected starting from a depth of 17.50m. This is due to the presence of limestone up to this depth. It is very difficult, or impossible, to create a continuous horizontal layer of SAP in a rocky material. On the other hand, high pressure can be used to iniect SAP starting from a depth of 17.50m due to the presence of limestone above.

The effects of inserting a soft SAP horizontal layer can first be studied through the one-dimensional local seismic response. By means of the STRATA calculation code the effect of inserting a soft layer of one metre thickness at a depth of 17.50m (immediately below the limestone) can be known. The properties of each individual soil layer have already been outlined in Figure 5. 21 and Figure 5. 22, while for the SAP layer it was decided to use a SAP80. Using the (4. 1) that considers the mean effective stress state it was possible to calculate the value of the shear wave velocity of the SAP80 at the depth of 17.50m, while the curves in Figure 4. 17 and Figure 4. 14 were used to model the equivalent non-linear properties of the SAP80. Maximum acceleration profile, shear deformations, shear stiffness and mobilized damping are shown in Figure 5. 56.

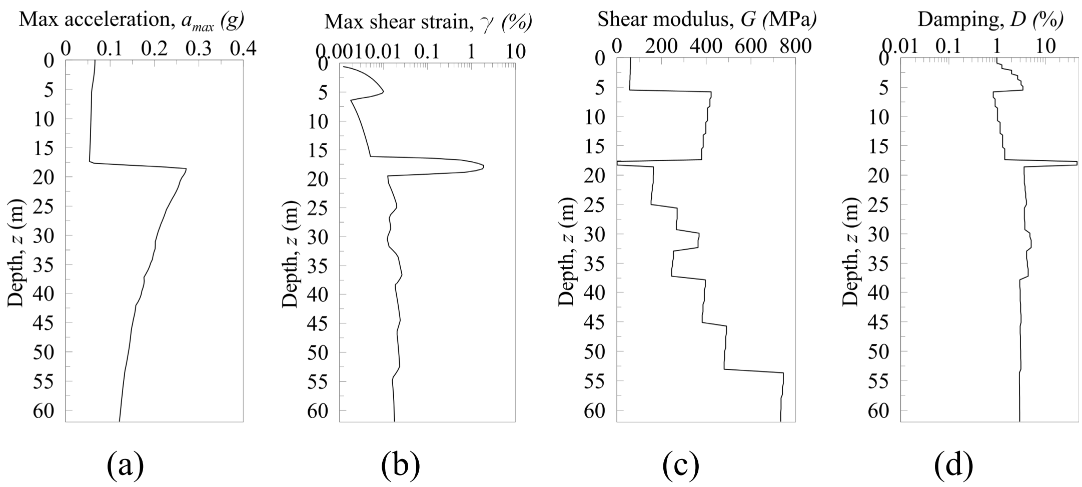

Figure 5. 56. Results of the dynamic analysis in terms of vertical profile of maximum acceleration (a), shear strain (b), shear modulus (c) and damping ratio (d).

Due to the very high shear deformations reached in the SAP layer (>1%) the mobilised damping is quite high (>20%). It is also possible to find the natural vibration periods of soil by means of the amplification function (Figure 5. 57).

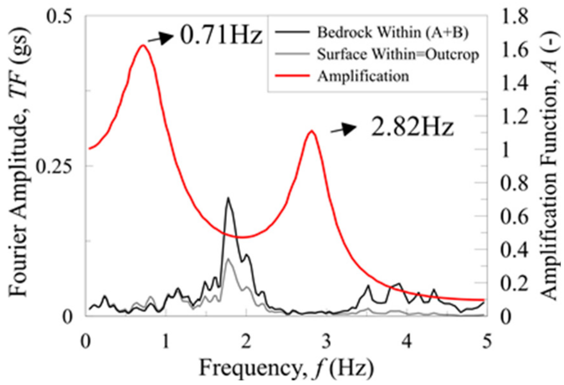

Figure 5. 57. Fourier response spectra and amplification function with SAP horizontal barrier.

A significant change in both the natural period of vibration of the ground and accelerations at the base of the structure is clearly generated by the SAP80 layer.

In the three-dimensional analyses, based on the design algorithm of Figure 4. 40, it was decided to create a quadrangular soft caisson with the dimensions 60mx60mx17.5m with 2-metre-thick side barriers and 1 metre thick horizontal barrier. In particular, considering also the lateral stiffness of the frontal and rear barriers, the equation (4. 7) was used. The calculation of the caisson mass is slightly more complex due to the presence of multiple layers of soil. The lateral stiffness of the soft caisson is equal to 7560345 kN/m while the total mass is 125042 Mg. For this reason, the estimated natural resonant period of the soft caisson is equal to 0.81sec both in X and Y direction. A natural vibration period of 0.81sec is far enough from the predominant period of Kocaeli earthquake and could generate significant reductions in seismic demand.

The designed soft caisson was imported into the three-dimensional finite element model Plaxis 3D (Figure 5. 58).

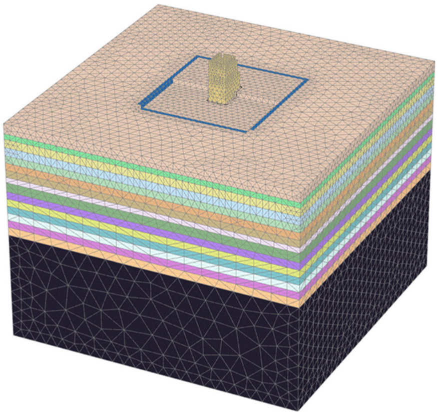

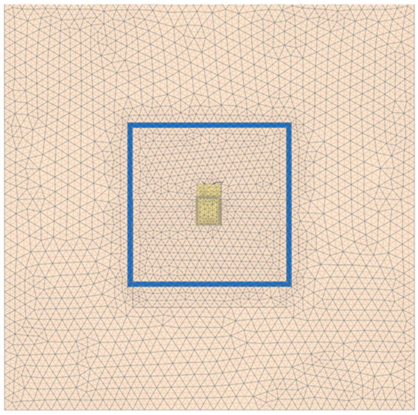

(a) (b)

Figure 5. 58. Axionometric view of numerical 3D model with Tower and soft caisson and plan view of the numerical model (b).

The domain has a dimension in X and Y equal to 160 metres (a larger domain extension is necessary due to the size of the soft box). The mesh has 155132 elements with 10 nodes and has been refined especially in the SAP layers and near the Tower where the soil-structure interaction is more relevant. The boundaries condition and the input seismic signal are identical to those already used and described in the previous three-dimensional numerical analyses. However, as the calculation domain is very large, the analyses are very time-consuming. In order to reduce this calculation time, the first 15 seconds of the signal, where the highest seismic stresses are concentrated, are computed. The equivalent visco-elastic properties of the SAP and soil layers were imported in the Plaxis 3D numerical model.

M1 Masonry Properties

It is possible to calculate the natural period of vibration of the soil with the insertion of the soft caisson through the amplification acceleration function between the base of soft caisson and the base of the structure (Figure 5. 59a). The numerically estimated caisson period is very close to that estimated using the analytical formulation (4. 7). This variation in the natural resonance period corresponds to a variation in the acceleration response spectrum (Figure 5. 59b).

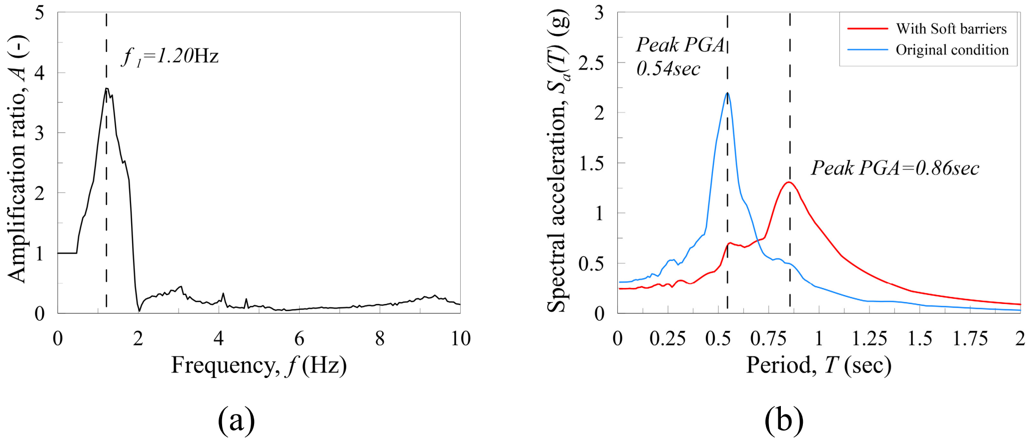

Figure 5. 59. (a) Acceleration mplification function between the bottom base of the soft caisson and the base of the structure; (b) acceleration response spectrum between the original soil condition and with soft caisson

There is a translation of the natural period of vibration of the ground compared to the case without intervention. In particular, the peak at a frequency of 1.20Hz corresponds to the translational vibration frequency of the soft caisson. Same results can be found with the earthquake in Y-direction (the soft caisson is symmetrical). The natural period of vibration of the structure with soil-structure interaction is identical to that already assessed for the isolated tower case (Figure 5. 32). The change in the frequency content of the seismic signal produced by the soft caisson obviously produces a different demand on the structure (Figure 5. 60).

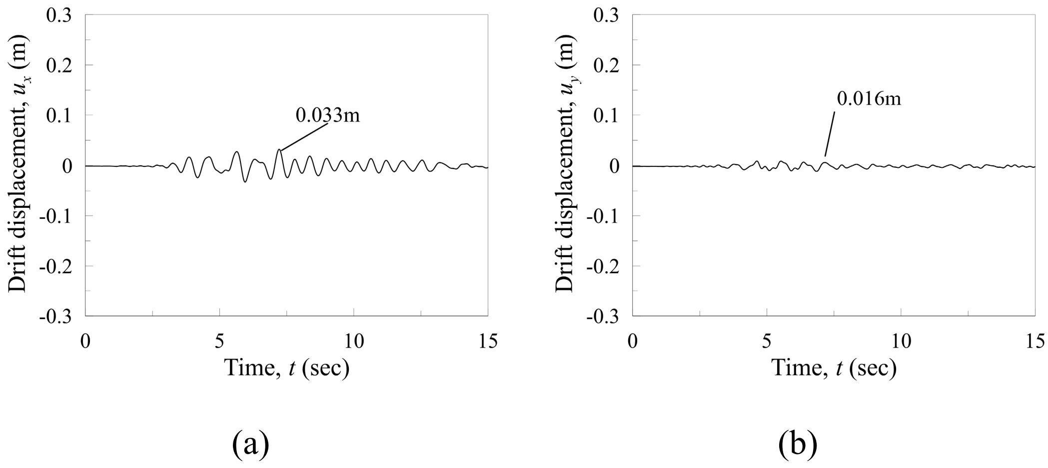

Figure 5. 60. Structural drift demand in complaint base condition with soft caisson in X-direction (a) and Y-direction with M1 masonry properties.

The reduction in structural displacement is enormous. The efficiency in the X-direction in terms of drift reduction is about 87% and in Y-direction about 57%.

M2 Masonry Properties

The considerations made with M1 type structure may be similar in the case of M2 structure. The period of the caisson is practically identical in the two cases. It is possible, therefore, to calculate the structural displacements.

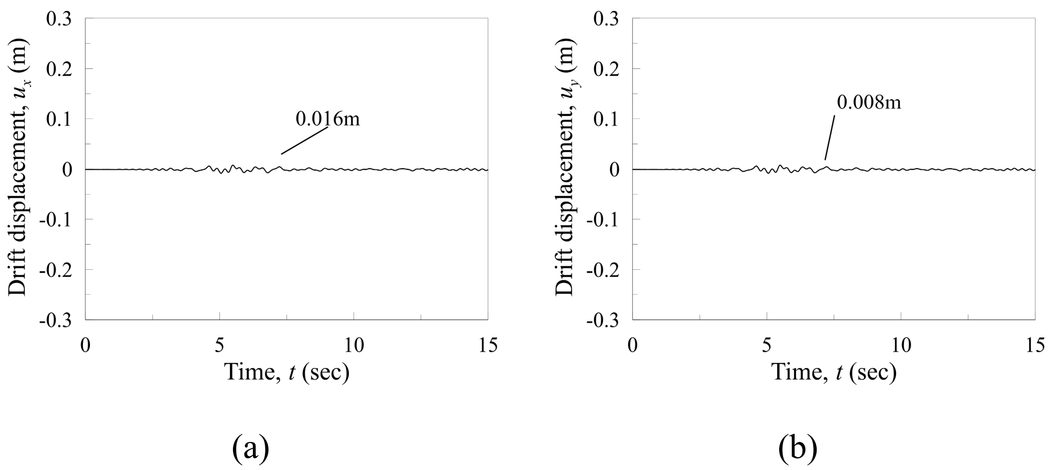

Figure 5. 61. Structural drift demand in complaint base condition with soft caisson in X-direction (a) and Y-direction with M2 masonry properties.

In this case the efficiency in terms of reduction of structural displacements is 68% in the X-direction and 38% in the Y-direction. The use of soft barriers, although much more technologically complicated than lateral disconnection, appears to be extremely efficient for the Tower.

The main difference between the lateral disconnection and the soft barrier interventions is the possibility to engineering design. While lateral disconnection necessarily depends on the ground conditions and can sometimes be completely useless or ineffective, the soft box can always be designed in such a way to generate reductions in seismic actions. Lateral disconnection has no real design but its effect can be studied and its possible benefits highlighted. Table 5. 8 shows the values of the structural displacements generated by the various geotechnical seismic isolation measures compared with the NO GSI case (Isolated Tower). In visco-elastic analyses, soft barriers are certainly the GSI intervention able to preserve and protect the conservation of the Tower19.

Table

Table 5. 8. Drift structural displacement in visco-elastic analysis with GSI tecniques.

MITIGATION PROVIDED BY GSI (visco-elastic)								
	Isolated Tower (NO GSI)		**Lateral Disconnection** (up to foundation level)		**Lateral Disconnection** (inside limestone layer)		**Soft Barrier** (60m X 60m X 17.5m)	
	$u_{d,x}$ (m)	$u_{d,y}$ (m)	$u_{d,x}$ (m)	$u_{d,y}$ (m)	$u_{d,x}$ (m)	$u_{d,y}$ (m)	$u_{d,x}$ (m)	$u_{d,y}$ (m)
M1	0.196	0.025	0.233	0.032	0.087	0.065	0.033	0.016
M2	0.053	0.014	0.124	0.017	0.063	0.046	0.016	0.008

5.5 Non-linear plastic analysis of Isolated Tower

In this chapter, the case of isolated tower with M1 properties will be investigated through non-linear plastic analysis. Since it was evident from the visco-elastic analyses that the M1 isolated tower is the most critical configuration, more advanced material model, to include non-linearities and plasticity both in the structure and in the soil, has been used.

The selected material model for the soil is *Hardening Soil Small Strain*. The strength parameters of the soil were obtained through the N_{SPT} values, while the stiffness parameters were calibrated in order to obtain the same small strain shear stiffness profile as in the visco-elastic analyses. The procedure used to find the HS_{ss} parameters has already been shown in paragraphs 3.3.2. The value of $\gamma_{0.7}$ was determined from the literature curves proposed for one-dimensional visco-elastic equivalent analyses. The *Drained* condition was set for all materials above the water table, while the *Undrained A* condition was set for those below the water table in which stiffness and strength are defined in terms of effective properties. Table 5. 9 shows all calibrated parameters for soil layers.

Table 5. 9. Calibration of HSss parameters for non-linear modelling

Parameters	Fill	LS-1	LS-2	LS-3	Clay-1	Clay-2	Clay-3	Sand	Clay-4	Clay-5	Clay-6	Clay-7	Clay-8	Clay-9	Clay-10
Material Type	Drained	Drained	Und-A	Und-A	Und-A	Und-A	Und-A	Und-A	Und-A	Und-A	Und-A	Und-A	Und-A	Und-A	Und-A
Unit weight, γ (kN/m^3)	18.4	21.4	21.2	21.0	19.3	19.2	20.0	20.6	19.9	20.5	20.4	20.8	20.7	21.4	20.7
Deviator reference mod., E_{50}^{ref} (MPa)	10	231	228	226	56	56	142	223	140	221	221	277	277	411	410
Compression reference mod., E_{oed}^{ref} (MPa)	10	231	228	226	56	56	142	223	140	221	221	277	277	411	410
Load-unloading mod., E_{ur}^{ref} (MPa)	29	692	685	679	169	169	426	668	421	664	662	831	830	1232	1232
Ref. shear strain, $\gamma_{0.7}$ *(-)*	0.4300E-3	0.1300E-3	0.1300E-3	0.1300E-3	0.4300E-3	0.4300E-3	0.4300 E-3	0.2400E-3	0.4300E-3	0.8000E-3	0.8000E-3	0.8000E-3	0.8000E-3	0.8000E-3	0.8000E-3
Ref. Shear modulus., G_0^{ref} (MPa)	60	433	428	425	174	173	289	417	288	415	414	520	519	770	769
Dependence of stress level, m (-)	0.5	0.5	0.5	0.5	0.5	0.5	0.5	0.5	0.5	0.5	0.5	0.5	0.5	0.5	0.5
Poisson ratio for loading-unloading, v_{ur}(-)	0.2	0.2	0.2	0.2	0.2	0.2	0.2	0.2	0.2	0.2	0.2	0.2	0.2	0.2	0.2
Ref. stress, p_{ref} (kPa)	27.50	67	107	132	154	172	192	211	230	253	275	295	316	341	362
Failure ratio, R_f	0.9	0.9	0.9	0.9	0.9	0.9	0.9	0.9	0.9	0.9	0.9	0.9	0.9	0.9	0.9
Cohesion, c (kPa)	40	135	135	135	125	125	200	1	180	220	250	250	250	250	250
Shear strength angle, φ (°)	27	40	40	40	27	27	27	40	27	27	27	27	27	27	27
Dilation angle, ψ (°)	0	0	0	0	0	0	0	10	0	0	0	0	0	0	0

Mohr-Coulomb model was used for the Tower material. The visco-elastic properties are identical to those already used in the previous analyses for M1 masonry, while an average uniaxial compressive strength, f_m, equal to 1MPa was selected. The limit value of tensile strength, f_t, has been set equal to 1/5 of the compressive strength (0.2 MPa). These values have been extrapolated from the Italian NTC2018 (IBC2018) code for existing masonry buildings.

From these values it was possible to derive the angle of friction and cohesion of Mohr-Coulomb model:

$$\varphi' = arcsen(\frac{f_m - f_t}{f_m + f_t}) \tag{5. 1}$$

$$c' = \frac{f_m}{2\sqrt{K_p}} \tag{5. 2}$$

The friction angle is equal to 41.81° while the cohesion is 223kPa. These properties result in very poor masonry that is highly prone to plasticisation.

The introduction of a more complex material model such as HS_{ss} generated much more time-consuming analyses. For this reason, as already done, only the first 15sec of seismic signal will be analysed. As first result, it is significant to compare the seismic signal (FIM=foundation input motion) at the base of the structure (-5.5m depth) between the visco-elastic model and the plastic model (HS_{ss}) (Figure 5. 62a). It is also possible to compare the acceleration spectrum between the two different analysis (Figure 5. 62b).

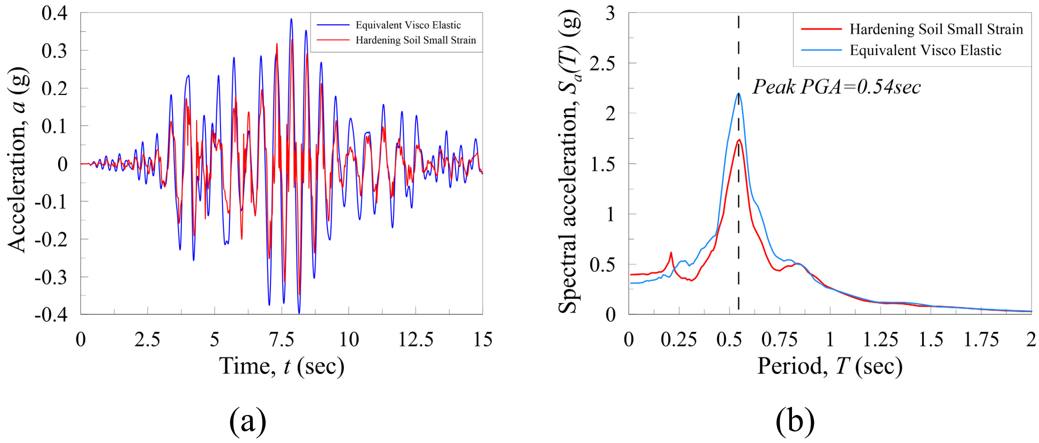

Figure 5. 62. (a) Comparison of seismic signal recorded in visco-elastic and HSss analyses; (b) acceleration response spectrum

The foundation input motion with HS_{ss} is slightly lower than visco-elastic analysis. This is a predictable effect. The study of the local seismic response using the Hardening Soil model is much more complex and is carried out in effective stress. On the basis of the mean effective stress state, the shear stiffness is updated for each step of the analysis and in the whole layers, beneath the water table, is imposed the *Undrained A* condition (stiffness and strength in terms of effective stresses). As result, possible variations of pore water pressures due to deviatoric-volumetric strain coupling under cyclic loading are considered. The local seismic response with visco-elastic models should coincide perfectly with the HS_{ss} local seismic response model only at low levels of shear deformation. As it is possible to see from Figure 5. 62b also in the analysis with HS_{ss} there is a peak of acceleration demand at about 0.54sec.

Regarding the material model of the Tower, it is important to highlight that the introduction of plasticity obviously leads to a different demand in terms of structural displacement. Due to the high seismic actions, the tower modifies its lateral stiffness and induces additional plasticisation in the adjacent soil (secondary plasticisation). For this reason, the natural period of vibration of the Tower is constantly changing during the dynamic non-linear analysis. The concept of a single natural period of vibration itself has no sense in non-linear plastic dynamic analyses. Subsequently, as damage parameter, both the roof structural displacements and the smallest compressive (or largest tension) principal stresses, in the instant of time of maximum roof displacement, are considered.

Figure 5. 63a and Figure 5. 64a show the values of the roof structural drifts in X and Y direction while Figure 5. 63b and Figure 5. 64b shows the principal minimal tensile stresses at the maximum roof structural displacement istant of time. With reference to Figure 5. 63b, it can be seen that the tensile stresses are very high, around 200kPa, in several areas. This means that several plastic points are generated in the Tower. The tensile limit strength is exceeded specially in the X-direction, at the points of greatest flexural stress (*i.e.* at the base of the load bearing masonry walls). According to the modal analysis in SAP2000, this is clearly determined by a cantilever vibration predominant mode (>60% effective mass). This obviously generates an alteration of the translational stiffness of the system. Please note that the areas circumscribed by the maximum tensile stresses (200kPa in red color) are plasticised in tension.

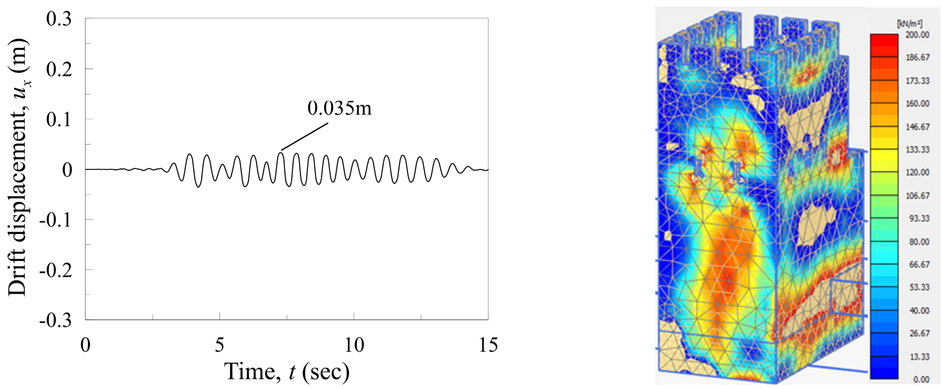

(a) (b)

Figure 5. 63. (a) Structural displacements in non-linear analyses with earthquake in X direction (b) largest tension principal stresses in the tower at the 5.94sec instant of time.

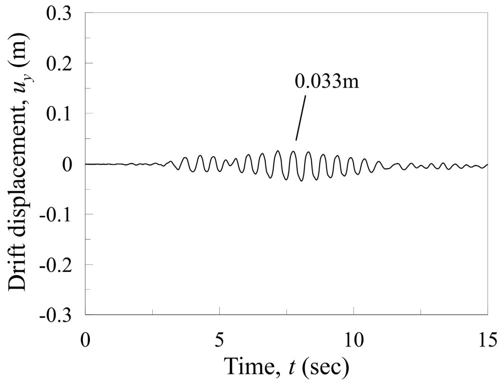

(a)

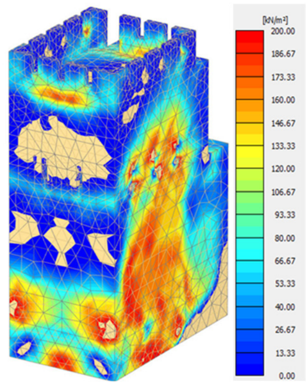
(b)

Figure 5. 64. (a) Structural displacements in non-linear analyses with earthquake in Y direction (b) largest tension principal stresses in the tower at the 7.15sec instant of time.

The demand in terms of structural displacement, with visco-plastic Mohr Coulomb model, especially in X-direction, shows significant differences with the visco-elastic one. This effect is linked to both a slightly different foundation input motion between the two types of analysis and to the local plasticisations of different structural and soil zones, which increase the natural period of vibration. In visco-elastic analyses, the natural period of vibration has a fixed and constant value throughout the whole analysis (almost coinciding with the peak acceleration spectrum in X-direction; close to 2g acceleration demand). In visco-plastic analyses, as soon as the tensile strength are reached, the lateral stiffness changes and the natural period of vibration increases. In particular, in the visco-elastic regime, the structural displacement, in the X-direction only, is greater than in the plastic regime. Indeed, in plastic analyses the tower responds dynamically as a totally different system characterised by a different stiffness due to the local plasticisations. As already stated, the maximum demand in terms of absolute acceleration is concentrated around natural period of vibration equal to 0.54sec as well as the maximum demand in terms of relative displacements. Once this value is exceeded, there is a sharp drop in acceleration and relative displacement demand. It can be seen that in the Y-direction this effect does not occur and the structural displacements are greater in the plastic domain. Obviously, this situation occurs for the particular earthquake selected and for the particular resonance conditions between the Tower and the FIM. A study conducted with 7 spectro-compatible earthquakes, or with different strength parameters for the Tower, would have led to different considerations.

To assess how the soil and structure plasticization influence the effectiveness of the geotechnical seismic isolation techniques described, the numerical analyses with the lateral disconnection intervention (up to the foundation laying level and up to the limestone layer) and soft barriers were carried out.

5.5.1 Lateral Disconnection up to foundation level.

The lateral confinement effect on the foundation, generated by the adjacent soil, was removed by generating a gap of 0.5m width. Even in plastic analyses, the demand in terms of displacement and principal tensile stresses contour show the ineffectiveness of this intervention especially in the X-direction (Figure 5. 65).

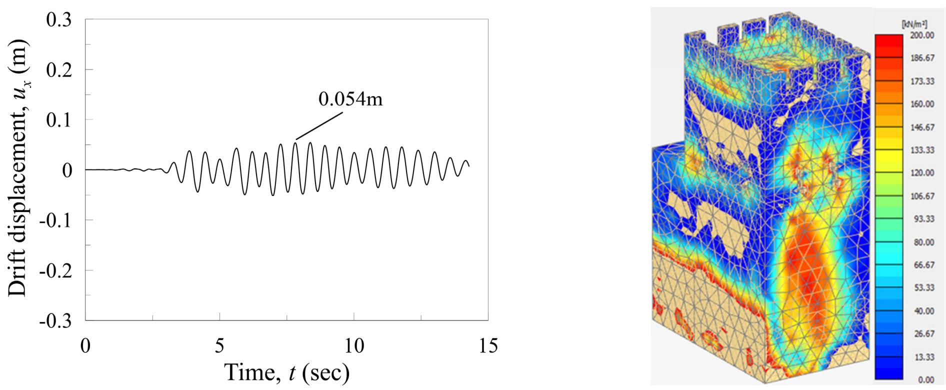

(a) (b)

Figure 5. 65. (a) Structural displacements in non-linear analyses with earthquake in X direction with lateral disconnection up to foundation level (b) largest tension principal stresses in the tower at the 5.59sec instant of time which correspond to the maximum total displacement of the tower roof.

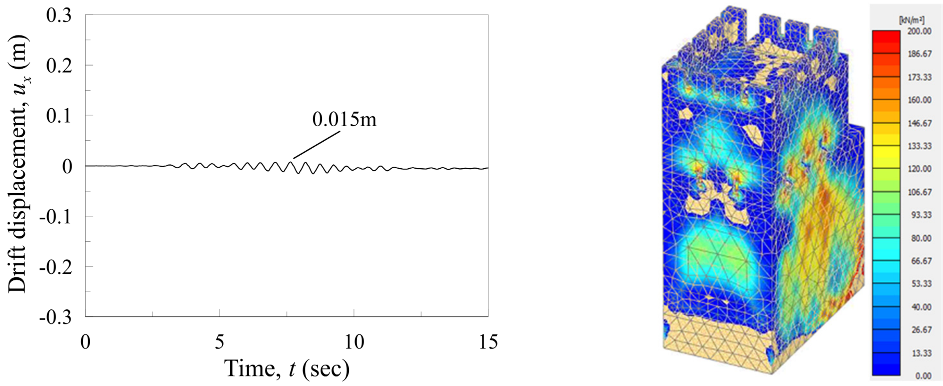

(a) (b)

Figure 5. 66. (a) Structural displacements in non-linear analyses with earthquake in Y direction with lateral disconnection up to foundation level (b) largest tension principal stresses in the tower at the sec instant of time which correspond to the maximum total displacement of the tower roof.

It is also possible to see that the largest tension principal stresses, especially in X direction, is very high (200kPa), indicating a rather widespread level of damage at the base.

5.5.2 Lateral Disconnection inside the limestone layer.

As already done in the visco-elastic analyses, the disconnection was also extended in the limestone for a length of 7.5m. Figure 5. 67 and Figure 5. 68 show the results in terms of roof structural displacement and the principal minimal tensile stresses.

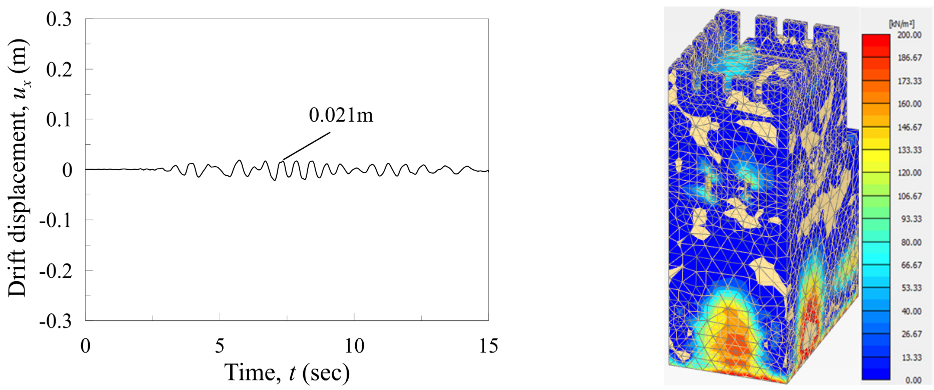

(a) (b)

Figure 5. 67. (a) Structural displacements in non-linear analyses with earthquake in X direction with lateral disconnection inside the limestone layer (b) largest tension principal stresses in the tower at the 5.24sec instant of time which correspond to the maximum total displacement of the tower roof.

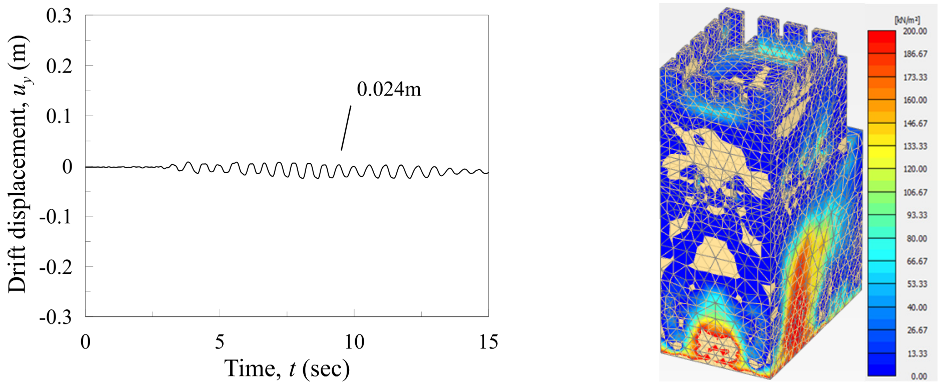

(a) (b)

Figure 5. 68. (a) Structural displacements in non-linear analyses with earthquake in Y direction with lateral disconnection inside the limestone layer (b) largest tension principal stresses in the tower at the 5.56sec instant of time which correspond to the maximum total displacement of the tower roof.

Observing the largest tension principal stresses, it is possible to notice that they have a more limited spreading in the structure. However, it is important to consider that the creation of a gap beyond the base of the foundation could generate a significant reduction in vertical static safety conditions that may be considered unacceptable when compared to the benefits in the seismic behaviour. For this reason, this intervention does not seem to be a viable solution.

5.5.3 Soft Barriers

Finally, the soft barriers were implemented in the numerical model with nonlinear tower and soil. As it is possible to see from Figure 5. 69 (in X direction) and Figure 5. 70 (in Y-direction), the maximum structural displacement values, as well as the largest tension principal stresses, are not very pronounced. The structure does not suffer major damage and it is not incipiently collapsing. The tensile stresses developed are far from their limit value.

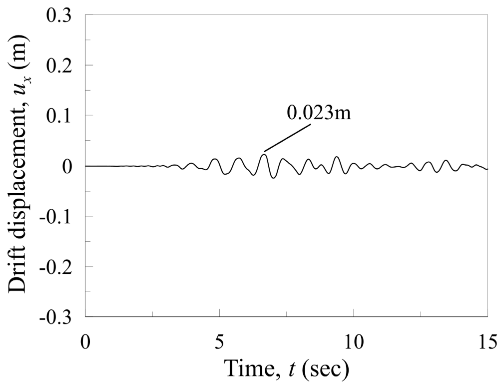

(a)

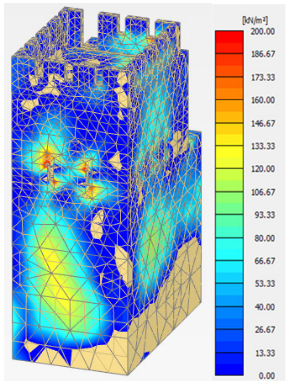

(b)

Figure 5. 69. (a) Structural displacements in non-linear analyses with earthquake in X direction with soft caisson (b) largest tension principal stresses in the tower at the 6.60sec istant of time which correspond to the maximum total displacement of the tower roof.

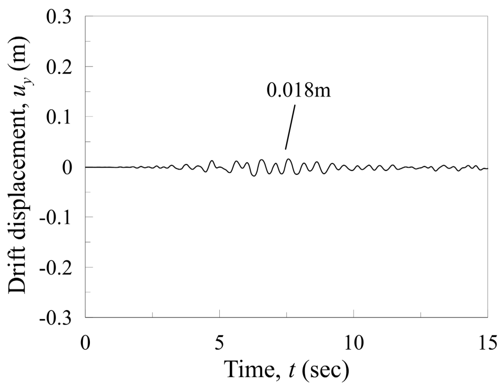

(a)

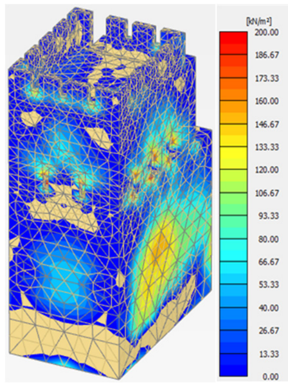

(b)

Figure 5. 70. (a) Structural displacements in non-linear analyses with earthquake in Y direction with soft caisson (b) largest tension principal stresses in the tower at the 6.25sec istant of time which correspond to the maximum total displacement of the tower roof.

The soft barriers seem to represent the geotechnical seismic isolation intervention that, in the best way (reduction of structural displacements and tensile stresses), manages to reduce the seismic vulnerability of the Tower.

Table 5. 10 shows all the structural displacement values recorded in order to show the mitigation generated by the different GSI techniques.

Table 5. 10. Mitigation provided by GSI techniques in plastic analysis in terms of structural roof displacement demand

MITIGATION PROVIDED BY GSI (plastic)								
	Isolated Tower (NO GSI)		**Lateral Disconnection** (up to foundation level)		**Lateral Disconnection** (inside limestone layer)		**Soft Barrier** (60m X 60m X 17.5m)	
	$u_{d,x}$ (m)	$u_{d,y}$ (m)	$u_{d,x}$ (m)	$u_{d,y}$ (m)	$u_{d,x}$ (m)	$u_{d,y}$ (m)	$u_{d,x}$ (m)	$u_{d,y}$ (m)
M1	0.035	0.033	0.054	0.015	0.021	0.024	0.023	0.018

As expected, lateral disconnection becomes slightly more efficient with plastic soil model. This is because plastic phenomena such as gapping or sliding are not allowed in the visco-elastic regime. Such non-linear phenomena tend, in general, to increase the dissipation of the earthquake energy in the soil and to reduce the seismic actions as well as further lengthening the period of the structure computing the SSI. However, these non-linear phenomena are also closely linked to the stiffness and strength properties of the soils and the structure. The major benefits of non-linear analyses can only be validated after a very specific site investigation on the Tower19 materials.

5.6 Final considerations

The study of the propagation of the 1999 Kocaeli seismic signal, with a direct FEM approach, highlighted the strong seismic vulnerability of the Tower19 and the high seismic hazard of the site considered. The case study analysed is very complex due to the lack of precise information regarding the tower material and for the particular seismic hazard. The effects of the soil-structure interaction, are generally moderate. The main problem is determined by a very high seismic signal at the base of the structure caused by a strong stratigraphic amplification in the soil bank. Furthermore, the structure in its most probable configurations (Isolated Tower or with adjacent wall) has a natural period of vibration very close to the peak of the acceleration spectrum. The Tower has considerably high global structural displacement demands both in the visco-elastic and plastic domain. The plastic analyses confirmed the plasticization of several zones with consequent structural damage.

The implementation of geotechnical seismic isolation measures such as lateral disconnection and soft barriers highlighted the strengths but also weaknesses of these techniques. Lateral disconnection up to the foundation level is a detrimental intervention for this particular structure and for this seismic input. Unfortunately, this is determined by the very simplicity of the technique which does not provide any anti-seismic engineering design but only the prediction of a different soil-structure interaction which if not leading to positive results cannot be altered. On the other hand, the introduction of soft barriers is definitely an intervention that leads to significant earthquake benefits. However, it is worth noting the size of the soft caisson built to achieve these benefits: 60mx60mx17.5m. The technological effort is considerable as well as, probably, the economic issues. The complexity of this case study highlights the importance to conduct local seismic response analyses and to consider the soil-structure interaction especially when designing geotechnical seismic isolation techniques. The fact that lateral disconnection technique up to the foundation level does not lead to positive results was a possibility already contemplated. Not all anti-seismic strategies can be followed in all cases but a negative result is still a result.

References

Amorosi, A., Boldini, D., Elia, G. (2010). “Parametric study on seismic ground response by finite element modelling”. *Computers and Geotechnics*, 515–528.

Flora, A., Chiaradonna, A., de Sanctis, L., Lignola, G.P., Nappa, V., Oztoprak, S., Ramaglia, G., Sargin, S. (2021). “Understanding the Damages Caused by the 1999 Kocaeli Earthquake on One of the Towers of the Theodosian Walls of Constantinople”. *International Journal of Architectural Heritage.* https://doi.org/10.1080/15583058.2020.1864512

Hashash, Y., Park, D. (2002). “Viscous damping formulation and high frequency motion propagation in nonlinear site response analysis”. *Soil dynamic earthquake engineering*, **22** (7):611–624.

Hudson, M., Idriss, I., Beirkae, M. (1994). QUAD4M User’s manual.

IBC2018 Italian Building Code: Ministerial Decree 17Geunary 2018, 2018. Aggiornamento Delle Norme Tecniche delle Costruzioni. Ministry of Infrastructure and Transport: Rome, Italy

Ince, G. C., Yildirim, M., Ozaydin K., Ozner P.T. (2008). “Seismic microzonation of the historic peninsula of Istanbul”. *Bulletin of Engineering Geology and the Environment* **67**:41-51. doi:10.1007/s10064-007-0099-9.

Ispir, M., Demir C., Alper I., Kumbasar N. (2014). “An outline of the seismic damages of several monumental structures in Istanbul after historical earthquakes”. *Workshop on Seismicity of Historical Structures*, Istanbul, November 2014**.**

Jiang, X., Yan, Z. (1998). “Earthquake response analysis of building foundation- building interaction system.” J. Vib. Eng. 11 (1): 31–37.

Kuhlemeyer, R. L., Lysmer J. (1973). “Finite Element Method Accuracy for Wave Propagation Problems”. *Journal of Soil Mechanics & Foundations*, Div. ASCE **99**(SM5):421–427.

Lourenco P.B., (1998). “Experimental and numerical issues in the modelling of the mechanical behaviour of masonry”. *In Structural Analysis of Historical Construction* II, ed. P. Roca, J. L. Gonzalez, E. Onate, and P. B. Lourenco.

Lourenco, P. B. (2002). “Computations of historic masonry structures”. *Progress in Structural Engineering and Materials* **4** (3):301–19. doi:10.1002/pse.120.

Park,W.J. (2010). “Effect of degree of weathering on dynamic properties of weathered granite soils”. *Proceedings of the 5th International Conference on Recent Advances in Geotechnical Earthquake Engineering and Soil Dynamics*, San Diego California.

Seed, H. B., Idriss, I. M. (1970). “Soil moduli and damping factors for dynamic response analysis”. *Report No EERC 70- 10*, University of California, Berkeley, California, USA.

Turnbull, S.R., Dennis, P. (2012) “The walls of Constantinople AD 324-1453”. *Bloomsbury Publishing*

Veletsos, A.S., Meek, J.W. 1974. “Dynamic behavior of building-foundation systems”. *Earthq Eng Struct Dyn*. 3(2):121-38.

Vucetic, M., Dobry, R. (1991). “Effect of soil plasticity on cyclic response”. *Journal of Geotechnical Engineering*, ASCE **117** (1):89–117

6. CONCLUSIONS

The aim of this thesis was to evaluate the effects of two geotechnical seismic isolation techniques. The "*Lateral Disconnection of shallow foundations from adjacent soil*", is mainly related to a modification of the soil-structure interaction and is completely new in the field of geotechnical seismic isolation techniques. The centrifuge test described has provided experimental evidence for the beneficial effect of introducing a lateral disconnection at foundation level as a simple and innovative technique to reduce the seismic vulnerability of existing buildings. The lateral disconnection was able to elongate the natural resonant period of the structure by about 60% relative to the structure with conventional embedded foundations during the centrifuge test. On the other hand, the effects in terms of reduction of static load-bearing capacity are irrelevant. The numerical back analysis of the centrifuge test showed some fundamental aspects about the lengthening of the natural period of vibration such as the importance of the structure to soil relative stiffness parameter. This result was the base for the next dimensionless parametric study. Based on the application of Buckingham's Theorem, all variables, influencing the natural period lengthening of a structure with SSI, have been a-dimensioned. In order to understand the importance of different adimensional parameters, several numerical FEM model were created. The relative structure to soil stiffness as well as the ratio between the embedment and width of the foundation are the parameters that most influence the period elongations related to the conventional embedded foundation. In particular, the higher these dimensionless parameters, the greater the period elongation generated by the lateral disconnection technique. A very simple and preliminary formulation has been proposed to estimate the period elongations between the connected (*NO GSI*) and disconnected (*GSI*) structure, in plane strain condition, under the visco-elasticity assumptions, depending on the most important adimensional parameters found. Subsequently, a study on the effects of the lateral disconnection technique in a real seismic hazard scenario was carried out. Seven spectro-compatible accelerograms were applied at the bottom base of the numerical model showing the different efficiency parameters generated by the lateral disconnection. With specific reference to traditional masonry structures with relatively deep direct foundations, the proposed geotechnical seismic isolation technique may provide a significant reduction of the structural distortions and hence damage caused by inertial forces, provided that rigid body rocking is possible from the kinematic point of view. However, the idea of increasing structural period by lateral disconnection may not be appropriate for all the structures and site conditions. In fact, for structures with a very short natural period, the lateral disconnection may generate higher seismic demand because the period of the structure will be closer to the peak of the acceleration response spectrum.

The use of "*Soft Lateral and Horizontal Inclusions*" as seismic risk mitigation intervention was first investigated through a large number of laboratory tests. In order to provide the dynamic parameters of sand-SAP mixture, bender element, resonant column and simple cyclic shear tests were carried out. A new formulation was proposed to compute the shear wave velocity in the soil-SAP mixtures as a function of the mean effective stress state and the volumetric percentage of SAP in the mixture. Simple cyclic shear tests, on the other hand, were able to confirm the high damping capacity of these mixtures as the shear deformation increases. The effect of inserting one meter of horizontal sand-SAP mixture in the soil, at different treatment depth, was then studied parametrically with mono-dimensional non linear equivalent analysis. Subsequently, the two-dimensional effects generated by a soft SAP caisson were studied with different numerical FEM model. By increasing the *B/H* ratio of the soft caisson, its natural traslational period of vibration increases and, therefore, the seismic isolation effect become remarkable. The effectiveness of the soft barriers has also been investigated in a real seismic hazard context, under the seismic loading of seven spectro-compatible earthquakes. In order to study the dynamic effect of the soft caisson, a simplified two degrees of freedom dynamic system was also proposed. In addition, a phase-by-phase intervention design strategy has been outlined, leading to excellent levels of seismic isolation. Finally, a number of important technological aspects were outlined, as well as some possibilities for implementing the soft caisson system in a real context.

In chapter 5, the two geotechnical seismic isolation techniques described are implemented for a real case study. A rigorous numerical study has characterised the condition in which the Tower 19, part of the defensive walls of Constantinople, was stood before it was affected by the 1999 Kocaeli earthquake that almost completely destroyed it. The amplification of the seismic signal in the soil bank is considerable and generates strong accelerations at ground level. Several contact configurations between the Tower and the wall were studied with visco-elastic material model. The Isolated Tower or Disconnected Wall Tower configuration generates significantly high stresses on the structure and may represent the most realistic geometric configuration. The technique of lateral disconnection up to the foundation base level has been implemented for the case of isolated tower. The conditions of the tower's resonance period with respect to the acceleration response spectrum (just to the left of the acceleration peak) foreshadowed the negative effects of such an intervention. The disconnection generates an increase in the natural period of vibration of the structure which, unfortunately, is not able to exceed the peak of the acceleration spectrum. On the contrary, it leads to an increase in seismic actions. The positioning of the Tower's foundations on the limestone made it possible to extend the lateral disconnection also inside the rock. In this case, a benefit of this technique could be observed for the poorer kind of masonry. However, the static vertical factor of safety, with this alternative solution, may be too low to be considered applicable. In contrast, the soft caisson design leads to an enormous reduction in seismic actions. The size of the soft caisson to be constructed is considerably large and the intervention may be costly. In the last part, more complex material models were used for both soil and structure modelling. The plasticisation of the soil as well as that of the structure lead to a different displacement demand than in visco-elastic regime. Nevertheless, such analyses confirm the ineffectiveness of the lateral disconnection technique up to the foundation level and the effectiveness of the soft barriers. It is important to note that this study considered the effect of a single earthquake. In the context of a vulnerability assessment, a single earthquake may not be sufficient to analyze the benefits of the above techniques. For this reason, future analyses will be performed using a set of 7 spectro-compatible earthquakes. The purpose of this chapter was to understand what would have happened if geotechnical seismic isolation techniques had been implemented during the Kocaeli earthquake.

These new geothecnical seismic isolation techniques outlined have their pros and cons. The pros of the **lateral disconnection** technique can be summarised as follows:

- Relative ease to implement for both existing and new buildings;
- Relatively low cost of implementation;
- The seismic improvements introduced by the technique do not significantly change the static factor of safety;
- Aesthetic integrity of historic buildings preserved;
- Depending on the seismic hazard and soil-structure interaction, the efficiencies in terms of reductions in total accelerations, Arias Intensity and structural displacements can easily reach values of more than 30-40%.

The cons of **lateral disconnection** are:

- Is not able to provide a total seismic isolation but it could be a valid partial seimic retrofitting;

- In order to achieve a total seismic retrofitting, structural interventions may also be necessary;
- Depending on the local seismic hazard and soil-structure interaction may be completely ineffective or detrimental;
- Does not provide any anti-seismic engineering design but only the prediction of a different soil-structure interaction which if not leading to positive results cannot be altered;

The pros of **Soft Barrier**:

- Based on the design algorithm outlined, it can lead to enormous advantages in terms of reductions in seismic action (*i.e.* total seismic isolation);
- The advantages of this technique are maximised for buildings with a low natural period of vibration; especially historic buildings are characterised by a low first natural period of vibration (generally less than 0.5sec)
- Aesthetic integrity of historic buildings preserved;

The cons of **Soft Barrier**:

- High technological complexity to create the soft caisson;
- Even if the SAP is not particularly expensive (*i.e* one Kg of SAP at powder state is able to absorg about 150 litres of water and costs about 50 euros), costs are expected to be high for the complex technology to be used in real scale implementation;
- The construction of the soft caisson requires large space at the side of the building which may not be available;
- It is necessary to evaluate the reduction of the static safety factor related to the load bearing in order to assess the feasibility of the intervention.

Future research work could evaluate the effects of such GSI techniques through real field tests. Especially for soft barriers their implementation below existing buildings is still an issue and should certainly be investigated. In order to compare the proposed GSI techniques with others structural stratregies, the benefits in terms of costs could be assessed and compared. A possible development of chapter 5 could be the evaluation of fragility curves for the Tower19 with and without GSI intervention.

This thesis hopes to communicate and convey to the reader the passion for geotechnical seismic isolation that has characterised all the studies conducted. Geotechnical seismic isolation is still in its infancy and future work may enhance its potential.

Author's publications

- Somma F., Bilotta E., Flora A., Viggiani G.M. (2021). Centrifuge modelling of shallow foundations lateral disconnection to reduce seismic vulnerability. Journal of Geotechnical and Geoenvironmental Engineering. doi: 10.1061/(ASCE)GT.1943-5606.0002746
- Somma F., Flora A., Bilotta E. Viggiani G.M. (2021). Numerical analysis on shallow foundations lateraldisconnection. 8th ECCOMAS Thematic Conference on Computational Methods in StructuralDynamics and Earthquake Engineering. Athens, Greece, 27–30 June 2021.
- Somma, F., Millen, M., Bilotta, E. et al. (2020). Vulnerability assessment of RC buildings to lateral spreading. Bull Earthquake Eng 18, 3629–3657 (2020). https://doi.org/10.1007/s10518-020-00847-7
- Somma F., Bilotta E., Flora A., Viggiani G.M. (2022). Lateral disconnection of foundations: a respectful seismic isolation of historic building. In Geotechnical Engineering for the Preservation of Monuments and Historic Sites, TC301.
- Somma F., Cozzolino E., Flora A. (2021). Experimental characterization of the dynamic properties of SAP-sand mixtures as seismically isolating barriers. Geotechnical and Geological Engineering (in Pubblication).
- Somma F., Lignola G., Ramaglia G., de Sanctis L., Iovino M, Oztoprak S., Flora A. (2022). An interdisciplinary approach to interpret earthqauake damages to an historic tower and to propose respectful mitigation measures. Bull Earthquake Eng. (submitted).